



A DEM for visualising damage evolution and  
predicting failure of composite lamina under  
uniaxial and biaxial loads

*by*

Yaser Ismail

A Thesis submitted for the degree of Doctor of Philosophy of the  
University of Lancaster

**Under supervision of**

Professor Jianqiao Ye  
Dr Dongmin Yang

June 2017

# 1 Contents

<b>1. Literature Review .....</b>	<b>4</b>
1.1 Background .....	4
1.2 Physical damage mechanism in fibre-reinforced composites .....	9
1.3 Micromechanical strategies used in composite materials.....	12
1.4 Analytical methods .....	14
1.4.1 Mean-field methods.....	14
1.4.2 Variational bounding methods.....	14
1.5 Representative volume element.....	14
1.6 Boundary conditions.....	15
1.6.1 Symmetric boundary conditions .....	15
1.6.2 Periodic boundary conditions .....	17
1.7 Computational methods .....	17
1.7.1 Periodic micro-field approaches .....	17
1.7.2 Windowing approach.....	18
1.7.3 Embedding approaches.....	19
1.8 Failure criteria in FRPs.....	20
1.8.1 Non-physical or not associate with the failure mode.....	21
1.8.2 Physical or associate with the failure mode.....	21

1.9	Damage levels in composites.....	23
1.9.1	Damages at macro-scale.....	23
1.9.1.1	Maximum stress criterion .....	24
1.9.1.2	Tsai-Hill criterion .....	25
1.9.1.3	Tsai-Wu failure criterion .....	26
1.9.1.4	Hashin's criteria .....	27
1.9.1.5	Puck's criterion.....	28
1.9.2	Damages at micro-level.....	30
1.10	Discrete element method .....	35
1.10.1	Force-displacement law.....	36
1.10.1.1	Contact-bond model.....	37
1.10.1.2	Parallel bond and moment resistance.....	40
1.10.1.3	Displacement-softening model.....	44
1.10.2	Law of motion .....	46
1.10.3	Mechanical timestep.....	48
1.10.4	Loading methods.....	50
1.10.5	Biaxial loading methods.....	50
1.10.5.1	Servo-control mechanism .....	50
1.10.5.2	Applied forces to boundary particles .....	52
<b>2</b>	<b>Generating random fibre distributions.....</b>	<b>53</b>
2.1	Introduction .....	53

2.2	Algorithm development using DEM .....	55
2.3	Statistical characterisation.....	58
2.3.1	Nearest neighbour distribution.....	59
2.3.2	Second-order intensity function .....	61
2.3.3	Radial distribution function .....	64
2.4	Prediction of mechanical properties .....	66
2.4.1	Finite element analysis .....	66
2.4.2	Analysis and results.....	69
2.4.2.1	Calculating mechanical elastic properties .....	69
2.4.2.2	RVE with continuous and non-continuous distributed fibres over edges	72
<b>3</b>	<b>Discrete element modelling of unidirectional fibre-reinforced polymers under transverse tension .....</b>	<b>74</b>
3.1	Introduction .....	74
3.2	RVE generation and discretisation .....	76
3.3	Contact models .....	79
3.4	Results and discussions .....	81
3.4.1	Stress distributions .....	81
3.4.2	Damage progression .....	82
3.4.3	Sensitivity study of interface parameters on interfacial debonding	85
<b>4</b>	<b>A DEM model for predicting elasticity of composite lamina .....</b>	<b>89</b>
4.1	Introduction .....	89
4.2	Analytical methods used in this chapter .....	90

4.2.1	The rule of mixtures (RoM) .....	90
4.2.2	The Mori-Tanaka method .....	90
4.3	Numerical methods .....	92
4.3.1	Finite element method .....	92
4.4	Discrete element model.....	94
4.4.1	Calibration of DEM model.....	95
4.4.2	DEM model generation.....	95
4.4.3	DEM simulation .....	97
4.4.4	Parametric study of contact stiffness .....	98
4.4.5	Effect of particle size on the Young's modulus and Poisson's ratio	
	103	
4.5	Results and comparison of methods .....	105
4.5.1	Effect of volume fraction on the elastic properties .....	105
4.5.2	Effect of RVE size on the elastic properties.....	109
<b>5</b>	<b>A DEM model for predicting fracture of composite lamina .....</b>	<b>112</b>
5.1	Introduction .....	112
5.2	Discrete element model to study the failure .....	114
5.2.1	Parametric study of bond strength.....	114
5.2.2	Parametric study of timestep.....	116
5.2.3	Effect of particle size on the strength.....	117
5.2.4	Prediction of stress-strain curves and damage progression under	
	transverse compression .....	119

5.2.5	Prediction of stress-strain curves and damage progression under transverse shear .....	123
5.2.6	Effect of RVE size on failure strength and failure strain.....	125
5.3	DEM modelling of RVEs under biaxial loads .....	128
5.3.1	DEM prediction of the failure envelope.....	129
5.3.2	DEM visualisation of damage evolution.....	133
5.3.3	Quantitative analysis of damage events .....	137
<b>6</b>	<b>Conclusions and future work.....</b>	<b>140</b>
6.1	Conclusions.....	140
6.2	Future work .....	143
	<b>Bibliography .....</b>	<b>147</b>
	<b>Appendix A: DEM script to generate random fibre distributions.....</b>	<b>161</b>

# List of Figures

FIGURE 1.1: TWO TYPICAL TYPES OF LAMINA. (A) UNIDIRECTIONAL LAMINA. (B) WOVEN LAMINA. (C) LAMINATE.....	5
FIGURE 1.2: BOTTOM-TOP MULTI-SCALE SIMULATION SCHEME TO PERFORM VIRTUAL MECHANICAL TESTS OF COMPOSITE MATERIALS. ....	8
FIGURE 1.3: FAILURE MICRO-MECHANISMS IN FRPs AS A FUNCTION OF LOAD CONDITIONS. (A) TRANSVERSE TENSION. (B) TRANSVERSE COMPRESSION. (C) LONGITUDINAL TENSION. (D) LONGITUDINAL COMPRESSION. (E) OUT-OF-PLANE SHEAR. (F) IN-PLANE SHEAR. ....	11
FIGURE 1.4: MATRIX CRACKS AND DELAMINATION OCCURRING AT 90/0 INTERFACE AT DIFFERENT TENSILE LOADING STAGES. ADAPTED FROM SCOTT ET AL., 2011.....	12
FIGURE 1.5: DISTRIBUTION OF FIBRES IN THE MATRIX. (A) PERIODIC SQUARE. (B) HEXAGONAL.....	16
FIGURE 1.6: DEFORMATION OF (A) SYMMETRIC BOUNDARY CONDITIONS UNDER UNIAXIAL LOADING FOR FIBRE A. (B) PERIODIC BOUNDARY CONDITIONS IN A RECTANGULAR TWO-DIMENSIONAL MODEL.....	16
FIGURE 1.7: SCHEMATIC SKETCH OF A RANDOM FIBRE/MATRIX MICROSTRUCTURE. (A) WINDOW APPROACH. (B) EMBEDDED CONFIGURATION. ....	19
FIGURE 1.8: STRESSES ON THE THREE-DIMENSIONAL OF UNIDIRECTIONAL COMPOSITE ELEMENT.....	22
FIGURE 1.9: PUCK’S ACTION PLANE (IMAGE FROM (DAVILA ET AL., 2005)). ....	29
FIGURE 1.10: STRESS–STRAIN RESPONSE OF THE MATRIX. ....	34
FIGURE 1.11: CALCULATION CYCLE IN DEM.....	36
FIGURE 1.12: CONTACT BETWEEN PARTICLES. (A) CONTACT BOND MODEL IN PFC2D (ITASCA, 2003). (B) NOTATION USED TO DESCRIBE PARTICLE-PARTICLE CONTACT BOND. ....	38
FIGURE 1.13: FORCE-DISPLACEMENT LAWS FOR THE CONTACT BOND MODEL: (A) NORMAL BEHAVIOUR, AND (B) SHEAR BEHAVIOUR.....	40
FIGURE 1.14: SCHEMATIC DIAGRAM OF THE PARALLEL BOND. ....	43
FIGURE 1.15: FORCE-DISPLACEMENT LAWS FOR THE PARALLEL BOND MODEL: (A) NORMAL BEHAVIOUR, AND (B) SHEAR BEHAVIOUR.....	44

FIGURE 1.16: CONSTITUTIVE BEHAVIOUR OF CONTACT DISPLACEMENT-SOFTENING MODEL: (A) NORMAL BEHAVIOUR, AND (B) SHEAR BEHAVIOUR.....	46
FIGURE 1.17: SCHEMATIC OF A SINGLE MASS-SPRING SYSTEM USED BY PFC TO CALCULATE THE CRITICAL TIMESTEP.....	49
FIGURE 1.18: SCHEMATIC OF A MULTIPLE MASS-SPRING SYSTEM USED BY PFC TO CALCULATE THE CRITICAL TIMESTEP. ....	49
FIGURE 2.1: SIZE DISTRIBUTION OF FIBRES. ....	55
FIGURE 2.2: PROCEDURE FOR GENERATING RANDOM FIBRE DISTRIBUTIONS USING DEM. (A) INITIAL FIBRE DISTRIBUTION IN REGULAR CUBIC ARRANGEMENT. (B) MORE DISCS ARE ADDED IN. (C) PERIODIC BOUNDARY CONDITION IS APPLIED TO MAINTAIN THE CONSTANT FIBRE VOLUME FRACTION.....	57
FIGURE 2.3: THREE FIBRE DISTRIBUTIONS WITH HIGH VOLUME FRACTIONS: (A) 60%, (B) 65%, AND (C) 68%. ....	58
FIGURE 2.4: RESULTS OF NEAR NEIGHBOUR DISTRIBUTIONS COMPARED WITH EXPERIMENTAL DATA AND RSE RESULTS. (A) 1 <sup>ST</sup> NEAREST NEIGHBOUR DISTRIBUTION. (B) 2 <sup>ND</sup> NEAREST NEIGHBOUR DISTRIBUTION FUNCTION.....	61
FIGURE 2.5: AN EXPLANATION OF THE VARIABLES IN THE SECOND-ORDER INTENSITY (OR RIPLEY'S $K$ ) FUNCTION. ....	62
FIGURE 2.6: SECOND-ORDER INTENSITY FUNCTION, COMPARED WITH EXPERIMENTAL, RSE METHOD AND CSR.....	63
FIGURE 2.7: AN EXPLANATION OF THE VARIABLES IN THE RADIAL DISTRIBUTION FUNCTION CONTAINING FOUR POINTS IN THE ANNULUS AREA. ....	65
FIGURE 2.8: RADIAL DISTRIBUTION FUNCTION FOR PRESENT METHOD AND COMPARED WITH EXPERIMENTAL RSE METHOD.....	66
FIGURE 2.9: PERIODIC BOUNDARY CONSTRAINTS APPLIED TO THE RVEs. (A) TENSION, AND (B) SHEAR.....	68
FIGURE 2.10: VON MISES STRESS DISTRIBUTION IN A RVE UNDER. (A) TENSION AND (B) SHEAR.....	69
FIGURE 2.11: RVE WITH DIFFERENT DISTRIBUTED FIBRES STYLE OVER EDGES. (A) CONTINUOUS. (B) NON-CONTINUOUS.....	72
FIGURE 3.1: FIBRE DISTRIBUTION AND DISCRETE ELEMENT DISCRETISATION. (A) REPRESENTATIVE AREA ELEMENT. (B) HEXAGONAL PACKING ARRANGEMENT. (C) CONTACT BETWEEN PARTICLES. ....	78

FIGURE 3.2: HEXAGONAL PACKING AND CONTACT STIFFNESS. ....	78
FIGURE 3.3: MACRO STRENGTH $\Sigma_{\text{MACRO}}$ VERSUS NUMBER OF PARTICLES.....	81
FIGURE 3.4: VON MISES STRESS (MPA) DISTRIBUTION IN THE RANDOM MODEL RESULTING FROM APPLYING MACRO STRESS OF 5 MPA.....	82
FIGURE 3.5: EXAMPLES OF A DISTRIBUTION OBTAINED IN THE CASE OF 9000 CONTACTS. ...	83
FIGURE 3.6: STRESS–STRAIN CURVES OF THE RVE COMPARED WITH THE EXPERIMENTAL RESULT .....	84
FIGURE 3.7: DAMAGE INITIATION AND PROGRESSION UNDER TRANSVERSE TENSION AND DIFFERENT STRAIN. (A) STRAIN OF 0.007. (B) STRAIN OF 0.01. (C) STRAIN OF 0.014. (RED LINES REPRESENT THE MATRIX CRACKS AND BLACK LINES REPRESENT INTERFACE DEBONDING). (C) EXPERIMENTAL RESULTS (YANG ET AL., 2012). ....	85
FIGURE 3.8: EFFECT OF INTERFACE STRENGTH ON THE STRESS-STRAIN RESPONSE. ....	86
FIGURE 3.9: EFFECT OF INTERFACE FRACTURE ENERGY ON THE STRESS-STRAIN RESPONSE. ....	87
FIGURE 3.10: EFFECT OF INTERFACIAL STIFFNESS ON THE STRESS-STRAIN RESPONSE. ....	88
FIGURE 4.1: APPROPRIATE UNIT CELLS (A) SQUARE (B) HEXAGONAL PACKING.....	94
FIGURE 4.2: THE DEM MODEL: (A) MODEL GEOMETRY AND PARTICLE ASSEMBLY, AND (B) PARTICLE SIZE DISTRIBUTION. ....	97
FIGURE 4.3: VIRTUAL UNIAXIAL TESTS OF A DEM MODEL: (A) COMPRESSION AND (B) SHEAR. ....	98
FIGURE 4.4: CALIBRATION OF MATRIX ELASTIC PROPERTIES; (A) INFLUENCE OF NORMAL STIFFNESS TO SHEAR STIFFNESS RATIO, $\alpha$ , ON THE YOUNG’S MODULUS AND POISSON’S RATIO; (B) EFFECT OF NORMAL STIFFNESS ON YOUNG’S MODULUS AND POISSON’S RATIO. ....	101
FIGURE 4.5: CALIBRATION OF FIBRE ELASTIC PROPERTIES; INFLUENCE OF NORMAL STIFFNESS TO SHEAR STIFFNESS RATIO, $\alpha$ , ON THE YOUNG’S MODULUS AND POISSON’S RATIO; (B) EFFECT OF NORMAL STIFFNESS ON YOUNG’S MODULUS AND POISSON’S RATIO. THE MICROSCOPIC PARAMETERS OBTAINED ARE PROVIDED IN TABLE 4.2 .....	102
FIGURE 4.6: DEM PREDICTIONS OF MATRIX YOUNG’S MODULUS USING DIFFERENT NUMBER OF PARTICLES.....	104
FIGURE 4.7: DEM PREDICTIONS OF MATRIX POISSON’S RATIO USING DIFFERENT NUMBER OF PARTICLES. ....	105

FIGURE 4.8: A RVE OF DEM MODEL SUBJECTED TO: (A) TRANSVERSE COMPRESSION AND (B) TRANSVERSE SHEAR (ARROWS INDICATE THE LOADING DIRECTIONS). .....	107
FIGURE 4.9: DEM PREDICTIONS OF TRANSVERSE YOUNG’S MODULUS OF DIFFERENT VOLUME FRACTION COMPARED TO OTHER ANALYTICAL, NUMERICAL AND EXPERIMENTAL RESULTS (SODEN ET AL., 1998B). .....	107
FIGURE 4.10: DEM PREDICTIONS OF TRANSVERSE SHEAR MODULUS OF DIFFERENT VOLUME FRACTION SIZES COMPARED TO OTHER ANALYTICAL, NUMERICAL AND EXPERIMENTAL RESULTS (SODEN ET AL., 1998B). .....	108
FIGURE 4.11: DEM PREDICTIONS OF TRANSVERSE POISSON’S RATIO OF DIFFERENT VOLUME FRACTION COMPARED TO OTHER ANALYTICAL, NUMERICAL AND EXPERIMENTAL RESULTS (SODEN ET AL., 1998B). .....	109
FIGURE 4.12: DEM PREDICTIONS OF YOUNG’S MODULUS OF DIFFERENT RVE SIZES COMPARED TO EXPERIMENTAL RESULTS (SODEN ET AL., 1998B). .....	110
FIGURE 4.13: DEM PREDICTIONS OF SHEAR MODULUS OF DIFFERENT RVE SIZES COMPARED TO EXPERIMENTAL RESULTS (SODEN ET AL., 1998B). .....	110
FIGURE 4.14: DEM PREDICTIONS OF POISSON’S RATIO OF DIFFERENT RVE SIZES COMPARED TO EXPERIMENTAL RESULTS (SODEN ET AL., 1998B). .....	111
FIGURE 5.3: INFLUENCE OF BOND STRENGTH AND TIMESTEP ON THE MACRO COMPRESSIVE STRENGTH OF A DEM MODEL. ....	116
FIGURE 5.4: DEM PREDICTIONS OF STRENGTH USING DIFFERENT NUMBER OF PARTICLES. ....	118
FIGURE 5.5: CRACK PATTERNS UNDER UNIAXIAL COMPRESSION WITH DIFFERENT PARTICLES DENSE. (A) 2,628 PARTICLES. (B) 4,106. (C) 7,300. (D) 16,426. (E) 20,280. (F) 25,667. ....	119
FIGURE 5.6: STRESS-STRAIN CURVES FROM DEM SIMULATIONS USING DIFFERENT TIMESTEPS COMPARED TO EXPERIMENTAL RESULTS (SODEN ET AL., 1998B). .....	120
FIGURE 5.7: STRESS–STRAIN CURVES OF FIVE RVEs UNDER UNIAXIAL COMPRESSION... ..	121
FIGURE 5.8: DAMAGE EVOLUTION UNDER TRANSVERSE COMPRESSION AT DIFFERENT LOADING STRAINS: (A) STRESS-STRAIN OF RVE #3 SHOWING THREE CHARACTERISTIC LOADING POINTS DAMAGE STUDIED AT (B) 0.7% (C) 1.3% (D) 1.7%. (RED DOTS ARE FIBRE/MATRIX DEBONDING AND BLACK DOTS ARE MATRIX CRACKS). .....	122
FIGURE 5.9: TRANSVERSE SHEAR STRESS-STRAIN CURVE USING FIVE DIFFERENT FIBRE ARRANGEMENTS COMPARED WITH (ROMANOWICZ, 2014) AND (YANG ET AL., 2015) .....	124

FIGURE 5.10: DAMAGE EVOLUTION UNDER TRANSVERSE SHEAR AT DIFFERENT STRAIN STAGES: (A) STRESS-STRAIN OF RVE #3 SHOWING THREE CHARACTERISTIC LOADING POINTS DAMAGE STUDIED AT (B) 0.87%, (C) 1.51%, AND (D) 2.13%. (RED DOTS ARE FIBRE/MATRIX DEBONDING AND BLACK DOTS ARE MATRIX CRACKS).....	125
FIGURE 5.11: VARIATION OF COMPRESSIVE STRENGTHS AND TRANSVERSE COMPRESSIVE FAILURE STRAINS WITH RVE SIZE, COMPARED WITH EXPERIMENTAL DATA (SODEN ET AL., 1998B): (A) COMPRESSIVE STRENGTHS, AND (B) TRANSVERSE COMPRESSIVE FAILURE STRAINS. ....	127
FIGURE 5.12: TRANSVERSE SHEAR STRENGTH OF RVEs WITH DIFFERENT SIZES.....	128
FIGURE 5.13: LOADING SCHEMES USED TO PERFORM BIAxIAL TESTS (ARROWS REPRESENT EXTERNAL FORCE AND ARROWS REPRESENT VELOCITY APPLIED): (A)-(B) SHEAR AND TENSION IN PART-A, AND (C)-(D) SHEAR AND COMPRESSION IN PART-B.	131
FIGURE 5.14: FAILURE ENVELOPE OF A FIBRE-REINFORCED COMPOSITE LAMINA IN THE $\sigma_{22} - \tau_{23}$ STRESS SPACE.....	132
FIGURE 5.15: ACCUMULATION OF DAMAGES IN THE COMPOSITE UNDER DIFFERENT LOADING COMBINATIONS IN PART-A. (EACH SUBFIGURE REPRESENTS A DATA POINT ON THE FAILURE ENVELOPE ACCORDING TO ITS LABEL; RED DOTS REPRESENT FIBRE/MATRIX DEBONDING AND BLACK DOTS REPRESENT MATRIX CRACKS.) .....	133
FIGURE 5.16: ACCUMULATED CRACKS IN THE COMPOSITE UNDER DIFFERENT LOADING COMBINATIONS. (EACH SUBFIGURE REPRESENTS A DATA POINT ON THE FAILURE ENVELOPE ACCORDING TO ITS LABEL; RED DOTS REPRESENT FIBRE/MATRIX DEBONDING AND BLACK DOTS REPRESENT MATRIX CRACKS.) .....	135
FIGURE 5.17: NUMBER OF FIBRE/MATRIX DEBONDING AND MATRIX CRACKS IN LOADING CASES IN PART-A. ....	138
FIGURE 5.18: NUMBER OF FIBRE/MATRIX DEBONDING AND MATRIX CRACKS IN LOADING CASES IN PART-B. ....	139
FIGURE 6.1: EXPERIMENTAL RESULTS OF FAILURE ENVELOPE OF A FIBRE-REINFORCED COMPOSITE LAMINA UNDER $\sigma_{11} = \sigma_{22} = \sigma_{33}$ VERSUS $\tau_{12}$ STRESSES (KADDOUR AND HINTON, 2013).....	144
FIGURE 6.2: EXPERIMENTAL RESULTS OF FAILURE ENVELOPE OF A FIBRE-REINFORCED COMPOSITE LAMINA UNDER $\sigma_{11} = \sigma_{33}$ VERSUS $\sigma_{22}$ STRESSES (KADDOUR AND HINTON, 2013).....	145

# List of Tables

TABLE 2.1: MATERIAL ELASTIC PROPERTIES.....	67
TABLE 2.2: CALCULATED EFFECTIVE PROPERTIES (E-GLASS/MY750/HY917/DY063).....	70
TABLE 2.3: CALCULATED EFFECTIVE PROPERTIES (AS4/3501-6).....	71
TABLE 2.4: PROOF OF TRANSVERSE ISOTROPY.....	71
TABLE 2.5: CALCULATED EFFECTIVE PROPERTIES FOR NON-CONTINUOUS DISTRIBUTED FIBRES (E-GLASS/MY750/HY917/DY063).....	73
TABLE 2.6: CALCULATED EFFECTIVE PROPERTIES FOR NON-CONTINUOUS DISTRIBUTED FIBRES (AS4/3501-6).....	73
TABLE 3.1: CONSTITUENT MATERIAL PROPERTIES (GONZÁLEZ AND LLORCA, 2007A). ....	79
TABLE 4.1: MECHANICAL PROPERTIES OF FIBRE AND MATRIX. ....	99
TABLE 4.2: MICRO-PARAMETERS FOR PARTICLES AND PARALLEL BONDS.....	102
TABLE 4.3: DEM PREDICTIONS OF THE ELASTIC PROPERTIES OF FIBRE AND MATRIX. ....	103
TABLE 4.4: MECHANICAL PROPERTIES FOR E-GLASS/MY750. ....	106
TABLE 5.1: MECHANICAL PROPERTIES OF FIBRE AND MATRIX. ....	115
TABLE 5.2: FAILURE STRENGTH USED IN HASHIN AND PUCK FAILURE CRITERIA.....	129

## **Acknowledgements**

I would like to thank the patient supervisors Professor Jianqiao Ye and Dr Dongmin Yang (Leeds University) for their help during long PhD road. I am also grateful for Dr Yong Sheng for his support and valuable comments.

I would like also to thank my wife Mrs Taymaa Dawwod for her support.

## **Abstract**

Fibre-reinforced composites have many outstanding advantages that attract commercial industries to use them such as, automotive industry, aerospace industry, marine industry, wind turbines, and sports goods. Fibre-reinforced composites characterised as a high strength/stiffness to weight ratio comparing with natural metals resulting in very lightweight structures which in turn reduce fuel consumed by aircraft, for instance. They also provide an excellent resistance to, corrosion, fatigue stress, impact force and chemical attack. The main concern in use of these materials is the complexity of damages that are taken place in different scale lengths starting from micro-scale level. With the development of computer power, however, the door is opened to enhance concepts such as a multi-scale analysis that can bridge micro-scale to macro-scale. The new tools provide excellent substitutes of the costly and time-consuming experimental tests.

In this thesis, Discrete Element Method (DEM) is developed for micromechanical modelling of fibre-reinforced composites. In Chapter 2, a new method is proposed for generating random fibre distribution. Unlike prior methods that have proposed, this method can be used to generate a high fibre volume fraction with any inter-fibres distance.

The new method is then applied throughout the thesis. In Chapter 3, a Representative Volume Element (RVE) containing fibres distributed randomly subjected to uniaxial transverse tension is studied. The DEM is showed to a genuine tool to investigate damage propagation in fibre-reinforced composites.

Chapter 4 is dedicated to determining the elastic properties of the fibre-reinforced composite using DEM. The results are then compared with selected analytical methods, namely Voigt and Mori-Tanaka methods, other numerical method such as Finite Element Method (FEM), and experimental results.

The methodology developed in previous chapters are then adopted in Chapter 5 to study the failure of fibre-reinforced composite under uniaxial compression,

transverse shear and biaxial transverse loads. Results are compared with experiments and analytical method such as Hashin and Puck models.

# Chapter 1

---

## 1. Literature Review

### **1.1 Background**

Composite materials are defined as a material that are created by assembling two or more different materials, and each one has its mechanical and chemical identities that differs from other. Therefore, the term 'composite material' is label used for many materials, such as fibre-reinforced polymers FRPs, fibre-reinforced metals, concrete, mortar etc.

Fibre reinforced composite materials are constituted from fibres of a high strength and stiffness that are embedded in a matrix with distinct boundaries that remain separated in the microstructure. The new-born material has highly specific mechanical properties that are normally not available in natural materials and are superior to those of the individual constituents. Its properties result from the nature and properties of the component materials, their geometry and distributions, and the interactions between them. FRPs are extensively used and can be classified into four categories according to the matrix type used to build them. These categories are polymer matrix composites, metal matrix composites, ceramic matrix composites and carbon matrix composites. Fibre-reinforced composites are also classified according to the arrangement of the fibres within the matrix; i.e. continuous or discontinuous. For high-strength applications, a laminate is made by assembling thin plies of unidirectional fibres or woven fibres in a matrix. Two typical plies (or lamina) with their fundamental material axes in line with the predefined co-ordinate system are shown in Figure 1.1a and b. Each ply is arranged so that the fibres in the ply follow some prescribed direction, which is usually called ply orientation, to fulfil the design requirements.

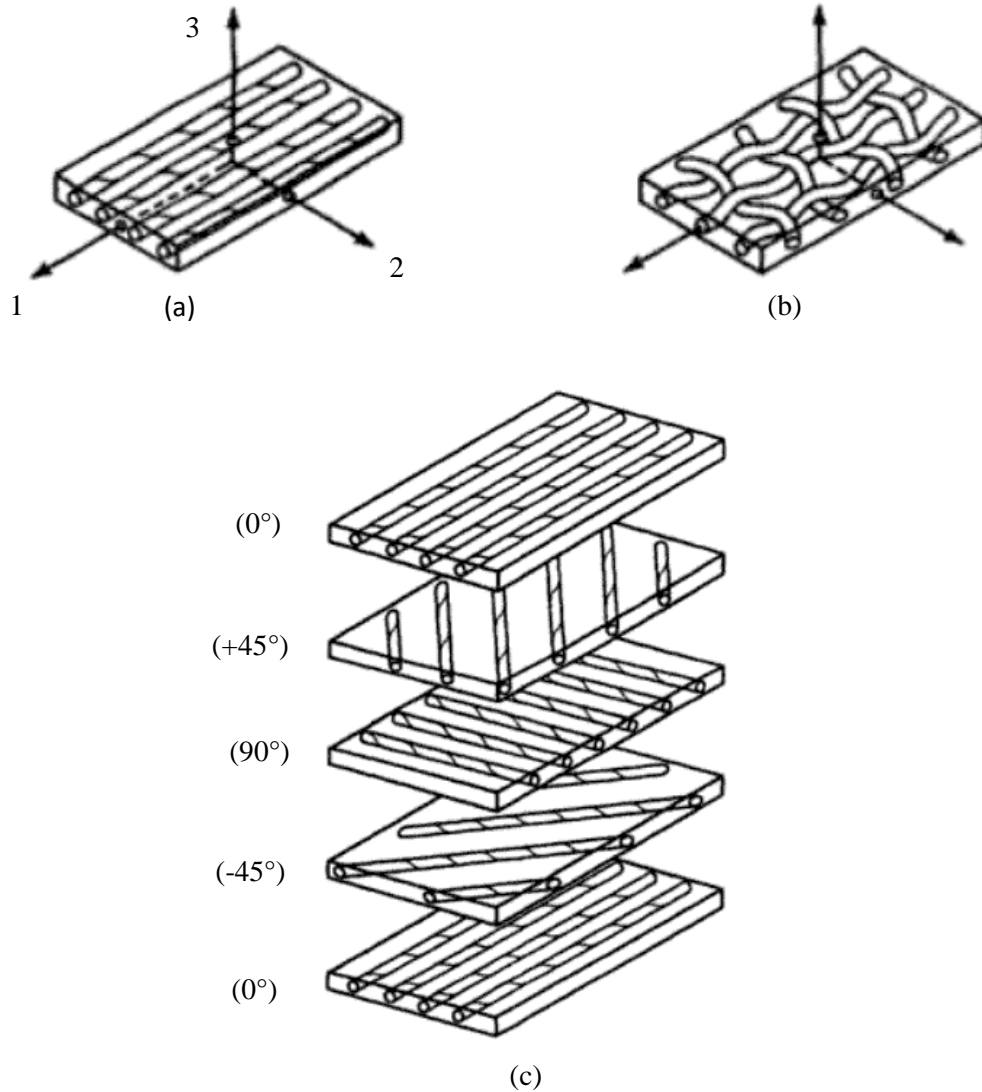


Figure 1.1: Two typical types of lamina. (a) Unidirectional lamina. (b) Woven lamina. (c) Laminate.

The strength and stiffness of a single ply are higher in the longitudinal direction (along the fibre direction) compared to other directions. A group of lamina with different fibre orientations are bonded together in one stack to build a laminate, as shown in Figure 1.1c. These plies are normally bonded together by the same matrix material that is used for an individual ply.

Due to the outstanding mechanical properties of FRP composites, they are widely used nowadays to build the structures of airplanes and in the automotive industry. FRPs have a higher strength and stiffness, and a lower weight compared with conventional materials. Thus, using these materials to manufacture the structure

components of aircrafts will allow fuel to be saved and extend the range of flying. A noticeable example of using composite materials can be found in the Boeing 787 aircraft. This aircraft is manufactured mainly from composite materials, which are used for the fuselage, wings and tail surfaces. It is also known that the Boeing 777 contains only 12% composites and 50% aluminium. Excellent tools are available nowadays for engineers to predict the stress state throughout the structures when material behaviour is linearly elastic. However, predicting the final failure of composite materials is quite difficult as it results from many damage modes that take place in different length scales.

Due to the failure complexity of FRPs, it is important to track failures at different scales and to couple these scales. The methodology used in the past to tackle failures in the FRPs was based on performing a numerical analysis of the whole structure (usually using finite element method) to detect the critical regions in which damage is possibly to take place. This method, therefore, passes information from higher to lower scales and is called *top-bottom* (also known as *global-to-local*) analysis. Then, these regions were subjected to extra refined analyses, and non-linear constitutive equations based on phenomenological models for the composite behaviour were used to predict the material behaviour until final failure. While this methodology has been used successfully in industries and has proved to be useful from the engineering point of view, it has many critical limitations. Firstly, this strategy requires a wide range, and costly experimental tests are required to reproduce parameters involved in the models used in the critical regions. Secondly, optimisations and innovations of composite materials are limited in this method due to the absence of data to assess the failure onset and propagation in the materials at different scales. Finally, extending the results beyond the initial environmental/loading conditions is very difficult owing to the phenomenological nature of the composite material models ([LLorca et al., 2013](#)).

Another approach that has been proposed recently to perform multi-scale simulation of composite material is called the *bottom-top* (also known as *local-to-global*) method. In this method, the material is divided into three length scales, or levels, (ply, laminate and component) and taking the reality that composite structures are made up of laminates that in turn consist of stacking separate plies with different fibre orientation. The bottom level, or micro-scale level, is the first step in the multi-

scale modelling. In this level, the ply properties are predicted from the thermo-mechanical properties of the constituents (fibre, matrix and interface). Typically, in micromechanical analysis, dozens of fibres are distributed (regularly or randomly) in the matrix to generate the representative volume fraction (RVE), which is then used to study the behaviour of the ply. The effects of volume fraction of the fibres, the spatial distribution of fibres and the geometry of the fibres are considered explicitly in this level. After solving the equilibrium problem at the micro-scale, all information from this level is then passed to the upper scale in multi-scale modelling, the meso-scale level, which is used to determine the mechanical response of the lamina. Finally, the macro-scale level is modelled to obtain the structure's failure, which is the last step in multi-scale simulation. It should be noted that this method still requires more improvement and development to find a robust strategy to bridge all levels. A variety of numerical techniques have been used to model aforementioned scales, such as the finite element method (FEM) ([Fish and Yuan, 2005](#), [Flores et al., 2011](#), [Ghosh et al., 2001](#), [Hund and Ramm, 2007](#), [Ladeveze, 2004](#), [Markovic and Ibrahimbegovic, 2004](#), [Matsui et al., 2004](#), [Miehe and Koch, 2002](#), [Miehe et al., 1999a](#), [Miehe et al., 1999b](#), [Terada and Kikuchi, 2001](#)), the boundary element method (BEM) ([Benedetti and Aliabadi, 2013](#), [Mrozek et al., 2007](#), [Sfantos and Aliabadi, 2007](#)), combined FEM/BEM ([Fernandes et al., 2015](#)) and X-FEM ([Belytschko et al., 2008](#), [Loehnert and Belytschko, 2007](#)). The overall multi-scale simulation strategy is shown in Figure 1.2.

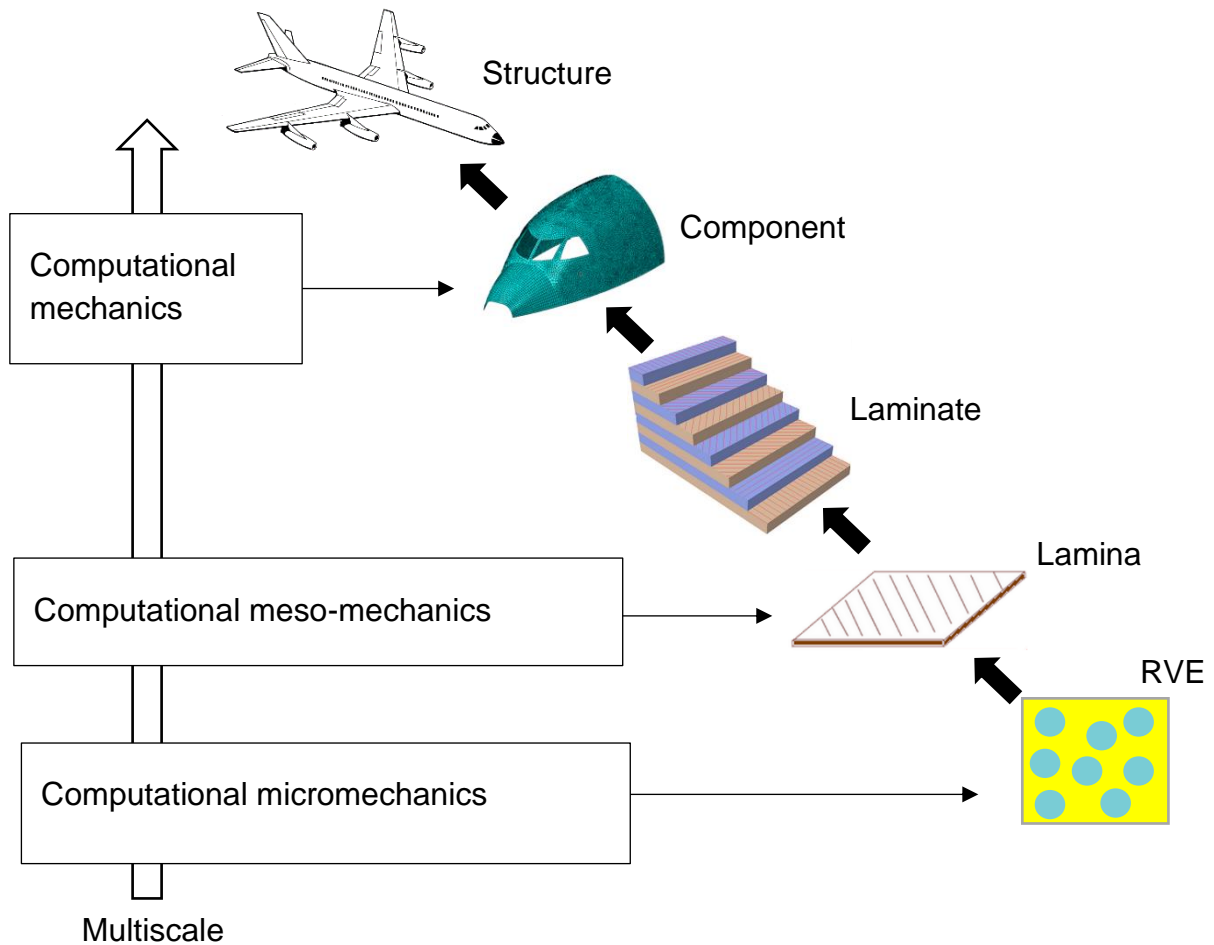


Figure 1.2: Bottom-top multi-scale simulation scheme to perform virtual mechanical tests of composite materials.

Numerous efforts have been made by researchers in the past to glue scales in multi-scale models, as explained below:

- **First-order homogenisation** method was developed in e.g. ([Feyel and Chaboche, 2000](#), [Ghosh et al., 1995](#), [Ghosh et al., 1996](#), [Miehe and Koch, 2002](#), [Terada and Kikuchi, 2001](#)). In this method, the macroscopic deformation is uniformly distributed over macrostructure and captured for each point, which is then transferred to the associated RVE in order to define the boundary value problem (BVP). After solving of the BVP, the deformed RVE is obtained. The macro-structural stress is finally obtained by averaging the stress field over the RVE. This method neglects the length scale effects and is suitable in a classical continuum mechanics.

There are some limitations of this method which are mainly stemmed from neglecting the length scale effects.

- **Second-order homogenisation** method was proposed by ([Geers et al., 2003](#), [Kaczmarczyk et al., 2008](#), [Kouznetsova et al., 2004](#), [Kouznetsova et al., 2002](#)). This model was developed to overcome the limitation arose from using the first-order model. The macroscopic deformation at each point is determined using Taylor series. The BVP remains same as the first-order and can be solved using a standard method. The method introduced the material length effects into the constitutive equations e.g. the size of RVE. Both first and second order methods cannot be handled for problems involve fracture, and thus many benefits of using computational power will miss out.
- **Continuous-discontinuous homogenisation** method has been developed to study cracks in a masonry wall ([Massart et al., 2007a](#), [Massart et al., 2007b](#)). The method incorporates first-order scheme twice to determine the response in the damaging and unloading material.

## ***1.2 Physical damage mechanism in fibre-reinforced composites***

Damage evolution in most structure materials is usually dominated by one physical failure mechanism upon applying deformation. For instance, damage in nearly all ductile materials is due to void nucleation, growth and coalescence this damage mechanism should only be included in micro-mechanism analysis. However, physical damage mechanisms in composites are very complex and not yet understood. Several damage mechanisms can occur upon applying deformation on composites; the dominant one depends on the loading direction with regard to fibres orientation, as depicted in Figure 1.3. Experimental and numerical studies have shown that the fracture in a ply loaded in transverse tension (perpendicular to the fibres) is mainly dominated by the matrix cracks and fibre/matrix interface debonding. Tensile fracture is brittle and propagated vertically between fibres ([Paris et al., 2003](#)), as shown in Figure 1.3a. A ply under transverse compression stress, on the other hand,

fails along an angle ( $\alpha$ ) perpendicular to the loading axis, which has been reported as having values  $\alpha = 50-56^\circ$  for polymer matrix composites ([González and LLorca, 2007a](#), [Pinho et al., 2006](#)), see Figure 1.3b. When longitudinal tensile stress applies on the ply (parallel to the direction of the fibres), the failure is primarily a result of fibre breakages whereas compressive failure is more complex and different failure modes are expected such as micro-buckling, kinking, and fibre failure ([Schultheisz and Waas, 1996](#)). The failure mode, therefore, depends on the initial imperfections during the manufacturing process, such as fibre misalignment, residual stresses, and porosity, Figure 1.3c and d. The behaviour of fibre-reinforced composites subjected to shear loads has also been carried out recently by many researchers. Composites under pure transverse shear is difficult to be performed in laboratory, Figure 1.3e. Therefore, numerical simulation based on a micromechanical model is mostly used to study damage composites and to quantify the effect of fibre/matrix interface on the behaviour of composites. Vaughan and McCarthy ([Vaughan and McCarthy, 2011b](#)) studied the influence of intra-lamina properties on the transverse shear deformation of a carbon fibre/epoxy composite. The interface strength was found to control shear strength while interface fracture energy mainly affected on the transverse failure strain. Totry *et al.* ([Totry et al., 2010](#)) examined the impact of fibre, matrix, and interface properties on the in-plane shear response using the V-notched Rail Shear Test. They used two composites made up of either high strength or high modulus fibres to reinforce the epoxy matrix. It has been found that matrix yield strength and interface properties were significantly controlled the in-plane shear behaviour and the cracks organised parallel to the fibres, as shown in Figure 1.3f.

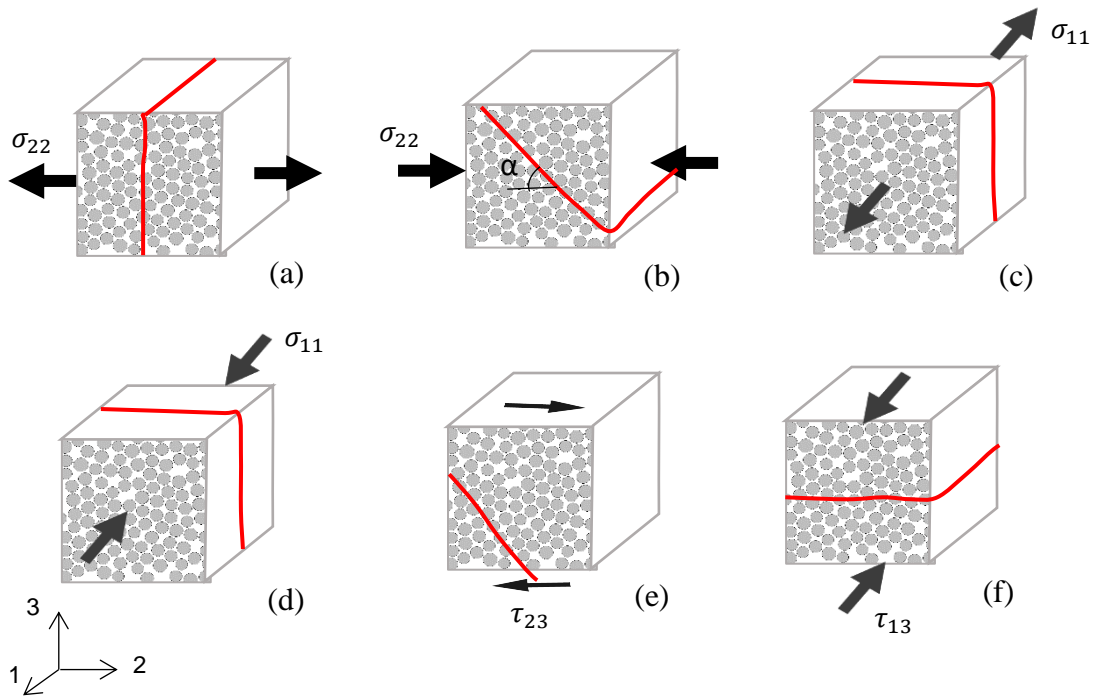


Figure 1.3: Failure micro-mechanisms in FRPs as a function of load conditions. (a) Transverse tension. (b) Transverse compression. (c) Longitudinal tension. (d) Longitudinal compression. (e) Out-of-plane shear. (f) In-plane shear.

Due to the complexity of failure in fibre-reinforced composite as explained above, many methods have recently been developed to assess damage evolution in composites materials, e.g. acoustic emission sensing ([Dzenis and Qian, 2001](#), [Sihn et al., 2007](#)), optical imaging ([Pierron et al., 2007](#)), scanning electron microscopy ([Pagano, 1998](#)), and synchrotron radiation computed tomography (SRCT) ([Moffat et al., 2008](#), [Scott et al., 2011](#), [Wright et al., 2008](#)). It has been found that in  $[90,0]_s$  laminate plates subjected to tensile stress for instance, the transverse ply cracks occur first at low applied strain followed by  $0^\circ$  splits. These crack modes are often the result of inter-lamina delamination between adjacent plies. All these cracks usually occur in advance of significant fibre breaks, which then lead to final failure. Figure 1.4 shows the damage evolution at different loading stages.

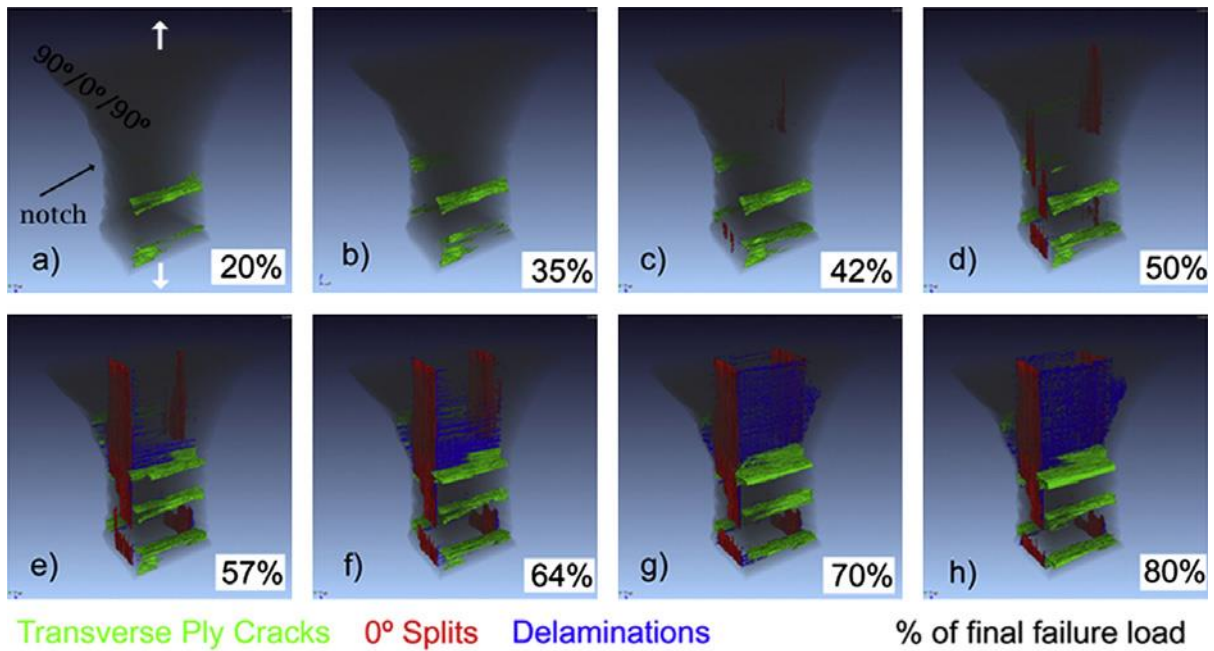


Figure 1.4: Matrix cracks and delamination occurring at 90/0 interface at different tensile loading stages. Adapted from [Scott et al., 2011](#).

### 1.3 Micromechanical strategies used in composite materials

Micromechanical methods can be defined as prediction of macroscopical or global effective properties of the composites (such as elasticity, strengths, thermal expansion, etc.) from the properties of their constituents (or phases). The relation between homogeneous constituents and inhomogeneous materials is achieved either by relating relevant properties of the constituents or by geometry and topology of inclusions which referred to as continuum micromechanics. These relationships can be studied at different length scales ranging from atomic scales to any other suitable scale. However, most FRPs studies are carried out at microscopic level, as this scale can homogenise fibre and matrix. In addition, fractures and fibre/matrix debonding normally take place at this scale.

In addition to prediction effective properties of composites, micromechanical methods can also be used to simulate the overall response of materials under simple loading conditions (e.g. uniaxial tensile, compression, and shear) or complex loading conditions (e.g. biaxial and triaxial). Moreover, micromechanical techniques are also used to provide the constitutive of structure components in framework of computational micromechanics. Computational micromechanics are significantly

important to identify the local stress, deformation and damage onset and evolution which in turn have significant repercussions on damages at higher length scales.

Micromechanical study of composites is a complex and an extensive body of literature covering this topic. Micromechanical methods can fundamentally be divided into two groups as:

- Analytical methods
  - Mean-field methods
  - Variational bounding methods
  
- Computational methods
  - Periodic micro-field methods
  - Windowing methods
  - Embedding methods

Analytical methods can be traced back to the classical bounds of Voigt ([Voigt, 1889](#)) and Reuss ([Reuss, 1929](#)) (see ([Mishnaevsky Jr, 2007](#))). They have been used to determine the overall elastic properties of composites. Many disadvantages can be found in analytical approaches among these, for instance, extending them to non-linear including (plasticity, creep, *etc.*) is quite complex and cannot always guarantee an accurate results ([Castaneda and Suquet, 1998](#)). However, due to the rapid development of computer power in the last few decades, computational methods have been rapidly employed to study the behaviour of composite materials and overcome limitations of analytical methods. Numerical methods have the advantage of high accuracy and provide useful insights into fracture onset and propagation.

## **1.4 Analytical methods <sup>1</sup>**

### **1.4.1 Mean-field methods**

Mean-field methods are used to find the effective properties of the composite from its constituent properties and volume fraction. These methods have been successfully used to describe the elastic response of the inhomogeneous materials in general and, in particular, the composite materials. Perfect bonding between the fibres and matrix is assumed in all methods. Methods such as Eshelby ([Eshelby, 1957](#)) and Mori-Tanaka ([Mori and Tanaka, 1973](#)) are examples of mean field methods.

### **1.4.2 Variational bounding methods**

These methods use variational principles to calculate upper and lower bounds on the overall elastic tensors, elastic properties, and other physical properties. Unlike mean field methods, which can be used for both homogenisation and localisation tasks, variational bounding methods are limited to homogenization. They can also be used as a tool to assess other methods. The simplest form of upper bounds were proposed by Voigt ([Mishnaevsky Jr, 2007](#), [Voigt, 1889](#)). He made use of minimum potential energy and the minimum complementary energy with uniform stress and strain distribution to derive the equations.

## **1.5 Representative volume element**

The mechanical behaviour of composite materials has been intensively studied (mainly in the last few decades due to the development of computer power) using different numerical methods (e.g. FEM and BEM) to analyse a RVE. The theory of RVE has been introduced by Hill ([Hill, 1963](#)) and referred to as a smallest sub-region of the composites contains sufficient information for describing the behaviour of composites.

---

<sup>1</sup> Details of the analytical methods used in the thesis will be introduced in Chapter 5.

In case of composite materials, the RVE must beat the minimum size in order to eliminate size effects and fluctuations of stress and stress fields due to the interactions between inclusions, fibres, or particles. Therefore, RVE size is particular important as it should be large enough to represent the composites behaviour; however very large RVE cannot be simulated and can become computationally expensive. Fortunately, recent numerical investigations have been done to study the micromechanical behaviour of composites found that a few dozen fibres or particles in the RVE were reasonably close to the exact solution ([Eckschlager et al., 2002](#), [Segurado and Llorca, 2002](#), [Segurado et al., 2002](#), [Totry et al., 2010](#), [Vaughan and McCarthy, 2011b](#)).

## **1.6 Boundary conditions**

The RVE together with its boundary conditions must be prescribed in such a way that provide valid deformed and unreformed states. Therefore, gaps and overlaps must be avoided between adjacent unit cells, as this may cause unreliable continuum mechanics. To attain this, the selected boundary conditions must cause a suitable RVE deformation mode for each load case under study. Two types of boundary conditions are commonly used to analyse the micromechanical model, namely symmetric and periodic boundary conditions.

### **1.6.1 Symmetric boundary conditions**

Periodic unit cell approaches can be used to describe the micro-geometry of the composites. For example, a simple square and hexagonal fibres arrangement is a good approximation of the microstructure of FRPs in two dimensional studies. Figure 1.5 shows possible unit cells<sup>2</sup> that can be handled from a basic fibres arrangement. In these cases, it is possible to apply symmetry boundary conditions on the unit cell in which the faces of the cell coincide with symmetry planes of the phase arrangement, as shown in Figure 1.6a.

Symmetric boundary conditions are usually useful to handle simple micro-geometries with little effort of modelling and low computational cost. However, they

---

<sup>2</sup> The concept of unit cell will be properly introduced in chapter 4.

are obviously limited to only uniform thermal loads, mechanical loads act in directions normal to one or more pairs of edges, and combinations of these loads.

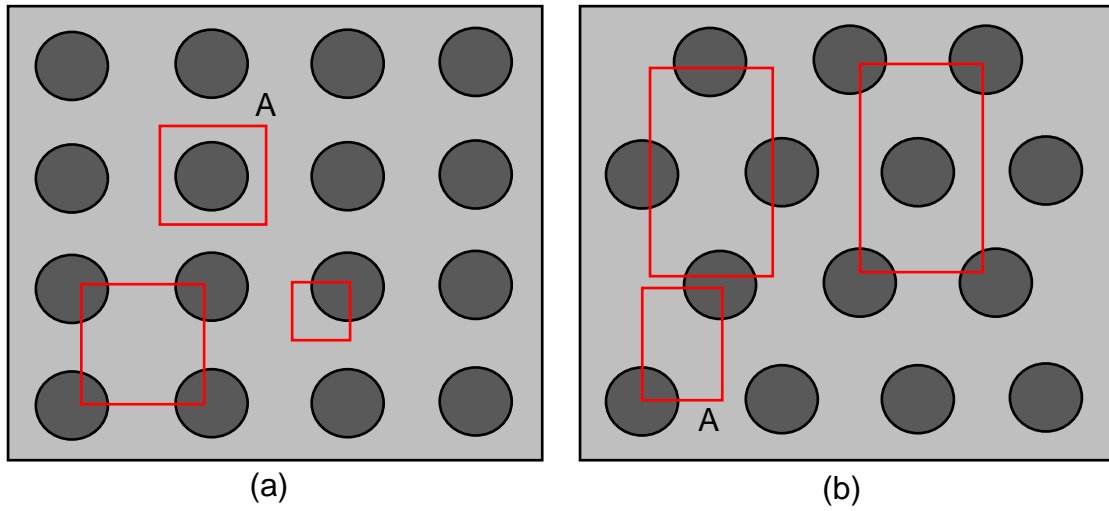


Figure 1.5: Distribution of fibres in the matrix. (a) Periodic square. (b) Hexagonal.

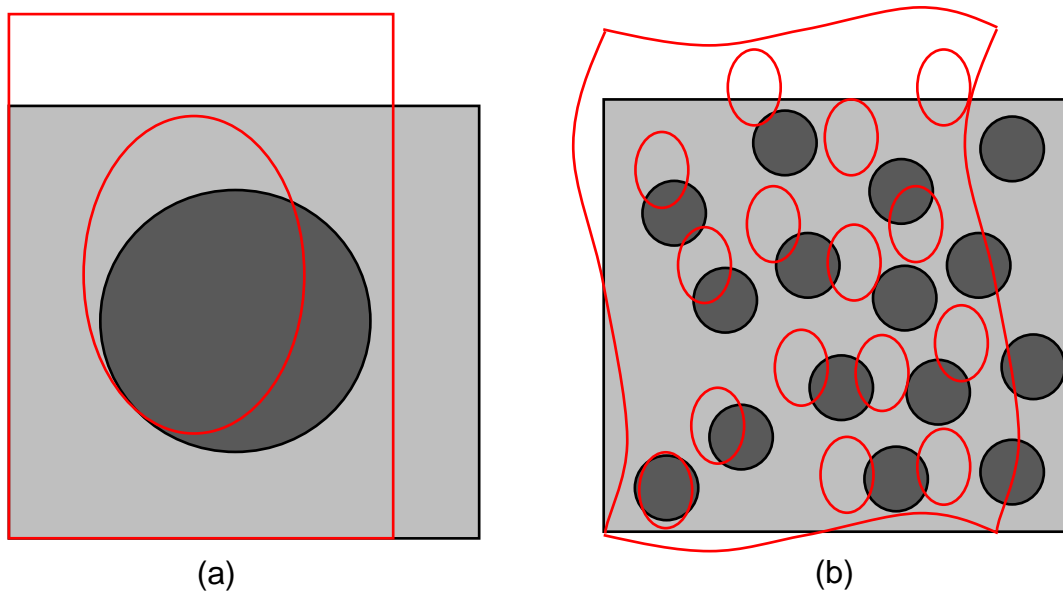


Figure 1.6: Deformation of (a) Symmetric boundary conditions under uniaxial loading for fibre A. (b) Periodic boundary conditions in a rectangular two-dimensional model.

### **1.6.2 Periodic boundary conditions**

To overcome the limitations arose from using symmetry boundary conditions, Periodic boundary conditions used to introduce far-field stress and strain into the edges of RVE. They are used mainly in the case of random fibre arrangements obtained from experimental techniques or other methods, Figure 1.6b. Several works can be found in literatures which either discuss periodic boundary conditions and their applications e.g. ([Li, 2008](#), [Sun and Vaidya, 1996](#), [Xia et al., 2003](#), [Xia et al., 2006](#)) or aim to develop a new periodic boundary condition that can be used in conjunction with reduced unit cells to reduce computational time, see ([De Carvalho et al., 2011](#)).

Periodic boundary conditions are actually computationally expensive, as they should link each node on edges with reference nodes and corresponding nodes on the opposite side, which indeed becomes more complex for tree-dimensional problems. Another important drawback of both symmetry and periodic boundary conditions appear in multiscale models especially in accounting for the effects of locally non-periodic regions within the composite structures. For instance, one of these regions is a free-edges boundary which, is a common damage onset zone in many composite structures ([Cater and Xiao, 2013](#)).

## **1.7 Computational methods**

### **1.7.1 Periodic micro-field approaches**

In these methods, an infinite volume of composites is simplified by assuming regularly distributed fibres in the space. Under such conditions, the composite materials can be characterised by a periodic unit cell to describe the micro-geometry of them, with periodic boundary conditions applying on the edges of the cell. An extensive number of unit cell models have been developed and varied primarily in the numerical techniques used to solve the boundary value problem. One of the first methods of periodic micro-fields is called method of cells, which was developed by Aboudi ([Aboudi, 1989](#)). In his basic form, fibres were located in a corners of a square arrangement and then each cell is discretised into four sub-cells. The local stress and strain fields are calculated by very modest analytical expression. This method provides insufficient information of stress and strain fields. Therefore, many attempts have been

made to develop an algorithm and led to the proposal of a generalised method of cells by same author ([Aboudi, 1996](#)). The unit cell model for periodic micro-field methods can be extracted from a very simple arrangement of fibres. For example, in the case of two dimensional studies, a square or hexagonal arrangements of inhomogeneous are used as shown on Figure 1.5a and b, respectively. A unit cell model, which captures the overall behaviour of the composites, is indicated by solid a red line ([Pettermann and Suresh, 2000](#)).

In addition to simple analytical expressions, numerical tools such as finite element, discrete element, and finite difference methods are employed to analyse complex cells. Despite the practical restrictions of numerical methods, they have been successfully used in recent years to obtain constitutive equations, analysing the mechanical properties and studying fracture onset and propagations within microstructures for composite materials ([Li, 2001](#), [Maheo et al., 2015](#), [Zhang et al., 2004](#), [Zhang et al., 2005](#)).

### **1.7.2 Windowing approach**

Micromechanical modelling of composite materials by windowing method is based on the analysis of images obtained experimentally or using such methods to generate a random distribution of fibres. This method is used to estimate the overall response of composite materials by RVE. The windowing approach can be conducted by placing a window on a random position of image sample or generated microstructure and then subjecting the resulting sample to stress, as shown in Figure 1.7a. The size of RVE must be adequate to ensure that it contains all relevant statistical information. However, due to computer power limitations, a small RVE is preferred in simulations. Due to the expansion of computer powers, the windowing approach has been intensively used in the last few years to estimate effective properties, stress-strain curves, and damage onset and propagation of composites with periodic boundary conditions applied on the RVE ([Totry et al., 2008a](#), [Vaughan and McCarthy, 2010](#), [Vaughan and McCarthy, 2011a](#), [Yang et al., 2015](#), [Yang et al., 2012](#)).

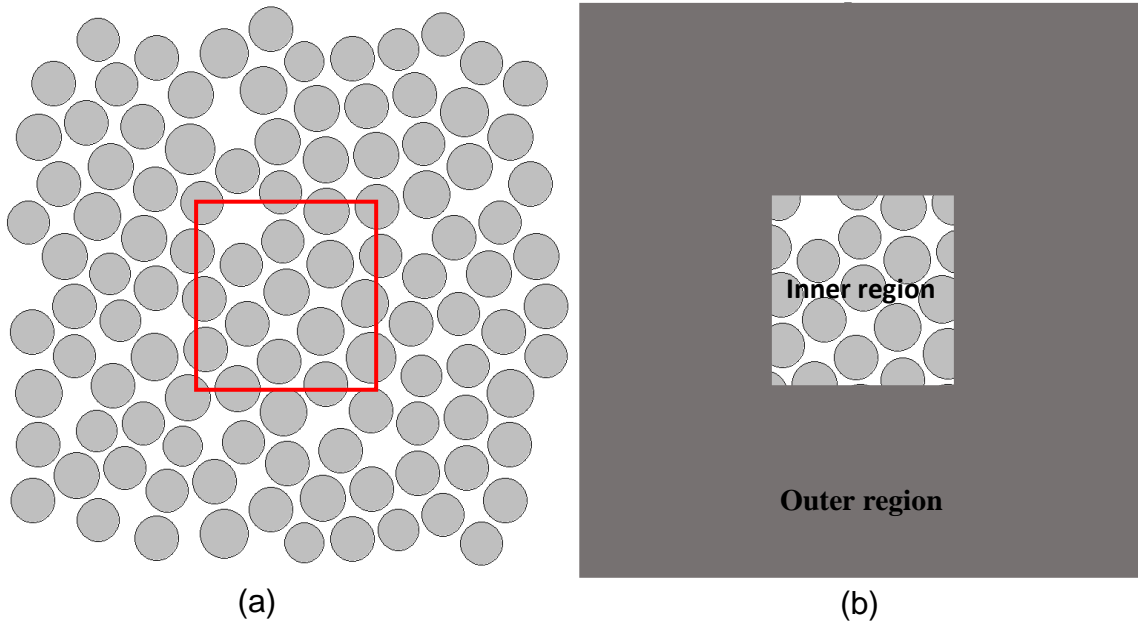


Figure 1.7: Schematic sketch of a random fibre/matrix microstructure. (a) Window approach. (b) Embedded configuration.

### 1.7.3 Embedding approaches

The purpose of embedded cell approaches is to predict the micro-fields in composite materials at high spatial resolution. In these methods, the material is divided into two regions. The inner region, (the core) that contains details of the microstructure (fibre, matrix and fibre/matrix interface) is embedded into the outer region that mainly serves transmitting the applied load to the core, Figure 1.7b. Cell embedding approaches can avoid the drawback of the periodic field method regarding the periodic restrictions ([Böhm, 1998](#)) and the time required to build constrain equations representing periodic boundary conditions. However, similar to the periodic method, stress and strain perturbations at the interface between inner and outer regions may occur using embedding cell ([Harper et al., 2012](#)).

Three types of embedded cell approaches are normally used depending on the outer region.

- The first method employs discrete microstructures for both inner and outer regions with a finer element size used to discretise the former region ([Sautter](#)

[et al., 1993](#)). This strategy is simple and can be used to reproduce whole structures thus avoiding the influence of interface interaction. However, they tend to be computationally expensive.

- In the second method of embedded cell, full details of composite microstructure, such as fibres, matrix, and their interface are resolved in the inner region whereas a simple constitutive law prescribed a priori based on any suitable empirical or micromechanical approximations is used for outer region. This approach has been used successfully to study crack propagation in composite materials ([Canal et al., 2012](#), [González and LLorca, 2007b](#), [Wulf et al., 1996](#)), stress strain concentrations around local defects ([Xia et al., 2001](#)) or near the crack tips ([Aoki et al., 1996](#)).
- The third type of embedding schemes is based on the calibration process of the inner and outer material properties. Firstly, trial material properties are given to the outer region, which are used to compute the stress and strain fields of the inner microstructure region. Secondly, the homogeneous response of the inner region is used to build the constitutive behaviour of the surrounding medium. This procedure is repeated until convergence is achieved ([Chen, 1997](#), [Qingsheng et al., 1994](#)). This method can be easily used for an elastic analysis but may lead to significant complexity when extended to the elasticplastic deformation case.

### 1.8 Failure criteria in FRPs

Failure criteria for composite materials are usually used to predict the failure initiation in a component while the whole structural parts should be tested experimentally in order to determine their design capacity. Therefore, several failure criteria have been proposed aiming to reduce the manufacturing time and costs of new components. In order to provide a comprehensive explanation of failure criteria and their capability to predict failures, a series of coordinated studies on these failure criteria have been carried out in World Wide Failure Exercise (WWFE) ([Hinton et al., 2004](#)). WWFE assessed nineteen common criteria used to predict the response of

FRPs. However, it shows the lack of confidence in the failure criteria at lamina or laminate level and no evidence to explain which of them can predict the failure accurately. The failure prediction difficulties is mainly due to the complexity of composites structure at all levels.

Failure criteria in FRPs are often classified into two types based on the approach followed to derive them:

### **1.8.1 *Non-physical or not associate with the failure mode***

Known as non-phenomenological failure criteria, these criteria predict the failure modes taking place but use mathematical expressions to calculate failure envelope. The well-known non-physical failure criteria that can be found in existing literature are Tsai-Hill's ([Tsai, 1965](#)), Hoffman's ([Hoffman, 1967](#)) and Tsai-Wu's ([Tsai and Wu, 1971](#)) criteria.

### **1.8.2 *Physical or associate with the failure mode***

Known as phenomenological failure criteria, these criteria predict failure envelope in FRPs and describe the physical failure process, which in turn provides information on the failure modes. Hashin and Rotem ([Hashin, 1980](#), [Hashin and Rotem, 1973](#)) were the pioneers that identified the heterogeneous nature of fibre-reinforced composite materials, which means that the final failure is due to the combination of constituents and their interfaces. Therefore, they proposed first failure criterion that predicts failure of each constituent separately. However, this model neglects the determination of actual orientation of the fracture failure; rather, it assumes a quadratic interaction between tractions acting on the failure plane.

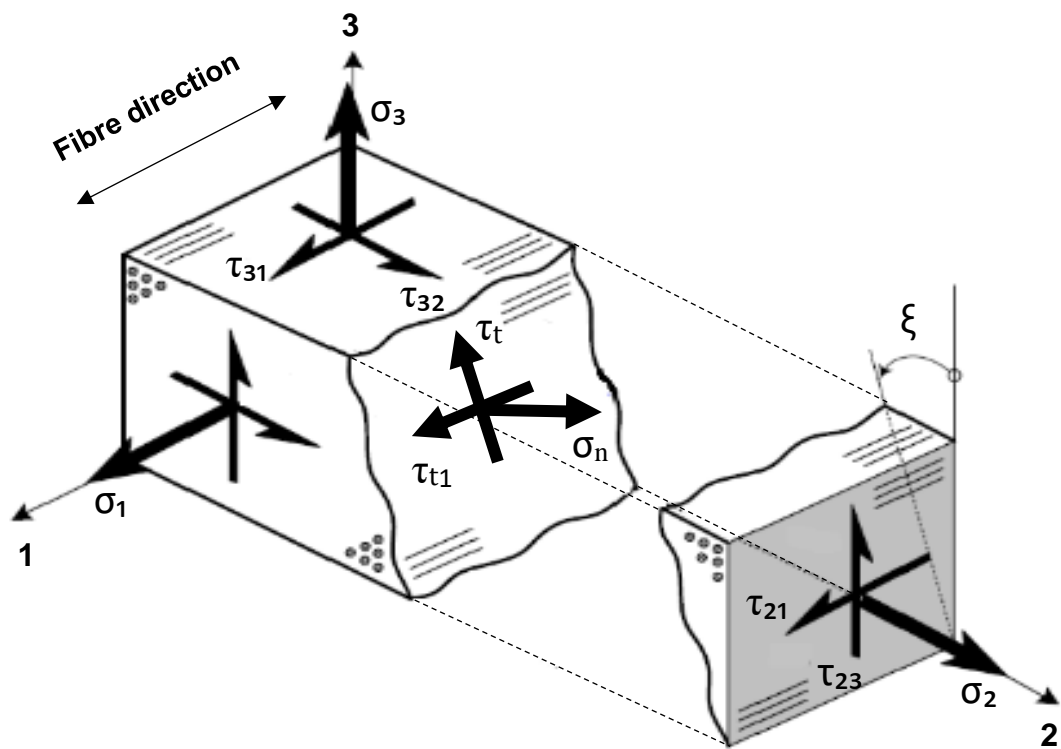


Figure 1.8: Stresses on the three-dimensional of unidirectional composite element.

Many models, therefore, have been proposed to improve Hashin's model, among them, the one proposed by Puck and Schürmann ([Puck and Schürmann, 2002](#)). They assumed that fracture occurred due to the normal,  $\sigma_n$ , and tangential,  $\tau_t$ , stress acting on the failure plane and that is the key element of the model, as shown in Figure 1.8. Puck's failure criteria were one of the best criteria in the WWFE for predicting composites experimental results. However, these criteria contain several non-physical parameters that need a significant experimental tests on a particular material to obtain them, which makes the criteria somehow impractical for engineers. To overcome this problem, Dávila *et al.* ([Davila et al., 2005](#)) proposed a new non-empirical set of criteria named LaRC03 that based on Hashin's concepts and use the failure plane concept proposed by Puck. The LaRC03 criteria presented an important improvement of Hashin's criteria and do not need experimental parameters but it fails to predict the failure of FRPs in some cases. This fact shows the need for further improvement of the existing criteria or another robust method to predict the failure.

## **1.9 Damage levels in composites**

In material science, the structural components are usually dimensioned according to their ability to withstand and resist the external events applied to them, such as mechanical loads (static or dynamic), environmental conditions (temperature, contact with chemical, humidity, i.e.) and impact load. All these events cause material degradation at the microscopic scale, which in the case of composite materials, a large number and different modes of degradations take place, as explained in Section 1.2.

In broad terms, *crack or fracture* can be defined as displacement of surfaces within the structural component. Fracture mechanics assumes the presence of an initial crack in the component and studies the condition that may lead to crack propagation. *Damage* can be defined as permanent changes in the material due to crack the propagation, for example. Damage mechanics determines the conditions for the propagation of damage, assesses the damage and their effect on the structural integrity and durability and provides the input for structural analysis and design.

Damage can be studied at different length scales. Mostly, in composites there is an initial damage in the form of micro cracks of the matrix that occurs in a lamina which does not, however, lead to the final failure, and is far away from the final failure. In other words, the micro cracks of the matrix does not change the stiffness of material. This initial damage is usually propagated within the lamina and is blocked by other adjacent layers of lamina with different fibre orientations, which in the end increases the strength of the laminate. As soon as the matrix micro crack tip reaches the interface of the adjacent lamina leads to further delamination. Therefore, damage in composites is studied in three different scale levels, as below.

### **1.9.1 Damages at macro-scale**

A macro-scale model refers to the structure level in which the whole structure is considered as homogeneous continuum and the constitutive relations are assumed to be anisotropic and incorporated into the structural analysis tools (e.g. finite element method). Many macro-mechanical models have been developed to predict nonlinear stress-strain behaviour of laminates ([Hahn and Tsai, 1973](#), [Petit and Waddoups,](#)

1969), plasticity models ([Sun and Chen, 1989](#), [Vaziri et al., 1991](#)) and progressive damage theory coupled with elasticity ([Allen et al., 1987](#)).

In this level, interlaminar stresses present at the interface between adjacent layers are the most important loads. This interface layer transfers loads and displacements from one layer to another. When this interface breaks, the adjacent layers are separated, leading to so called ‘delamination’. It has been found that delamination is the most important failure mode at the macro-scale level and significantly reduces the strength and stiffness of the structure. Furthermore, it causes stress concentration along the edges of the layers, which results in a progressive failure in the laminate. Fibre orientation of each lamina has an important influence on the laminate’s ability to prevent the propagation of delamination. In order to optimise laminate strength, the fibre orientations are changed to minimise the number of layer and increase the strength of the laminate ([Ghiasi et al., 2010](#)).

### 1.9.1.1 Maximum stress criterion

According to maximum stress criterion, the failure in occurs whenever one stress component along one of the principal material axes attains the corresponding limited value. This failure criterion ignores the interaction between stresses and thus comes under the non-interactive criteria category. It is mathematically expressed as:

$$\begin{aligned}
 \sigma_{11} &\geq X_T, & (\sigma_{11} > 0) \\
 \sigma_{11} &\geq -X_C, & (\sigma_{11} < 0) \\
 \sigma_{22} &\geq Y_T, & (\sigma_{22} > 0) \\
 \sigma_{22} &\geq -Y_C, & (\sigma_{22} < 0) \\
 \sigma_{33} &\geq Z_T, & (\sigma_{33} > 0) \\
 \sigma_{33} &\geq -Z_C, & (\sigma_{33} < 0) \\
 |\tau_{12}| &< S_{12} \\
 |\tau_{13}| &< S_{13} \\
 |\tau_{23}| &< S_{23}
 \end{aligned} \tag{1.1}$$

where subscripts *T* and *C* refer to, respectively, tension and compression, *X*, *Y* and *Z*, are the longitudinal strength (along the fibre direction), transverse strength (perpendicular to the fibre) and through-thickness strength, respectively, *S*<sub>12</sub>, *S*<sub>13</sub> and

$S_{23}$  are the in-plane shear strength, transverse shear strength and through-thickness shear strength, respectively.

### 1.9.1.2 Tsai-Hill criterion

This criterion was derived at two stages: firstly Hill (see [\(Hill, 1998\)](#)) used the well know von Mises yield criterion of isotropic materials to anisotropic materials. Then Aziz and Tsai ([\(Azzi and Tsai, 1965\)](#)) extended the theory to unidirectional lamina. Therefore, the theory is known as the Tsai-Hill criterion. The criterion mathematically expressed as:

$$(G + H)\sigma_1^2 + (F + H)\sigma_2^2 + (F + G)\sigma_3^2 - 2H\sigma_1\sigma_2 - 2G\sigma_1\sigma_3 - 2F\sigma_2\sigma_3 + 2L\tau_{23}^2 + 2M\tau_{13}^2 + 2N\tau_{12}^2 = 1 \quad (1.2)$$

where  $F$ ,  $G$ ,  $H$ ,  $L$ ,  $M$  and  $N$  are the material strength parameters. According to this criterion, any stress state lying within the failure surface is safe and any lying on or outside the surface constitutes for failure. Since this criterion has a quadratic form, it considers stress interaction. The theory assumes three independent shear strengths of unidirectional composites. For example, if only transverse shear  $\tau_{23}$  acts on the body and the corresponding shear strength is  $S_{23}$ , Eq. (1.2) becomes:

$$2L = \frac{1}{S} \quad (1.3)$$

Similarly, by assuming  $\tau_{12}$ ,  $\tau_{13}$ ,  $\sigma_1$ ,  $\sigma_2$  and  $\sigma_3 \neq 0$  and solving simultaneous equations, one obtains:

$$\begin{aligned} 2N &= \frac{1}{R} \\ 2M &= \frac{1}{T} \\ 2H &= \frac{1}{X^2} + \frac{1}{Y^2} - \frac{1}{Z^2} \\ 2F &= \frac{1}{Y^2} + \frac{1}{Z^2} - \frac{1}{X^2} \\ 2G &= \frac{1}{X^2} + \frac{1}{Z^2} - \frac{1}{Y^2} \end{aligned} \quad (1.4)$$

where  $X$ ,  $Y$ , and  $Z$  are the longitudinal material strengths in directions  $x$ ,  $y$  and  $y$ , and,  $S$ ,  $R$  and  $T$  are the through-thickness shear strength, in-plane shear strength and transverse shear strength and, respectively. The main drawback of the criterion is that it does not distinguish between tension and compression normal strengths. In other words, the sign of normal strengths is always positive, which is different in the case of composite materials.

### 1.9.1.3 Tsai-Wu failure criterion

To overcome the drawback associated with using the Tsai-Hill criterion, Tsai and Wu ([Tsai and Wu, 1971](#)) proposed a tensor polynomial failure that is more general than the previous criterion. Unlike Tsai-Hill, Tsai-Wu considers both distortion energy and dilatation energy for predicting failure. Tsai-Wu is based on the expansion of the stress tensor. The criterion assumes that a failure envelope exists in the form:

$$F_i \sigma_i + F_{ij} \sigma_i \sigma_j = 1 \quad i, j = 1, 2, \dots, 6 \quad (1.5)$$

where  $F_i$  and  $F_{ij}$  are the strength tensors and can be obtained from experimental tests with uniaxial loadings on a specimen. Eq. (1.5) is quite complicated, but can be simplified assuming orthotropic material and tensorial symmetry of the coordinates ( $F_{ij} = F_{ji}$ ), and that there is no coupling between normal and shear stresses ( $\sigma_{ii} \times \sigma_{jj} = null$ ). Thus, Eq. (1.5) is reduced to:

$$F_1 \sigma_1 + F_2 \sigma_2 + F_3 \sigma_3 + F_{11} \sigma_1^2 + F_{22} \sigma_2^2 + F_{33} \sigma_3^2 + F_{44} \sigma_4^2 + F_{55} \sigma_5^2 + F_{66} \sigma_6^2 + 2F_{12} \sigma_1 \sigma_2 + 2F_{13} \sigma_1 \sigma_3 + 2F_{23} \sigma_2 \sigma_3 = 1 \quad (1.6)$$

$F_{12}$ ,  $F_{13}$  and  $F_{23}$  are the coefficients of the product  $\sigma_i$  and  $\sigma_j$  in Eq. (1.6) and cannot be obtained by a uniaxial test. However, they are found to have little effect on the final results and are usually assumed null. Also, Eq. (1.6) considers that shear strengths in principal material coordinates are sign-independent of shear stresses, leading to vanish the first power shear stress terms,  $F_4 = F_5 = F_6 = 0$ .

Other failure criteria, such as Hoffman ([Hoffman, 1967](#)) and Chamis ([Chamis, 1969](#)), were proposed in the 1960s. These failure criteria are quadratic criteria, similar to Tsai-Wu, varying the coefficients  $F_i$  and  $F_{ij}$  to ensure a best curve-fitting failure

envelope to the experimental data. However, they added more difficulty to their criteria, which limited their application. Finally, it is important to note that the abovementioned criteria are purely mathematically based criteria, and use plasticity theory for their derivation. Another way to establish failure criteria is based on the physical reality of composite failure.

#### 1.9.1.4 Hashin's criteria

Hashin and Rotem ([Hashin and Rotem, 1973](#)) were considered pioneers in the development of physically based failure criteria. Their criteria are based on real laboratory observations of failure of composites with different fibre orientations, and they concluded that there are two failure mechanisms: one related to fibre failure and the other to matrix failure. Each failure mechanism is distinguished between tension and compression. The criteria are found to be sufficient for the composites under study. However, it may be argued that not all failure modes can be apparent in other composite materials. The Hashin-Rotem failure criteria is summarised below:

- Hashin-Rotem criteria ([Hashin and Rotem, 1973](#))
  - Fibre failure in tension,  $\sigma_{11} \geq 0$

$$\sigma_{11} = X_T \quad (1.7)$$

- Fibre failure in compression,  $\sigma_{11} < 0$ ;  $X_c > 1$

$$-\sigma_{11} = X_c \quad (1.8)$$

- Matrix failure in tension,  $\sigma_{22} \geq 0$

$$\left(\frac{\sigma_{22}}{Y_T}\right)^2 + \left(\frac{\tau_{12}}{S_L}\right)^2 = 1 \quad (1.9)$$

- Matrix failure in compression,  $\sigma_{22} < 0$

$$\left(\frac{\sigma_{22}}{Y_c}\right)^2 + \left(\frac{\tau_{12}}{S_L}\right)^2 = 1 \quad (1.10)$$

Hashin ([Hashin, 1980](#)) later proposed his own criteria under the three-dimensional stress state. In his new criteria, Hashin used a quadric interaction between stress

invariants, as a linear approach underestimates the material strength. It is assumed that failure initiates when one of the following condition is met:

- Hashin criteria ([Hashin, 1980](#))

- Fibre failure in tension,  $\sigma_{11} \geq 0$

$$\left(\frac{\sigma_{11}}{Y_T}\right)^2 + \frac{1}{S_L^2}(\tau_{12}^2 + \tau_{13}^2) = 1 \quad \text{or} \quad \sigma_{11} = X_T \quad (1.11)$$

- Fibre failure in compression,  $\sigma_{11} < 0$

$$-\sigma_{11} = X_c \quad (1.12)$$

- Matrix failure in tension,  $(\sigma_{22} + \sigma_{33}) \geq 0$

$$\frac{1}{Y_T^2}(\sigma_{22} + \sigma_{33})^2 + \frac{1}{S_T^2}(\tau_{23}^2 - \sigma_{22}\sigma_{33}) + \frac{1}{S_L^2}(\tau_{12}^2 + \tau_{13}^2) = 1 \quad (1.13)$$

- Matrix failure in compression,  $(\sigma_{22} + \sigma_{33}) < 0$

$$\frac{(\sigma_{22} + \sigma_{33})}{Y_c} \left[ \left( \frac{Y_c}{2S_T} \right)^2 - 1 \right] + \left( \frac{\sigma_{22} + \sigma_{33}}{2S_T} \right)^2 + \frac{\tau_{23}^2 - \sigma_{22}\sigma_{33}}{S_T^2} + \frac{\tau_{12}^2 + \tau_{13}^2}{S_L^2} = 1 \quad (1.14)$$

where  $X_c$  and  $X_T$  are the longitudinal compressive and tensile strengths,  $Y_c$  and  $Y_T$  are the transverse compressive and tensile strengths, and  $S_T$  and  $S_L$  are the transverse and longitudinal shear strengths, respectively.

#### 1.9.1.5 Puck's criterion

Despite the ability of Hashin's failure criterion to predict the damage in the lamina under normal and transverse shear, numerous studies over the last decades have shown that it does not always agree accurately with experimental results, especially the failure envelope under combined transverse compression and in-plane shear. This drawback of the Hashin criterion is due to its neglecting the determination of the actual fracture plane and its orientation. In addition, using a quadratic approach to account for the interaction between the stress invariants may underestimate the material strength, whereas a higher polynomial degree would lead to more complicated expressions. With increasing computational capacity, many models have therefore been proposed to improve Hashin's criterion including, the one proposed by Puck and

Schürmann ([Puck and Schürmann, 2002](#)). Puck's model is based on the Mohr-Coulomb hypothesis and assumes that fracture is triggered due to the normal stress  $\sigma_n$  and tangential stress  $\tau_t$ , acting on the failure plane with a specific inclination angle to the material plane, which is the key element of the model, as shown in Figure 1.9. Therefore, Puck's criteria are also called 'action plane strength criteria'.

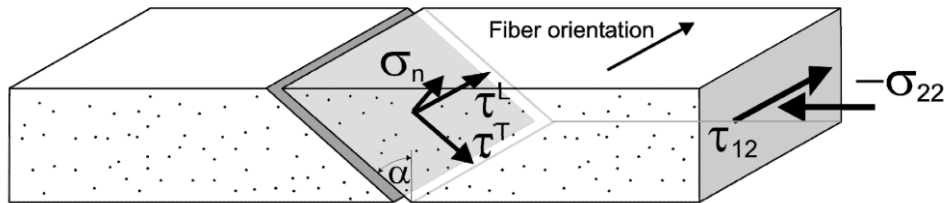


Figure 1.9: Puck's action plane (image from ([Davila et al., 2005](#))).

The criterion is expressed as:

$$\sqrt{\left[\left(\frac{1}{Y_T} - \frac{2p_{\perp\perp}(1+p_{\perp\perp})}{Y_C}\right)\sigma_n(\xi)\right]^2 + \left[\frac{2(1+p_{\perp\perp})}{Y_C}\tau_t(\xi)\right]^2} + \frac{2p_{\perp\perp}(1+p_{\perp\perp})}{Y_C}\sigma_n(\xi) = 1 \quad \sigma_n \geq 0 \quad (1.15)$$

$$\sqrt{\left[\frac{2(1+p_{\perp\perp})}{Y_C}\tau_t(\xi)\right]^2 + \left[\frac{2p_{\perp\perp}(1+p_{\perp\perp})}{Y_C}\sigma_n(\xi)\right]^2} + \frac{2p_{\perp\perp}(1+p_{\perp\perp})}{Y_C}\sigma_n(\xi) = 1 \quad \sigma_n < 0 \quad (1.16)$$

with

$$\sigma_n(\xi) = \sigma_{22} \frac{1 + \cos(2\xi)}{2} + \tau_{23} \sin(2\xi) \quad (1.17)$$

$$\tau_t(\xi) = -\tau_{23} \frac{\sin(2\xi)}{2} + \tau_{23} \cos(2\xi) \quad (1.18)$$

where  $\xi$  is the fracture angle plane, and  $\varphi$  is friction angle. The fracture angle plane in the case of biaxial loading is slightly different from that for uniaxial compression and given by:

$$\xi = 45 + \frac{\varphi \mp \beta}{2} \quad (1.19)$$

in which  $\beta = \arctan(2\tau_{23}/\sigma_{22})$ . Note that in case of uniaxial loading,  $\tau_{23} = 0$ , Eq. (1.19) is reduced to one of uniaxial loading,  $p_{\perp\perp}$  is the inclination coefficient which does not have a clear physical meaning and it is usually fitted to the  $(\sigma_n, \tau_t)$  failure slope angle that is experimentally deduced. However, Puck and Schürmann ([Puck and Schürmann, 2002](#)) recommended to use  $p_{\perp\perp}$  in the range of 0.2-0.25 for a typical glass-fibre/epoxy composites.  $p_{\perp\perp} = 0.22$ , a value in the middle of the range, is used in the study.

### **1.9.2 Damages at micro-level**

In the simulation of composite materials at the micro-level, each constituent of the composite material (matrix, fibre and fibre/matrix interface) is considered as a homogeneous material and exhibits its own behaviour (see Chapter 2, 3 and 4). The experimental observations concluded that a composite matrix such as epoxy, which is known to be a pressure sensitive material, shows different yield stresses in tension and compression. Therefore, the traditional failure models, such as von Mises and Tresca may not accurately estimate the yield stress of this material.

Several failure criteria have been proposed to predict damage initiation and propagation of the constituents. Among the early attempts was developed by ([Bowden and Jukes, 1972](#), [Raghava et al., 1973](#)). Their criteria were based on modification of the Tresca and von Mises failure model to account for hydrostatic stress.

Asp et al. ([Asp et al., 1996a](#), [Asp et al., 1995](#)) conducted experimental tests on three types of epoxy under uniaxial, biaxial and triaxial stress states. They suggested using their proposed dilatational energy density criterion when dilatational effects are dominant, and deviatoric effects (or known as distortional energy density) are zero or low. It is worth mentioning that deviatoric effects can be eliminated or reduced by applying equibiaxial or equitriaxial stress, as these stress states prevent the change of shape. The dilatational energy density criterion can be expressed as:

$$U_v = \frac{1 - 2\nu}{6E} (\sigma_{11} + \sigma_{22} + \sigma_{33})^2 \quad (1.20)$$

where  $E$  and  $\nu$  are the Young's modulus and Poisson's ratio, respectively, and  $\sigma_{11}$ ,  $\sigma_{22}$  and  $\sigma_{33}$  are the principal stresses. Later, Asp et al. ([Asp et al., 1996b](#)) used the criterion to simulate a unidirectional fibre composite subjected to transverse tension. They compared their results with the von Mises criterion and found that the strengths predicted by a dilatational energy density criterion corresponded more closely to experimental results than those predicted by von Mises. However, there are two major limitations of the criterion. Firstly, it is applicable only in the case of low effect of the distortional energy density, which is not possible to be achieved in a composite material with random fibre distribution. Secondly, it does not take into account the propagation of damage in the material.

To overcome these limitations, Gosse and Christensen ([Gosse and Christensen, 2001](#)) proposed strain invariant failure theory (SIFT) to predict the failure initiation of the matrix. The authors of the criterion used first invariant strain (volumetric strain invariant),  $J_1$ , to represent the volume increase in the matrix material. The first invariant strain is defined as:

$$J_1 = \varepsilon_{xx} + \varepsilon_{yy} + \varepsilon_{zz} \quad (1.21)$$

where  $\varepsilon_{xx}$ ,  $\varepsilon_{yy}$  and  $\varepsilon_{zz}$  are the strain components. The first invariant strain is valid only for tension-tension biaxial load where the failure is controlled by volume increase. The matrix in this situation fails by microcavitation (also known as crazing). To consider material yielding resulting from change of shape (distortional), a function of second deviatoric strain,  $f_2$ , is used. The second deviatoric strain is expressed as:

$$f_2 = \frac{1}{6} [(\varepsilon_{xx} - \varepsilon_{yy})^2 + (\varepsilon_{yy} - \varepsilon_{zz})^2 + (\varepsilon_{xx} - \varepsilon_{zz})^2] - \frac{1}{4} (\varepsilon_{xy}^2 + \varepsilon_{yz}^2 + \varepsilon_{xz}^2) \quad (1.22)$$

The theory employed von Mises (or equivalent) strain as:

$$\varepsilon_{eqv} = \sqrt{3f_2} \quad (1.23)$$

To define the matrix failure, the material properties required are the critical first invariant strain,  $J_1^{cr}$ , the critical second deviatoric strain,  $J_2^{cr}$  and critical equivalent strain,  $\varepsilon_{eqv}^{cr}$ . This method is close to those models used in meso-scale level as there is no direct influence of the properties of the individual constituents. However, to make use of the method at the micro-scale level, Tay et al. ([Tay et al., 2005](#)) amplified these strain invariants through FE analyses of a unit cell and determined 'the strain amplification factor', SAF.

Swaminathan and Ghosh ([Swaminathan and Ghosh, 2006](#)) developed Voronoi cell finite element method to study damage initiation and propagation of a microstructure of an RVE. The fibre/matrix interface was simulated using a bilinear cohesive zone law. They assumed that there was no failure in the matrix.

Bulsara et al. ([Bulsara et al., 1999](#)) used a finite element method to analyse an RVE with random fibre distribution. A simple maximum normal stress failure criterion was used to identify fibre/matrix debonding and radial matrix cracking.

Paris et al. ([Paris et al., 2003](#)) used a boundary element method to study the fibre/matrix interface damage mechanism under uniaxial and biaxial loads applied to a single fibre embedded in a matrix. An initial crack at the fibre/matrix interface was assumed, which would progress to a certain length around the fibre. At this stage under transverse tension, the debonding angle was about 130° perpendicular to the load direction. Then the interface crack would kink towards the matrix and penetrate the matrix in a radial direction. The second failure mechanism (penetration of the interface crack into the matrix) was studied separately by Paris et al. ([Paris et al., 2007](#)). Eventually, these cracks merge, causing final failure of the composite. Correa et al. ([Correa et al., 2008](#)) pursued similar concepts but applied transverse compression. Correa and co-workers found that the initial interface crack angle was almost 135°. They showed that this crack would propagate unstably up to 130° upwards and 206° downwards. Next, the interface crack would either continue along in the interface or change its direction and kink into the matrix. It has been demonstrated that the kinking crack inclination was between 50° and 58°.

Canal et al. ([Canal et al., 2009](#)) studied the mechanical behaviour of fibre-reinforced composites made up of a ductile rubber-toughened epoxy matrix under transverse tension, transverse shear, and a biaxial load of transverse tension and transverse shear. Since a rubber-modified matrix was used in the study, it was modelled with an elasto-viscoplastic constitutive model developed by Jeong ([Jeong, 2002](#)). Interface damage propagation was also taken into account and modelled with cohesive elements. The results were compared with the Hashin ([Hashin, 1980](#)) and Puck ([Puck and Schürmann, 2002](#)) failure criteria. The comparison revealed the need to improve current failure criteria in order to include more realistic matrix and interface behaviour, especially a weak interface.

González and LLorca ([González and LLorca, 2006](#)) analysed the behaviour of a polymer-matrix composite material subjected to transverse compression stress. The study was carried out using FEM and a square RVE with randomly distributed fibres. The matrix was assumed isotropic at the micro-scale level and modelled with elasto-plastic constitutive model following the Mohr-Coulomb yield criterion. The fracture plane angle was assumed to be  $52.5^\circ$ , based on observations of an epoxy matrix laminate failure subjected to transverse compression. The fibre/matrix interface was also modelled by cohesive elements. Three interface strength cases were studied: weak, strong and perfect. The results showed that debonding was the dominant damage mechanism when a weak interface was used, while in the case of strong and perfect interface strength, shear band propagation in the matrix was the controlling failure mechanism.

A follow up study was conducted by Totry et al. ([Totry et al., 2008a](#)) to predict the failure envelope of fibre-reinforced composite lamina subjected to combined transverse compression and transverse shear stress. The results were compared with other failure criteria: namely ([Hashin, 1980](#)), Puck ([Puck and Schürmann, 2002](#)) and LaRC ([Davila et al., 2005](#)). Two interface strength cases were also investigated. The predicted failure envelopes agreed well with other failure models in the case of a strong interface. However, a weak interface, the results were underestimates compared to other failure models. Later, Totry et al. ([Totry et al., 2008c](#)) used a three-dimensional RVE to predict the failure envelope of C/PEEK composites under transverse compression and longitudinal shear. Their results were compared with experimental

data available in ([Vogler and Kyriakides, 1999](#)). The results gained from computational micromechanics were in excellent agreement with the experimental data. This also showed the potential of micromechanical analysis in the study of failure progression, to predict macroscopic properties of lamina, and could be used to assess the validity of current failure criteria.

Yang et al. ([Yang et al., 2012](#)) studied the mechanical behaviour of fibre-reinforced composites under transverse tension and compression. It has been assumed that matrix failure occurs in two stages: initial yielding and damage onset. They used the extended Drucker-Prager criterion to predict yield in the matrix, while the ductile criterion was used for damage onset prediction. The stress-strain response of the matrix used in this study is illustrated in Figure 1.10. The matrix response is initially linear elastic (a–b), followed by plastic yielding (b–c) which is predicted by the Drucker-Prager criterion. Beyond point c, there is a significant reduction of load-carrying capability until the final failure, (c–d). Point c in the figure represents the damage onset and is predicted by the ductile damage criterion. Whereas the stress-strain response (c–d) is governed by damage evolution, the dashed curve denotes the behaviour in the absence of damage.

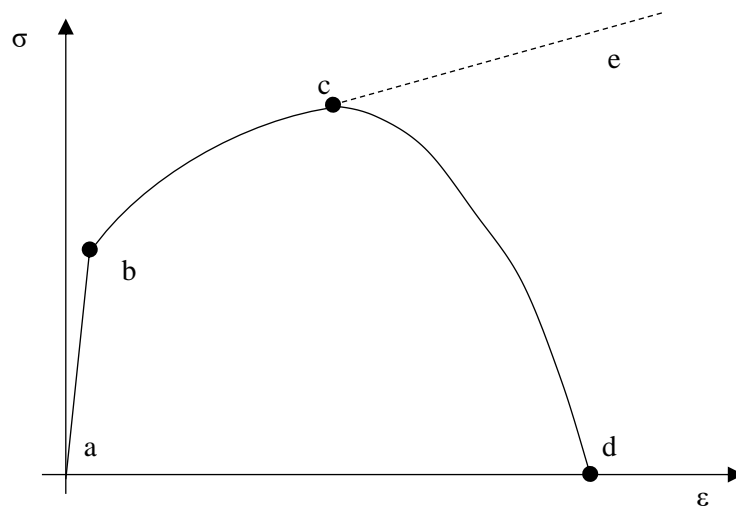


Figure 1.10: Stress–strain response of the matrix.

In a follow-up study of ([Yang et al., 2012](#)), Yang et al. ([Yang et al., 2015](#)) used the same matrix model to study the failure of UD fibre-reinforced composites under

transverse and longitudinal shear. The stress-strain curves obtained under longitudinal shear were compared with experimental results. The average predicted strength of five RVEs was almost 15% lower than the experimental results.

### *1.10 Discrete element method*

The discrete element method DEM is based on explicit finite difference principles, introduced by Cundall ([Cundall, 1971](#)) for the analysis of rock mechanics problems, which then applied to soils by Cundall and Strack ([Cundall and Strack, 1979](#)). With the continuous development of computer power over the last three decades, there has been a great accumulated body application of DEM in different science areas such as concrete ([Hentz et al., 2004a](#), [Hentz et al., 2004b](#)), asphalt ([Kim et al., 2008](#), [Wu et al., 2010](#), [You and Buttlar, 2004](#)) and composites ([Sheng et al., 2010](#), [Yang et al., 2011b](#), [Yang et al., 2011a](#)).

To understand DEM, assume two circular discrete particles (named  $A$  and  $B$ ) with radii of  $r_A$  and  $r_B$ , respectively, are in contact. In the DEM, the interaction of these particles is treated in a dynamic procedure mode with equilibrium state developing whenever the internal forces balance. The contact forces are calculated by tracing a group of particles within a measurement circle, while particle displacements are calculated by tracing the movement of an individual particle. Particles movement are performed by applying velocity or force on a group of particles or walls, which result in disturbances of the system. Since DEM is based on a dynamic process, the disturbance of an individual particle should not propagate further to its immediate neighbours. To satisfy the above constraints, the applied velocity on the system is kept constant, followed by determining the timestep based on the physical properties of the system.

The calculations in the DEM swap between the application of Newton's second law of motion on the particles and a force-displacement used for contacts between particles. Figure 1.11 illustrates the calculation that takes place in each timestep. At the beginning of each timestep, particles and walls position are updated. Next, force-displacement law is applied to each contact to calculate contact forces. Then, equation

of motion is applied to each particle to update its position based on total forces acting on the particle that emerges from its contacts and calculated from the previous step and any external forces applied on it. There are different force-displacement contact models available in literature. Models used in this thesis are introduced in the next subsections.

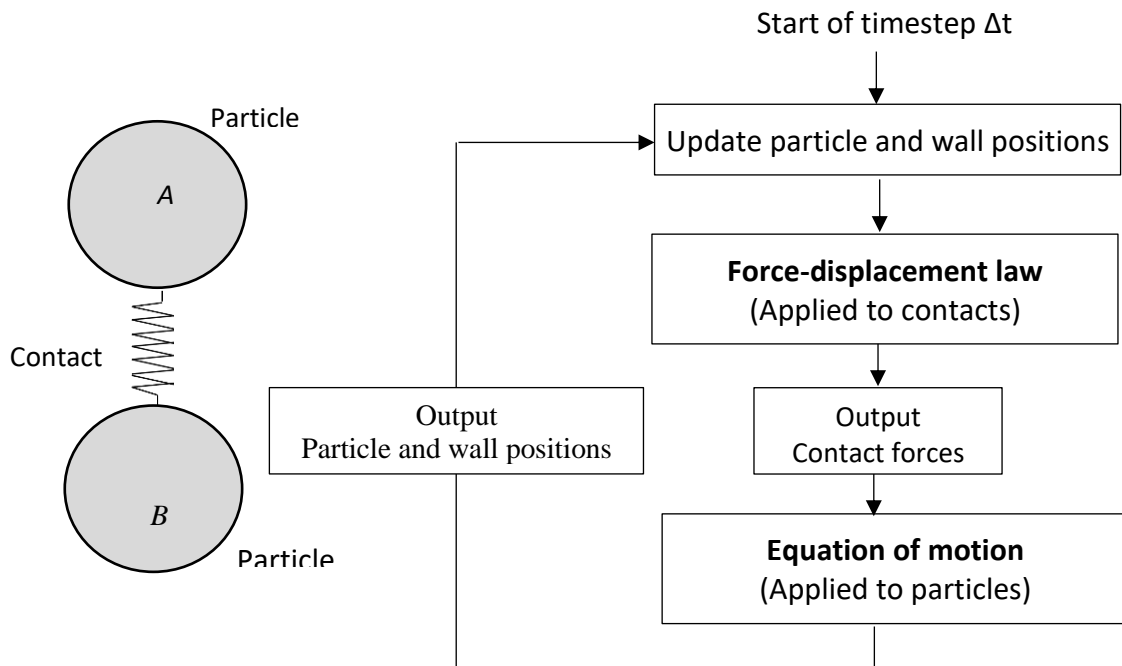


Figure 1.11: Calculation cycle in DEM.

### 1.10.1 Force-displacement law

Force-displacement law relates the relative displacement between two particles to the contact force acting on them. Many contact models are available in the existing literature; each one has its own behaviour and is used for solving different problems. For example, linear hysteretic model ([Luding, 2008b](#), [Luding, 2008a](#)), local rupture criterion similar to Mohr-Coulomb criterion ([Camborde et al., 2000](#), [Hentz et al., 2004a](#)) and Burger's model ([Abbas et al., 2007](#), [Cai et al., 2013](#), [Liu and You, 2010](#)). This section gives an overview of the contacts model used in this study.

### 1.10.1.1 Contact-bond model

In the DEM, the constitutive behaviour of the material is simulated by associating the contact model with each contact. The contact-bond model is one of the most popular models and can be formed to bond ball-to-ball or ball-to-wall. It can be envisaged as a pair of elastic springs with constant normal and shear stiffness acting at the contact point. These two springs have stated properties, namely contact tensile strength  $F_c^n$  [force], shear strength  $F_c^s$  [force], normal stiffness  $k^n$  [force/displacement], and shear stiffness  $k^s$  [force/displacement]. A typical contact bond is shown schematically in Figure 1.12a. The contact normal strength and shear strength limit the total normal force and shear force that can be carried by the contact, respectively. When applied force on the contact exceeds the contact's strength, the contact breaks. Since the contact bond acts over a vanishingly small area, it does not transmit the moment that develops between interacted particles. The stiffness of the contact consists of the contact stiffness arising from particle-particle overlap. The interparticle force,  $F_i$ , acting at the contact point represents the action of particles  $A$  and  $B$  and can be decomposed into normal,  $F^n$ , and shear,  $F^s$ , forces with respect to the contact plane:

$$F = F^n + F^s \quad (1.24)$$

The normal contact force relates to relative displacements as:

$$F^n = k^n U^n n_i \quad (1.25)$$

And the increment shear force,  $\Delta F^s$ , is calculated using:

$$\Delta F^s = -k^s \Delta U^s \quad (1.26)$$

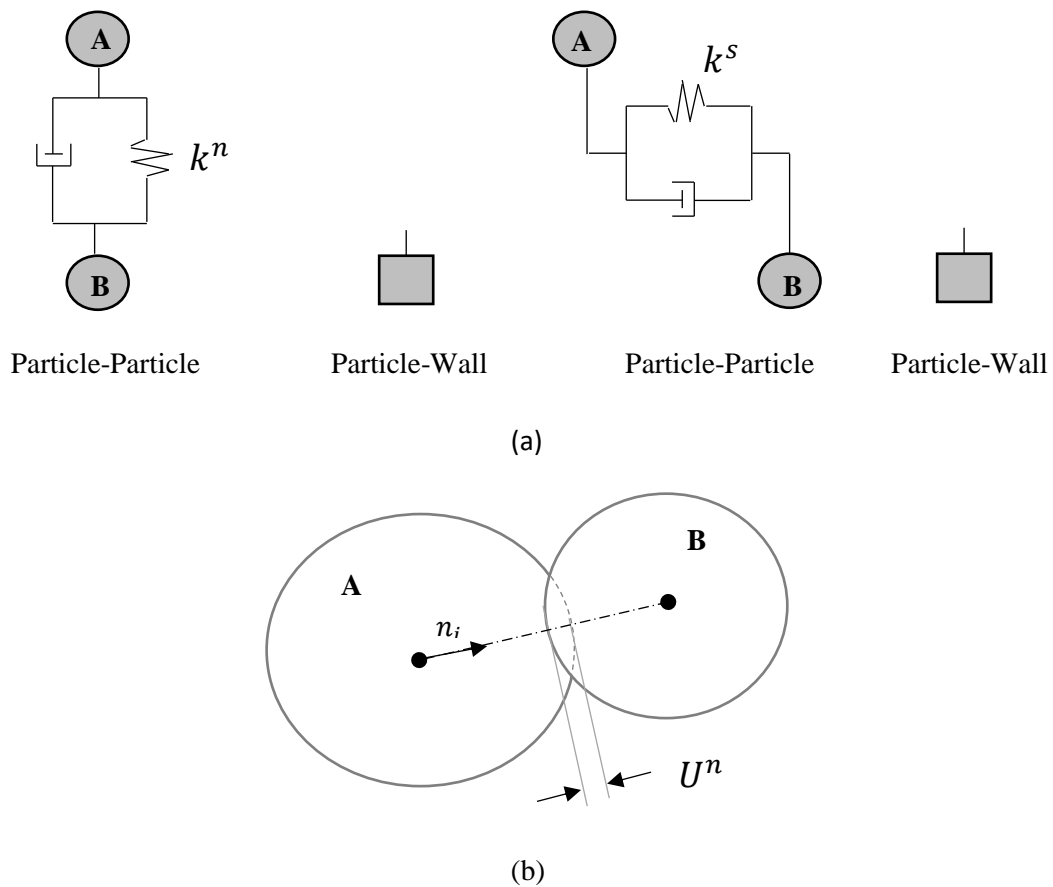


Figure 1.12: Contact between particles. (a) Contact bond model in PFC2D (Itasca, 2003). (b) Notation used to describe particle-particle contact bond.

where  $U^n$  is the overlapping magnitude of two particles as shown in Figure 1.12b;  $n_i$  is the unit normal vector and  $\Delta U^s$  is the increment shear displacement. The normal vector is a straight line along the shortest distance between the centre of two bonded particles. While in the case of particle to wall contact, the normal vector is defined as the shortest distance between the particle centre and the wall. It is important to note that the normal contact stiffness is a secant modulus because it relates the total force and the total normal displacement, whereas the shear stiffness is a tangent modulus because it relates shear force and increment shear displacement. When contacts are formed, shear forces are set to zero; at each subsequent timestep contact shear forces are calculated and are added to the current value to form the new shear force which is used for the next cycle as follows:

$$F^s = \{F^s\}^{current} + \Delta F^s \quad (1.27)$$

Contact forces update every cycle and are used to in the following cycle to determine the acceleration by means of Newton's Second Law. The acceleration is then integrated to obtain the velocity and displacement of particles. The presence of contact bond superposes the slip that occurs between particles. Slip between particles, however, is important to mimic the real behaviour of the materials. In the DEM, slip is provided by the relationship between normal force, shear force and the friction coefficient of balls  $\mu$  [dimensionless]. The contact is checked for slipping by calculating the maximum allowable contact shear force,  $F_{max}^s$ :

$$F_{max}^s = \mu |F^n| \quad (1.28)$$

If  $|F^s| > F_{max}^s$ , then slip is allowed to occur during the subsequent cycle by setting the value of  $F^s$  equal to  $F_{max}^s$  via:

$$\begin{aligned} F^s &= -|F_{max}^s| & \text{if } F^s < 0 \\ F^s &= |F_{max}^s| & \text{otherwise} \end{aligned} \quad (1.29)$$

The contact stiffness of the contact bond model is computed from the two contacting entities (particle-to-particle or particle-to-wall) by assuming that springs forming the contact act in series. The normal contact stiffness (secant stiffness) is given by:

$$k^n = \frac{k_n^{(A)} k_n^{(B)}}{k_n^{(A)} + k_n^{(B)}} \quad (1.30)$$

and the shear stiffness (tangent stiffness) is given by:

$$k^s = \frac{k_s^{(A)} k_s^{(B)}}{k_s^{(A)} + k_s^{(B)}} \quad (1.31)$$

where  $k_n^{(A)}$ ,  $k_n^{(B)}$ ,  $k_s^{(A)}$  and  $k_s^{(B)}$  [force/displacement] are the normal and shear stiffness of the contacted particles. Force-displacement laws for the contact bond model are shown in Figure 1.13.

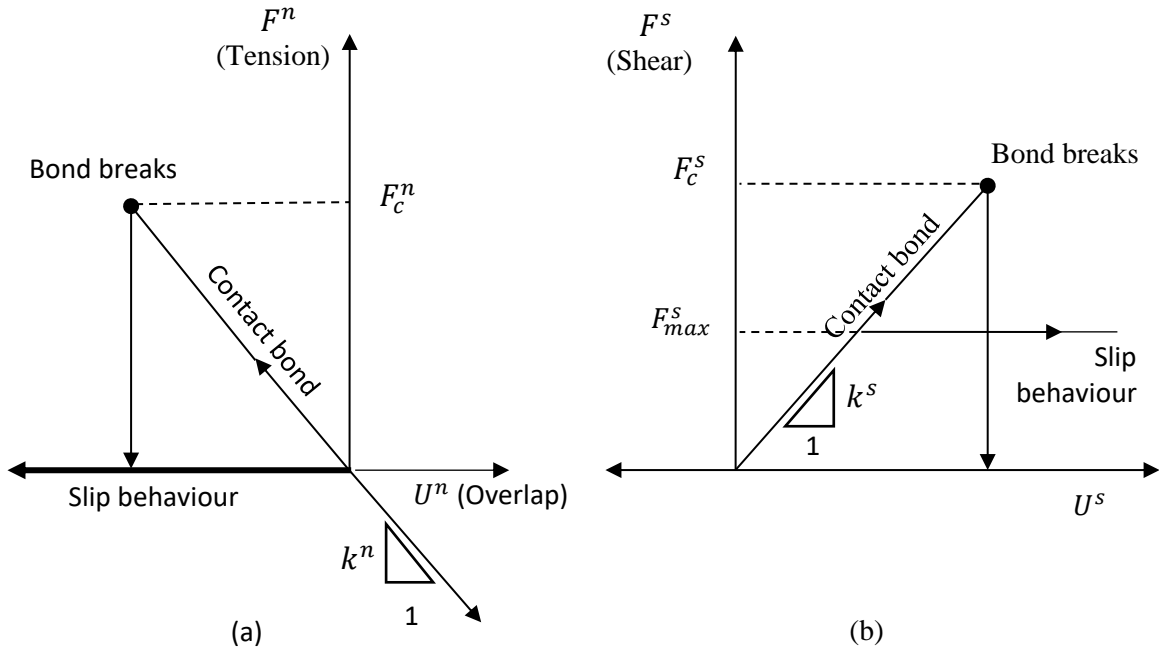


Figure 1.13: Force-displacement laws for the contact bond model: (a) normal behaviour, and (b) shear behaviour.

### 1.10.1.2 Parallel bond and moment resistance

The parallel bond provides the force-displacement through a finite-sized piece of cementitious material deposited between two particles. It can be envisioned as a set of springs with constant normal and shear stiffness distributed over a circular disk or rectangular cross-section lying on the contact plane and centred at the contact point. Parallel bond acts in *parallel* with contact bond or slip described in the previous section, therefore the presence of parallel bond does not prevent the possibility of slip. Unlike contact bond, parallel bond can transmit both forces and moment that develop between particles and should only be installed between two balls. The total force and moment carried by the parallel bond are shown in Figure 1.14. The force vector can be resolved into normal and shear force components with the plane perpendicular to the straight line along particle centres as:

$$\bar{F} = \bar{F}^n n_i + \bar{F}^s n_j \quad (1.32)$$

the parallel bond moment is resolved into a shear and normal moment as:

$$\bar{M} = \bar{M}^s + \bar{M}^n \quad (2D \text{ model: } \bar{M}^n = 0) \quad (1.33)$$

where  $\bar{F}^n, \bar{F}^s$  and  $\bar{M}^s$  are the normal and shear force and shear moment, respectively,  $n_i$  and  $n_j$  are the unit vectors defining the contact plane. The parallel bond force and moment are set to zero when the parallel bond is formed. Each following relative displacement increment and rotation increment at the contact results in an increment of elastic force and moment that is added to the current values. Over a cycle with timestep  $\Delta t$ , the elastic force increments are calculated by:

$$\Delta \bar{F}^n = (-\bar{k}^n A \Delta \bar{U}^n) n_i \quad (1.34)$$

$$\Delta \bar{F}^s = -\bar{k}^s A \Delta U^s \quad (1.35)$$

$$\text{with } \Delta U = V \Delta t \quad (1.36)$$

and the elastic moment increment is given by

$$\Delta \bar{M}^s = -\bar{k}^n I \Delta \theta^s \quad (1.37)$$

$$\text{with } \Delta \theta = (\omega^{[B]} - \omega^{[A]}) \Delta t \quad (1.38)$$

where  $\bar{k}^n$  and  $\bar{k}^s$  [stress/displacement] are normal and shear stiffness, respectively,  $V$  is the contact velocity,  $A$  is the area of the bond and  $I$  is the moment of inertia of the disk cross section about an axis through the contact point and in the direction of  $\Delta \theta^s$ , they are given by

$$A = 2\bar{R}t \quad (1.39)$$

$$I = \frac{2}{3} t \bar{R}^2 \quad (1.40)$$

where  $\bar{R}$  is the bond radius and calculated from the radius of the balls as:

$$\bar{R} = \min(R^{(A)}, R^{(B)}) \quad (1.41)$$

The new force and moment vectors associated with the parallel bond are determined by adding elastic force and moment increment vectors in the new timestep to the existing values. This procedure should be done after rotating shear component vectors to account for the motion of the contact plane. It is important to note, since parallel bonds act in parallel with contact bonds, then the stiffness of the entire beam is equivalent to that for contact bond and parallel bond and given by:

$$K = (k^{n/s})_{\text{contact bond}} + (A\bar{k}^{n/s})_{\text{parallel bond}} \quad (1.42)$$

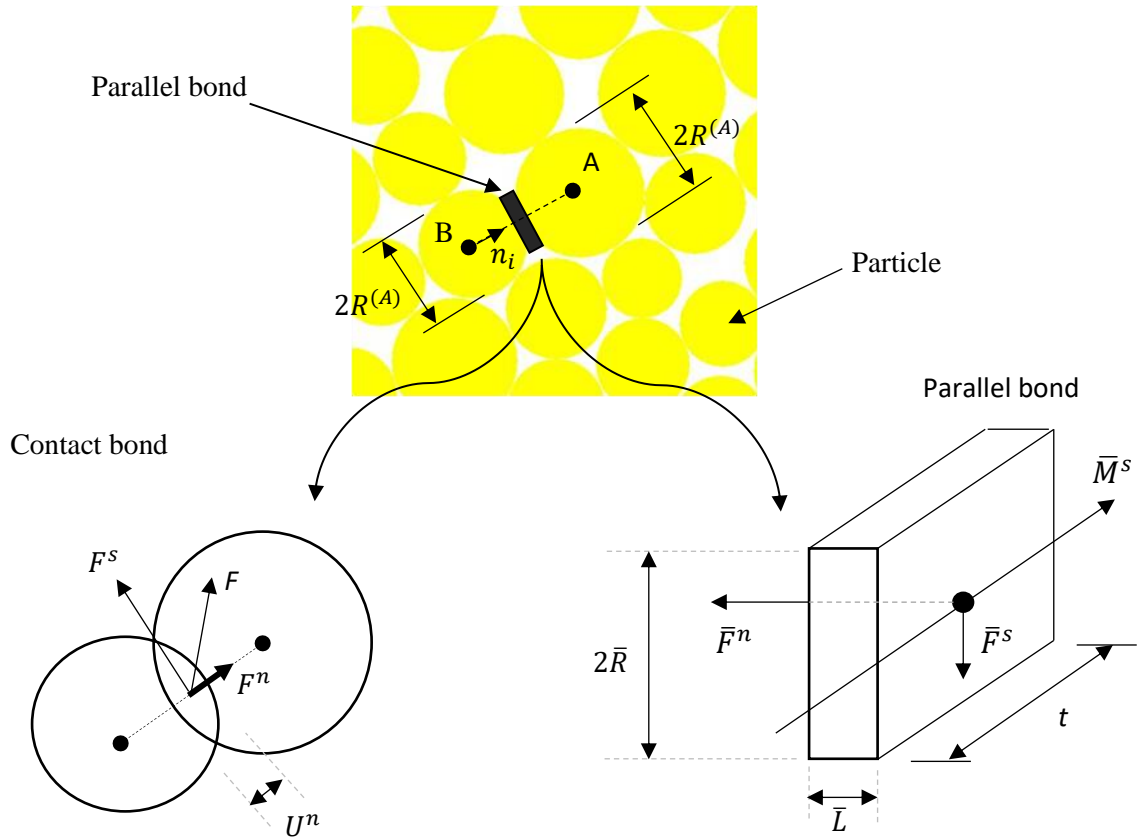


Figure 1.14: Schematic diagram of the parallel bond.

Failure in the parallel bond depends on the cross-sectional nature of the bond. The maximum tensile,  $\bar{\sigma}$  [stress] and shear,  $\bar{\tau}$  [stress] stresses acting on the bond periphery are calculated using beam theory as:

$$\bar{\sigma} = \frac{-\bar{F}^n}{A} + \frac{|\bar{M}_3|}{I} R \quad (1.43)$$

$$\bar{\tau} = \frac{|\bar{F}^s|}{A} \quad (1.44)$$

If the maximum tensile stress exceeds the normal strength ( $\bar{\sigma} > \bar{\sigma}_c$ ), or the maximum shear stress exceeds the shear strength ( $\bar{\tau} > \bar{\tau}_c$ ) then the parallel bond breaks. Potyondy and Cundall ([Potyondy and Cundall, 2004](#)) were the first to introduce the idea of a parallel bond to develop the bonded particle model (BPM) for rock. They simulated various virtual tests with different micro parameters and proved that the BPM is capable of representing all of the important behaviour mechanism in rock.

Finally, the stress-displacement laws for the parallel bond model are shown in Figure 1.15.

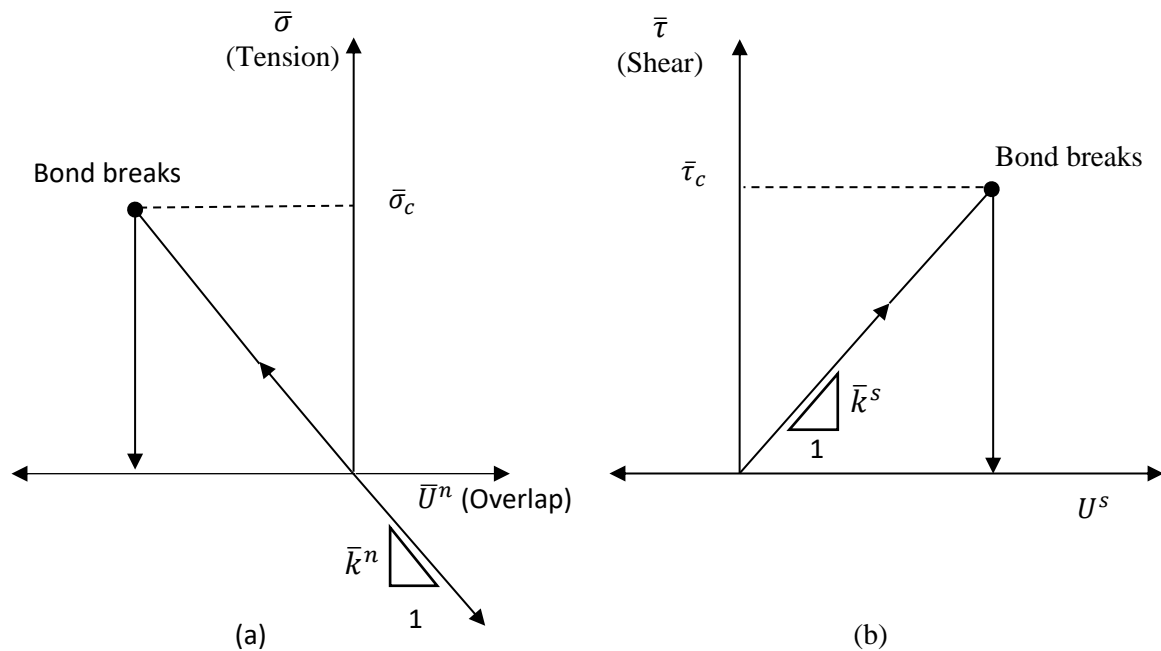


Figure 1.15: Force-displacement laws for the parallel bond model: (a) normal behaviour, and (b) shear behaviour.

### 1.10.1.3 Displacement-softening model

The displacement softening model (DSM) in DEM is similar to the well-known cohesive model that is used in continuum. A Cohesive model is usually used to describe interfaces in composite materials such as fibre/matrix and interaction between plies. The DSM force-displacement curve is shown in Figure 1.16. The initial response of DSM is linear in absence of damage. Damage is assumed to initiate when the force applied in the contact reaches the initial contact bond strength, i.e.  $\Delta F^n > F_c^n$  or  $\Delta F^{n/s} > F_c^s$ . After this point, the applied force reduces linearly following a softening curve. If unloading occurs during the softening, the bond is rebounding along the elastic path. When the plastic displacement limit,  $U_{pmax}$ , reaches, then the contact removes from the model and assumes an inactive state.

The elastic normal and shear force increment,  $\Delta F^{n/s}$ , calculated as a function of displacement,  $\Delta U^{n/s}$  via:

$$\Delta F^{n/s} = k^{n/s} \Delta U^{n/s} \quad n: \text{normal}, s: \text{shear} \quad (1.45)$$

And the resultant contact force determined as:

$$F = \sqrt{F^n^2 + F^s^2} \quad (1.46)$$

In the case of mix mode fracture, the contact strength,  $F_{max}$ , is calculated from the two strength parameters (*i.e.*  $F_c^n$  and  $F_c^s$ ) as a function of the current orientation of the contact force. It is assumed that the contact strength is a linear function of the angle,  $\alpha$ :

$$F_{max} = \left(1 - \frac{2\alpha}{\pi}\right) \cdot F_c^n + \frac{2\alpha}{\pi} \cdot F_c^s \quad (1.47)$$

The yielding of the bond in tension is determined by comparing the resultant contact, Eq. (1.46), with the contact strength, Eq. (1.47). If  $F > F_{max}$ , then the contact yields. If the contact is under compression, failure may take place due to shear. The strength of the contact in this case is calculated as:

$$F_{max} = \mu |F^n| + F_c^s \quad (1.48)$$

where  $\mu$  is the friction coefficient.

The particle assembly is first generated with a linear contact law, then displacement softening contact models are assigned in interface. To get the complete DSM parameters,  $U_{pmax}$  is calculated by assuming that the area under the force-displacement curve represents the energy required to create a new crack, thus one has:

$$G_I = \frac{1}{2} \sigma_{max} U_{pmax} \quad (\text{Mode I}) \quad (1.49)$$

$$G_{II} = \frac{1}{2} \tau_{max} U_{pmax} \quad (\text{Mode II}) \quad (1.50)$$

$$G_{III} = \frac{1}{2} \sigma_{max} U_{pmax} + \frac{1}{2} \tau_{max} U_{pmax} \quad (\text{Mix mode}) \quad (1.51)$$

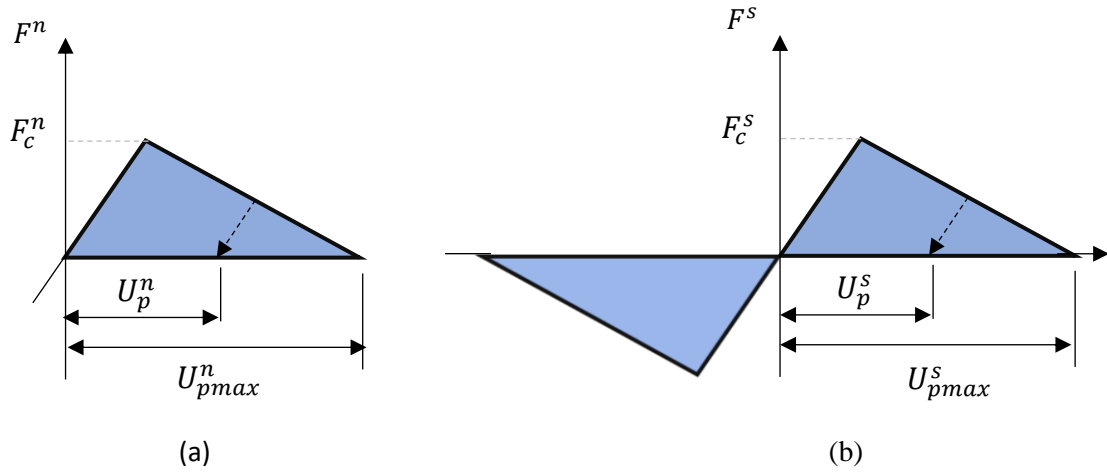


Figure 1.16: Constitutive behaviour of contact displacement-softening model: (a) normal behaviour, and (b) shear behaviour.

where  $G_I$ ,  $G_{II}$  and  $G_{III}$  are the energy release rate, and  $\sigma_{max}$  and  $\tau_{max}$  are the cohesive strength. In the DEM model, we assumed that the mechanical behaviour of the softening-displacement contact is equivalent to that of an elastic beam with its ends at the centres of two contacting balls, similar to the parallel bond in the previous section. Therefore, the stress acting over the cross section of the beam can be expressed as:

$$\sigma_{max} = \frac{F_c^n}{A} \quad (1.52)$$

$$\tau_{max} = \frac{F_c^s}{A} \quad (1.53)$$

### 1.10.2 Law of motion

The motion of an individual particle is governed by the resultant force and moment acting upon it, and can be characterised in terms of translational motion and rotational motion of the centre of particles. The equation of motion can be expressed by two vector equations: one relates the resultant force to the translational motion of the particles and the other relates the resultant moment to the rotational motion as:

$$F = m (\ddot{x}_i - g_i) \quad \text{Translational motion} \quad (1.54)$$

$$\bar{M}_3 = I \dot{\omega}_3 \quad \text{Rotational motion} \quad (1.55)$$

where  $i = 1, 2, 3$  indicates the component in the x-, y-, z-directions,  $F$  is the resultant force (sum of the all externally applied forces acting on the particle),  $\ddot{x}_i$  is the acceleration of the particle,  $m$  is the mass of the particle,  $g_i$  is the body force acceleration vector (i.e. gravity loading),  $\bar{M}_3$  is the component of the resultant moment in z-direction acting on the particle,  $\dot{\omega}_3$  is the angular velocity and  $I$  is the moment of inertia of the particle. The equations of motion given in Eq. (1.54) and (1.55) are solved using a central finite difference procedure involving the timestep of  $\Delta t$ . The quantities  $\ddot{x}_i$ ,  $\dot{\omega}_3$ ,  $F$  and  $\bar{M}_3$  are computed at the primary interval of  $(t \pm \Delta t)$ . The translational and rotational accelerations are then calculated at time  $t$  as:

$$\ddot{x}_i^{(t)} = \frac{1}{\Delta t} \left( \dot{x}_i^{(t+\Delta t/2)} - \dot{x}_i^{(t-\Delta t/2)} \right) \quad (1.56)$$

$$\dot{\omega}_3^{(t)} = \frac{1}{\Delta t} \left( \omega_3^{(t+\Delta t/2)} - \omega_3^{(t-\Delta t/2)} \right) \quad (1.57)$$

The velocities at time  $(t + \Delta t/2)$  can be then solved by inserting Eq. (1.54) and (1.55) into Eq. (1.56) and (1.57). Hence,

$$\dot{x}_i^{(t+\Delta t/2)} = \dot{x}_i^{(t-\Delta t/2)} + \left( \frac{F^{(t)}}{m} g_i \right) \Delta t \quad (1.58)$$

$$\omega_3^{(t+\Delta t/2)} = \omega_3^{(t-\Delta t/2)} + \left( \frac{\bar{M}_3^{(t)}}{I} \right) \Delta t \quad (1.59)$$

Finally, the position of particle centre is updated by integrating velocities in (1.58) and (1.59) as

$$x_i^{(t+\Delta t)} = x_i^{(t)} + \dot{x}_i^{(t+\Delta t/2)} \Delta t \quad (1.60)$$

The calculation cycle for law of motion can be summarised as follows. Firstly, Eqs. (1.58) and (1.59) are used to obtain  $\dot{x}_i^{(t+\Delta t/2)}$  and  $\omega_3^{(t+\Delta t/2)}$  based on given values

of  $\dot{x}_i^{(t-\Delta t/2)}$ ,  $\omega_3^{(t-\Delta t/2)}$ ,  $F_i^{(t)}$  and  $M_3^{(t)}$ . Then, this value is used to obtain  $x_i^{(t+\Delta t)}$  by applying Eq. (1.60). The values of  $F_i^{(t+\Delta t)}$  and  $M_3^{(t+\Delta t)}$ , to be used in the next cycle, are obtained by application of the force-displacement law ([Itasca, 2003](#)).

### 1.10.3 Mechanical timestep

As discussed earlier, DEM uses a central finite difference scheme to integrate the equations of motion, Eqs. (1.58) and (1.59). It is also assumed that the velocities and accelerations are constant during each timestep. The solution procedure of these equations remains stable only if the timestep does not exceed a critical value. In other words, the timestep should be small enough so the disturbance cannot propagate from any particle further than its immediate neighbours during each timestep. By default, the PFC ([Itasca, 2003](#)) automatically calculates the critical timestep at the start of each cycle and then the actual timestep is treated as a fraction of the calculated critical value.

The way the approach uses by PFC to estimate the critical timestep is evaluated by considering a single one-dimensional mass spring system described by mass,  $m$ , and stiffness,  $k$ , as shown in Figure 1.17. For this single of freedom system, Bathe and Wilson ([Bathe and Wilson, 1976](#)) found that the critical timestep is simply given by:

$$t_{crit} = \frac{T}{\pi} \tag{1.61}$$

$$T = 2\pi \sqrt{m/k} \tag{1.62}$$

where  $T$  is the period of free vibration of the degree of freedom.

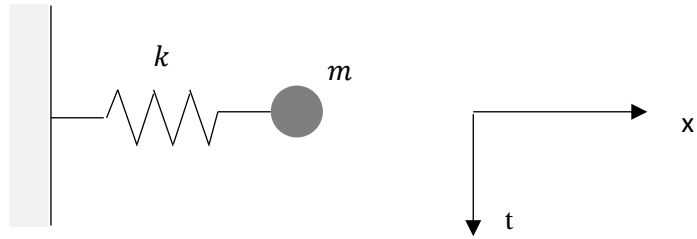


Figure 1.17: Schematic of a single mass-spring system used by PFC to calculate the critical timestep.

Next, consider an infinite series of point masses and springs, as shown in Figure 1.18, which illustrates particles and contacts in a system, respectively. The smallest period of this system occurs when the masses are moving synchronously in opposed directions so that no motion occurs at the centre of each spring. The motion of a single point mass can therefore be described by a two equivalent system as shown in Figure 1.18b and c. Thus, the critical timestep for this system is found as:

$$t_{crit} = 2\sqrt{\frac{m}{4k}} = \sqrt{m/k}. \quad (1.63)$$

It has also been suggested ([ltasca, 2003](#)) to multiply the critical time increment by a safety factor, which is by default being 0.8.

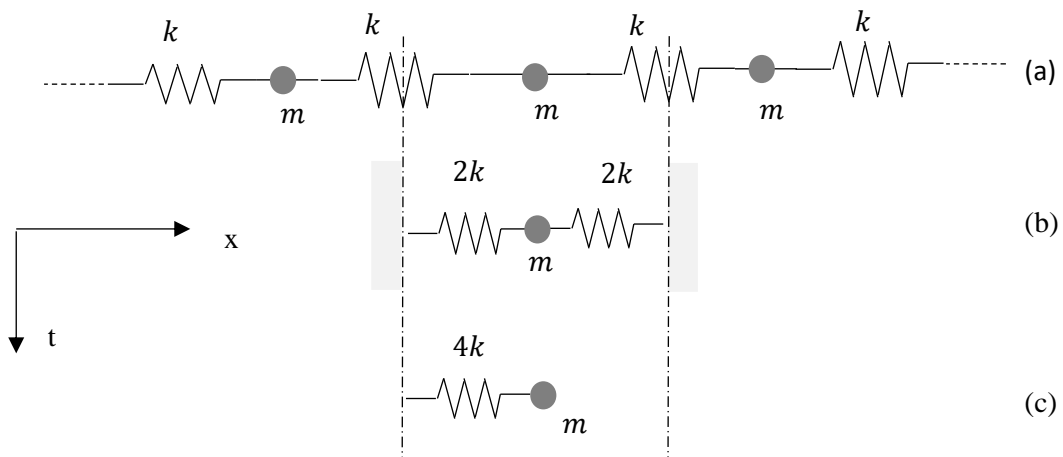


Figure 1.18: Schematic of a multiple mass-spring system used by PFC to calculate the critical timestep.

For the quasi-static discrete element simulations analysis, which is usually considered in the geotechnical, to be as the same conditions as in laboratory would be computationally expensive. Therefore, the timestep bound can be alleviated slightly by either particle density, mass scaling or the strain rate. For example, Thornton ([Thornton, 2000](#)) used a strain rate equal to that of experimental and increased the particle density in order to increase the critical timestep determined in Eq. (1.62) and limit the quasi-static effects. While Plassiard *et. al.* ([Plassiard et al., 2009](#)) kept the density at a constant value and increased the strain rate without generating inertial effects. Finally, it is important to note that for when simulations with high frequency response are necessary, then the mass scaling is not recommended ([O'Sullivan and Bray, 2004](#)).

#### **1.10.4 Loading methods**

The external forces in DEM can be either applied by walls or by velocity/force applied on a set of particles. The first method can be done by moving walls at a constant velocity and the resulting forces and moments acting on the walls are then recorded. This method is appropriate for many tests, such as the uniaxial compression test and Brazilian test. However, it cannot be used for uniaxial and shear tests and the second method, therefore, is frequently used to conduct these tests. It is started by creating a 'string' of particles, usually those touching walls. Then, these particles are fixed and given a constant velocity, after removing the walls.

#### **1.10.5 Biaxial loading methods**

There are some simulations (e.g. the biaxial test and the constant creep test) that require stress-control during the test. This can be achieved in many ways based on the loading methods discussed in the previous section.

##### **1.10.5.1 Servo-control mechanism**

The numerical servo-control mechanism is a function that controls the walls velocity in order to maintain a constant confining stress throughout the simulation. This function is called in every cycle to determine the current wall stress and to compare it with required wall stress. Then, it adjusts the wall velocity to reduce the difference

between current measured wall stress and target wall stress. The wall velocity is given by:

$$\dot{u}^{(wall)} = G(\sigma^{(wall)} - \sigma^{(target)}) = G\Delta\sigma \quad (1.64)$$

where  $G$  is the “gain” parameter which is estimated using the following reasoning and  $\sigma^{(wall)}$  is the wall stress at each cycle and arises from the particle assembly that is in contact with the wall as:

$$\sigma^{(wall)} = \frac{\sum_{N_c} F^{(wall)}}{A} \quad (1.65)$$

where  $F^{(wall)}$  is the force applied to a particle on the wall, and calculated as in Eq. (1.66),  $A$  is the area of the wall that is in contact with the particle assembly, and the summation is taken over all particle-wall contacts,  $N_c$ .

$$\Delta F^{(wall)} = k_n^{(w)} \dot{u}^{(wall)} \Delta t \quad (1.66)$$

where  $k_n^{(w)}$  is the sum of the contact stiffness of all contacts with wall. Hence, the change in wall stress is

$$\sigma^{(wall)} = \frac{k_n^{(w)} \dot{u}^{(wall)} \Delta t}{A} \quad (1.67)$$

For stability reasons, the absolute change in wall stress must be less than the absolute difference between the measured and required stress. This avoids overshooting of the required stress, which then leads to an oscillation about the required stress and grows in an unbounded manner and leads to instability. Therefore, it is important that the wall stress reaches the required stress in as smoothly a manner as possible. To fulfil this stability requirement, a relaxation factor,  $\alpha$ , is introduced such that the stability requirement becomes:

$$|\Delta\sigma^{(wall)}| < \alpha |\Delta\sigma| \quad (1.68)$$

Substituting Eqs. (1.64) and (1.67) into Eq. (1.68) gives:

$$\frac{k_n^{(w)} G |\Delta\sigma| \Delta t}{A} < \alpha |\Delta\sigma| \quad (1.69)$$

and then:

$$G \leq \frac{\alpha A}{k_n \Delta t} \quad (1.70)$$

Before each cycle, the wall velocity is adjusted by substituting Eq. (1.70) into Eq. (1.64) to achieve the target wall stress in numerical servo-control.

### **1.10.5.2      *Applied forces to boundary particles***

Another method for the biaxial test is based on switching between velocity and forces applied on a set of particles on the edge. This approach is initially similar to uniaxial loading, in that we fix particles on the boundary and then apply velocity. Once target stress is achieved, force applies on each boundary particle equal and opposite to the unbalanced force. All particles on the boundary are then freed of any constraint. At this point, the assembly would be in equilibrium under a force boundary condition. This method can be used to perform tension load combined with another (e.g. shear load), which cannot be done using the method explained in Section 1.10.5.1.

# Chapter 2

---

## 2 Generating random fibre distributions

In this chapter, a novel approach is presented for generating random distribution of fibres in the representative volume element (RVE) of fibre reinforced composite laminates. The approach is based on discrete element method (DEM) and experimental data of fibre diameter distribution. It overcomes the jamming limit appeared in previous methods and is capable for generating high volume fractions of fibres with random distributions and any specified inter-fibre distances. Statistical analysis is then carried out on the fibre distributions generated within the RVEs which show good agreement with experiments in all statistics analysed. The effective elastic properties of the generated RVEs is finally analysed by finite element method, which results show more reasonable agreement with the experimental results than previous methods.

### 2.1 Introduction

Several approaches have been reported in the literature for generating statistically equivalent RVEs (SERVEs) of composite materials with non-uniform distributions of fibres. A SERVE has the smallest volume size but can still maintain the same stress-strain relationship as that of the entire composite ([Swaminathan et al., 2006](#)). Usually the hard-core model (also called random sequential absorption model) was used to generate a SERVE. In a 2D hardcore model the fibres are represented by discs randomly distributed in a square domain without any overlap. The hard-core model is natural and simple, and its only disadvantage is that it has difficulties in generating a random distribution of fibres with a volume fraction higher than 50% due to a jamming limit ([Buryachenko et al., 2003](#)). This limitation was later eliminated by Wongsto and Li ([Wongsto and Li, 2005](#)) who proposed a method that generated random distribution by shaking an initial hexagonal packing of the fibres. Therefore this approach was also called initially periodic shaking model (IPSM) ([Yang et al.,](#)

[2013b](#)). However, no statistics analysis was performed on this algorithm and the initial periodic arrangement might not be fully changed by the shaking procedure. Melro *et al.*, ([Melro et al., 2008](#)) developed a hard-core shaking model (HCSM) in which the classical hard-core model was used to generate an initial fibre distribution and then small arbitrary displacements were assigned to the fibres to enable random motions. During the process matrix rich regions were created in certain areas where more fibres could be placed in order to achieve higher volume fractions. Because the hard-core model involves uncertainties in generating the initial configuration, it requires a relatively complex algorithm for the fibres to move. A simpler algorithm, random sequential expansion (RSE), was recently developed by Yang *et al.*, ([Yang et al., 2013b](#)). The algorithm was still based on hard-core model and the inter-fibre distances were controllable. However, the fibre diameters in this algorithm were assumed to be uniform, and the inter-fibre distance had to be zero in order to achieve a volume fraction of 68%. This zero inter-fibre distance could cause numerical difficulties when analysing RVE using FEM because there has to be a sufficient distance between two neighbouring fibre surfaces to ensure adequate elements to cover those areas as matrix ([González and LLorca, 2007a](#)).

Besides the above mentioned numerical approaches, there are also some experimental image based models. The idea of those models is to obtain digital images of transverse sections using scanning electronic microscopic (SEM) or high-resolution optical microscopic and then use a computer software to locate the fibre centroids by detecting a colour 'threshold' of the fibres. For instance, Vaughan and McCarthy ([Vaughan and McCarthy, 2010](#)) measured the diameter distribution and used a nearest neighbour algorithm (NNA) to define the inter-fibre distances for generating a SERVE of high strength composite laminates. The obvious benefit of image-based method is that it can be used to generate a microstructure exactly the same as the original cross section area of the composite material. However, this is time-consuming and requires specific computer software to process the images in order to identify the locations of the fibres.

## 2.2 Algorithm development using DEM

In this section an algorithm is developed in DEM to generate random distributions of fibres with high volume fractions, which is combining experimental and shaking approaches.

A variable fibre diameters were drawn from the experimentally measured data and used for fibre generation in DEM software package PFC2D ([Itasca, 2003](#)). The diameters of the fibre in this study conform to normal distribution with mean fibre diameter of 6.6  $\mu\text{m}$  and standard deviation of 0.3106 ([Vaughan and McCarthy, 2010](#)), as shown by the solid curve in Figure 2.1. The fibre volume fraction used in this case is 60%, the same as used in ([Vaughan and McCarthy, 2010](#)). The new method is explained bellow and illustrated in Figure 2.2.

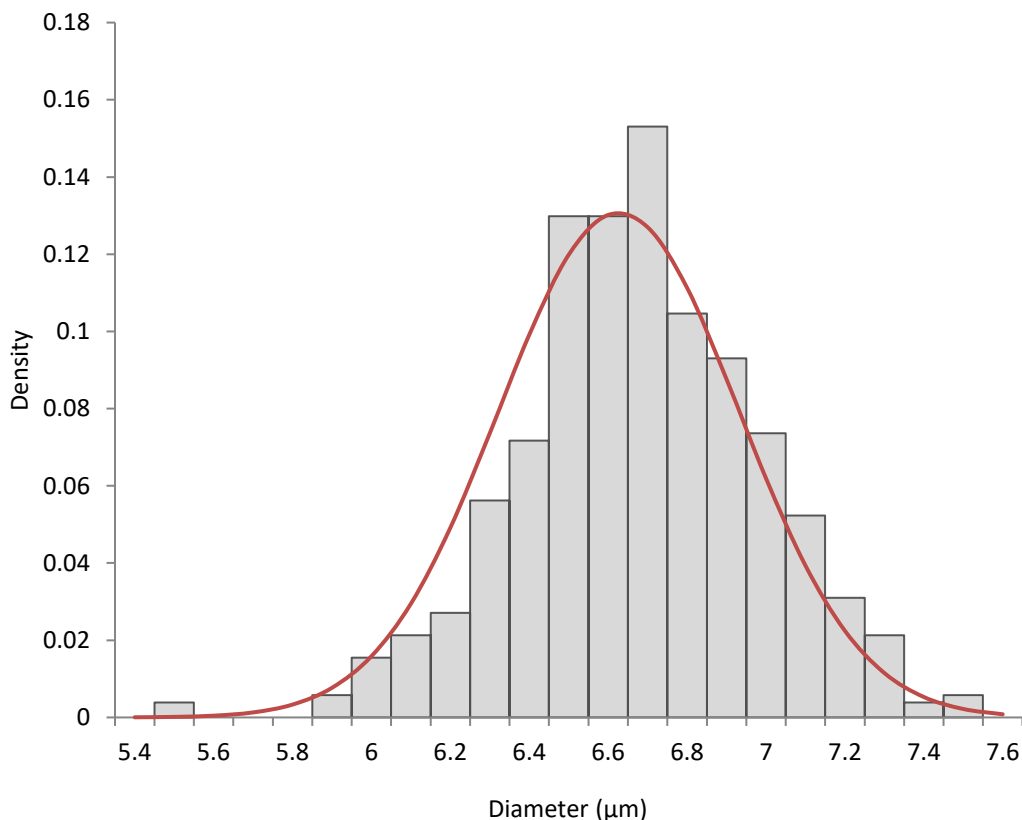


Figure 2.1: Size distribution of fibres.

(i) Using the mean fibre diameter,  $\bar{D}_f$ , the required number of fibres,  $N_f$  is approximately determined by the following simple calculation:

$$N_f = \frac{4V_f L^2}{\pi \bar{D}_f^2} \quad (2.1)$$

Once the number of fibres is known, a random number,  $\alpha$ , between -1 and 1 is created in DEM software PFC2D and used to calculate the diameter of each fibre to be generated,  $D_f$ , following the Gaussian normal distribution function:

$$D_f = \bar{D}_f + \alpha \delta_f \quad (2.2)$$

In the 2D DEM modelling, each fibre is represented by a disc in PFC2D. The diameter distribution of discs/fibres in the DEM model is also plotted in Figure 2.1, which matches the distribution function extracted from experimental data. The discs/fibres are initially placed in a regular cubic arrangement, as shown in Figure 2.2a.

(ii) Since the fibre diameters are not identical, in some cases the resultant fibre volume fraction could be smaller than the target fibre volume fraction. Therefore, more discs/fibres are added one by one in random places and overlap with those generated earlier in order to achieve the target volume fraction, as shown in Figure 2.2b. The instant volume fraction is re-calculated after every single disc is added, and the process terminates when the target fibre volume fraction is reached.

(iii) Random velocity is applied simultaneously to each of the discs that moves in a way similar to the Brownian motion. The motion of the discs is governed by the Newton's Second Law and the collisions between any two discs are according to a Hertz contact law ([Itasca, 2003](#)). In this step there are two major groups of discs, as shown in Figure 2.2c. The grey ones are the internal discs staying within the RVE, and the red ones are those moving across the RVE boundary from the inside. As a consequence of the motion of the red discs, the fibre volume fraction of the RVE is reduced. To compensate this loss and maintain the initial fibre volume fraction, paired discs, denoted by the blue ones, are added along the opposite boundary mapping the respective positions of the red outgoing red discs. This is achieved using periodic boundary condition available in PFC2D ([Itasca, 2003](#)). The velocity of each disc is then set to zero after a sufficient period of time of free motion, and the whole model gradually reaches a static equilibrium state.

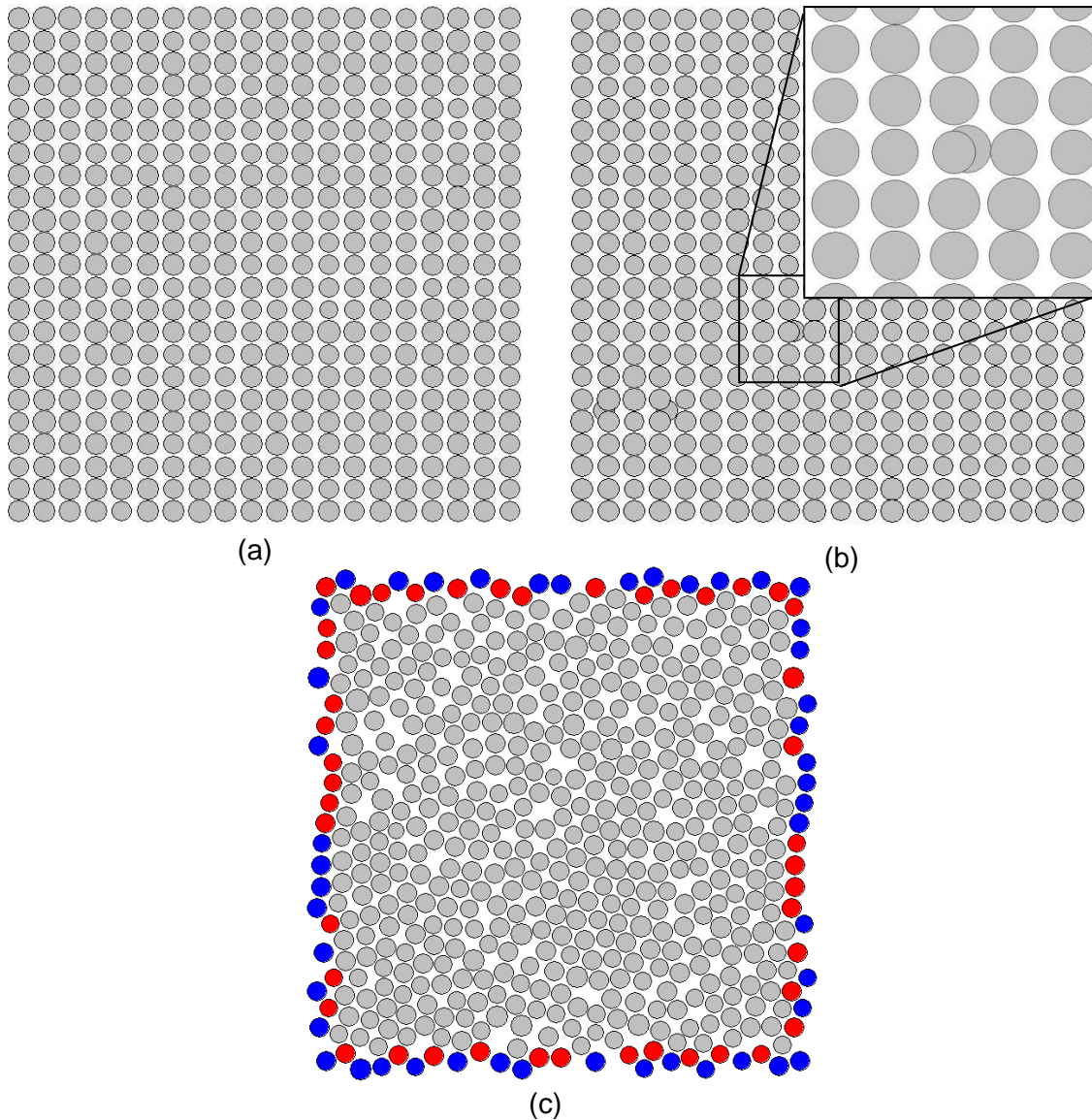


Figure 2.2: Procedure for generating random fibre distributions using DEM. (a) Initial fibre distribution in regular cubic arrangement. (b) More discs are added. (c) Periodic boundary condition is applied to maintain the constant fibre volume fraction.

(iv) At this stage, there might exist overlaps between some discs, while in reality there are normally small distances between fibre surfaces. To resolve this issue, the radii of all the discs are increased by half of the minimum required distance between two neighbouring fibre surfaces. By Hertz contact law, there will be repulsive forces at the contact between any two particles with an overlap to produce relative displacement and consequently increase the distance between them. After this additional redistribution, the whole model reaches an equilibrium state again and the radii of all the discs are reduced back to their initial values.

This algorithm can be used to generate high fibre volume fractions with any specified inter-fibre distances. Examples of fibre distributions with fibre volume fractions of 60%, 65% and 68%, and a minimum inter-fibre distance of  $0.8 \mu\text{m}$  are shown in Figure 2.3. The results have demonstrated that the presented algorithm is capable of generating microstructures of composites with required high fibre volume fractions. The method is conducted using PFC2D ([Itasca, 2003](#)) and the codes can be found in Appendix A.

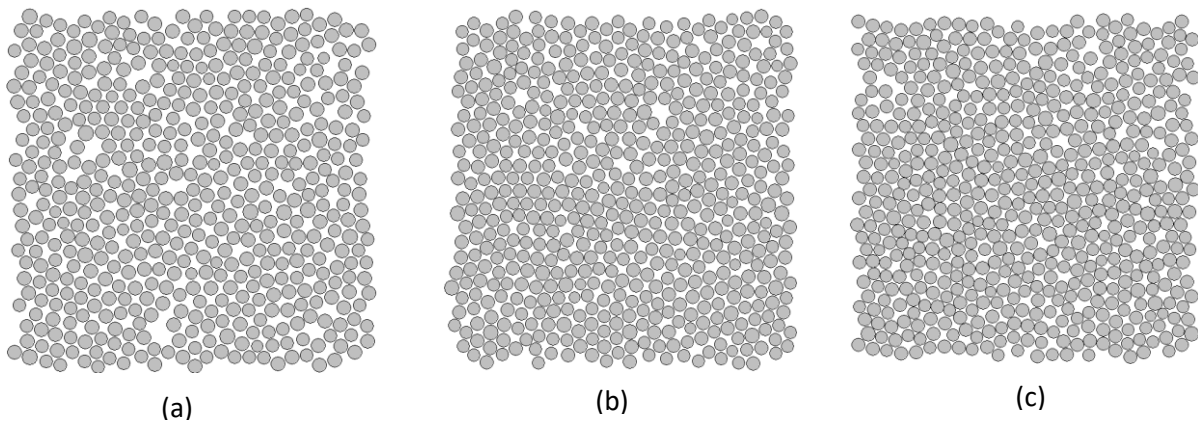


Figure 2.3: Three fibre distributions with high volume fractions: (a) 60%, (b) 65%, and (c) 68%.

### **2.3 Statistical characterisation**

This section is dedicated to the statistical analysis of the fibre distributions generated by the present algorithm. The statistical methods employed here are normally used to quantitatively describe the random point distributions in the space. For the purpose of comparison, exactly the same statistical descriptors used in ([Vaughan and McCarthy, 2010](#), [Yang et al., 2013b](#)) are adopted in this study and the positions of all fibres are considered as a spatial point pattern ([Illian et al., 2008](#)).

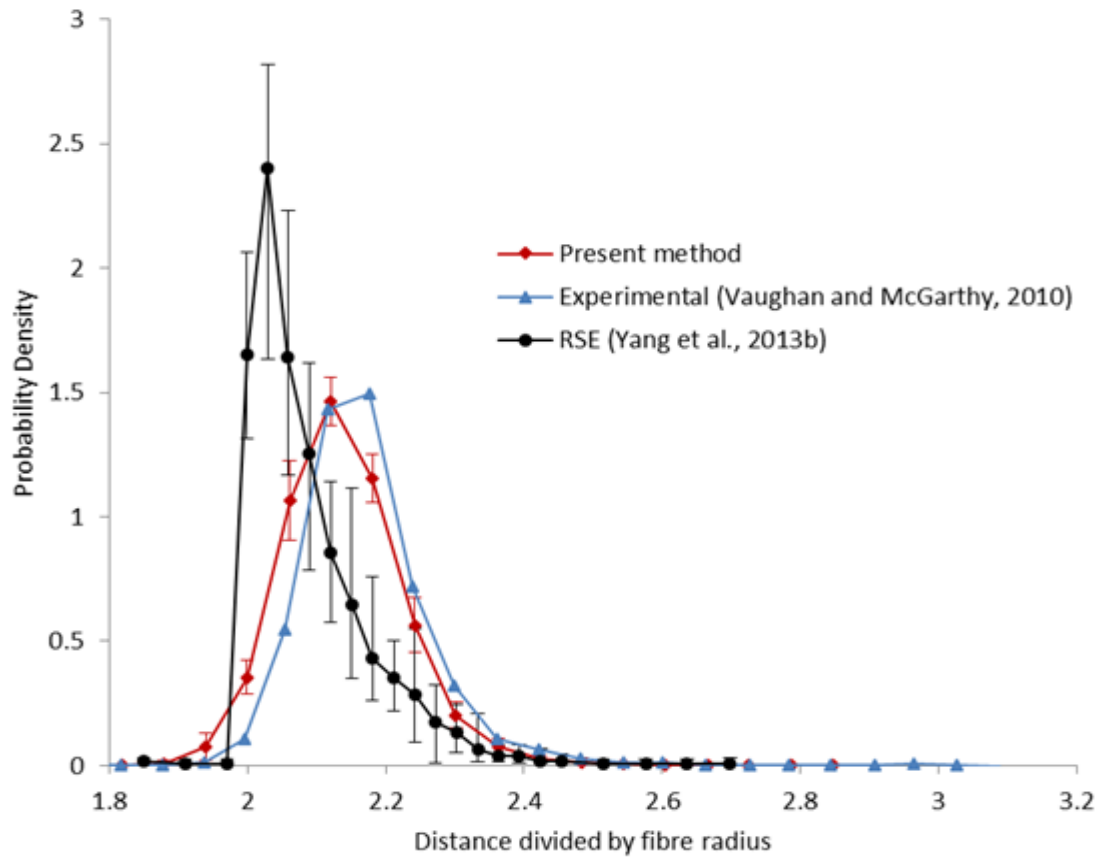
Four statistical descriptors are adopted, *i.e.*, nearest neighbour distribution function, cumulative distribution function, second-order intensity function and pair distribution function. Several parameters are considered such as the side length of RVE,  $L$ , volume fraction,  $V_f$  and fibre radius,  $r_f$ . The RVE size can be described by the variable  $\delta$ , which defines the relationship between the side length of RVE and the fibre radius as:

$$\delta = \frac{L}{r_f} \quad (2.3)$$

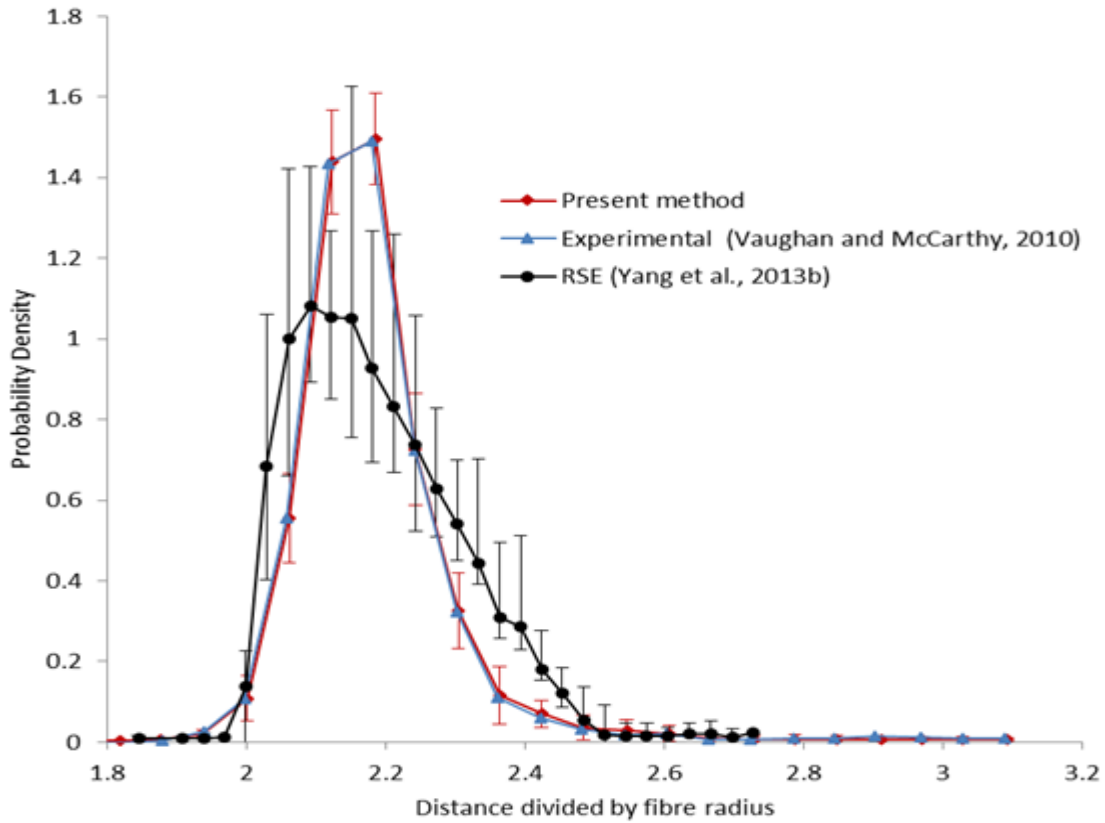
The size of RVE needs to be sufficiently large to characterise the behaviour of a bulk material. For a typical composite material such as carbon fibre reinforced polymer (CFRP) with a fibre volume fraction of 50%, Trias *et al.*, ([Trias et al., 2006](#)) found that the minimum size of RVE was  $\delta=50$ . The values used for the input variables in this study were same as those used in ([Melro et al., 2008](#), [Vaughan and McCarthy, 2010](#), [Yang et al., 2013b](#)), *i.e.*,  $\delta=50$ ,  $V_f=60\%$  and the fibre diameters were obtained from a normal distribution. A total of twenty-five RVEs were generated and each of them had the same size of  $165 \mu\text{m} \times 165 \mu\text{m}$ . Results of the four statistical functions were compared with the experimental data reported by Vaughan and McCarthy ([Vaughan and McCarthy, 2010](#)) and the recent RSE algorithm proposed by Yang *et al.*, ([Yang et al., 2013b](#)). MATLAB ([MATLAB, 2012](#)) was used to calculate all statistical descriptors explained later in this section.

### **2.3.1 Nearest neighbour distribution**

As one of the basic functions to characterise a system of interacting points in the space, nearest neighbour distribution is defined as the probability density of finding a nearest neighbour of a reference point. Therefore it can be used as an indicator to assess whether the fibres in a RVE are random, regular or clustered. Figure 2.4a and 4b show the results of the 1st and 2nd nearest neighbour distributions of twenty-five RVEs, respectively.



(a)



(b)

Figure 2.4: Results of near neighbour distributions compared with experimental data and RSE results. (a) 1<sup>st</sup> Nearest neighbour distribution. (b) 2<sup>nd</sup> Nearest neighbour distribution function

### 2.3.2 Second-order intensity function

The second-order intensity function, also called Ripley's  $K$  function, is another statistical tool that has been extensively used to analyse a spatial pattern (Pyrz, 1994). The function is defined as the number of more points to be added within a radial distance,  $r$ , of an arbitrary point divided by the number of points per unit area,  $N$ . Unlike the 1st and 2nd nearest neighbour distributions which depend on the local information of the points, the edge of the domain,  $w$ , and overlap effects are taken into account by the Ripley'  $K$  function because they have a significant effect when calculating this function. The Ripley's  $K$  function is estimated by:

$$K(r) = \frac{A}{N^2} \sum_i \sum_{i \neq j} \omega_{ij}^{-1} I(r_{ij} \leq r), \quad (2.4)$$

where  $A$  is the area of the domain,  $N$  is the total number of points (fibres) in the domain,  $I(\cdot)$  is the indicator function with the value of 1 if the expression between the brackets is true, otherwise it is 0,  $r_{ij}$  is the distance between points  $i$  and  $j$ , and  $\omega_{ij}$  is a weight function for edge effects and defines as the ratio of the circumference contained within the domain to the whole circumference of the circle  $r_{ij}$ . For example, if a sample with radius,  $r$ , is completely within the observed area,  $\omega_{ij}$  equal to 1. Figure 2.5 graphically explains the variables used in Eq. (2.4), variables value also given on the figure for two samples.

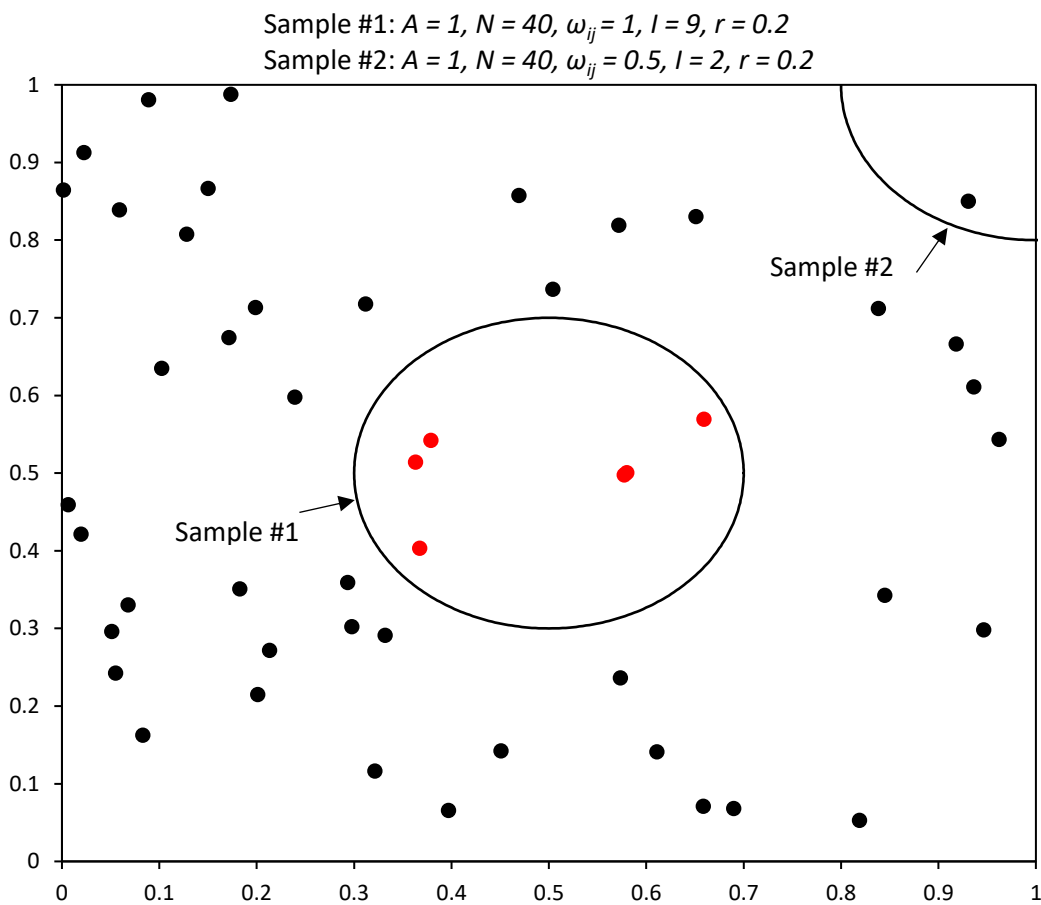


Figure 2.5: An explanation of the variables in the second-order intensity (or Ripley's  $K$ ) function.

Point fields are usually compared with the complete spatial randomness (CSR) pattern, and the Ripley's  $K$  function computed by ([Illian et al., 2008](#)):

$$K(r) = \pi r^2. \quad (2.5)$$

The comparison between the shape of  $K(r)$  and the shape of CSR patterns provides important information for assessing the fibre distribution. For instance, when the  $K(r)$  curve of is below the CSR curve , it gives an indication that the distribution is somehow regular, otherwise it means that some fibres are clustered in the area ([Melro et al., 2008](#)). Shown in Figure 2.6 are the mean second-order intensity functions for twenty-five RVEs generated using the present method, experimental, RSE and CSR results. The results can be split into two areas. When distances are shorter (*i.e.*,  $r \leq 15$ ), the curve obtained from the present work is close and above the experimental and both show stair-shape-likes, as shown in the zoom-in view of Figure 2.6. The curve is also above the CSR, which indicates the fibre distribution is regular at these distances as explained above, but it is gradually separating from the other two at larger distances (*i.e.*,  $r > 15$ ), as a result of the long range clustering.

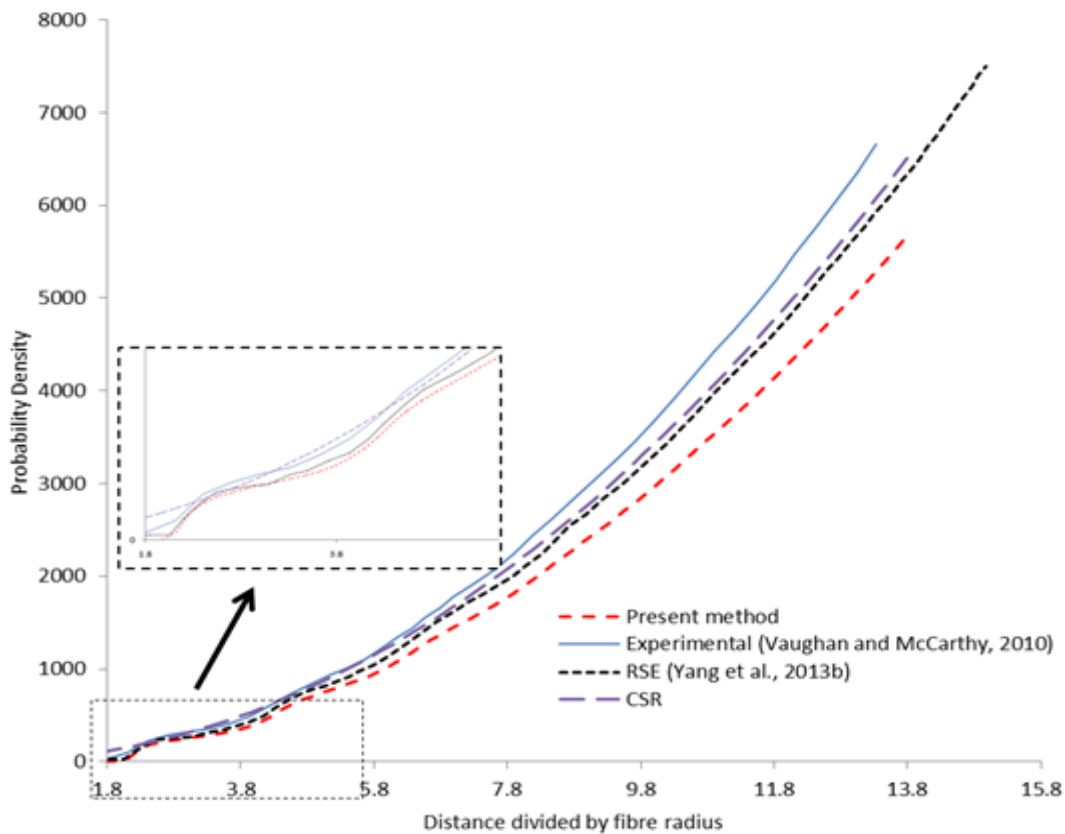


Figure 2.6: Second-order intensity function, compared with experimental, RSE method and CSR.

### 2.3.3 Radial distribution function

The radial distribution function is an important statistical tool that is mostly used to study a system of particles such as atoms or molecules. The function describes the change of the average fibre density as a function of distance from a reference point which, in our case, is a given fibre centre. It is mathematically related to  $K(r)$  (Eq. (2.4)) as ([Swaminathan et al., 2006](#)):

$$g(r) = \frac{1}{2\pi r} \frac{dK(r)}{dr}, \quad (2.6)$$

where  $g(r)$  is the intensity of the fibre distances and  $K(r)$  is the second-intensity function. This function is also defined as the probability of finding an additional points (fibres) within an annulus area of inner radius,  $r$ , and outer radius  $r + dr$ . Figure 2.7 visually explains the variables used in Eq. (2.6) variables value also given on the figure.

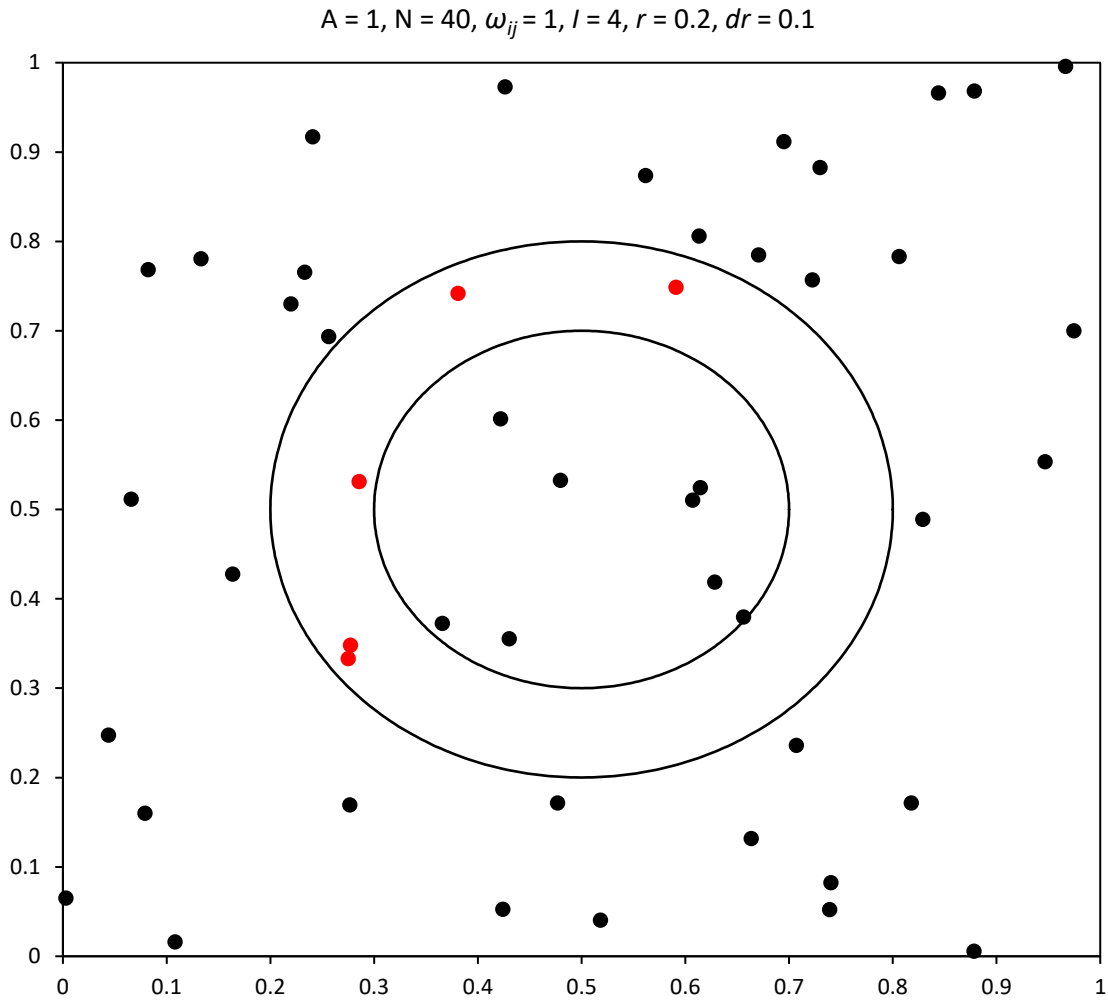


Figure 2.7: An explanation of the variables in the radial distribution function containing four points in the annulus area.

Figure 2.8 shows the mean radial distribution functions for the microstructures generated by the present DEM method, together with the experimental and RSE microstructures. Again, excellent agreement is found between the present method and experimental data and this can be seen at larger distances when both tend to 1, which confirms the randomness distributions of fibres. Therefore, it is proved that the developed algorithm using DEM is a useful tool for generating random fibre distributions in RVEs of composite materials for micromechanical analysis.

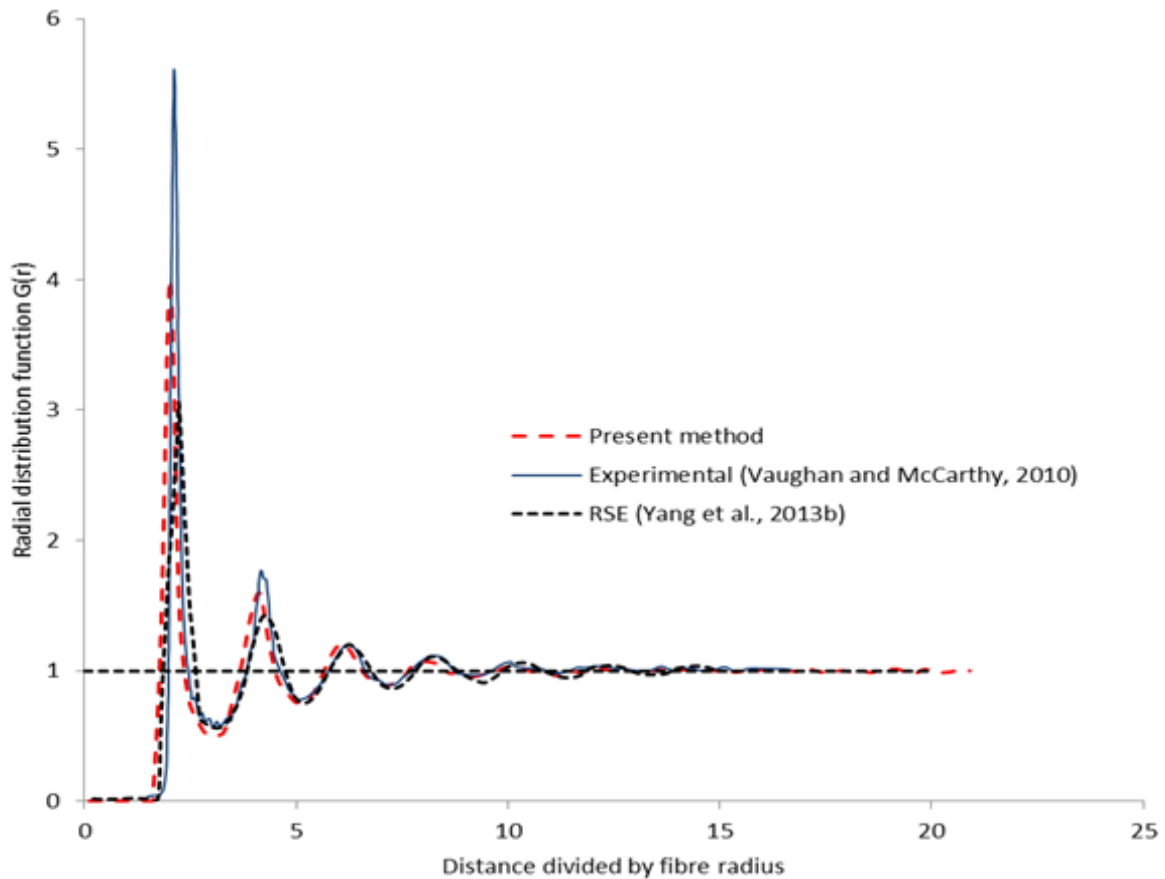


Figure 2.8: Radial distribution function for present method and compared with experimental RSE method.

## 2.4 Prediction of mechanical properties

As done for other algorithms ([Vaughan and McCarthy, 2010](#), [Yang et al., 2013b](#)), the present algorithm is used to generate the RVEs of the transverse section of a composite lamina. The effective elasticity from the properties of their constituents is then evaluated by finite element models.

### 2.4.1 Finite element analysis

In this chapter, two materials have been chosen to study, the first is E-glass embedded in MY750/HY917/DY063 epoxy matrix, as well as AS4 carbon combined with 3501-6 epoxy matrix. The properties have been reported in the World Wide Failure Exercise (WWFE) ([Soden et al., 1998b](#)) and used by ([Melro et al., 2008](#), [Yang et al., 2013b](#)). Both the matrix and the fibre are treated as isotropic for the 2D model.

The elastic properties of the fibre and the matrix for both material are given in in Table 2.1.

Table 2.1: Material elastic properties.

Material	$E_m$ (GPa)	$\nu_m$	$E_f$ (GPa)	$\nu_f$
E-Glass/MY750/HY917/DY063	3.35	0.35	74	0.2
AS4/3501-6	4.2	0.34	15	0.2

Finite element (FE) analysis was carried out using ABAQUS ([ABAQUS, 2010](#)) under plane strain condition. In the ABAQUS model both the matrix and the fibres were meshed using free meshing technique with quad-dominated element shapes. The two-dimensional 4-node bilinear plane strain quadrilateral elements (CPE4) were chosen to mesh the fibre and the matrix. There were also a relatively small amount of 3-node linear plane strain triangle elements (CPE3) due to the free meshing technique used. Since each model has about 500 fibres, it is difficult and time consuming to generate each RVE manually. Therefore, python scripts have been written to generate and distribute fibres in the FE models of the RVEs in ABAQUS ([ABAQUS, 2010](#)). Twenty RVEs spatial distributions with  $V_f=60\%$  were generated, each containing approximately 55,000 elements.

Periodic boundary conditions were applied on the RVEs to ensure the compatibility of strain and stress at macro level, similar to those used by ([Van der Sluis et al., 2000](#), [Yang et al., 2013b](#)). These consist of a series of constrains in which, the deformation of each pair of nodes on the opposing edge of the RVE were subject to the same amount of displacements, *i.e.*:

$$u_{23} - u_{v2} = u_{14} - u_{v1} \quad (2.7)$$

$$u_{43} - u_{v4} = u_{12} - u_{v1} \quad (2.8)$$

where  $u_{ij}$  is the  $y$  or  $z$  displacement of nodes on the edges and  $u_{vi}$  is the displacement of vertex node,  $i$ . Nodes in Eqs. (2.7) and (2.8) are connected by the “equation” constrains available in ABAQUS ([ABAQUS, 2010](#)). High number of equations required to build the periodic boundary, which cannot be done manually. Therefore, a python script containing the mesh information, such as node coordinates,

are firstly written in the scrip. Then equations are converted in a set of keywords and also written in the script in order to implement them into the ABAQUS model.

Figure 2.9a and Figure 2.9b show the periodic boundary conditions for tension and shear, respectively.  $E_2$  and  $v_{23}$  are determined by applying a horizontal displacement on node 2 while to determine  $E_3$  and  $v_{32}$  a vertical displacement is applied on node 4, as shown in Figure 2.9a.  $G_{23}$  is determined by applying a horizontal displacement on node 4, as shown in Figure 2.9b.

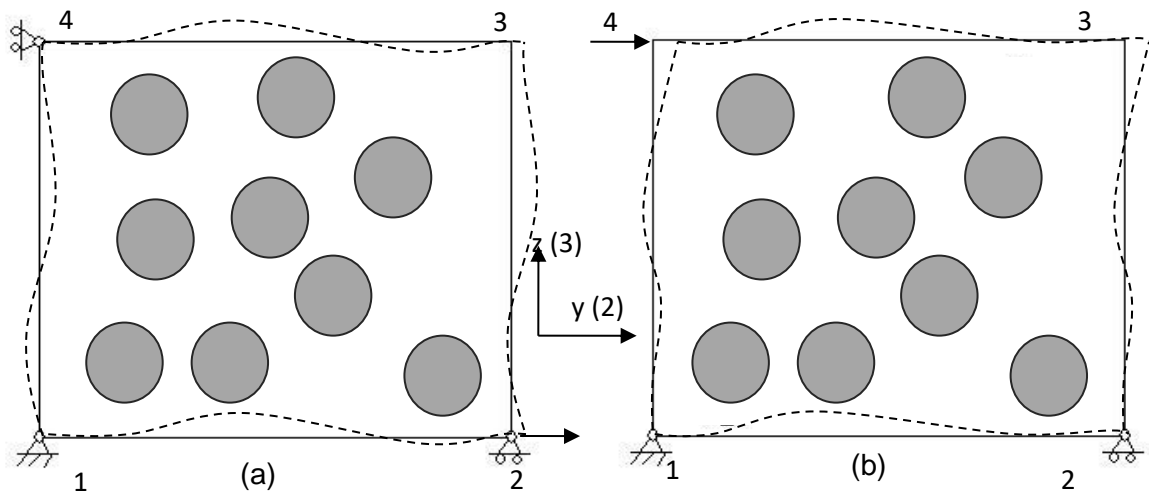


Figure 2.9: Periodic boundary constraints applied to the RVEs. (a) Tension, and (b) Shear.

The elastic properties were evaluated based on volumetric homogenisation procedure using the following equations ([Melro et al., 2008](#)):

$$E_k = \frac{\sum_{i=1}^N \sigma_{kk}^i A^i}{\sum_{i=1}^N \varepsilon_{kk}^i A^i} \quad \varepsilon_{jk} = -\frac{\sum_{i=1}^N \varepsilon_{kk}^i A^i}{\sum_{i=1}^N \varepsilon_{jj}^i A^i} \quad G_{23} = -\frac{\sum_{i=1}^N \sigma_{23}^i A^i}{\sum_{i=1}^N \varepsilon_{23}^i A^i}, \quad (2.9)$$

where  $N$  is the total number of FE elements in the RVE,  $\sigma_{kk}^i$  and  $\varepsilon_{kk}^i$  are the average  $k$ -components of stress and strain of element  $i$  respectively, and  $A^i$  is the area of element  $i$ .

## 2.4.2 Analysis and results

### 2.4.2.1 Calculating mechanical elastic properties

The pattern of stress distribution in the RVEs is examined first, in case of using E-Glass/MY750/HY917/DY063 composite. To this end, a displacement of 3  $\mu\text{m}$  is applied on the RVEs for both tension and shear cases (see Figure 2.9). The von Mises stress contour plot for a RVE is shown in Figure 2.10. The von Mises stress varies from 24.1 MPa to 505 MPa under transverse tension while the stress varies from 16.7 MPa to 353.8 MPa under transverse shear, as illustrated in Figure 2.10. In addition, it seems that the most of the high stresses area are located at interfaces especially where the distances between fibres are small. This is mainly due to the large differences of the mechanical properties between fibres and matrix.

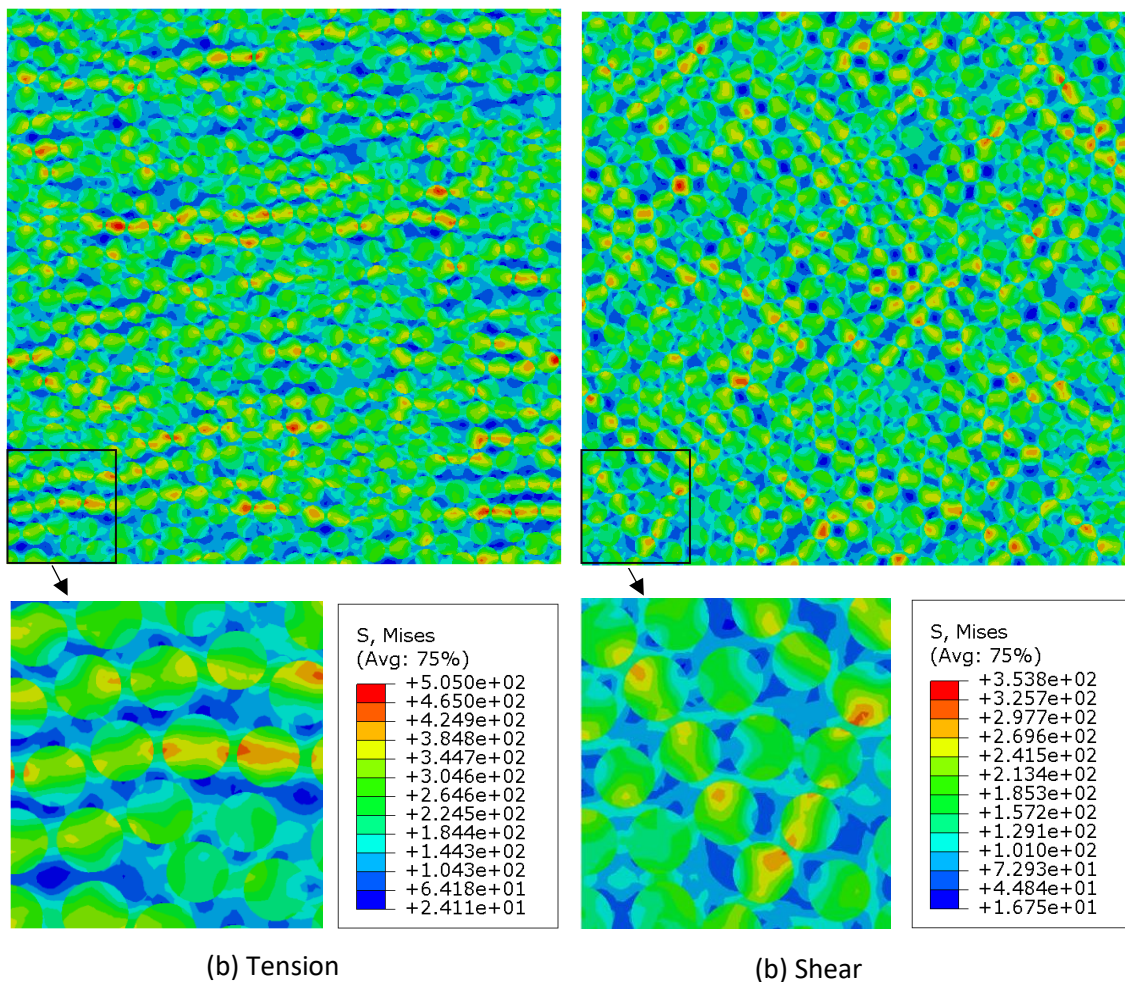


Figure 2.10: Von Mises stress distribution in a RVE under. (a) Tension and (b) Shear.

Effective properties are calculated numerically for generated twenty microstructures using Eq. (2.9) and shown in Table 2.2, where their mean values and the standard deviations are also presented. The table also contains mechanical properties of the unidirectional lamina measured experimentally ([Soden et al., 1998b](#)) and by other methods ([Melro et al., 2008](#), [Yang et al., 2013b](#)).

Table 2.2: Calculated effective properties (E-Glass/MY750/HY917/DY063).

	$E_2$ (GPa)	$E_3$ (GPa)	$\nu_{23}$	$\nu_{32}$	$G_{23}$ (GPa)
Mean values	13.914	13.964	0.401	0.403	4.992
Standard deviations	0.661	0.794	0.031	0.022	0.251
Variation coefficient	0.048	0.057	0.077	0.056	0.050
Ref ( <a href="#">Melro et al., 2008</a> )	13.367	13.387	0.370	0.371	4.851
Ref ( <a href="#">Yang et al., 2013b</a> )	13.047	13.068	0.405	0.405	4.673
Experimental ( <a href="#">Soden et al., 1998b</a> )	16.2	16.2	0.4	0.4	5.786
Error (% , compared to experimental)	14.11	13.80	0.23	0.74	13.72

As seen from the table the average predicted Young's modulus and shear modulus of all RVEs are higher than those attained by ([Melro et al., 2008](#), [Yang et al., 2013b](#)) and much closer to the experimental results, *i.e.*, the shear modulus shows 13.7% smaller than the experimental one in comparison with Yang's *et al.*, ([Yang et al., 2013b](#)) prediction of 19% smaller.

The predicted effective properties of AS4/3501-6 are also calculated and are summarised in Table 2.3. The error associated with the predicting elastic properties for this material was slightly higher than previous one. The error for this case are increased by almost 3%.

Table 2.3: Calculated effective properties (AS4/3501-6).

	$E_2$ (GPa)	$E_3$ (GPa)	$\nu_{23}$	$\nu_{32}$	$G_{23}$ (GPa)
Mean values	9.039	9.032	0.379	0.387	3.263
Standard deviations	0.097	0.102	0.022	0.003	0.048
Variation coefficient	0.011	0.011	0.059	0.009	0.015
Experimental ( <a href="#">Soden et al., 1998b</a> )	11	11	0.4	0.4	3.928
Error (% , compared to experimental)	17.82	17.82	5.14	3.36	16.93

As the material is assumed to be transverse isotropic in the x-z plane, the well-known consistent relationships which relate five independent elastic constants exist. The relationship between Young's modulus and Poisson's ratio is described as:

$$\frac{E_2}{\nu_{23}} = \frac{E_3}{\nu_{32}} \quad (2.10)$$

The transverse isotropy is determined by the following relationships:

$$E_2 = E_3, \nu_{23} = \nu_{32}, \bar{G}_{23} = \frac{E_2}{2(1 + \nu_{23})}. \quad (2.11)$$

Table 2.4: Proof of transverse isotropy.

Material	$\frac{E_2\nu_{32}}{E_3\nu_{23}}$	$\frac{E_3}{E_2}$	$\frac{\nu_{23}}{\nu_{32}}$	$\frac{\bar{G}_{23}}{G_{23}}$
E-Glass/ MY750/HY917/DY063	1.002	0.996	1.005	0.995
AS4/3501-6	1.020	1.001	1.019	1.004

The mean values of the elastic properties that provide in Table 2.2 and Table 2.3 are used as the input for Eqs. (2.10) and (2.11). Table 2.4 shows the transverse isotropy of Eqs. (2.10) and (2.11) are approximately satisfied using the predicted values in Table 2.2. It shows that all ratios are very close to 1 which concludes that the generated random fibre distributions have almost the same transverse isotropy as the real material.

#### 2.4.2.2 RVE with continuous and non-continuous distributed fibres over edges

In order to effectively use periodic boundary conditions given in Eqs. (2.7) and (2.8), it is important that the number of nodes on each edges equal to those on the opposite side. However, this task may not be straightforward in case of using RVE with continuously distributed fibres over edges as shown in Figure 2.11a. Fortunately, the proposed method in the work can also generate RVE with non-continuous distributed fibres over edges, in which all fibres are accommodated within the RVE as shown in Figure 2.11b.

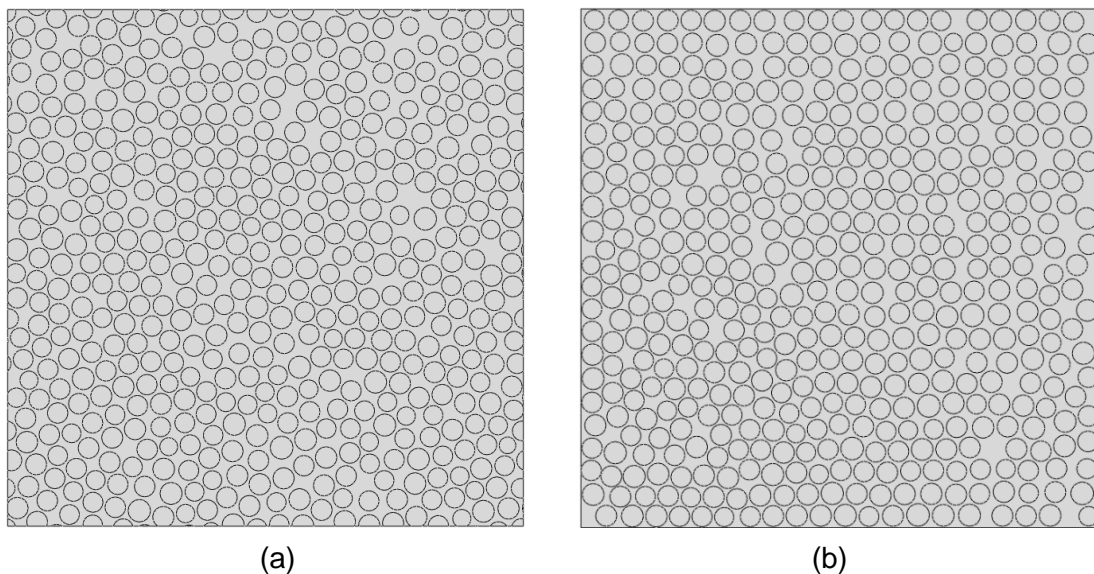


Figure 2.11: RVE with different distributed fibres style over edges. (a) Continuous. (b) Non-continuous.

Effective properties using non-continuous distributed fibres are calculated numerically for generated twenty microstructures for both materials use in this study and shown in Table 2.5 and Table 2.6, where their mean values and the standard deviations are also presented. It can be seen that the percentage of error for material properties for E-Glass/MY750/HY917/DY063 composite has increased significantly compare to continuous edges case given in Table 2.2. The elastic properties for AS4/3501-6 are almost identical in both cases, unless shear modulus that is increased slightly using non-continuous edges, Table 2.6.

Table 2.5: Calculated effective properties for non-continuous distributed fibres (E-Glass/MY750/HY917/DY063).

	$E_2$ (GPa)	$\nu_{23}$	$G_{23}$ (GPa)
Mean values	12.918	0.380	4.153
Standard deviations	0.222	0.022	0.203
Variation coefficient	0.017	0.058	0.049
Experimental ( <a href="#">Soden et al., 1998b</a> )	16.2	0.4	5.786
Error (% , compared to experimental)	20.27	4.92	28.23

Table 2.6: Calculated effective properties for non-continuous distributed fibres (AS4/3501-6).

	$E_2$ (GPa)	$\nu_{23}$	$G_{23}$ (GPa)
Mean values	9.119	0.378	3.189
Standard deviations	0.060	0.006	0.047
Variation coefficient	0.007	0.017	0.015
Experimental ( <a href="#">Soden et al., 1998b</a> )	11	0.4	3.928
Error (% , compared to experimental)	17.10	5.62	18.81

# Chapter 3

---

## 3 Discrete element modelling of unidirectional fibre-reinforced polymers under transverse tension

The mechanical behaviour of unidirectional fibre-reinforced polymer composites subjected to transverse tension was studied using a two dimensional discrete element method. The Representative Volume Element (RVE) of the composite was idealised as a polymer matrix reinforced with randomly distributed parallel fibres. The matrix and fibres were constructed using disc particles bonded together using parallel bonds, while the fibre/matrix interfaces were represented by a displacement-softening model. The prevailing damage mechanisms observed from the model were interfacial debonding and matrix plastic deformation. Numerical simulations have shown that the magnitude of stress is significantly higher at the interfaces, especially in the areas with high fibre densities. Interface fracture energy, stiffness and strength all played important roles in the overall mechanical performance of the composite. It was also observed that tension cracks normally began with interfacial debonding. The merge of the interfacial and matrix micro-cracks resulted in the final catastrophic fracture.

### **3.1 Introduction**

Micromechanics has been one of the major tools that have been used to study the failure of lamina, since its mechanical behaviour cannot be characterised accurately by a simple homogenization approach, particularly when it is subject to a transverse loading. Also, micromechanical models are capable of predicting failure as a function of the properties of each material constituent are capable of predicting failure as a function of the properties of each material constituent ([González and LLorca, 2007a](#)).

Computational micromechanics using the finite element method (FEM) has become the most widely used method to predict the strength of composites as well as the damage progression. This includes the studies on the effect of particle morphology ([Chawla et al., 2006](#)) and reinforcement spatial distribution on tensile deformation ([Segurado et al., 2003](#), [Segurado and LLorca, 2006](#)) of particle reinforced composite materials. Zhang et al. ([Zhang et al., 2005](#)) developed a micromechanical model for damage initiation and growth of FRP laminates, where the nonlinear viscoelastic and cohesive models were used, respectively, to simulate the deformation of matrix and the progressive interface de-cohesion. Failure locus and mechanical behaviour of composite lamina under transverse compression, tension, shear and the combined loadings were also computed by using micromechanical FEM models ([Zhang et al., 2006](#), [Zhang et al., 2013](#), [Ye and Zhang, 2012](#), [Totry et al., 2010](#), [Totry et al., 2008a](#), [Moraleda et al., 2009](#), [Canal et al., 2009](#)). Vaughan and McCarthy ([Vaughan and McCarthy, 2011a](#), [Vaughan and McCarthy, 2011b](#)) presented a comprehensive study to examine the effect of fibre–matrix properties on the transverse behaviour of a unidirectional of fibre/epoxy composites. They highlighted the respective roles played by the intra-ply debonding and the matrix plasticity on the macroscopic response of the composite. All the above-mentioned papers have used FEM as the computational framework to analyse the microstructure of RVEs.

In this chapter, a Discrete Element Method (DEM) is used to simulate the damage progression of FRP lamina subjected to transverse tension. Unlike a FEM model, in which the nonlinear behaviour of matrix phase is often accounted by Mohr–Coulomb or Drucker–Prager yield criteria, bond breakages in DEM are responsible for the non-linear stress–strain response through continuous decrease of modulus until a failure load is reached. Therefore, bonds in DEM are assigned with random breaking thresholds for matrix and interface to represent a non-linear response ([Wittel et al., 2003](#)). The displacement-softening model, which is similar to the cohesive zone model (CZM) ([Xie and Waas, 2006](#)), is used to predict the onset of fibre/matrix debonding. A parametrical study is carried out to examine the detailed effects of interfacial properties on the transverse mechanical behaviour.

### 3.2 RVE generation and discretisation

A square RVE, which contains a random and homogeneous distribution of circular fibres embedded in a polymeric matrix, was selected to study the behaviour of a lamina under transverse loading. The RVE of the microstructure is large enough to possess the same properties with macroscopic material. Random and homogeneous distributions of 28 monosized fibres of radius  $R = 3.3 \mu\text{m}$  were generated in a square RVE of dimensions  $L_0$  by  $L_0$  ( $L_0 = 40 \mu\text{m}$ ) as shown in Figure 3.1. The RVE of DEM model is generated using the approach developed in previous chapter which can overcome jamming limit and can be used for fibres with any inter distances. Previous studies have shown that this size is sufficient in order to produce the overall macroscopic response of a composite ([González and LLorca, 2007a](#)). The RVE was discretised using a hexagonal packing arrangement as shown in Figure 3.1b. For regular packing such as square and hexagonal packing arrangement, the contact stiffness (see Figure 3.1c) can be related to the engineering material properties such as Young's modulus and Poisson's ratio. For instance, ([Kim et al., 2008](#), [Sawamoto et al., 1998](#), [Tavarez and Plesha, 2007](#)) derived formulae to relate contact parameters and material properties for isotropic material. Liu and Liu ([Liu and Liu, 2006](#)) extended these formulae to include anisotropic materials. One most drawback of these formulae their restriction to Poisson's ratio of 1/3 and 1/4 for plane stress and plane strain, respectively. In this work, the general expressions developed in ([Kačianauskas and Vadluga, 2009](#)) for anisotropic materials used. Thus for a 2D homogeneous isotropic continuum, the contact stiffness are:

$$k^n = 2K^N, \quad (3.1)$$

$$k^s = 2K^S. \quad (3.2)$$

where

$$\begin{aligned} K_{n1} &= \frac{\sqrt{3}}{36} (9d_{11} - 6d_{12} + d_{22}) \lambda \\ K_{s1} &= \frac{\sqrt{3}}{18} (3d_{12} - d_{22} - 3\sqrt{3}d_{13} + \sqrt{3}d_{23}) \lambda \\ K_{n2} &= \frac{\sqrt{3}}{9} (d_{22} + 2\sqrt{3}d_{23} + 3d_{33}) \lambda \\ K_{s2} &= \frac{\sqrt{3}}{18} (3d_{12} - d_{22} + 3\sqrt{3}d_{13} - \sqrt{3}d_{23}) \lambda \end{aligned} \quad (3.3)$$

$$K_{n3} = \frac{\sqrt{3}}{9} (d_{22} + 2\sqrt{3}d_{23} + 3d_{33}) \lambda$$

$$K_{s3} = \frac{\sqrt{3}}{9} (d_{22} - 3d_{33}) \lambda$$

In the above equations,  $E$  is the modulus of elasticity; the superscripts  $n$  and  $s$  denote normal and shear stiffness, respectively.  $K_{n1}$  and  $K_{s1}$  are the normal and the tangential spring constants between disc 0 and disc 1, and between disc 0 and disc 4, respectively;  $K_{n2}$  and  $K_{s2}$  are the normal and the tangential spring constants between disc 0 and disc 2, and between disc 0 and disc 5, respectively;  $K_{n3}$  and  $K_{s3}$  are the normal and the tangential spring constants between disc 0 and disc 3, and between disc 0 and disc 6, respectively (see Figure 3.2);  $\lambda$  is the element thickness and  $d_{ij}$  ( $i=3, j=3$ ) are the elastic coefficients of the stiffness matrix for plane stress as follows,

$$[D] = \begin{bmatrix} d_{11} & d_{12} & d_{13} \\ & d_{22} & d_{23} \\ sym & & d_{33} \end{bmatrix}, \quad (3.4)$$

In which  $d_{11} = d_{22} = E/(1 - \nu^2)$ ,  $d_{12} = \nu E/(1 - \nu^2)$ ,  $d_{33} = E/2(1 + \nu)$  and  $d_{13} = d_{23} = 0$ .

For a 2D homogeneous isotropic continuum,  $K_{n1} = K_{n2} = K_{n3} = K^N$  and  $K_{s1} = K_{s2} = K_{s3} = K^S$ , Eqs. (3.1) and (3.2) is simplified, respectively, as

$$k^n = \frac{2E\lambda}{2\sqrt{3}(1 + \nu)} \left(1 + \frac{2}{3(1 - \nu)}\right) \quad (3.5)$$

$$k^s = \frac{2|(3\nu - 1)E\lambda}{6\sqrt{3}(1 - \nu^2)}, \quad (3.6)$$

Since this chapter focuses only on transverse behaviour of uniaxially reinforced lamina, the 2D cross-section and the chosen RVE can be modelled by an assembly of two groups of distinctive isotropic particles, representing the fibres and the matrix, respectively. Therefore, Eqs. (3.5) and (3.6) will be used to determine the bond stiffness between particles of the same constituent material. It is important to note that in previous works ([González and LLorca, 2007a](#), [Vaughan and McCarthy, 2011b](#), [Yang et al., 2012](#), [Yang et al., 2013a](#)) plane strain conditions were assumed within the framework of the finite element deformations theory. However, In DEM the

deformability and strength parameters and equations discussed in this section relate deformability micro-parameters to material properties and thus assuming plane stress would not alter the strength.

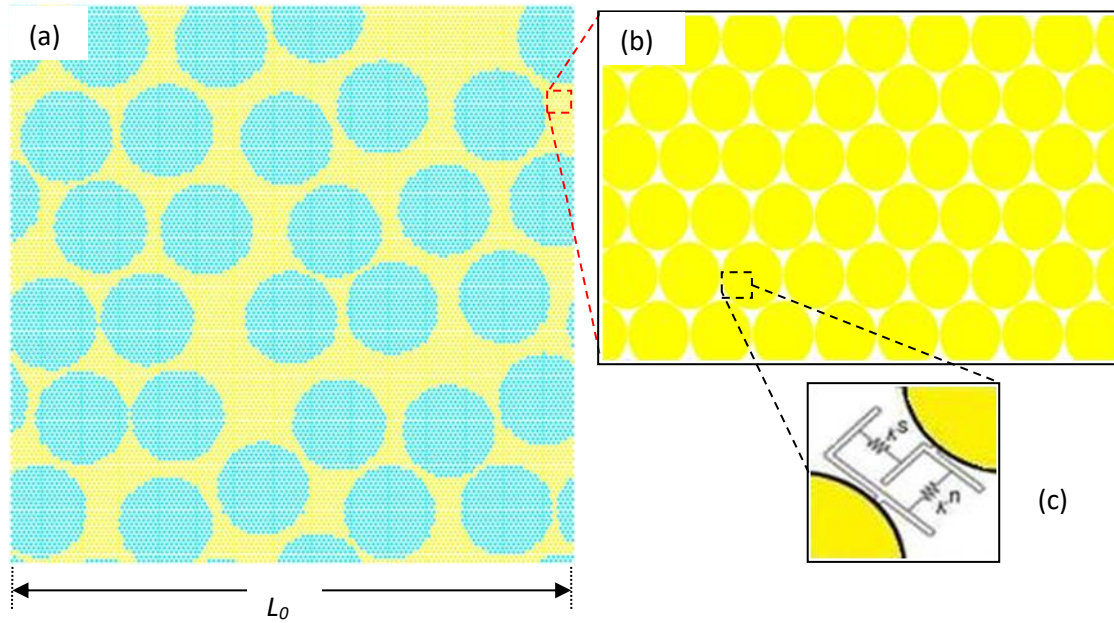


Figure 3.1: Fibre distribution and discrete element discretisation. (a) Representative area element. (b) Hexagonal packing arrangement. (c) Contact between particles.

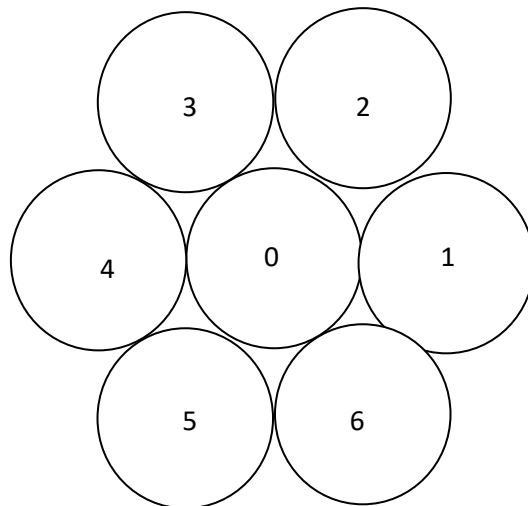


Figure 3.2: Hexagonal packing and contact stiffness.

### 3.3 Contact models

Particles in a DEM model of fibres and matrix are bonded together at contacts using the parallel bonds. The constitutive law of parallel bond is shown in Figure 1.14 and more details are described in Chapter 1. In this chapter, the fibres are assumed to be linear elastic and no fibre damage occurs when the loading is applied transversely. It is often shown that a polymer matrix is sensitive to hydrostatic stresses ([Fiedler et al., 2001](#)), therefore, Mohr–Coulomb criterion is normally used to predict its yielding ([González and LLorca, 2007a](#)), where the cohesion stress and the internal friction angle can be related to tensile strength by:

$$\sigma_{mt} = 2c \frac{\cos(\theta)}{1 + \sin(\theta)}, \quad (3.7)$$

where  $\theta$  is the angle of internal friction,  $c$  is the cohesion yield stress and  $\sigma_{mt}$  is the matrix tensile strength. Once  $\theta$  was fixed for a given simulation, the corresponding cohesion is calculated from Eq. (3.7) using the matrix tensile strength given in Table 3.1.

Table 3.1: Constituent material properties ([González and LLorca, 2007a](#)).

	Fibre	Matrix	Interface
Modulus, $E_{f/m}$ (GPa)	40	4	
Poisson's ratio, $\nu_{f/m}$	0.25	0.35	
Friction angle, $\theta$		15	
Tensile strength, $\sigma_{mt}$ (MPa)		60	
Fracture energy, $G$ (J/m <sup>2</sup> )			100

Since this chapter only focuses on the failure mechanism of fibre-reinforced composite under transverse tension therefore only tensile strength of the matrix is used.

The behaviour of the fibre–matrix interface was modelled using the displacement-softening model, explained in Chapter 1. The principle of this model is similar to the discrete cohesive zone model DCZM ([Xie and Waas, 2006](#)). The constitutive law of the displacement-softening model is shown in Figure 1.16. The mechanical properties of the fibres, matrix and interface used in the analysis are given in Table 3.1.

Since DEM has only recently been used to model fibre reinforced composites ([Yang et al., 2011b](#), [Yang et al., 2011a](#)), there are no well-established and robust relationships between the micro and macro strength parameters. Attempts were made in this chapter to calibrate the contact tensile strength against macro tensile strength by using particle assemblies with different number of particles for isotropic matrix materials. As a hexagonal arrangement was used in this study, it was assumed that the relationships between micro and macro strength was linear and the following formula could be used:

$$\sigma_{micro} = \beta \sigma_{macro} \quad (3.8)$$

where  $\beta$  is a constant factor. Figure 3.3 shows how an overall macro strength of a matrix material ( $\sigma_{macro} = 60$  MPa) was achieved through factorization for using different number of particles. It is important to note that the shear strength of the parallel bond for the matrix was assumed to be high enough to prevent any shear failure before tension failure occurred. It was found that when the number of particles is more than 5530, a factor of  $\beta = 1.7$  yielded an almost constant macro strength close to 60 MPa. Therefore, 1.7 was used throughout this chapter to estimate the micro strength of the bonds.

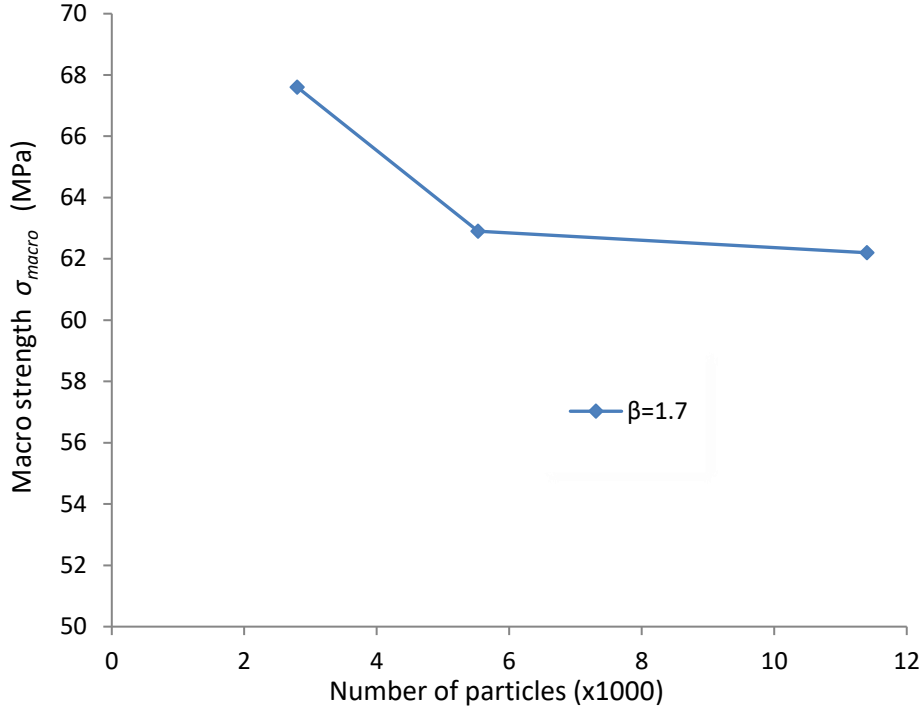


Figure 3.3: Macro strength  $\sigma_{macro}$  versus number of particles.

### 3.4 Results and discussions

#### 3.4.1 Stress distributions

Stress is a continuum quantity and, thus, does not exist at each point in a particle assembly due to the discrete medium. In order to calculate stresses, the RVE is divided to small elements and the contact forces and particles displacements in each element are calculated and transferred to continuum stresses using the following averaging procedure,

$$\bar{\sigma}_{ij} = \left( \frac{1-n}{\sum_{N_p} V^{(p)}} \right) \left( \sum_{N_p} \sum_{N_c^{(p)}} (x_i^{(c)} - x_i^{(p)}) F_j^{(c,p)} \right), i = \{1,2\} \quad (3.9)$$

where  $V^{(p)}$  is the volume of particle,  $n$  is the porosity of the element region,  $x_i^{(p)}$  and  $x_i^{(c)}$  are the locations of a particle centroid and its contact, respectively,  $N_p$  and  $N_c^{(p)}$  are the number of particles in the element region and the contacts along the surface of a particle, respectively and  $F_j^{(c,p)}$  is the force acting on particle ( $p$ ) at the contact ( $c$ ) (Itasca, 2003). Figure 3.4 shows the local microscopic stress state of the

matrix and at the fibre-matrix interface when a transverse tensile stress of 5 MPa is applied to the RVE with a volume ratio of 60%. From Figure 3.4, it can be seen that the stresses at the interfaces are significantly higher than those at other locations. This becomes more obvious in the area of high fibre density. This is attributed to the smaller relative deformation of the fibres due to their higher stiffness.

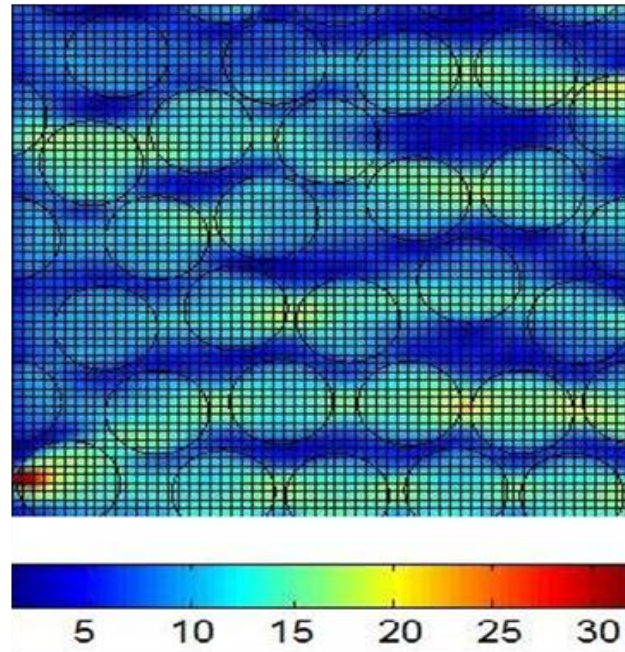


Figure 3.4: Von Mises stress (MPa) distribution in the random model resulting from applying macro stress of 5 MPa.

### 3.4.2 *Damage progression*

It should be mentioned that since the hexagonal packing is used in this paper for both fibres and matrix, any topological disorder of the composite system would be neglected and the final failure is similar to the failure of a brittle-like material. Therefore, disorders in contact strengths were considered by introducing a normal distribution of the tensile strength of the parallel bonds and interfaces, as:

$$\sigma_{micro} = \beta(\sigma_{macro} + m \times grand) \quad (3.10)$$

where  $m$  is the standard deviation of normal strength and  $grand$  is the random number drawn from the normal (Gaussian) distribution, with a mean of 0.0 and a standard deviation of 1.0. Figure 3.5 shows an example of a strength distribution obtained in the

case of 9000 contacts with the mean strength,  $\sigma_{macro}$ , being 60 MPa and two different standard deviations.

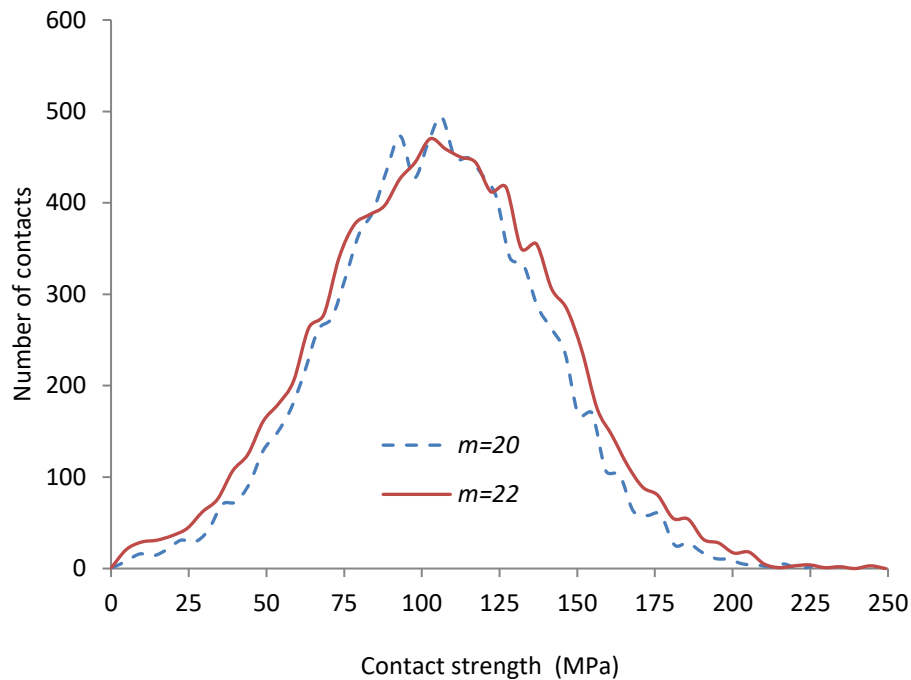


Figure 3.5: Examples of a distribution obtained in the case of 9000 contacts.

Since the contact strength is distributed randomly throughout the RVE, one can expect that the stress–strain curves will not be the same in each run of calculation because a different random number grand is generated by computer. The model containing approximately 11,000 particles and the computational analysis was carried out using a personal computer. A typical run time was in the region of 12 h on a Dual Core Processor 2.30 GHz. The stress–strain curves of the three runs under the same transverse tension are shown in Figure 3.6. It can be seen from the figure that the elastic parts of all the curves are almost identical and the discrepancies occur after the onset of damage. For all the three runs, the mean tensile strength is 55.5 MPa, which is a bit smaller than the given macro matrix strength (60 MPa).

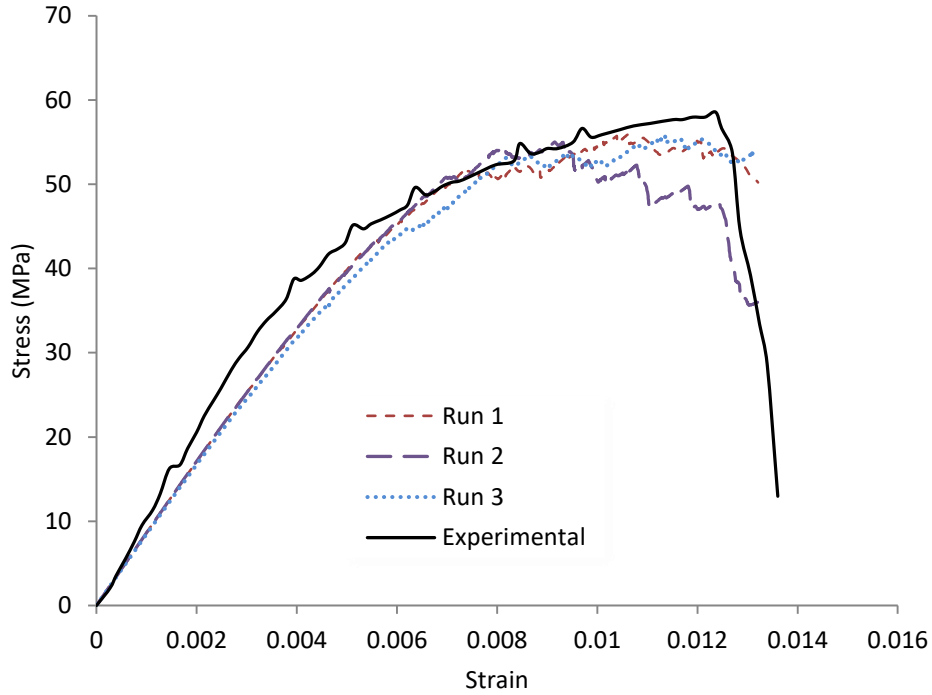


Figure 3.6: Stress–strain curves of the RVE compared with the experimental result

The most important feature of the current model is the prediction of damage initiation and progression. Moreover, the damage states at different loading levels can be clearly identified. Figure 3.7 shows the damage progression of the composite RVE subject to transverse tension at different strain stages, and the comparisons with the microscopic images from experiments ([Yang et al., 2012](#)). The initial elastic response is followed by a non-linear hardening region started from a strain of about 0.7% (see Figure 3.6 and Figure 3.7a). Matrix cracks were observed to concentrate in the vicinity of the debonded fibre/matrix interfaces (Figure 3.7b). However, a few random matrix cracks were observed as a result of the statistical distribution of contact strength. Finally, the failed interfacial bonds joined with matrix cracks, resulting in the final fracture failure of the lamina (Figure 3.7c).

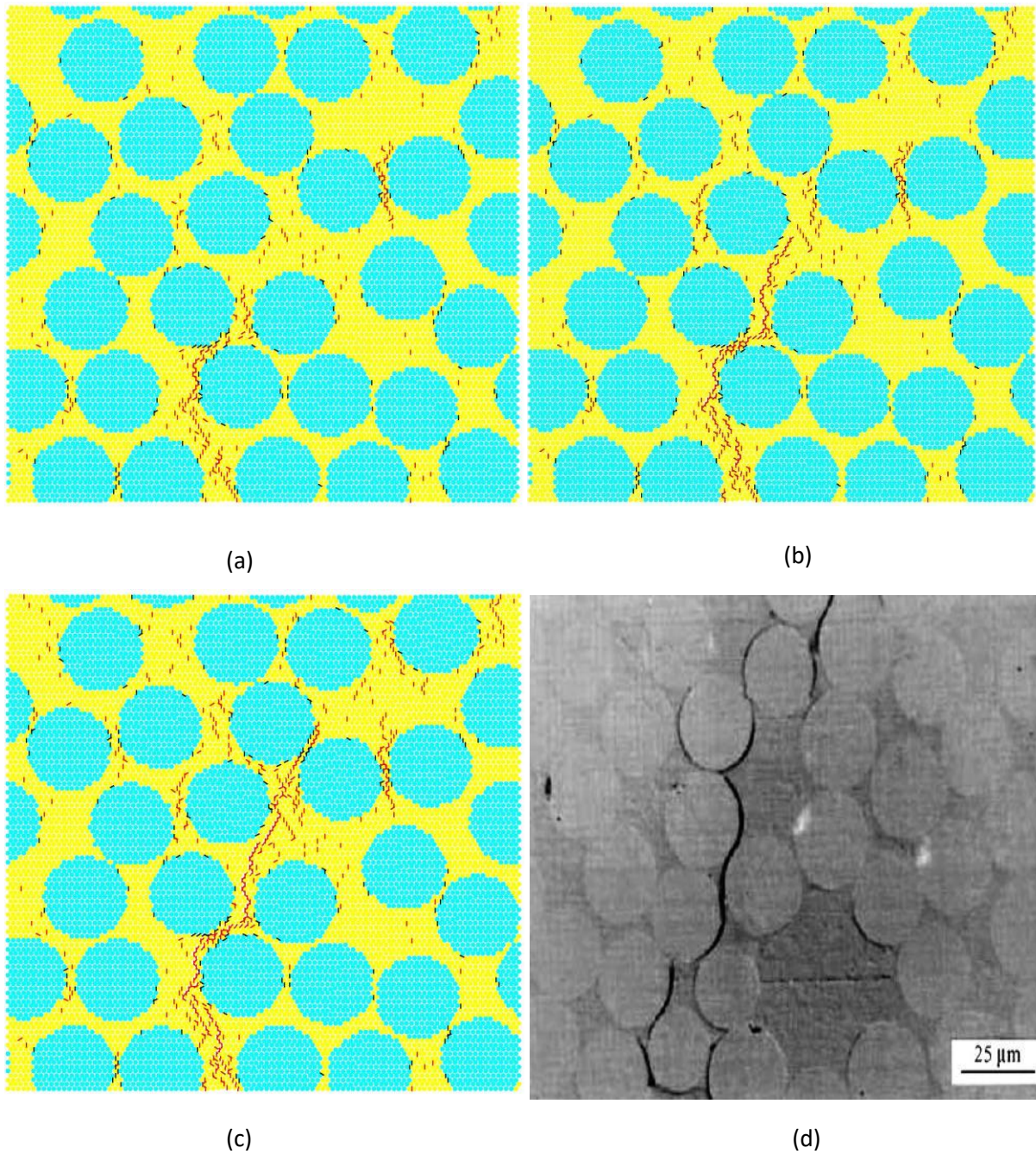


Figure 3.7: Damage initiation and progression under transverse tension and different strain. (a) strain of 0.007. (b) strain of 0.01. (c) strain of 0.014. (red lines represent the matrix cracks and black lines represent interface debonding). (c) Experimental results ([Yang et al., 2012](#)).

### 3.4.3 Sensitivity study of interface parameters on interfacial debonding

Computational simulations of interfacial debonding in fibre-reinforced composites require input data such as interfacial strength and interfacial fracture energy. Unfortunately, these data are not accurately known because they are difficult

to measure from simple laboratory experiments. The effect of interfacial strength using a displacement-softening model for the fibre–matrix interfaces was first examined (Yang et al., 2012, Zhou et al., 2001). Assuming a constant interfacial fracture energy  $G_I = G_{II} = 100 \text{ J/m}^2$  (González and LLorca, 2007a). Two cases *i.e.*, strong interfaces ( $F_c^n = F_c^s = 2c$ ) and weak interfaces ( $F_c^n = F_c^s = 0.5c$ ); were studies, where  $F_c^n$  and  $F_c^s$  are tensile and shear strengths of the displacement-softening contact, respectively, as shown in Figure 1.16, and  $c$  is the cohesion yield stress calculated in Section 3.3. The influence of interfacial strength on the stress–strain curves in transverse tension is shown in Figure 3.8. It is apparent that the fibre–matrix interface strength considerably affects the stress– strain curves, and the tensile strength decreased remarkably by 15% when a weak interface was considered. For the strong interface, the damage starts at the peak point in the form of matrix cracking without obvious interfacial debonding. This continues to spread until the ultimate failure occurs. However the tensile strength is increased only by 6% when interfacial strength is doubled, as shown in Figure 3.8.

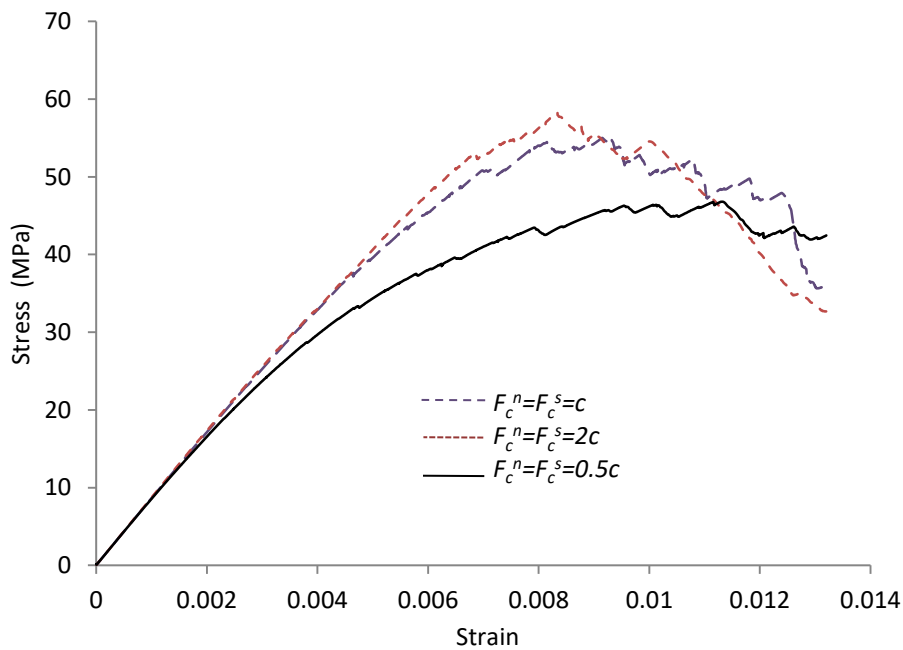


Figure 3.8: Effect of interface strength on the stress-strain response.

The effect of interfacial fracture energy on the stress–strain response was studied for  $G = 10 \text{ J/m}^2$  and  $G = 100 \text{ J/m}^2$ . Figure 3.9 shows the stress–strain curves

of the RVE with the above fracture energies and a fixed interfacial strength of 39.1 MPa. It can be seen from Figure 3.9 that despite of reducing the interfacial fracture energy by 90%, the two curves are still very close. With a fixed interfacial strength, lower fracture energy leads to a smaller softening strain ( $U_{pmax}$  in Figure 1.16) and thus the interface becomes more brittle and damage occurs earlier (region A in Figure 3.9)

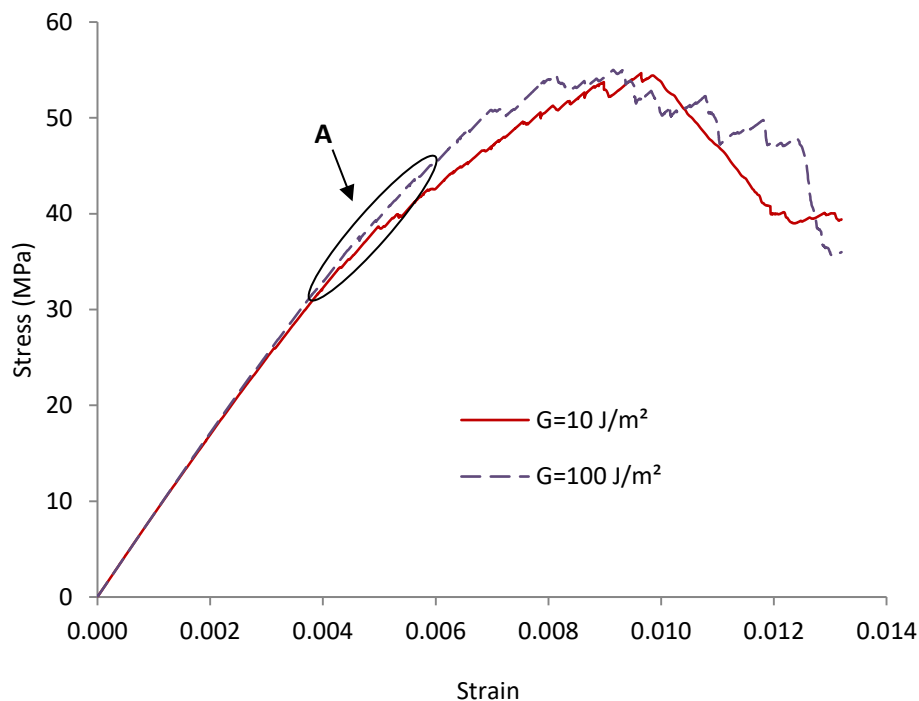


Figure 3.9: Effect of interface fracture energy on the stress-strain response.

Various values of the interfacial stiffness have been used for fibre/matrix interface, e.g., Yang *et al.*, and González and Llorca ([Yang et al., 2012](#), [González and Llorca, 2007a](#)) used a large value of  $K = 108$  GPa/m, while Vaughan and McCarthy ([Vaughan and McCarthy, 2011b](#), [Vaughan and McCarthy, 2011a](#)) used a much smaller value of  $K = 105$  GPa/m. To examine the effect of the interfacial stiffness on the damage behaviour of the composites, Figure 3.10 shows the stress–strain relationship of the two RVEs in which two different values were used for fibre/matrix stiffness, *i.e.*, matrix stiffness and fibre stiffness. It is shown that though the overall

stiffness of the composite RVEs exhibits notable differences, the ultimate strength of the material is not affected.

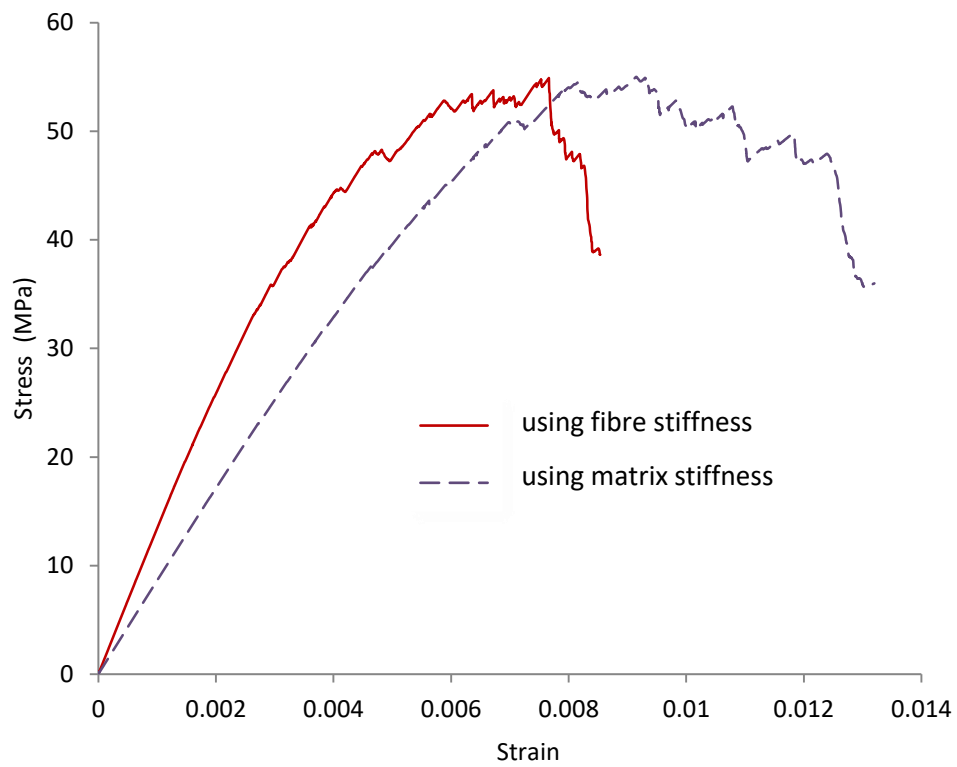


Figure 3.10: Effect of interfacial stiffness on the stress-strain response.

# Chapter 4

---

## 4 A DEM model for predicting elasticity of composite lamina

In the chapter, a methodology is developed to determine the elastic properties of a composite lamina using DEM. The algorithm developed in chapter 2 is used to generate a random distribution of fibres with different volume fractions. The present chapter starts by reviewing of two well-known analytical methods and numerical method (e.g. FEM) that are used to compute the elastic properties of the composite materials found in the literatures. The results obtained by DEM are finally compared with FEM analytical methods.

### **4.1 Introduction**

When dealing with an isotropic homogeneous material (e.g. metal and aluminium), It is obvious that the elastic properties are independent and their determination is straightforward. However, composite materials are assumed to be heterogeneous materials, as they are constituted of two or more phases, and each phase has its own mechanical properties. Consequently, it is difficult to obtain their properties experimentally.

In order to overcome this difficulty, many analytical and numerical methods have been developed over the last century. All methods are, essentially, based on the separation of the constituents of the composite material, and all of the methods assume that each constituent has its own elastic properties. The geometric information at micromechanical level (e.g. size of RVE, fibre volume fraction inter-fibre distances), which is usually variable, can be explicitly taken into account when using numerical methods.

## 4.2 Analytical methods used in this chapter

### 4.2.1 The rule of mixtures (RoM)

The rule of mixture (RoM) model (also known as the Voigt model) was derived by Woldemar Voigt in 1889 ([Mishnaevsky Jr, 2007](#), [Voigt, 1889](#)). This approach is based on the assumption that the average strain of each constituent (fibre and matrix) is equal to the applied strain on the material, thus:

$$\varepsilon_f = \varepsilon_m = \varepsilon_c \quad (4.1)$$

where  $\varepsilon_f$ ,  $\varepsilon_m$  and  $\varepsilon_c$  are the strains at fibre, matrix and composite, respectively.

Thus the composite effective stiffness tensor,  $C_{ijkl}$ , can be determined as:

$$C_{ijkl} = V_f C_{ijkl}^f + V_m C_{ijkl}^m \quad (4.2)$$

where  $V_f$  and  $V_m$  are the fibre and matrix volume fraction, respectively. Eq. (4.2) states, in other words, that each individual engineering constant of a lamina can be determined from the engineering constant of the fibre and the matrix made from ([Herakovich, 1998](#)).

### 4.2.2 The Mori-Tanaka method

The Mori-Tanaka method was proposed by Mori and Tanaka ([Mori and Tanaka, 1973](#)). This method (as is the case for typical mean-field models) assumes that fourth order concentration tensors relate the average strain tensor in the fibre to the average strain tensor in the matrix. This tensor states the relation between the uniform strain in a single fibre embedded in an infinite matrix and the lamina that subjects to uniform strain at the boundary. The equations linking the overall moduli to the elastic moduli of the fibre,  $k_f$ ,  $m_f$  and  $p_f$ , and elastic moduli of the matrix,  $k_m$ ,  $m_m$  and  $p_m$  as:

$$m = \frac{m_m m_f (k_m + 2m_m) + k_m m_m (V_f m_f + V_m m_m)}{k_m m_m + (k_m + 2m_m) + (V_f m_m + V_m m_f)} \quad (4.3)$$

$$p = \frac{2V_f p_f p_m + V_m (p_f p_m + p_m^2)}{2V_f p_m + V_m (p_f + p_m)}$$

$$l = \frac{V_f l_f (k_m + m_m) + V_m l_m (k_f + m_m)}{V_f (k_m + m_m) + V_m (k_f + m_m)}$$

$$n = V_f n_f + V_m n_m + (l - V_f l_f - V_m l_m) \frac{l_f - l_m}{k_f - k_m}$$

$$k = \frac{k_f k_m + m_m (V_f k_f + V_m k_m)}{V_f k_m + V_m k_f + m_m}$$

The relationship between overall moduli and the engineering moduli are given as:

$$m = G_{23}$$

$$p = G_{12}$$

$$l = 2k\nu_{12} \tag{4.4}$$

$$n = E_1 + 4k\nu_{12}^2$$

$$k = \left[ \frac{1}{G_{23}} - \frac{4}{E_2} + \frac{4\nu_1^2}{E_1} \right]^{-1}$$

with

$$E_2 = 2(1 + \nu_{23})G_{23} = \frac{4km}{(k + qm)}$$

$$\nu_{23} = \frac{(k - qm)}{(k + qm)} \tag{4.5}$$

$$q = 1 + \frac{4k\nu_{12}^2}{E_1}$$

If the constituent is isotropic with bulk modulus,  $k$ , and shear modulus,  $G$ , then:

$$k = \frac{G}{(1 - 2\nu)} \tag{4.6}$$

$$l = k - \frac{2G}{3}$$

$$n = k + \frac{4G}{3}$$

$$m = p = G$$

### **4.3 Numerical methods**

Improvements in computer speed over the last few decades have led researchers to put a considerable amount of effort into determining the effective properties of composite materials by means of micromechanics using numerical methods (e.g. boundary element method BEM and FEM). In the following subsections, the methodologies for simulating the composite material at the micromechanical level, which have been intensively used by others researchers, are presented. The proposed DEM model for determining the elasticity of composite is then outlined.

#### **4.3.1 Finite element method**

The simplest way of representing the heterogeneity of material is by assuming that the fibres are periodically distributed in the matrix. This method is easy, and performing the analysis does not require enormous amounts of time or resources. Different types of periodic distribution have been found in the literatures; the two types that are most frequently used are square and hexagonal (see Figure 1.5). Due to the periodicity of the fibres, only a small portion of the composite can be chosen to represent the FEM model; this is indicated by the letter “A” in Figure 1.5. Li ([Li, 2001](#)) presented an extensive summary of the features of two unit cells produced from square and hexagonal fibres arrangements for unidirectional fibre-reinforced composites. He established equations for displacement and traction boundary conditions and defined the application of loads in terms of macroscopic stresses and effective properties. The macroscopic strains are then taken as independent degrees of freedom and applied on the edge nodes. Aghdam *et al.* ([Aghdam et al., 2001](#)) performed axial, longitudinal, transverse and off-axis loads on 2D and 3D cell unit of SiC/Ti composites with different fibre orientation in the range of 0°–90°. Symmetric boundary conditions were used for the 2D model while periodic boundary conditions were considered for the 3D model. Coulomb friction was used to model the fibre/matrix interface. However, there is some doubt whether this model is acceptable to represent

the interface as there is no information on the friction coefficient on the interface. The friction coefficient plays an important role in the amount of shear stress transferring between matrix and fibre. In other words, the interface is perfectly debonded when the friction coefficient tends to zero, which in turn reduces the strength of the composite, while a high level of friction increases the strength significantly. Ha *et al.* ([Ha et al., 2008](#)) determined the failure envelope of a composite lamina under biaxial loads by modelling unit cells of square and hexagonal fibre arrangement. A good agreement was achieved in the prediction of biaxial failure envelopes and the stress-strain curve. Van der Sluis *et al.* ([Van der Sluis et al., 2000](#)) carried out a comparative study of unit cells with mixed and periodic conditions. They studied the stress distribution in a square unit cell with centred and off-centred fibre. It was concluded that periodic boundary conditions are more appropriate.

In real life, however, it is very difficult to manufacture composite materials with periodic fibre arrangements. Consequently, considering periodicity of fibre arrangements may lead to incorrect results in the prediction of mechanical properties and the detection of fracture progress. Therefore, many researchers have used another approach to analysis the composites, by considering an RVE with several dozen of randomly distributed fibres. Intensive studies have been carried out to find the effects of RVE size, the position of fibres, and the internal distance between fibres on the elastic properties as well as the strength of FRP composite lamina. For instance, Trias *et al.*, ([Trias et al., 2006](#)) concluded that the minimum size of carbon fibre reinforced polymer with a volume fraction of 50% is  $\delta = L/r_f$ , where  $L$  is the side of the element and  $r_f$  is the fibre radius. Yang *et al.* ([Yang et al., 2013a](#)) found that inter-fibre spacing has a significant impact on the transverse strength of composites especially when thermal residual stress is taken into account.

For comparison, FE analysis was carried out on three different models in this work; these are unit cells with square and hexagonal fibre packing Figure 4.1 as well as RVEs with random fibre distribution. Fibre and matrix were meshed using two-dimensional 4-node bilinear plane strain quadrilateral elements (CPE4). Periodic boundary conditions were applied to unit cells and RVEs to ensure the compatibility of

strain and stress at macro level, similar to those in Chapter 2. Eq. (4.7) gives the relationship between side length and volume fraction,  $V_f$ .

$$b = r \sqrt{\frac{\pi}{V_f}} \quad \text{Square} \quad (4.7)$$

$$b = r \sqrt{\frac{\pi}{2\sqrt{3}V_f}} \quad \text{hexagonal}$$

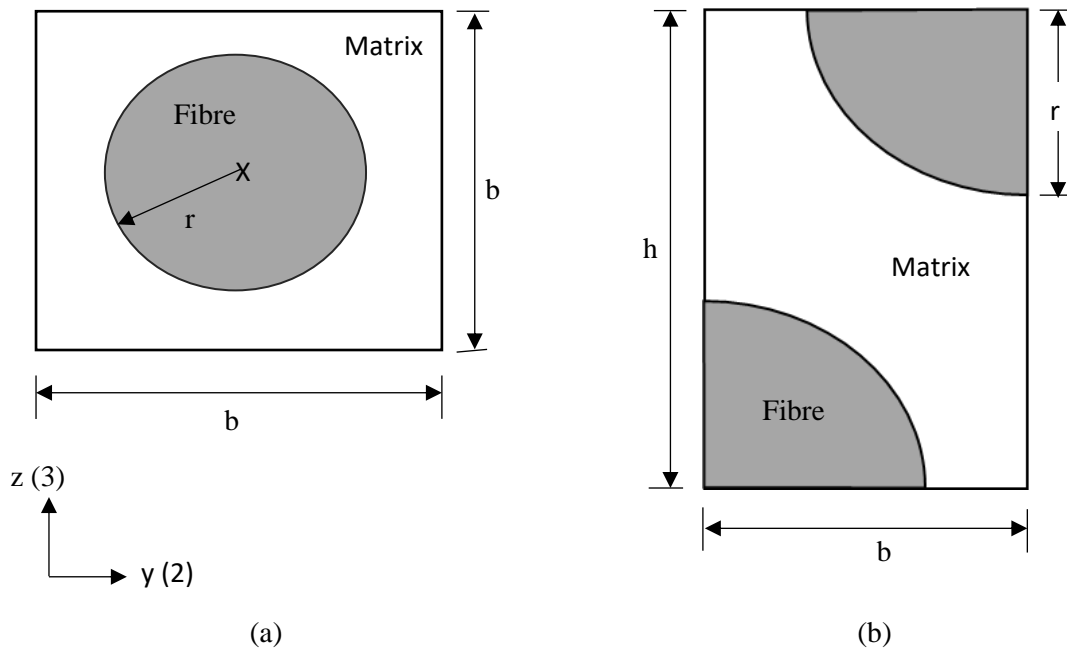


Figure 4.1: Appropriate unit cells (a) Square (b) Hexagonal packing.

#### 4.4 Discrete element model

The objective of this section is to explain the methodology of the DEM which is used to determine the elastic properties of the composite from its constituents material properties. RVEs studied contains fibres distributed randomly, with similar configuration used both DEM and FEM. Particles represent fibres and matrix are connected together using parallel bond, while displacement-softening model used to model fibre/matrix interface. These contact models are explained in Section 1.10.1.2 and 1.10.1.3, respectively. Throughout this chapter, RVEs were generated by assembly of arbitrary sized particles. Therefore, micro-parameters must be related to a set of relevant material properties using calibration procedure.

#### **4.4.1 Calibration of DEM model**

In continuum mechanics based models, the input properties such as modulus and strength can be obtained directly from tests performed on laboratory samples. However, in a DEM model with arbitrarily sized particles, there is no rigorous formula to correlate the micro-parameters (contact and particle stiffness as well as bond strength) in DEM with the real material properties. In general, the relation between micro-parameters that characterise a DEM model and macro-properties (such as elastic constant and peak strength) is found by means of virtual calibration tests such as uniaxial compression test and tension test. Each micro-parameter is related to a relevant material property and the DEM parameter is trialled in order to match the virtual macro-properties of the DEM specimen with those of the real material. This process is repeated in different virtual tests until all the necessary macro-properties are matched.

#### **4.4.2 DEM model generation**

As discussed in Section 4.4.1, sample preparation is a step of particular importance in DEM modelling. Many packing methods have been proposed in previous studies. Methods available in the literature can be fundamentally classified into two groups: dynamic and constructive. The dynamic method is based on dynamic simulations to fill the domain with particles. The main dynamic methods described in the literature are DEM, molecular dynamic growth algorithm ([Kansal et al., 2002](#), [Lubachevsky and Stillinger, 1990](#)) and isotropic compression ([Martin et al., 2003](#)). One of the earliest method so called Lubachevsky-Stillinger algorithm ([Lubachevsky and Stillinger, 1990](#)) which is a molecular dynamic growth method developed to produce a dense packing. In this method, particles are firstly distributed randomly positions. Then, they are given linear or angular velocities and they expanded uniformly at a certain expansion rate until jammed packing reaches. However, these methods are computationally expensive and controlling material properties such as density is hard.

Therefore, constitutive approaches have been used excessively in both academic and industrial purposes. They are based on the geometrical computations, and as thus they are also known as geometric methods. The majority of the methods

compute the position of new particles randomly base on the information particles previously inserted. For example, Feng et al. ([Feng et al., 2003](#)) are along those that first proposed the constitutive packing method. The method starts by adding three particles randomly in the centre of the domain. Then new particles are inserted by continuously advancing the front until the domain is filled. Another approach uses random sequential addition (RSA) technique to disperse particles in the required area. This method is purely relying on randomness principles and has been used to generate disks ([Hinrichsen et al., 1986](#)), spheres ([Cooper, 1988](#)) and ellipsoids ([Sherwood, 1997](#)). The volume fraction,  $\phi$ , of the generated disks was found to be  $\phi=0.547$ , while for three-dimensional spheres  $\phi=0.385$  ([Williams and Philipse, 2003](#)).

In the present chapter, a *radii expansion* procedure is used ([Itasca, 2003](#)) to generate two dimensional square samples with dimension of  $63 \mu\text{m} \times 63 \mu\text{m}$ . This method starts with placing an initial set of particles with artificially small radii in a square area enclosed by four rigid frictionless walls (see Figure 4.2a). The particle sizes varies from  $0.1 \mu\text{m}$  to  $0.166 \mu\text{m}$  according to a uniform distribution, which ensuring adequate particles cover the region between fibres. Then particles are expanded by a multiplier factor until the desired porosity is achieved. The formula bellow is used to calculate the radii multiplier,  $m$ , in order to change the porosity of the space from initial assumed porosity,  $n_0$ , to the desired,  $n$ .

$$m = \sqrt{\frac{1 - n}{1 - n_0}} \quad (4.8)$$

Finally, a number of simulation cycles are applied to bring the system into equilibrium. This method has been used by many researches ([Boutt and McPherson, 2002](#), [Nguyen et al., 2009](#), [Yan et al., 2009](#)) to generate densely packed particle assemblies and readers can refer to ([Itasca, 2003](#)) for more details. The assembly representing the numerical specimen studied in the section consists of 16,451 particle and the histogram of the particle sizes are shown in Figure 4.2b.

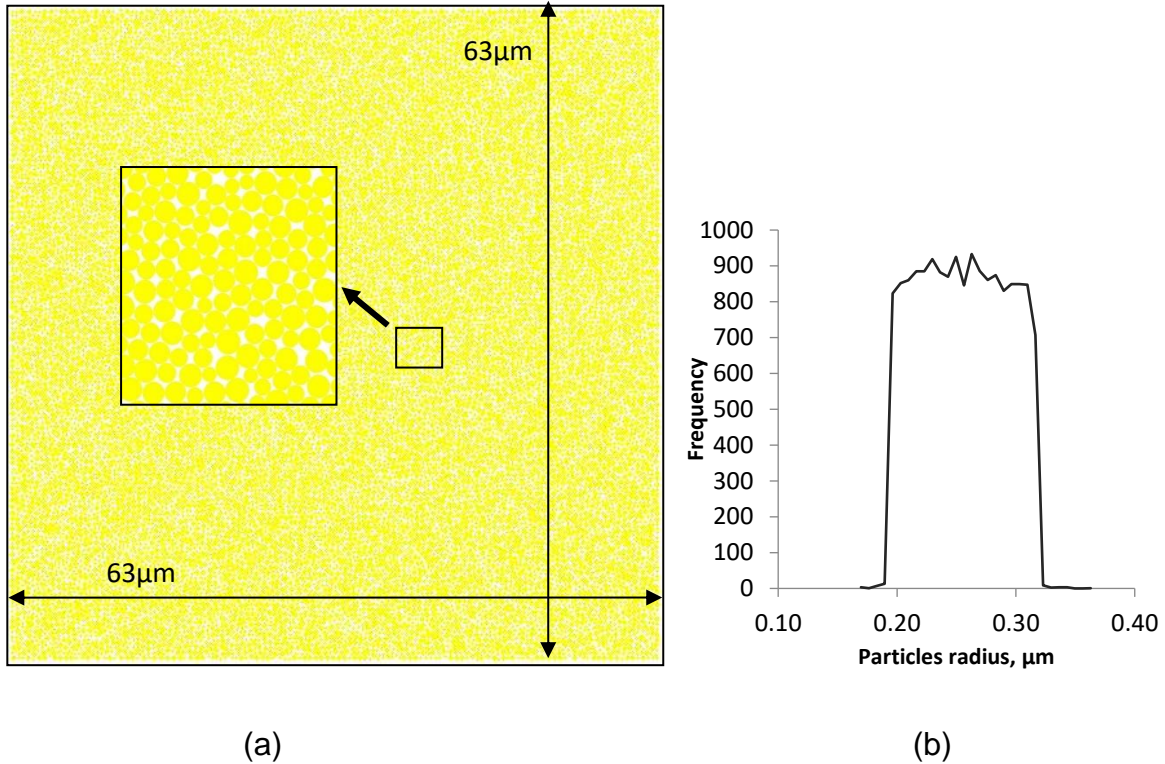


Figure 4.2: The DEM model: (a) model geometry and particle assembly, and (b) particle size distribution.

#### 4.4.3 DEM simulation

Once the sample is prepared, numerical tests are conducted to find the relationship between the micro-parameters and the macro-properties as shown in Figure 4.3. The uniaxial compression test is conducted by moving the right and left rigid walls at a constant and very small velocity (see Figure 4.3a). Whilst in the direct shear test, the boundary particles are first identified and then assigned with a constant velocity to produce shear displacement, as shown in Figure 4.3b. The loading rate needs to be slow enough to ensure the sample remains in quasi-static equilibrium throughout the test and should be stable so as to not induce any possible dynamic strains (Cho et al., 2007). On the other hand, too small loading rate would be computationally expensive. If not indicated otherwise, the loading rate used in this paper is chosen to “5 mm/s” which could be considered as a fast one in the real experimental tests. However, since discrete element method is based on small time integration scheme, thus timestep  $\Delta t$  is chosen in each cycle to be very small (*i.e.*,  $1 \times 10^{-9}$ s). In other words, the velocity of 5 mm/s used in this paper can be translated to

$2.5 \times 10^{-12}$  mm/step which means it requires more than 80,000 steps to move the loading walls to a distance of 0.22 mm.

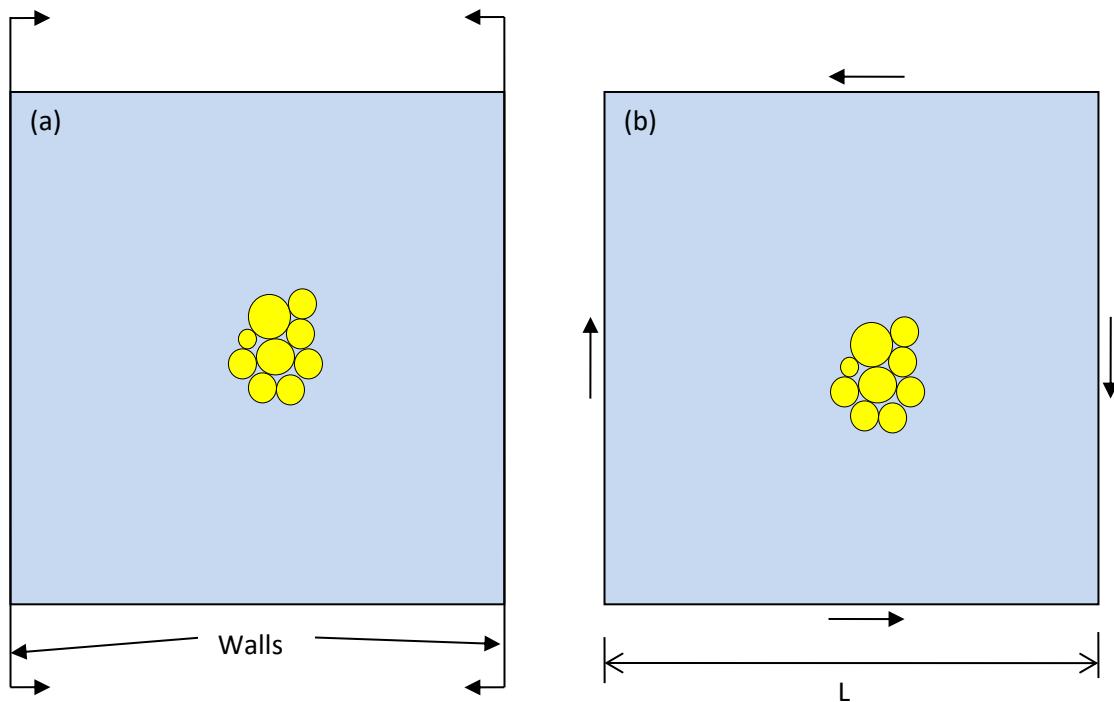


Figure 4.3: Virtual uniaxial tests of a DEM model: (a) compression and (b) shear.

#### 4.4.4 Parametric study of contact stiffness

Generally the mechanical properties of an elastic material can be characterised by its elasticity (*i.e.*, elastic modulus, shear modulus and Poisson's ratio) and strength (*i.e.*, compressive strength, tensile strength and shear strength). It has been found that local elastic parameters of particles and the contacts between particles, *e.g.*, particle stiffness and parallel bond stiffness, play a major role in the macroscopic elastic response of the entire DEM model, and thus calibrations are required ([Itasca, 2003](#)). As the DEM model of a composite material consists of two constituents (fibre and matrix) with different properties, each constituent is calibrated individually before combined together with interface stiffness which is assumed equal to that of fibres similar to that in Chapter 3. Usually the macroscopic Young's modulus of the matrix is directly proportional to the stiffness of particles ( $k^n$ ,  $k^s$ ) and those of parallel bonds ( $\bar{k}^n$ ,  $\bar{k}^s$ ). While the macroscopic Poisson's ratio is directly proportional to ratios of  $k^n/k^s$  and  $\bar{k}^n/\bar{k}^s$  ([Itasca, 2003](#)). The material is E-glass/MY750/HY917/DY063 which

is chosen from the World Wide Failure Exercise (WWFE) ([Soden et al., 1998b](#)). Both fibre and matrix are considered isotropic with mechanical properties given in Table 4.1.

Table 4.1: Mechanical properties of fibre and matrix.

Fibre	Transverse modulus, $E_f$ (GPa)	74
	Poisson's ratio, $\nu_f$	0.2
Matrix	Modulus, $E_m$ (GPa)	3.35
	Shear Modulus, $G_m$ (GPa)	1.24
	Poisson's ratio, $\nu_m$	0.35
	Compressive strength, $Y_{mc}$ (MPa)	120
	Tensile strength, $Y_{mt}$ (MPa)	80

The elastic properties given in Table 4.1 are measured under plane stress condition ([Davila et al., 2005](#)) and they can be converted to properties under plane strain condition, under which the DEM models are carried out in this work, by ([Ugural and Fenster, 2003](#)):

$$\bar{\nu}_{f,m} = \frac{\nu_{f,m}}{1 + \nu_{f,m}} \quad (4.9)$$

$$\bar{E}_{f,m} = E_{f,m}(1 - \bar{\nu}_{f,m}^2) \quad (4.10)$$

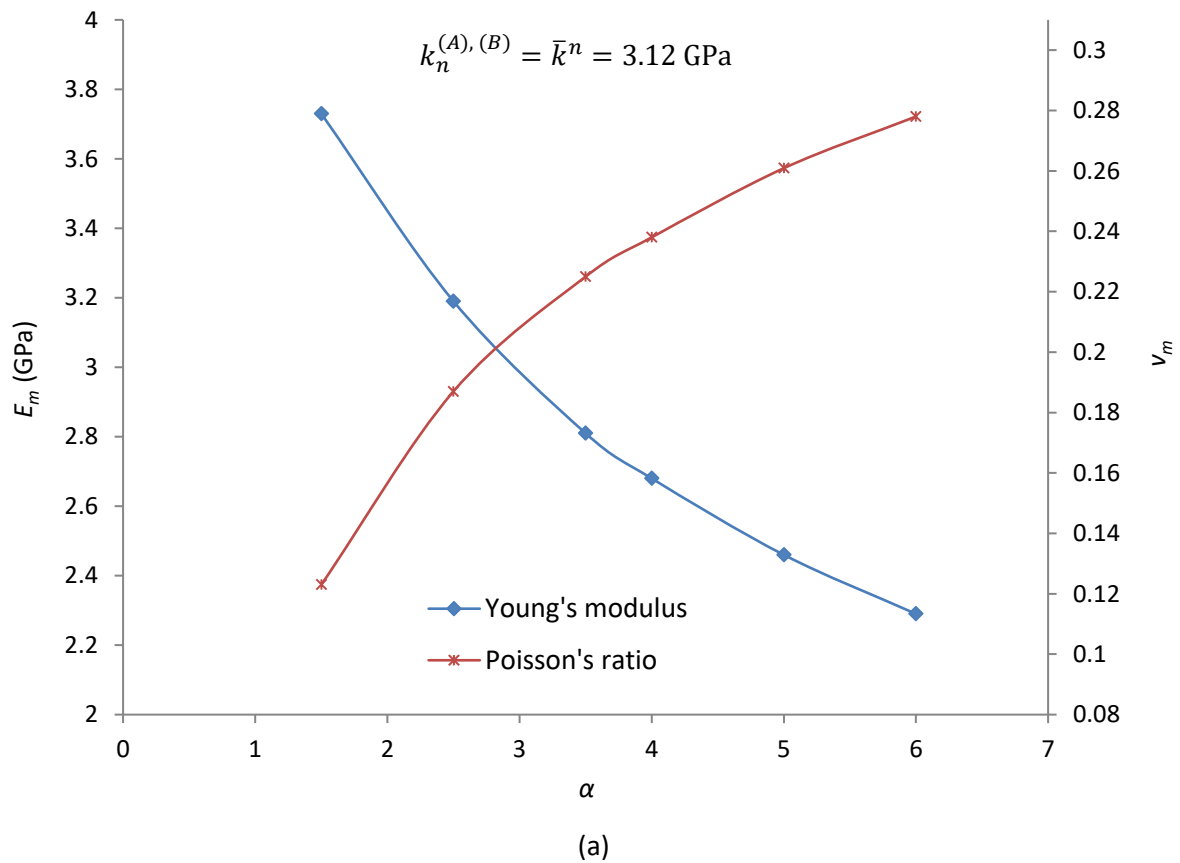
Using Eqs. (4.9) and (4.10) together with the material properties in Table 4.1, the Poisson's ratio and Young's modulus for both fibre and matrix under plane strain condition are calculated as  $\bar{\nu}_f = 0.166$ ,  $\bar{E}_f = 71.96$  GPa,  $\bar{\nu}_m = 0.259$  and  $\bar{E}_m = 3.12$  GPa, respectively.

In the calibration process, it is convenient to define a ratio between the normal and tangential stiffness for both particles and parallel bonds as:

$$\alpha \equiv \left( k_n^{(A),(B)} / k_s^{(A),(B)} \right)_{particles} \text{ and } (\bar{k}^n / \bar{k}^s)_{parallel\ bonds} \quad (4.11)$$

Figure 4.4a and Figure 4.5a show the relationship between the ratio,  $\alpha$ , and macroscopic elastic properties obtained from axial compressive tests of the DEM

model of matrix and fibre when normal stiffness for particles and parallel bonds are kept constant at 3.12 GPa 71.9 GPa, respectively. It can be seen that as  $\alpha$  increases the Young's modulus decreases while Poisson's ratio increases for the chosen range of values. As both elastic modulus and Poisson's ratio vary with  $\alpha$ , the calibration is carried out as follows. First, the value of  $\alpha$  is chosen for the matrix and the fibre from Figure 4.4a and Figure 4.5a to produce the desired value of Poisson's ratio. Then,  $\alpha$  is kept constant and a series of simulation tests are conducted with a range of normal stiffness ( $\underline{K}^n = k_n^{(A),(B)} = \bar{k}^n$ ) as shown in Figure 4.4b and Figure 4.5b. As can be seen from these figures the Poisson ratio is independent of  $\underline{K}^n$  and remains constant for all chosen  $\underline{K}^n$ , whereas Young's modulus increases with the  $\underline{K}^n$ . The target value of  $E_m$  and  $E_f$  can then be found.



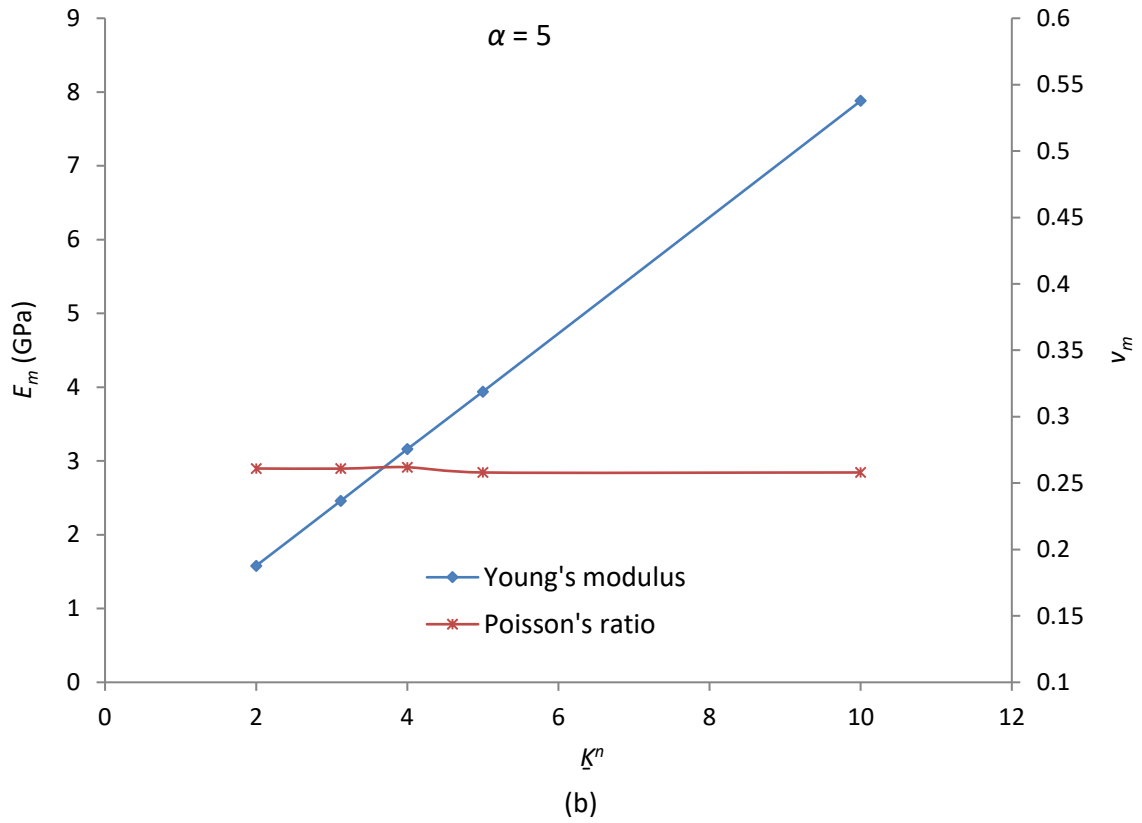
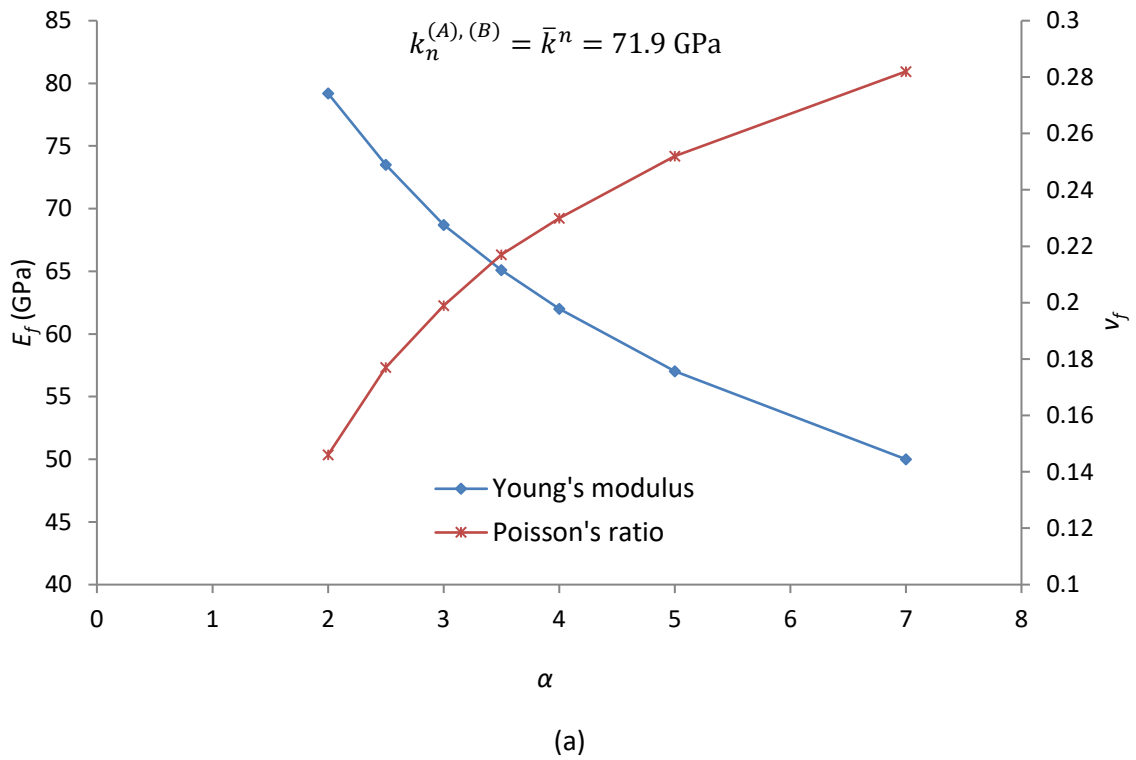
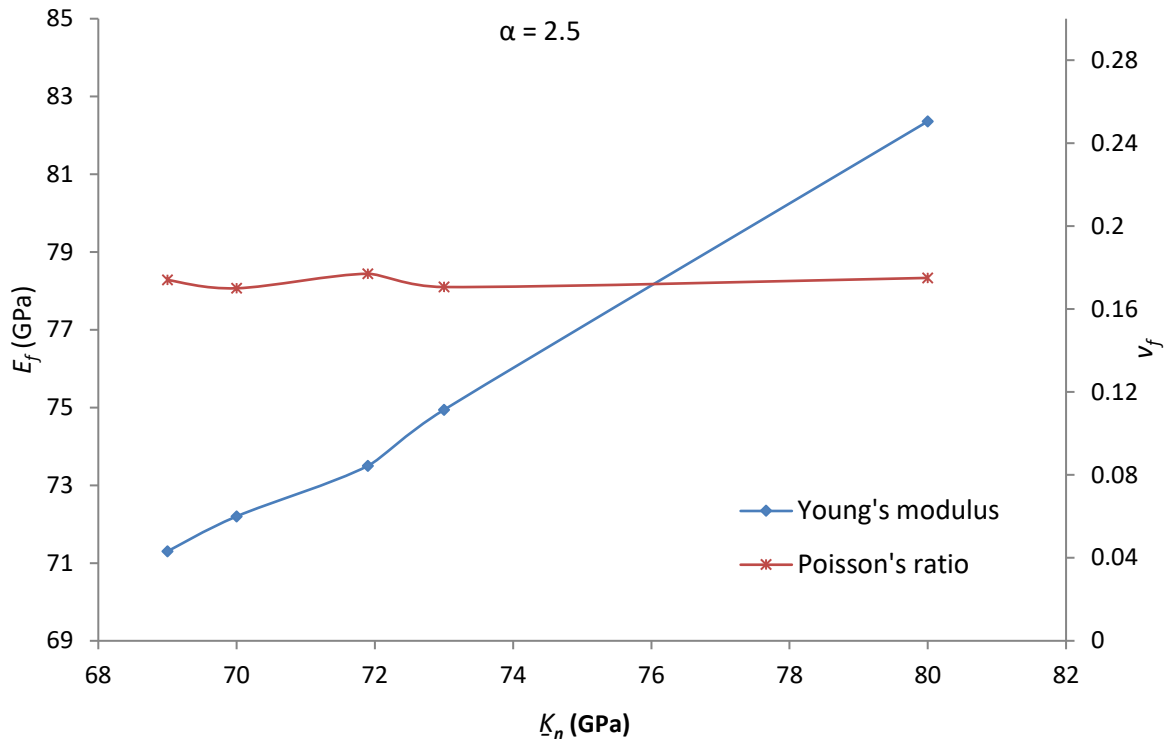


Figure 4.4: Calibration of matrix elastic properties; (a) Influence of normal stiffness to shear stiffness ratio,  $\alpha$ , on the Young's modulus and Poisson's ratio; (b) Effect of normal stiffness on Young's modulus and Poisson's ratio.





(b)

Figure 4.5: Calibration of fibre elastic properties; Influence of normal stiffness to shear stiffness ratio,  $\alpha$ , on the Young's modulus and Poisson's ratio; (b) Effect of normal stiffness on Young's modulus and Poisson's ratio. The microscopic parameters obtained are provided in Table 4.2

Table 4.2: Micro-parameters for particles and parallel bonds.

		<u>Fibre</u>	<u>Matrix</u>
Particles	$k_n^{(A),(B)} / k_s^{(A),(B)}$	2.5	5
	$k_n^{(A),(B)}$ (GPa)	70	4
Parallel bond	$\bar{k}^n / \bar{k}^s$	2.5	5
	$\bar{k}^n$ (GPa)	70	4

In order to make sure that these parameters are correct and to verify the DEM model, a numerical shear test is also performed to predict the shear modulus,  $G_m$ , of the matrix. The elastic properties for both fibre and matrix obtained from DEM are compared with those from experimental ([Soden et al., 1998b](#)) in Table 4.3. It can be

seen that the predicted elastic properties are very close to those from experiments. However, it is important to note that the results obtained are valid for only this particles packing.

Table 4.3: DEM predictions of the elastic properties of fibre and matrix.

	Experimental (Soden et al., 1998b)	DEM	Error (%)
$E_f$ (GPa)	71.96	72.2	0.33
$\nu_f$	0.166	0.170	2.3
$E_m$ (GPa)	3.12	3.16	1.2
$\nu_m$	0.259	0.262	1.1
$G_m$ (GPa)	1.24	1.21	2.4

#### 4.4.5 Effect of particle size on the Young's modulus and Poisson's ratio

Particle size sensitivity test was also conducted in this study to ensure that the particle size used in the previous section was adequate. Since this chapter is solely devoted to study the elasticity only, therefore the particle number was drawn as a function of Young's modulus and Poisson's ratio. Six models with different particle size range from 2,628-25,667 particles are chosen. The contact and particle parameters are kept constant and equivalent to those for matrix listed in Table 4.2. Figure 4.6 show the variation of Young's modulus with particle size for the RVE size of  $63 \mu\text{m} \times 63 \mu\text{m}$ . Overall, it can be seen that Young's modulus has slightly effected by changing particles size. The models with particle number less than 15,000 particles show considerable diversion while models with dense particles converge well.

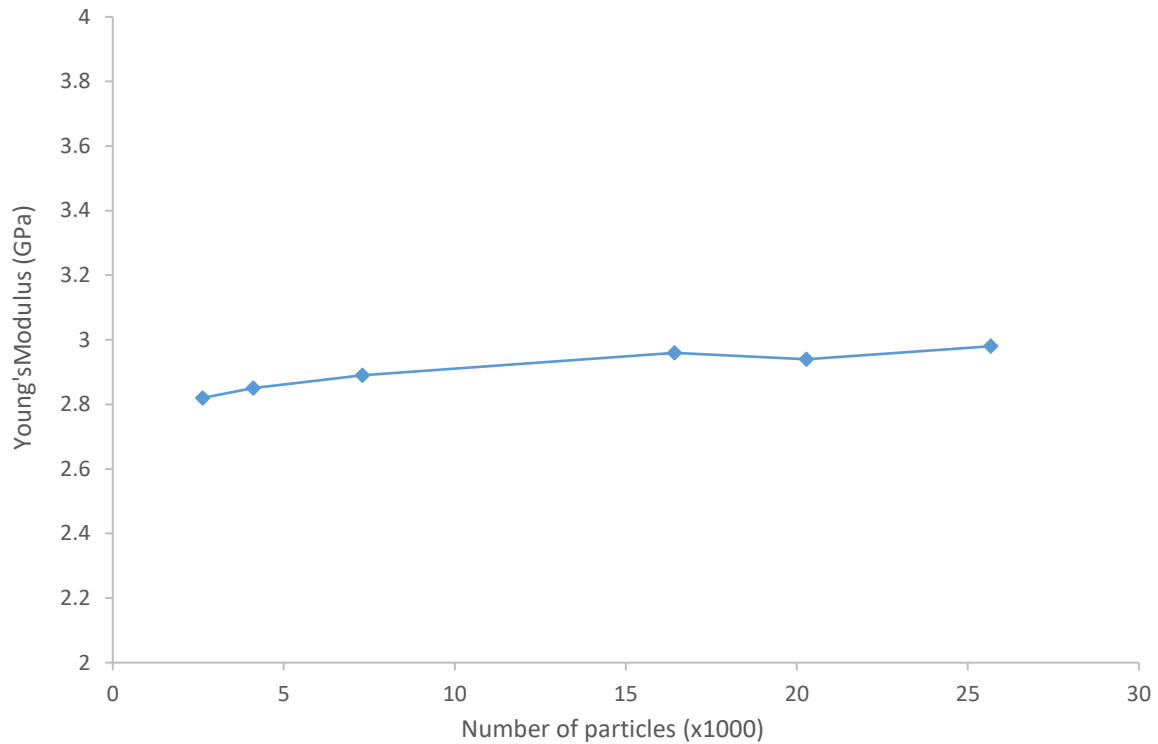


Figure 4.6: DEM predictions of matrix Young's modulus using different number of particles.

The effect of particle size on Poisson's ratio is also considered and shown in Figure 4.7. Poisson's ratio is fluctuated with particles size and ranges from 0.27-0.29. The elastic mechanical properties predicted in this section are different from those in previous section this due to altering particles packing arrangement.

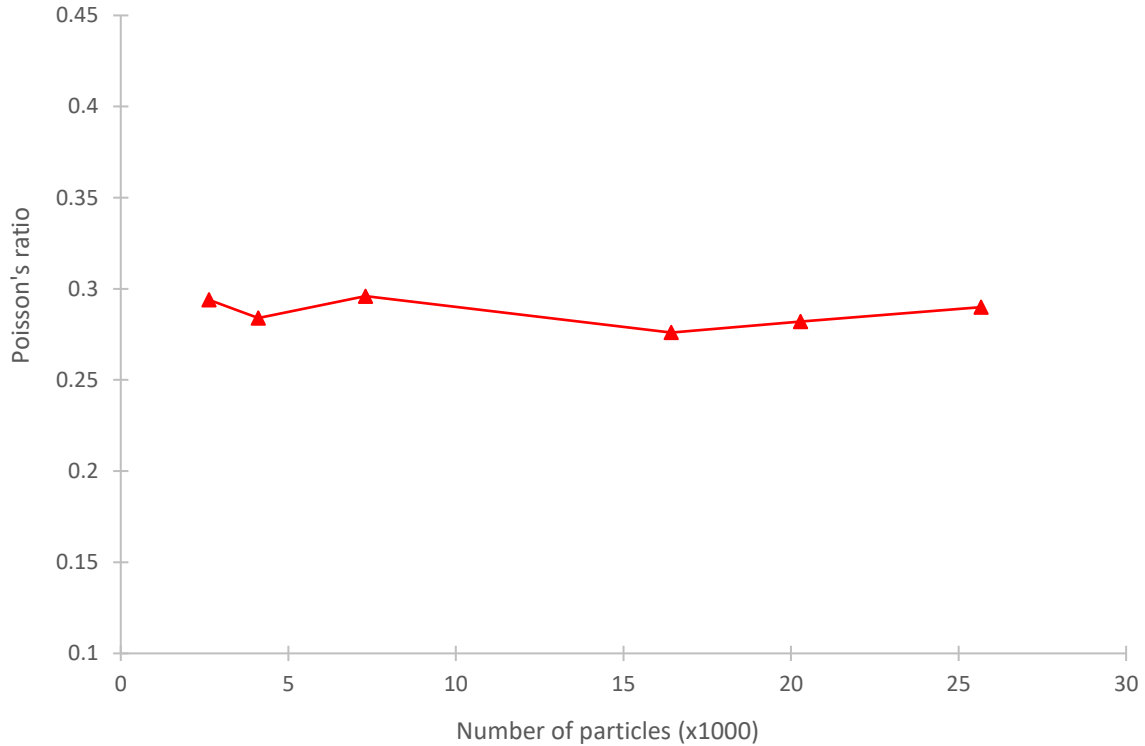


Figure 4.7: DEM predictions of matrix Poisson's ratio using different number of particles.

## 4.5 Results and comparison of methods

### 4.5.1 Effect of volume fraction on the elastic properties

After presenting the different numerical and analytical methods to estimate the elastic properties of composite materials, a comparison of estimates is then performed. The material used here is E-glass fibre with MY750/HY917/DY063 epoxy matrix, with constituents properties are given in Table 2.2. A typical RVE of DEM model under transverse compression and transverse shear is illustrated in Figure 4.8. As can be seen, the RVE consists of three phases, *i.e.*, matrix, fibre and interface. Micro parameters of matrix and fibres are calibrated in the previous section and given in Table 4.2. Micro parameters of interface are assumed to be same as those of the fibres. Regarding the size of RVE, González and LLorca ([González and LLorca, 2007a](#)) have suggested that an RVE size of  $63 \mu\text{m} \times 63 \mu\text{m}$  is adequate to represent the macroscopic material. This suggestion is adopted first and the effective elastic

properties are then computed for a range of volume fraction from 45% to 65% as shown in Figure 4.9-4.11. The figures also include results of two analytical methods, Voigt and Mori-Tanaka, and FEM of two unit cells using a square and hexagonal periodic fibre distribution (as explained Figure 4.1). The experimental data given in Table 4.4 are also plotted on the figures after converted to plane strain using Eqs. (4.9) and (4.10).

It can be seen that the transverse Young's modulus and shear modulus predicted by DEM model are well agree with FEM and Mori-Tanaka for volume fraction less than 55%. However, DEM model has slightly overestimate the moduli properties for volume fraction greater than 55%. The most obvious difference in estimating moduli properties can be seen between DEM model and Voigt model. On the other hand, the results of DEM provide very close estimation of Young's and shear modulus comparing with experimental data. This outcome is expected as numerical methods are taking into account the geometry of the microstructure, and thus there results must be more accurate.

Finally, results discrepancies between all models were very notable in the prediction of Poisson's ratio. From an overview of the results, It can be concluded that DEM, Voigt and FEM (square) are predicted the Poisson's ratio very well for volume fraction 60%. While other methods significantly overestimated it.

Table 4.4: Mechanical properties for E-glass/MY750.

	Experimental ( <a href="#">Soden et al., 1998b</a> )
$E_{22}$ (GPa)	16.2
$G_{23}$ (GPa)	5.7
$\nu_{23}$	0.4

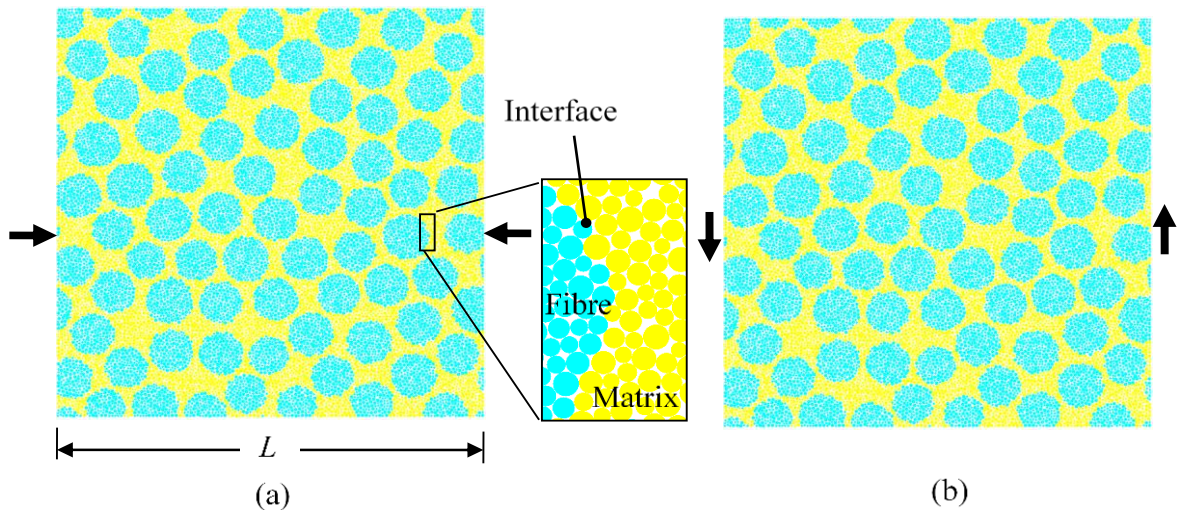


Figure 4.8: A RVE of DEM model subjected to: (a) transverse compression and (b) transverse shear (arrows indicate the loading directions).

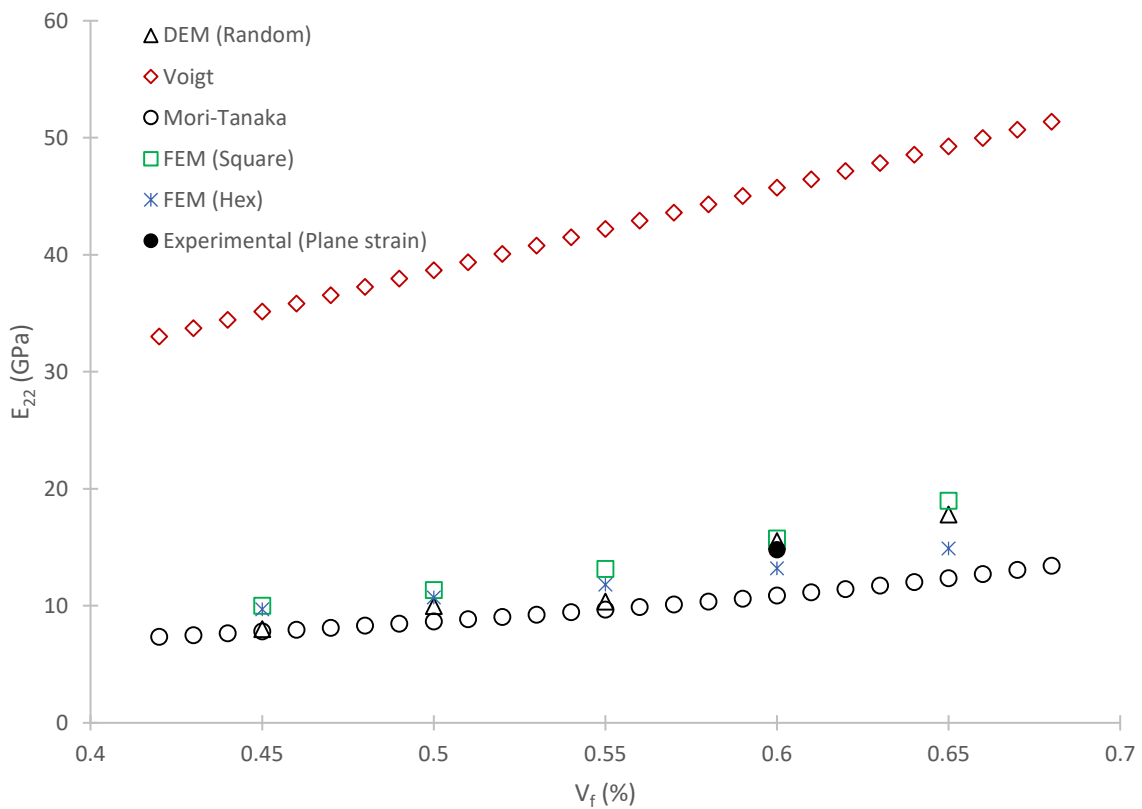


Figure 4.9: DEM predictions of transverse Young's modulus of different volume fraction compared to other analytical, numerical and experimental results ([Soden et al., 1998b](#)).

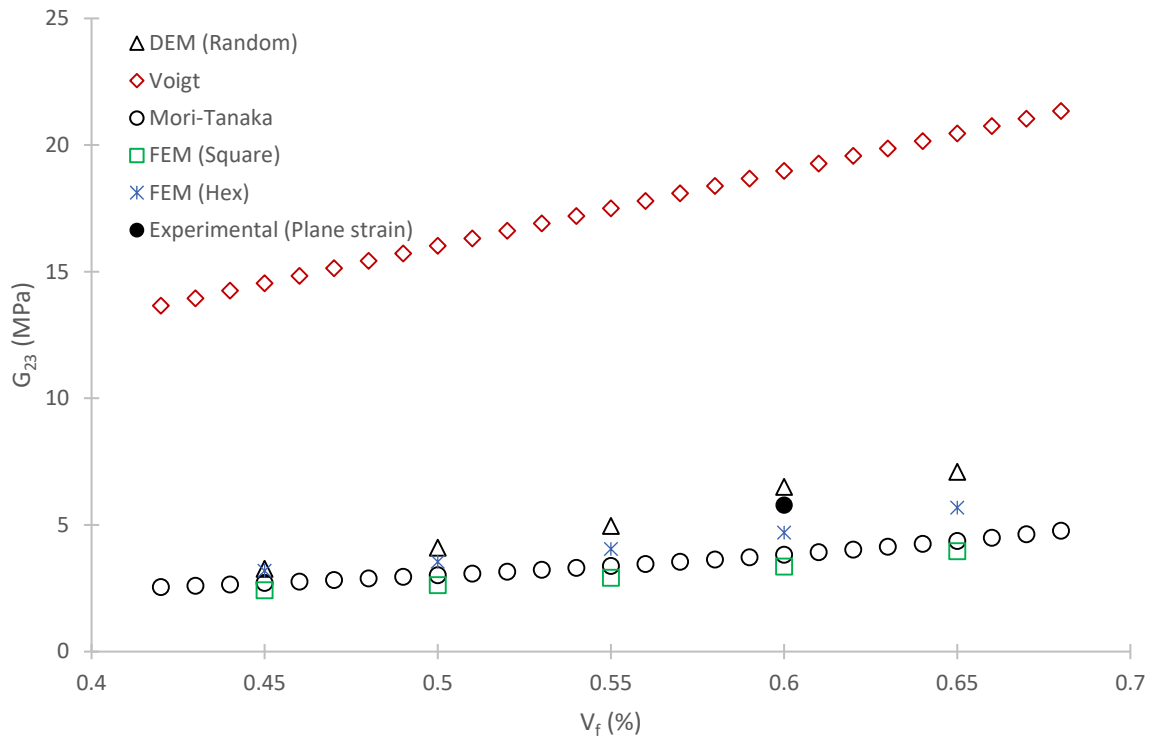


Figure 4.10: DEM predictions of transverse shear modulus of different volume fraction sizes compared to other analytical, numerical and experimental results (Soden et al., 1998b).

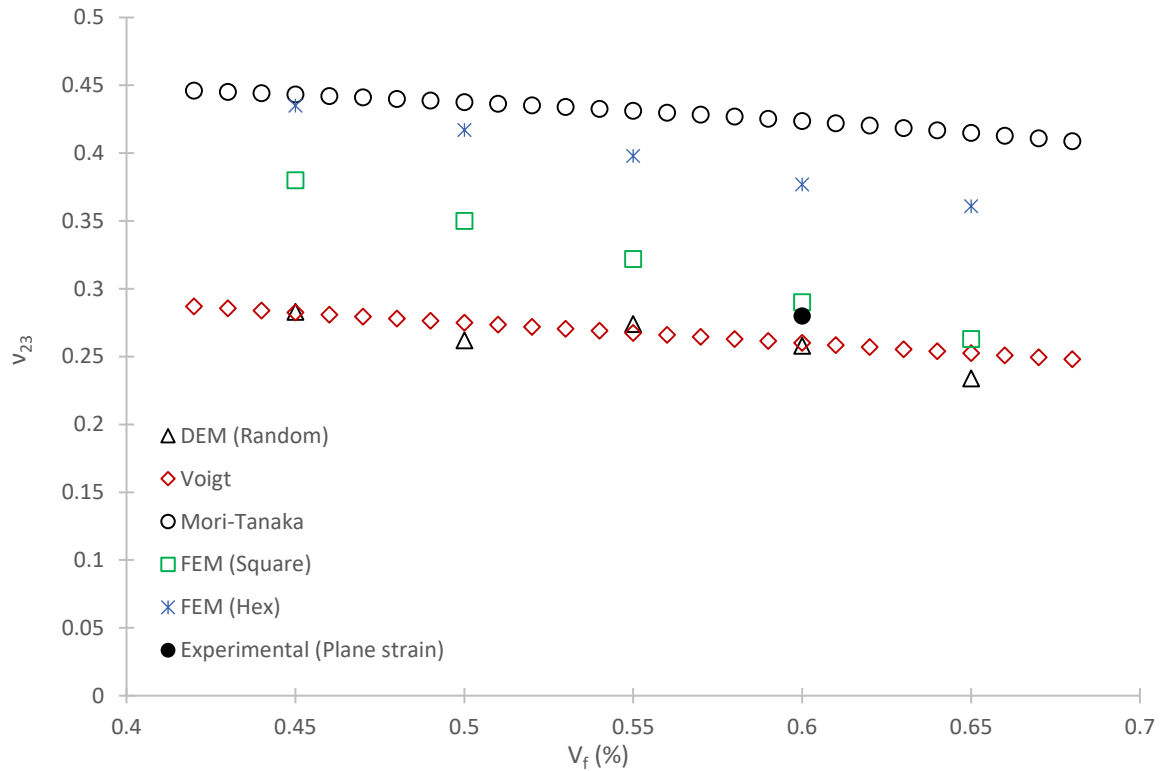


Figure 4.11: DEM predictions of transverse Poisson's ratio of different volume fraction compared to other analytical, numerical and experimental results (Soden et al., 1998b).

#### 4.5.2 Effect of RVE size on the elastic properties

To study the effect of the RVE on the three independent engineering elastic properties, six different RVE sizes range from  $30 \mu\text{m} \times 30 \mu\text{m}$  to  $100 \mu\text{m} \times 100 \mu\text{m}$  were selected. Identifying the smallest valid RVE is quite important as it helps to reduce DEM computational time. The same constituents were used in this analysis as previous section. The volume fraction and the inter-fibre distance between two neighbour fibres are kept constant in this section at 60% and  $0.8\mu\text{m}$  for all RVEs, respectively. Figure 4.12-Figure 4.14 show the elastic properties calculated using different RVE sizes. The RVE of each size is tested five times, and each time the RVE has a different random distribution of fibres. The secondary horizontal axis  $r_f$  on the top represents the relationship between the side length of RVE,  $L$ , and the mean fibre radius,  $r_f$ , as:  $r_f = L/r_f$ .

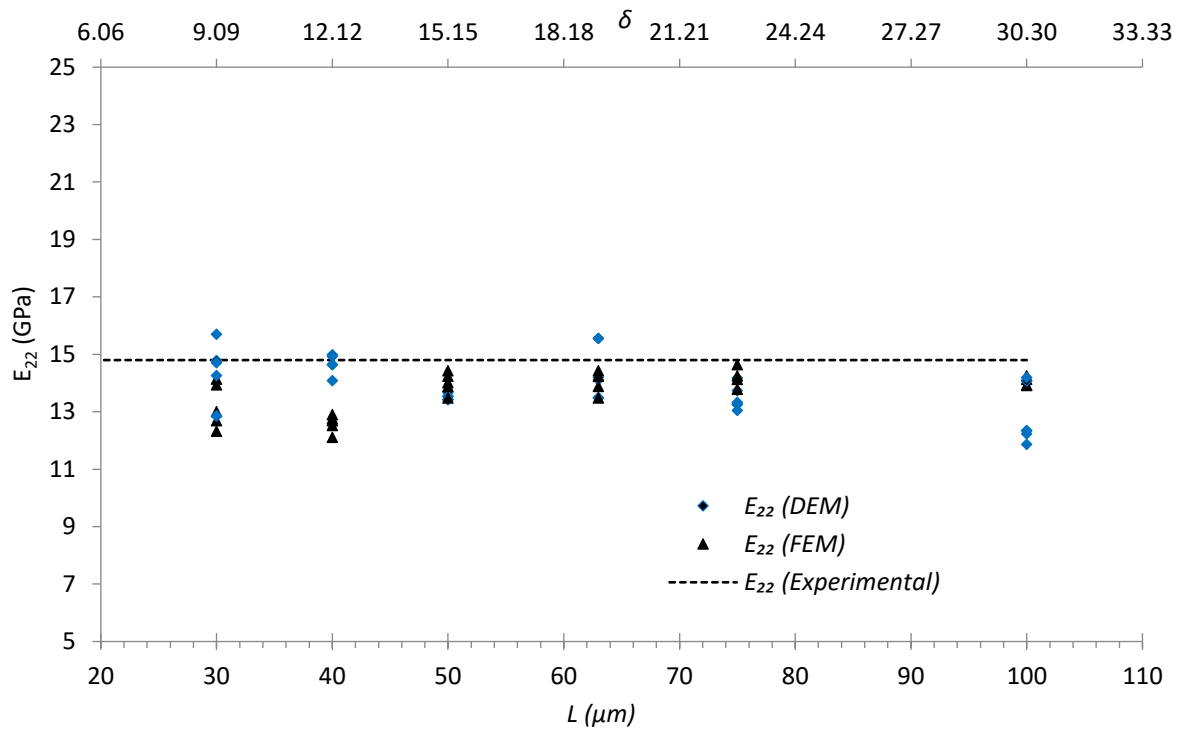


Figure 4.12: DEM predictions of Young's modulus of different RVE sizes compared to experimental results ([Soden et al., 1998b](#)).

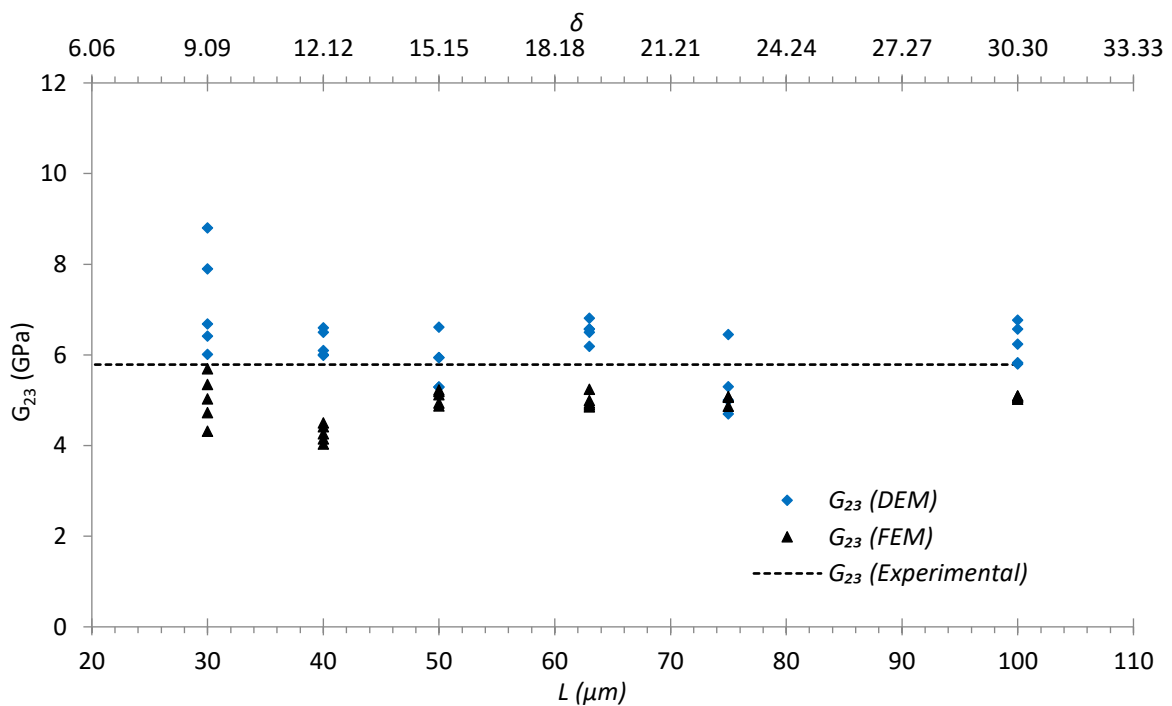


Figure 4.13: DEM predictions of shear modulus of different RVE sizes compared to experimental results ([Soden et al., 1998b](#)).

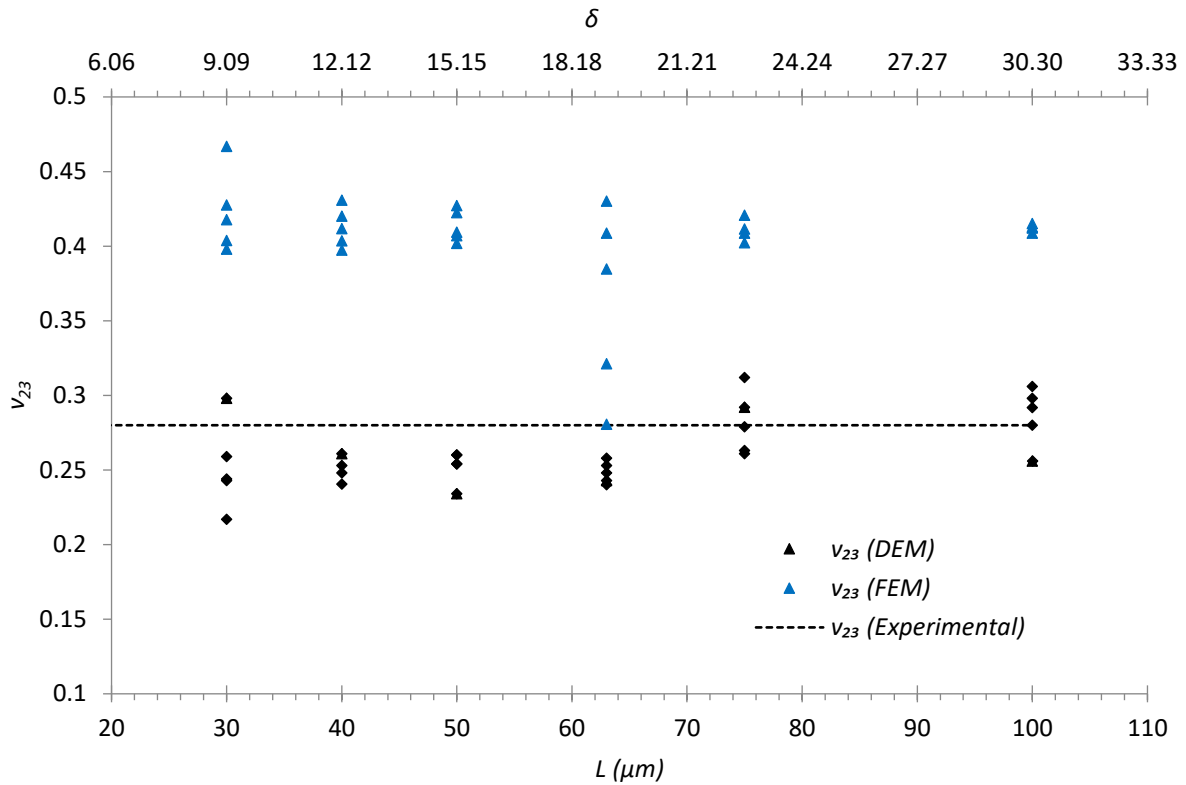


Figure 4.14: DEM predictions of Poisson's ratio of different RVE sizes compared to experimental results ([Soden et al., 1998b](#)).

As can be seen from the Figure 4.12 and Figure 4.13, both Young's modulus and shear modulus of the RVE with a size of  $63\mu\text{m} \times 63\mu\text{m}$  are close to the experimental results with little differences from one model to another. The discrepancy is likely caused by the change of fibre arrangements, which leads to increase or decrease of the number of contacts and particles representing the fibres, matrix and interface. However, the DEM model still gives good predictions of Young's modulus and shear modulus, compared with FEM using the same approach for generating random fibre distributions. In this study, the predicted Poisson's ratio, Figure 4.14, seems more sensitive to RVE size and the variation could reach 19%. Similar findings from other numerical models have also been reported. For instance, Wongsto and Li ([Wongsto and Li, 2005](#)) found that the predicted effective properties using various theoretical and numerical methods were smaller than the experimental data.

# Chapter 5

---

## 5 A DEM model for predicting fracture of composite lamina

In this present chapter, a two dimensional particle model based on the discrete element method (DEM) is developed for micromechanical modelling of fibre reinforced polymer (FRP) composite lamina under uniaxial transverse compression, transverse shear and biaxial transverse loads. Random fibre distribution within representative volume element (RVE) is considered for the micromechanical DEM simulations. In addition to predicting the stress-strain curves under transverse compression and transverse shear against the experimental results and other numerical methods, the model is able to capture the initiation and propagation of all micro damage events. Fibre distribution is found to have a significant influence on the ultimate failure of composite lamina under transverse shear, while it has much less effect in the case of transverse compression. The failure envelope of composite lamina under biaxial transverse compression and transverse shear is predicted and compared with Hashin and Puck failure criteria, showing a reasonable agreement. The predicted failure envelope is correlated with the damage evolution and the quantitative analysis of failure events, which improves the understanding of the failure mechanisms.

### **5.1 Introduction**

Despite the wide use of fibre-reinforced polymer (FRP) composite laminates over the past 30 years in the aerospace industry, and the great success that has resulted from the estimation of the elastic properties of these composites, there is yet no universal model or approach to predict accurately the failure strength of FRP composite laminates under biaxial or triaxial loads in real applications ([Kaddour and Hinton, 2013](#)). A large number of experimental tests need to be carried out to obtain the failure strength of FRP composite laminates, which are usually designed with a

strength that is much greater than required under real loading conditions. This means that in many cases FRP composites are over-safely designed and their advantages of light weight and design flexibility have not been maximised. In addition, experimental tests are affected by the testing environment and the results are very diverse, especially when materials are subjected to a system of loads, including transverse load that is very difficult to reproduce. Therefore, an accurate and universal approach for predicting the strength of FRP composite laminates is always highly in demand.

Generally composite laminates present five different failure mechanisms depending on the loading conditions ([Hinton et al., 2004](#)), as explained in Section 1.2. There are a few theoretical failure criteria available for predicting the failure modes separately as well as the failure envelope of composite lamina/laminates under different loading conditions. Among them, physically based phenomenological failure criteria ([Hashin, 1980](#), [Matzenmiller et al., 1995](#), [Puck and Schürmann, 2002](#), [Davila et al., 2005](#)) are capable of predicting accurately the failure envelope of composite lamina/laminates under certain loading conditions ([Kaddour and Hinton, 2013](#)). In particular, Puck's failure criteria are some of the best in the WWFE for predicting composite laminate failure. However, these criteria contain several non-physical parameters that need to be obtained from specific experimental tests, which makes their application quite difficult.

It has been shown that the predictions of failure strength under some loading conditions (in particular biaxial and triaxial loads) by existing failure criteria are not sufficiently accurate. One of the main reasons is that those criteria have not considered the effects of heterogeneous material microstructure and the interaction, as well as the progression, between different failure modes. In theoretical analysis it is not straightforward to correlate dynamically the different failure modes during the failure process as the random and heterogeneous microstructure of composite lamina/laminates are difficult to consider. Computational micromechanics is a useful tool to study the mechanical behaviour of FRP composite laminates and to understand their damage process and failure strength. Within the framework of micromechanical modelling, the macroscopic properties are obtained through a representative volume element (RVE) of the microstructure. As compared to conventional homogenisation techniques, micromechanical modelling can take into account the influence of the

geometry and spatial distribution of fibres and also compute the stress and strain microfields throughout the microstructure, leading to precise estimations of the onset and propagation of damage, and accurate predictions of the failure strength ([González and LLorca, 2007a](#)).

Apart from FEM modelling, the discrete element method (DEM) has been recently introduced in previous work to model the initiation and propagation of damage in composites. For instance, the crack propagation and stress-strain curves of composite materials under transverse tensile loading have been simulated by DEM ([Sheng et al., 2010](#)). It was concluded that DEM has the advantages of tracing the crack path within the microstructures in addition to predicting the final failure strength. Yang *et al.* ([Yang et al., 2011b](#), [Yang et al., 2011a](#)) also investigated the transverse cracks and delamination in cross-ply laminates and predicted the crack density using two-dimensional DEM. With the growth of computer power DEM becomes more beneficial to study crack propagation at the microscopic scale, even in three dimensions. For instance, Maheo *et al.*, ([Maheo et al., 2015](#)) used three-dimensional DEM to model the failure of a composite material under uniaxial tension.

## **5.2 Discrete element model to study the failure**

### **5.2.1 Parametric study of bond strength**

In order to enable the DEM model to predict the failure behaviour of a material, it is also necessary to correlate the local bond strength parameters to the DEM model's macro strength. Normally two failure modes are predominating in composite lamina under transverse loading, *i.e.*, matrix cracks and fibre/matrix debonding. The material used in this chapter is same as that in the previous chapters and the mechanical properties in given in Table 5.1. Mohr-Coulomb failure criterion has been widely used by to describe the plastic deformation of the epoxy matrix ([González and LLorca, 2007a](#), [Totry et al., 2008a](#), [Totry et al., 2010](#)), and is adopted to determine the strength of the parallel bonds for the matrix in the DEM model. When using the contact softening model to represent the fibre/matrix interface, both interfacial strength and fracture energy must be known. Unfortunately, these properties are difficult to obtain from simple laboratory experiments ([Ogihara and Koyanagi, 2010](#)). In this study, the

interfacial strength is assumed to be equal to the cohesion of the matrix,  $c$ , and according to the Mohr-Coulomb failure criterion the relationship between the cohesion and matrix strength is given by:

$$c = Y_{mc} \frac{1 - \sin \varphi}{2 \cos \varphi} \quad (5.1)$$

here  $\varphi$  is the friction angle and can be related to the fracture surface angle  $\xi$  by:

$$\xi = 45 + \varphi/2 \quad (5.2)$$

Typically  $50^\circ < \xi < 60^\circ$  is found for epoxy matrices ([González and LLorca, 2007a](#)), and thus  $\varphi$  is between  $10^\circ$  and  $30^\circ$ . Assuming  $\varphi = 23^\circ$  gives a cohesion  $c$  of 39.7 MPa. Wang and Tonon ([Wang and Tonon, 2010](#)) found that micro tensile strength of the bond directly determines the strength of material regardless the magnitude of bond shear strength. Therefore, for simplicity  $\bar{\sigma}_c = \bar{\tau}_c$  is assumed. Then a series of uniaxial compression tests are carried out with different bond strength values to find the relationship between bond strength and material strength, as shown in Figure 5.1. The macro strength of the DEM model is the maximum value of axial stress acting on the walls at peak load. Figure 5.1 indicates that macro strength increases linearly with the bond strength. At this stage, the smallest timestep  $\Delta t_1$  is used. The effect of timestep on macro compressive strength is studied in the next section.

Table 5.1: Mechanical properties of fibre and matrix.

Fibre	Transverse modulus, $E_f$ (GPa)	74
	Poisson's ratio, $\nu_f$	0.2
Matrix	Modulus, $E_m$ (GPa)	3.35
	Shear Modulus, $G_m$ (GPa)	1.24
	Poisson's ratio, $\nu_m$	0.35
	Compressive strength, $Y_{mc}$ (MPa)	120
	Tensile strength, $Y_{mt}$ (MPa)	80

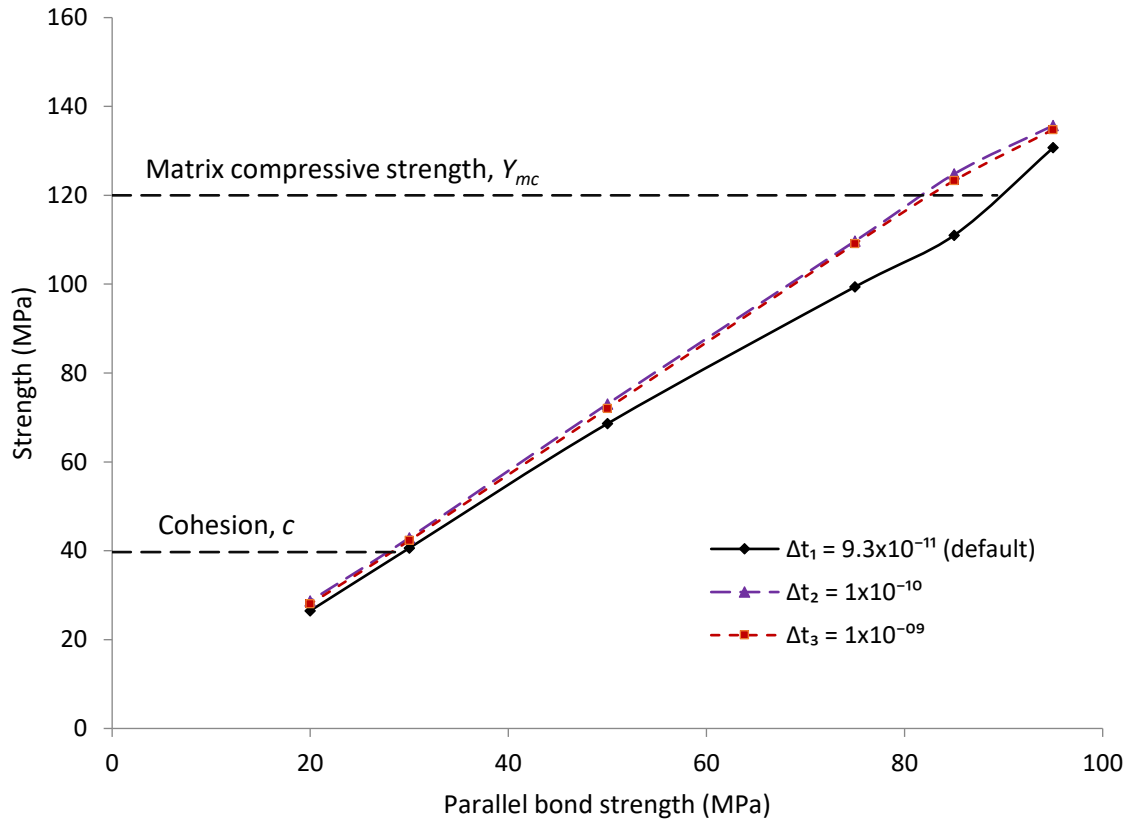


Figure 5.1: Influence of bond strength and timestep on the macro compressive strength of a DEM model.

### 5.2.2 Parametric study of timestep

An important consideration in the DEM modelling is the timestep. DEM uses a central difference time integration approach to solve the equations of particle motion, and to maintain a stable integration the timestep must not exceed the critical timestep  $\Delta t_{crit}$ :

$$\Delta t_{crit} < \sqrt{m/K} \quad (5.3)$$

where  $K$  is the contact stiffness and  $m$  is the particle mass. Choosing a suitable timestep is of particular importance because it has direct effect on the total computational time. The effect of timestep on the macro strength is therefore investigated, trying to find a large but still valid timestep and thus reduce the computational time. Three values of timestep are chosen,  $\Delta t_1 = 9.3 \times 10^{-11}$ s,  $\Delta t_2 =$

$1 \times 10^{-10}$  s and  $\Delta t_3 = 1 \times 10^{-09}$ s. The first one is the default value calculated by the software itself ([ltasca, 2003](#)) based on mass of particles and contact stiffness according to Eq. (5.3). Note that, for all timesteps, the loading velocity is kept constant at 5 mm/s. Figure 5.1 shows the macro strength of the sample under these three different timesteps, with matrix compressive strength and cohesion also plotted. It is demonstrated that the strength values are almost identical for all timesteps for low bond strength. The two cases with  $\Delta t_2$  and  $\Delta t_3$  almost give the same strength while they are both diverted from  $\Delta t_1$  about 10% at bond strength of 85 MPa. Thus the choice of timestep needs to be further investigated by plotting out the complete stress-strain curves in the later section of modelling failure process.

### **5.2.3 Effect of particle size on the strength**

Particle size sensitivity test was also investigated in this thesis. Similar to what has been done in the previous chapter, six models with different particle size range from 2,628-25,667 particles are chosen. The contact and particle parameters are kept constant and equivalent to those for matrix listed in Table 4.2. Figure 5.2 shows that the variation of strength with particle size for the RVE size of  $63 \mu\text{m} \times 63 \mu\text{m}$ . It can be seen that the strength has considerably effected by number of particles. However, the strength has almost converged for dense models that contain than 15,000 particles.

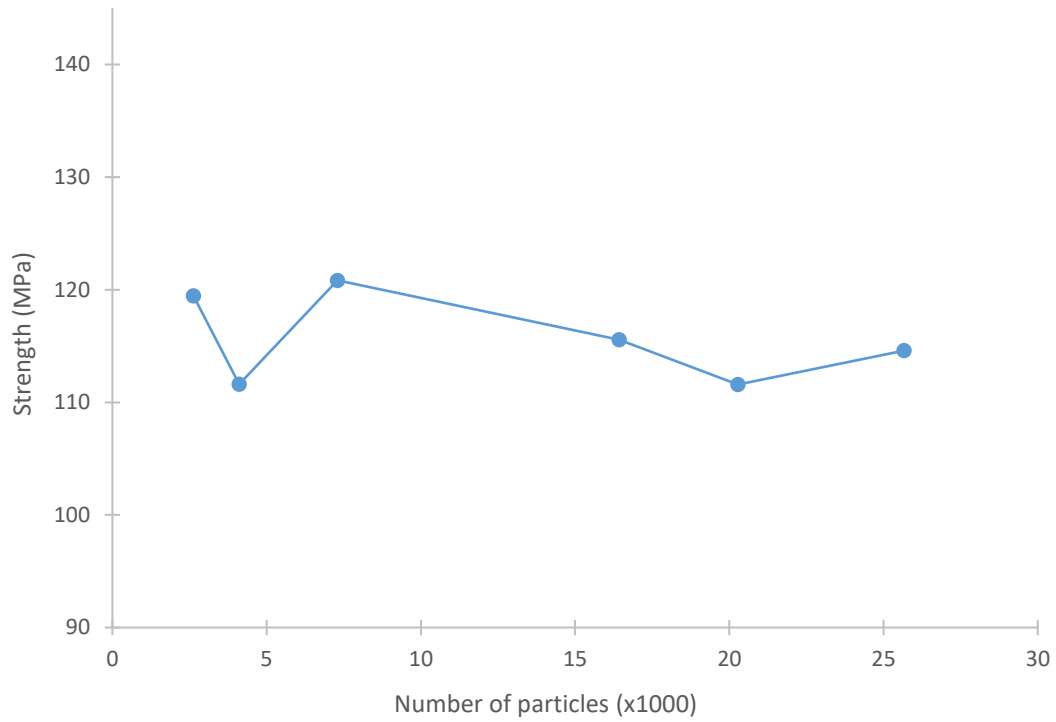


Figure 5.2: DEM predictions of strength using different number of particles.

The final fracture patterns for each case has also studies and plotted in Figure 5.3. It found that during early stage of loading, a few scattered cracks form and distribute throughout the model. These cracks are eventually integrated to form one or more inclined failure plane across the model.

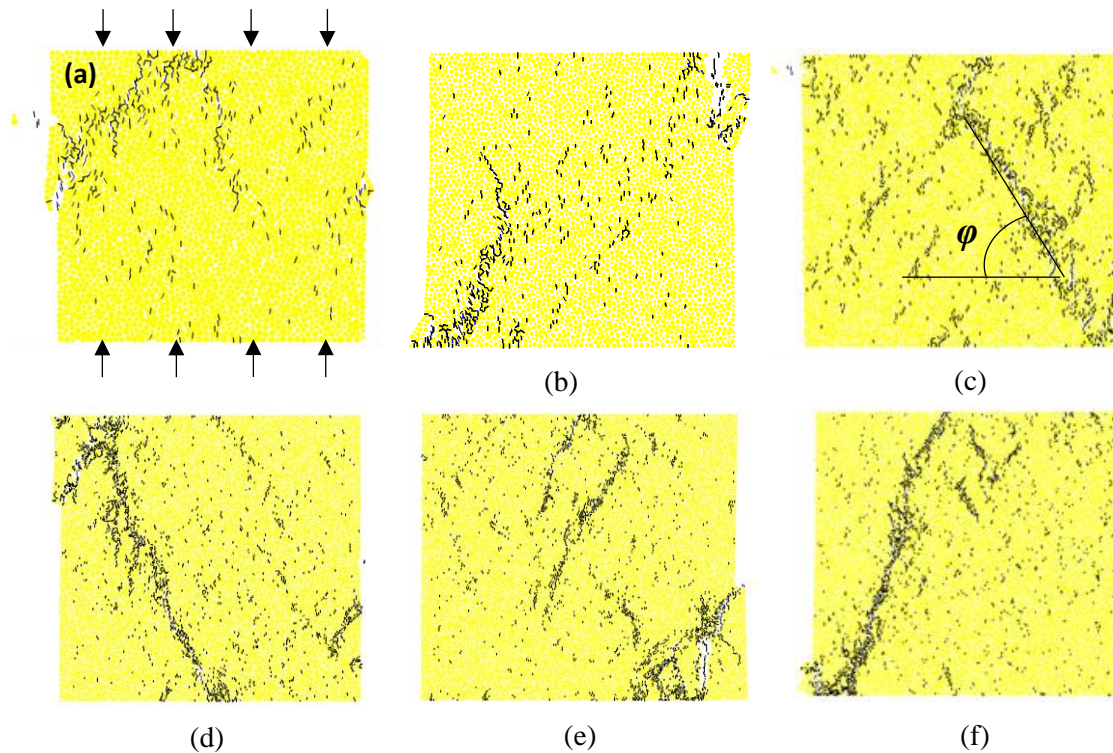


Figure 5.3: Crack patterns under uniaxial compression with different particles dense. (a) 2,628 particles. (b) 4,106. (c) 7,300. (d) 16,426. (e) 20,280. (f) 25,667.

#### **5.2.4 Prediction of stress-strain curves and damage progression under transverse compression**

In this section the failure of RVEs subjected to transverse compression is studied. The RVEs used in this section and next section have an identical size of  $63 \mu\text{m} \times 63 \mu\text{m}$ . The effect of timestep on the stress-strain curve of a typical RVE, which is of particular importance for saving computational time, is examined in Figure 5.4. Within the elastic region (under 20 MPa), the simulation results are almost identical and agree well with the experimental one. The final failure appears to become more brittle when timesteps are reduced, confirming that small timesteps lead to better redistribution of the stress within the system and the model is more stable. Also, as DEM is a dynamic method therefore higher strength is obtained with increasing strain rate applies on the sample (Gilat et al., 2002). For all the DEM simulations in Figure 5.4, the mean compressive strength is 156.3 MPa which is greater than experimental result by 7%. Therefore, the timestep of  $\Delta t = 1 \times 10^{-9} \text{s}$  will be used in later simulations. The nonlinear mechanical response of the stress-strain of the DEM model is not well captured comparing with experimental data. The nonlinear behaviour of the curve

would be more obvious in case of longitudinal shear and off-axis loading. However, the nonlinear contact law could be introduced in the future to solve the problem. While geometric nonlinearity (e.g. fibre rotation) is not important under transverse loading.

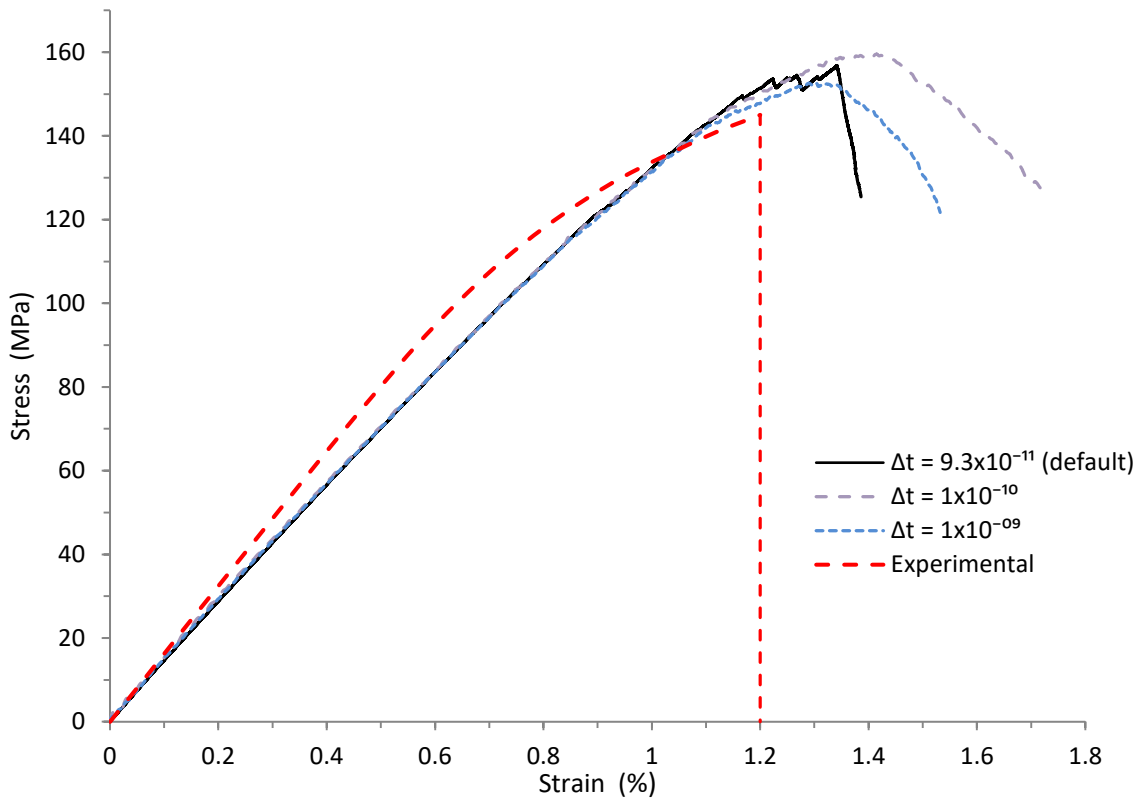


Figure 5.4: Stress-strain curves from DEM simulations using different timesteps compared to experimental results ([Soden et al., 1998b](#)).

The influence of fibres distribution in the RVEs on the mechanical response is also studied by comparing the results obtained from five different fibre arrangements. The stress-strain curves of all five RVEs under transverse compression are shown in Figure 5.5. It can be seen that the failure strength ranges from 151 MPa to 167 MPa giving the smallest and the largest differences of 4% and 14%, respectively, in comparison with the experimental results. An interesting outcome of using DEM is that the transverse compressive failure strains of the RVEs are also obtained whilst they have not been reasonably achieved in previous studies using FEM due to numerical convergence difficulties ([González and LLorca, 2007a](#), [Vaughan and McCarthy, 2011b](#), [Vaughan and McCarthy, 2011a](#)). To show the accuracy of the DEM modelling,

the results are also compared with two recent FEM models ([Yang et al., 2012](#), [González and LLorca, 2007a](#)) in Figure 5.5.

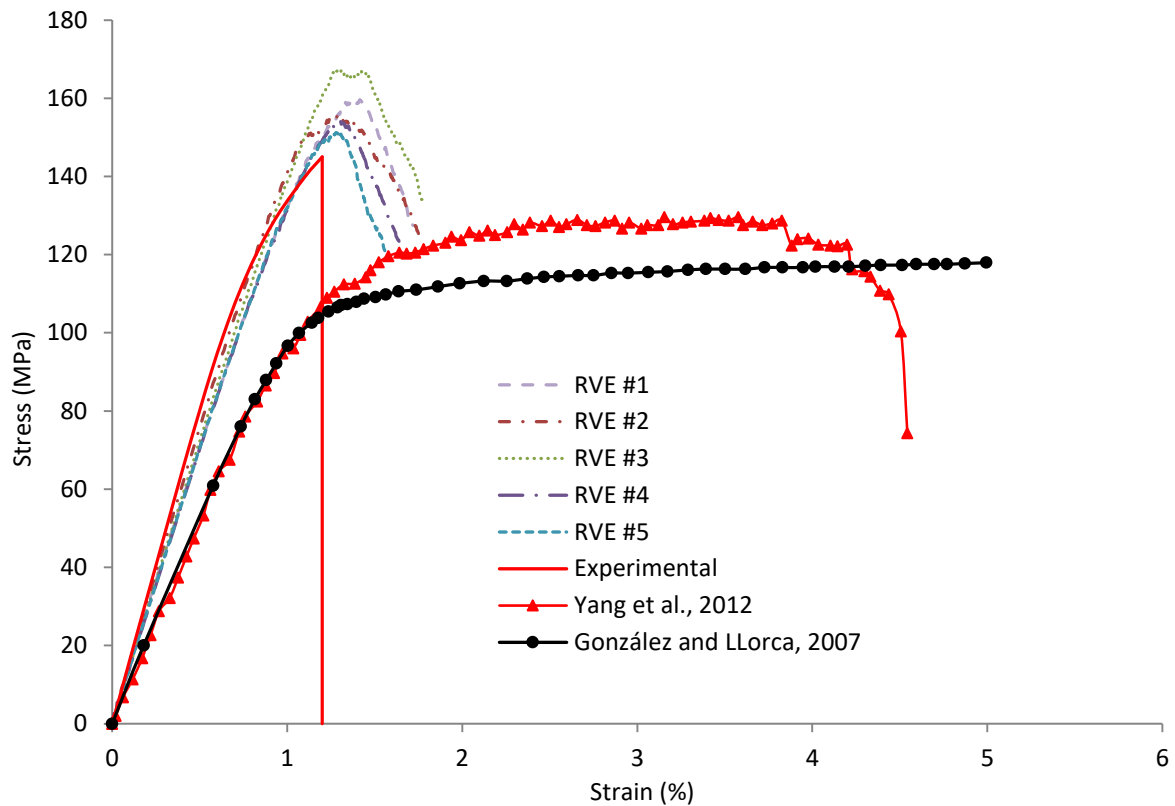


Figure 5.5: Stress–strain curves of five RVEs under uniaxial compression.

Another major feature of DEM modelling is its capability to predict and visualise the damage initiation and propagation process. Taking RVE #3 as an example, Figure 5.6 shows the damage progression in the composite under transverse compression, where a stress-strain curve and the damage profiles corresponding to the three characteristic loading points are also included. Point (a) in the stress-strain curve represents the state of a loading strain of 0.7% and its corresponding damage pattern is shown in Figure 5.6b. It can be seen that the fibre/matrix debonding (indicated by red dots) appears to be the major damage mechanism at this stage. After this point, the matrix cracks starts to appear, especially in the highly stressed areas where fibres are too close. The cracking leads to certain fluctuations in the stress-strain curve as indicated from the figure. Then, interfacial debonding and matrix cracks are emerged throughout the RVE before reaching the peak strength, as shown in Figure 5.6c. The

inclination angle  $\alpha_c$  of the critical plane is about  $53^\circ$  at this point, and it is a little smaller than the failure plane angle  $\xi=56.5^\circ$  calculated from Eq. (5.2).

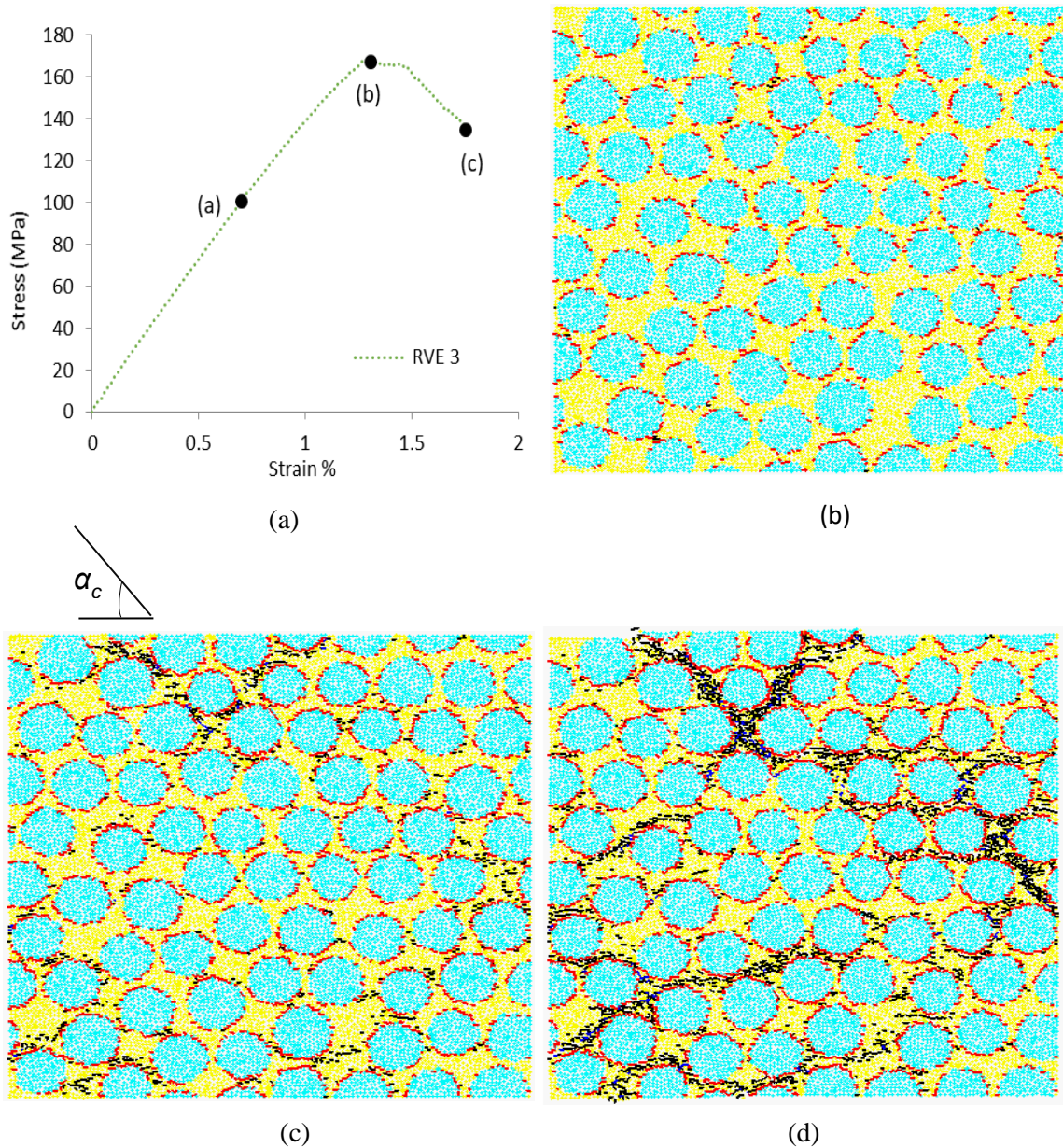


Figure 5.6: Damage evolution under transverse compression at different loading strains: (a) stress-strain of RVE #3 showing three characteristic loading points damage studied at (b) 0.7% (c) 1.3% (d) 1.7%. (Red dots are fibre/matrix debonding and black dots are matrix cracks).

Finally, more matrix cracks appear with further increase of loading and the final failure is shown in Figure 5.6d. From the last graph one can see that there are several possibilities for developing a critical plane across the RVE. The failure mode shown in

Figure 5.6d is similar to the final accumulated failure of the RVE in FEM when perfectly plastic matrix assumption is used ([Romanowicz, 2014](#)). However, it is quite different from those models using other failure criteria to represent matrix yielding, such as Mohr-Coulomb model ([González and LLorca, 2007a](#)) and Drucker-Prager ([Yang et al., 2012](#)).

### **5.2.5 Prediction of stress-strain curves and damage progression under transverse shear**

It is very difficult to carry out a laboratory test on a composite lamina/laminate under transverse shear. Finding a robust numerical method to simulate the test is then always beneficial, in particular, to capture the behaviour of the lamina until failure. Many factors could alter the damage behaviour of a lamina under transverse shear including fibre arrangements and fibre/matrix interface properties. Attempts have been made by researchers to find a relationship between the transverse shear strength and transverse compressive strength. Some researchers assumed the transverse shear strength,  $S_T$ , to be half of the compressive strength,  $Y_C$ , *i.e.*,  $S_T = 0.5 Y_C$  ([Davila et al., 2005](#)), where  $Y_C$  is the transverse compressive strength of the lamina. This is also adopted in this study. The transverse compressive strength of the lamina is 145 MPa (see experimental stress-strain curve in Figure 5.4), therefore, we assume that  $S_T = 72.5$  MPa.

The transverse shear of five different RVEs with different fibre distribution is modelled and the stress-strain curves are shown in Figure 5.7, along with the FEM results extracted from ([Romanowicz, 2014](#)) and ([Yang et al., 2015](#)) for comparisons. The figure shows that all the stress-strain curves from DEM modelling are almost identical and linear before reaching a loading stress of 35 MPa. A short line depicts the experimental initial shear modulus is also plotted. It is evident that the current simulation results are closer to the experimental shear modulus. After this point, the stress-strain curves of the RVEs start to divert from each other. This discrepancy is attributed to the development of micro-cracks that, similar to what was observed from the simulations of transverse compression described in the previous section, depends on the fibre distributions. The shear failure strength slightly varies for different fibre arrangements. In addition, for all the RVEs in Figure 5.7 the mean shear strength is

70 MPa, which is just slightly smaller than experimental result of  $S_T = 72.5$  MPa, and about 9% less than the strength predicted in (Romanowicz, 2014) and about 19% higher than that from (Yang et al., 2015).

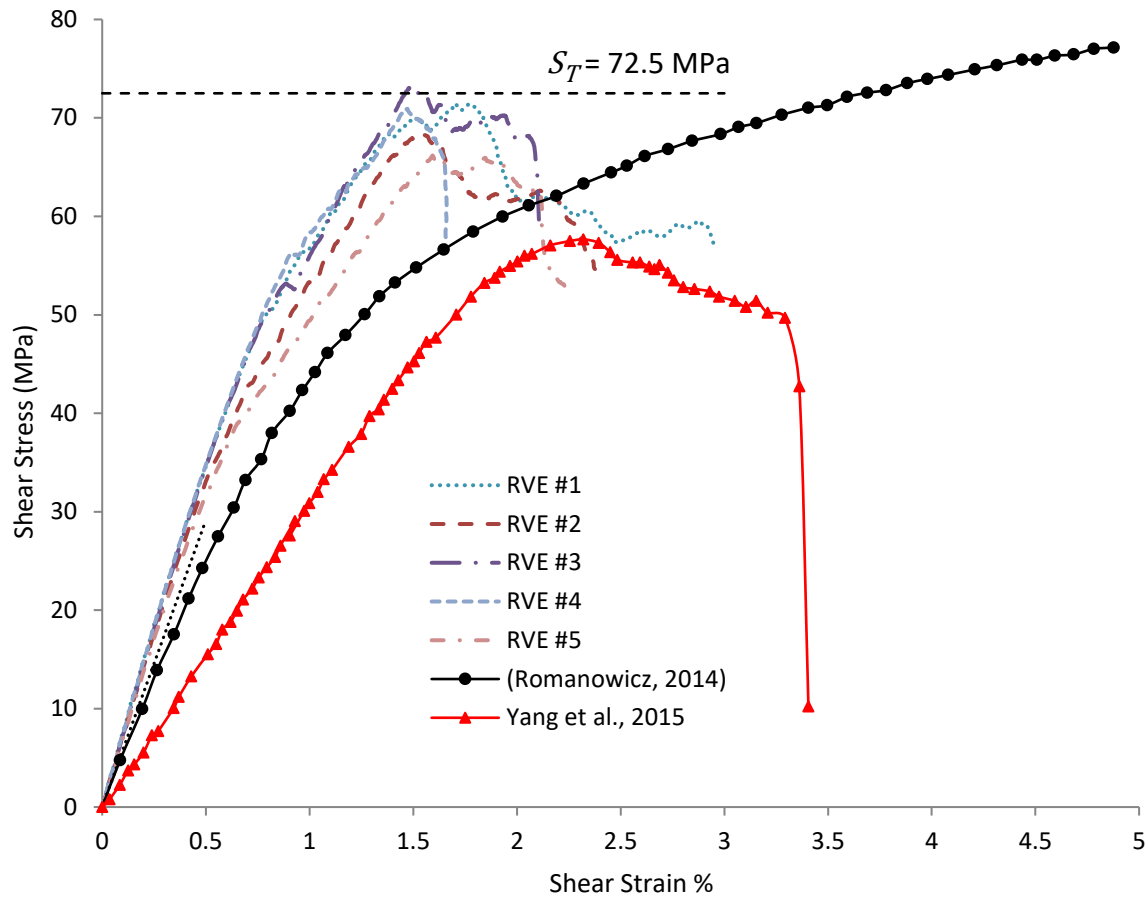


Figure 5.7: Transverse shear stress-strain curve using five different fibre arrangements compared with (Romanowicz, 2014) and (Yang et al., 2015)

While the stress-strain curve and damage evolution in RVE #3 under transverse shear is shown in Figure 5.8. The stress-strain curve drops at point (a) (Figure 5.8b) due to matrix cracking at the right-bottom of the RVE close to the edge. However, this crack does not propagate longer because it is constrained by the two surrounding fibres. After this point, more interfacial debonding occurs until the peak point (b), (see Figure 5.8c). Afterwards, matrix cracks appear mainly in the middle of the RVE and propagate fast and diagonally between fibres, leading to the ultimate failure at point (c), Figure 5.8d.

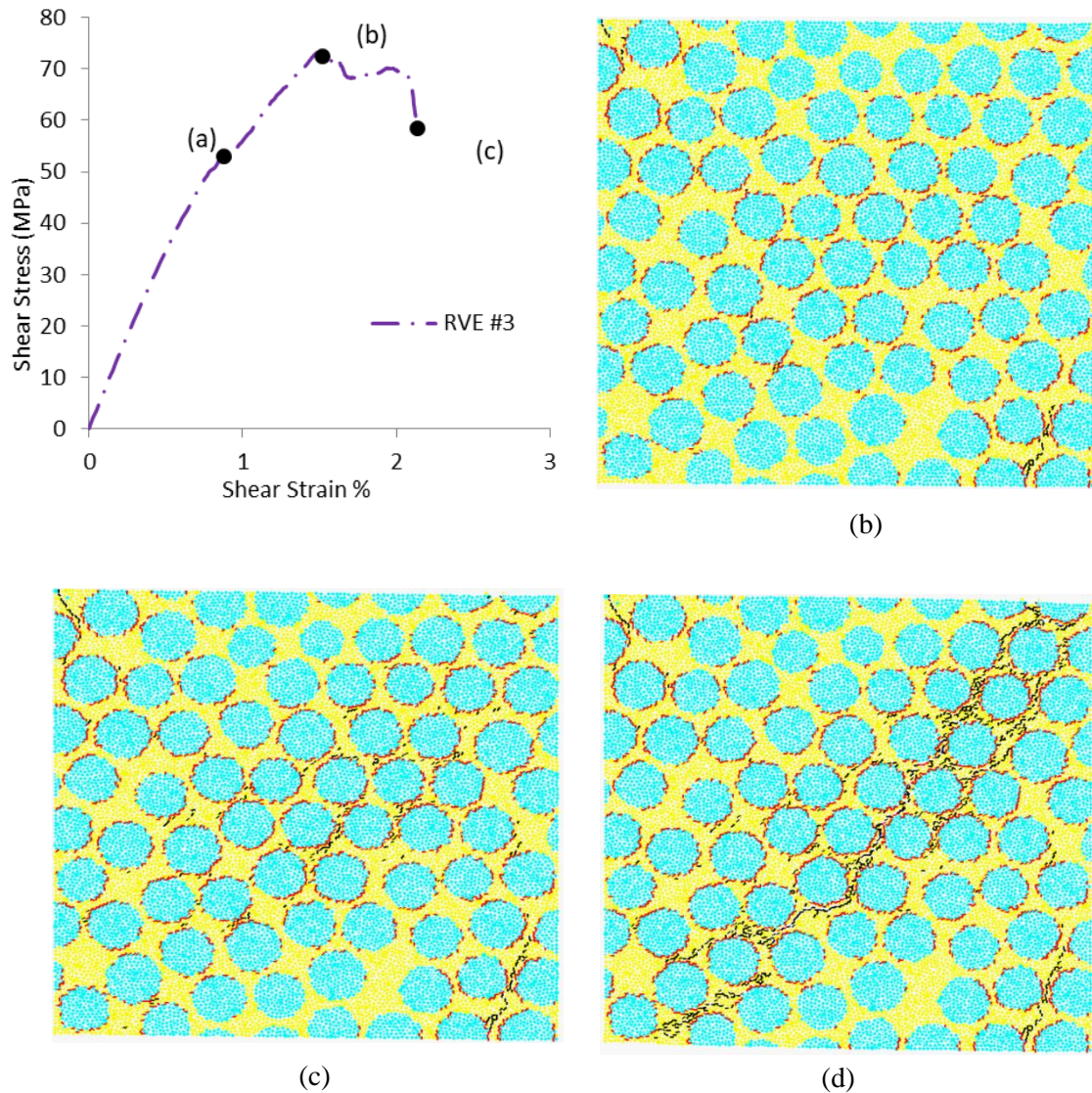
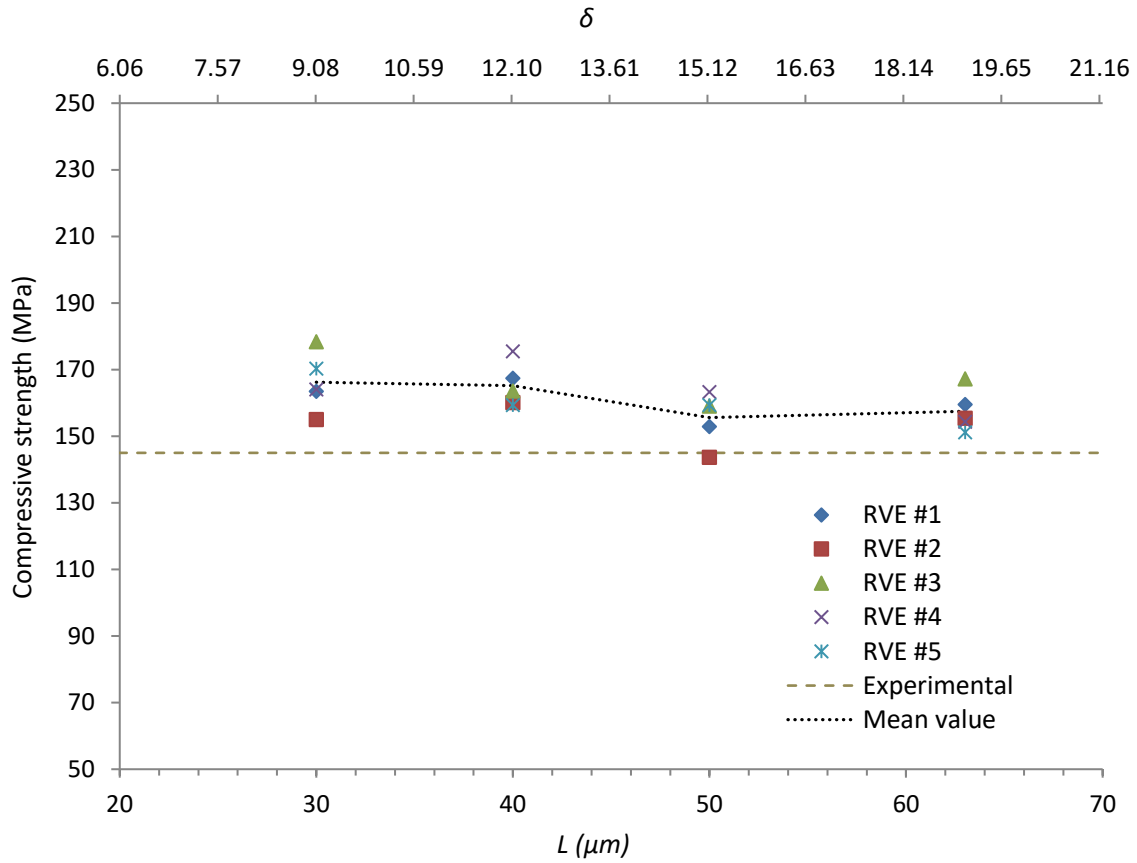


Figure 5.8: Damage evolution under transverse shear at different strain stages: (a) stress-strain of RVE #3 showing three characteristic loading points damage studied at (b) 0.87%, (c) 1.51%, and (d) 2.13%. (Red dots are fibre/matrix debonding and black dots are matrix cracks).

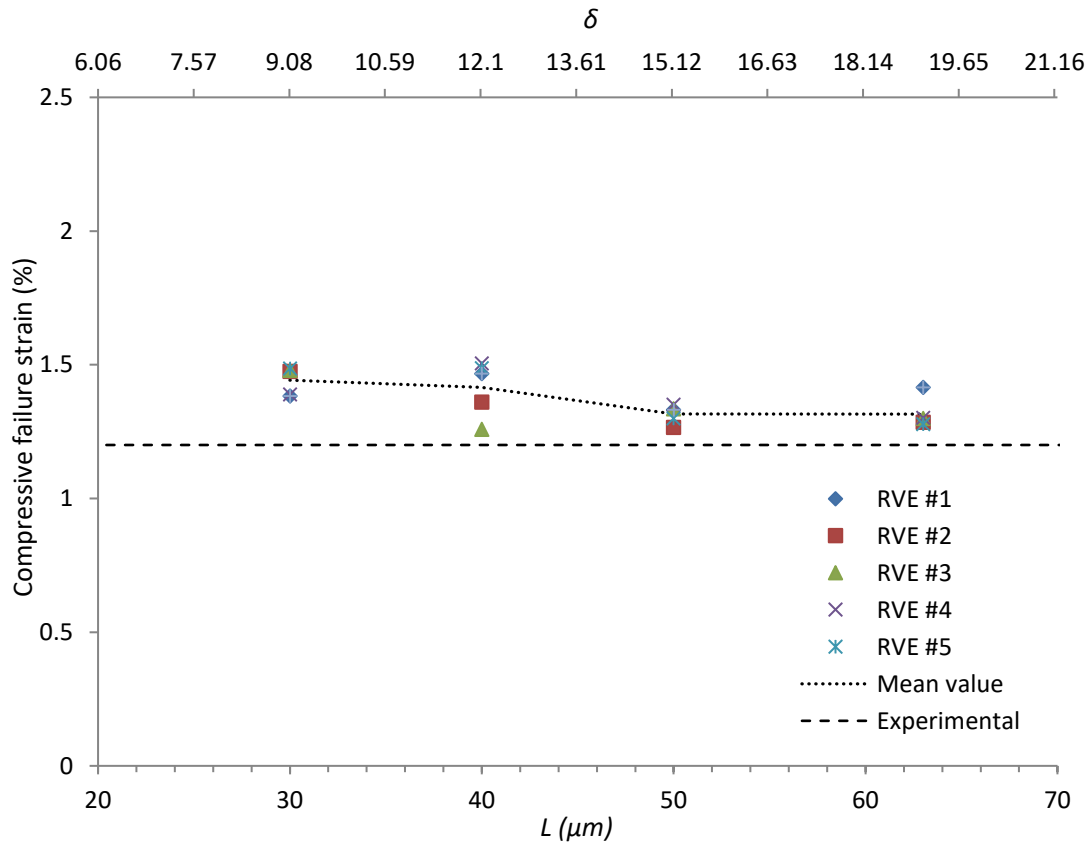
### 5.2.6 Effect of RVE size on failure strength and failure strain

As an attempt to reduce the computational cost, RVEs with sizes smaller than  $63 \mu\text{m} \times 63 \mu\text{m}$  are simulated. Variations of compressive strength for five different RVE sizes are shown in Figure 5.9a. The results show that the size of RVE has slight influences on the failure strength and there is no obvious trend of convergence for the RVE size. The smallest RVE of  $30 \mu\text{m} \times 30 \mu\text{m}$  is most diverted away from the experimental result, while the RVE of  $50 \mu\text{m} \times 50 \mu\text{m}$ , has a mean compressive

strength closer to the experimental result than  $63 \mu\text{m} \times 63 \mu\text{m}$ . Figure 5.9b shows the failure strains for the RVEs of different sizes. The overall trend of results tends to be higher than the experimental one and the smallest RVE has the largest difference.



(a)



(b)

Figure 5.9: Variation of compressive strengths and transverse compressive failure strains with RVE size, compared with experimental data (Soden et al., 1998b): (a) compressive strengths, and (b) transverse compressive failure strains.

Figure 5.10 shows the variation of transverse shear strength with RVE sizes. As can be seen from the figure, the mean values of shear strength of the five RVEs show fluctuations rather than clear convergence towards  $S_T = 0.5 Y_C$ , although the closest mean shear strength is from the largest RVE of  $63 \mu\text{m} \times 63 \mu\text{m}$ . In summary, the RVEs of  $63 \mu\text{m} \times 63 \mu\text{m}$  give overall better predictions of failure strength and failure strains, and this further confirms an RVE size of  $63 \mu\text{m} \times 63 \mu\text{m}$  should be used in the next sections of DEM simulations of biaxial loading.

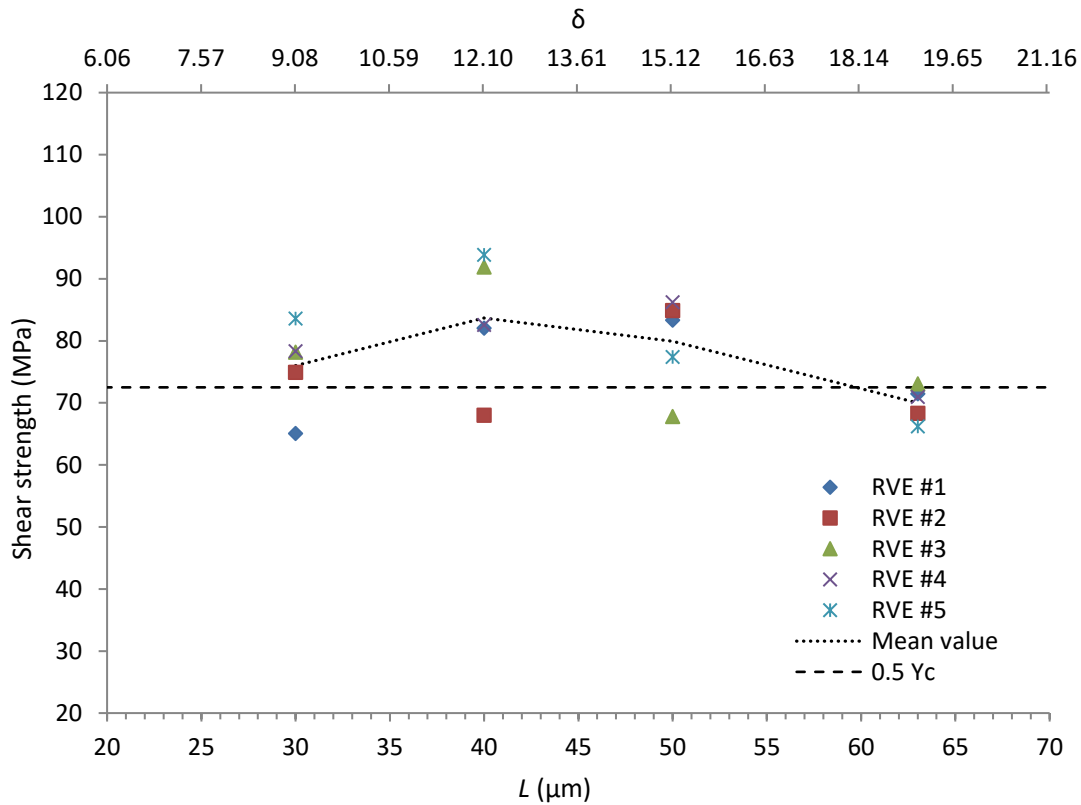


Figure 5.10: Transverse shear strength of RVEs with different sizes.

### 5.3 DEM modelling of RVEs under biaxial loads

The ultimate goal of this chapter is to visualise the damage evolution and predict the failure envelop of composite lamina under biaxial loads. An accurate and reliable failure criteria have been pursued for the past few decades, and an effort has been made by the organisers of the first ([Hinton et al., 2004](#), [Soden et al., 1998a](#)) and second ([Kaddour and Hinton, 2013](#)) WWFE to compare the experimental results with the predictions from different failure criteria. 19 failure criteria were evaluated and ranked according to their capability to predict the stress-strain curves under different uniaxial loading as well as the failure envelope in a series of test cases including biaxial loading. The comparisons revealed that the predictions of many failure criteria varied considerably from experimental results. WWFE also highlighted the importance of capturing the progressive failure in composite laminates. Generally, it was found that most failure criterions performed well when damage initiates in a single ply followed intimately by the catastrophic failure, or brittle failure. However, most criterions were not accurate enough when noticeable nonlinearity occurred before the final

catastrophic failure. Therefore, it is important to develop a suitable numerical method to capture and visualise the entire process of damage initiation and progression in composite laminates.

### 5.3.1 DEM prediction of the failure envelope

For the purpose of modelling biaxial loads using DEM, the RVEs are subjected to a combination of transverse normal stress,  $\sigma_{22}$ , and transverse shear,  $\tau_{23}$ , to obtain  $\sigma_{22}$ - $\tau_{23}$  failure envelope. The RVEs have a size of  $63 \mu\text{m} \times 63 \mu\text{m}$ . The DEM results are compared with predictions from two theoretical criteria developed by Hashin ([Hashin, 1980](#)) and Puck and Schürmann ([Puck and Schürmann, 2002](#)). Assuming isotropic composite lamina in the  $y$ - $z$  (or 23) plane, the three dimensional Hashin failure theory in Eqs. (1.13) and (1.14) are reduced for two dimensional under combined transverse normal stress and transverse shear, respectively, as:

$$\left(\frac{\sigma_{22}}{Y_T}\right)^2 + \left(\frac{\tau_{23}}{S_{23}}\right)^2 = 1 \quad \sigma_{22} \geq 0 \quad (5.4)$$

$$\left(\frac{\sigma_{22}}{2S_{23}}\right)^2 + \left[\left(\frac{Y_C}{2S_{23}}\right)^2 - 1\right] \frac{\sigma_{22}}{Y_C} + \left(\frac{\tau_{23}}{S_{23}}\right)^2 = 1 \quad \sigma_{22} < 0 \quad (5.5)$$

The Puck model used in this section is given in Eqs. (1.15) and (1.16).

To use these two failure criteria, the material failure strengths are required. In this study, the input failure strengths are those obtained from DEM simulations of RVE #1, given in Table 5.2.

Table 5.2: Failure strength used in Hashin and Puck failure criteria.

$Y_C$ (MPa)	159.5
$Y_T$ (MPa)	35
$S_T$ (MPa)	71.5

For biaxial loading, there are certain possible loading paths. For example, the normal and shear loads may be applied proportionally at the same time, or the loading

could start by applying uniaxial compression until a required compressive stress, then transverse shear is applied while the compressive stress is kept constant, or vice versa. The effect of loading path on the failure envelope has been investigated experimentally in ([Vogler and Kyriakides, 1999](#)) and numerically using FEM in ([Hsu et al., 1999](#), [Totry et al., 2008b](#)), and all concluded that the loading path did not affect or change the failure envelope significantly. However, the influence of loading path in DEM modelling is not studied.

Two loading paths are used in this study to simulate a biaxial test in DEM, as shown in Figure 5.11. The first path (Figure 5.11a and b) is used to apply transverse tension and shear on the RVE, the results of which are shown in Part-A of Figure 5.12. Following the same procedure as described in Section 4.4.3 for the pure shear test, the particles on the right- and left-hand side edges of the RVE are taken as boundary particles that are subsequently subjected to a constant velocity tangent to the edges until the desired shear stress is reached. Once the target shear stress is reached, the unbalanced force of each particle on the boundary is replaced by an external force of equal magnitude but in the opposite direction, see Figure 5.11b. Finally, a velocity normal to the edge is taken by the right- and left-hand side boundary particles to apply transverse normal load until the final failure, as shown in Figure 5.11b. By varying the initial shear stress applied on the boundary particles, the failure envelope of Part-A in Figure 5.12 is constructed. The second loading process is used to simulate transverse compression and shear quadrant only, *i.e.*, Part-B in Figure 5.12. In this loading method, the right- and left-hand side walls act as loading platens and their horizontal moving velocity is controlled by a servo-mechanism to maintain a constant transverse compression stress, see Figure 5.11c. Then, a constant velocity is applied on the right and left boundary particles until the final shear failure, as shown in Figure 5.11d.

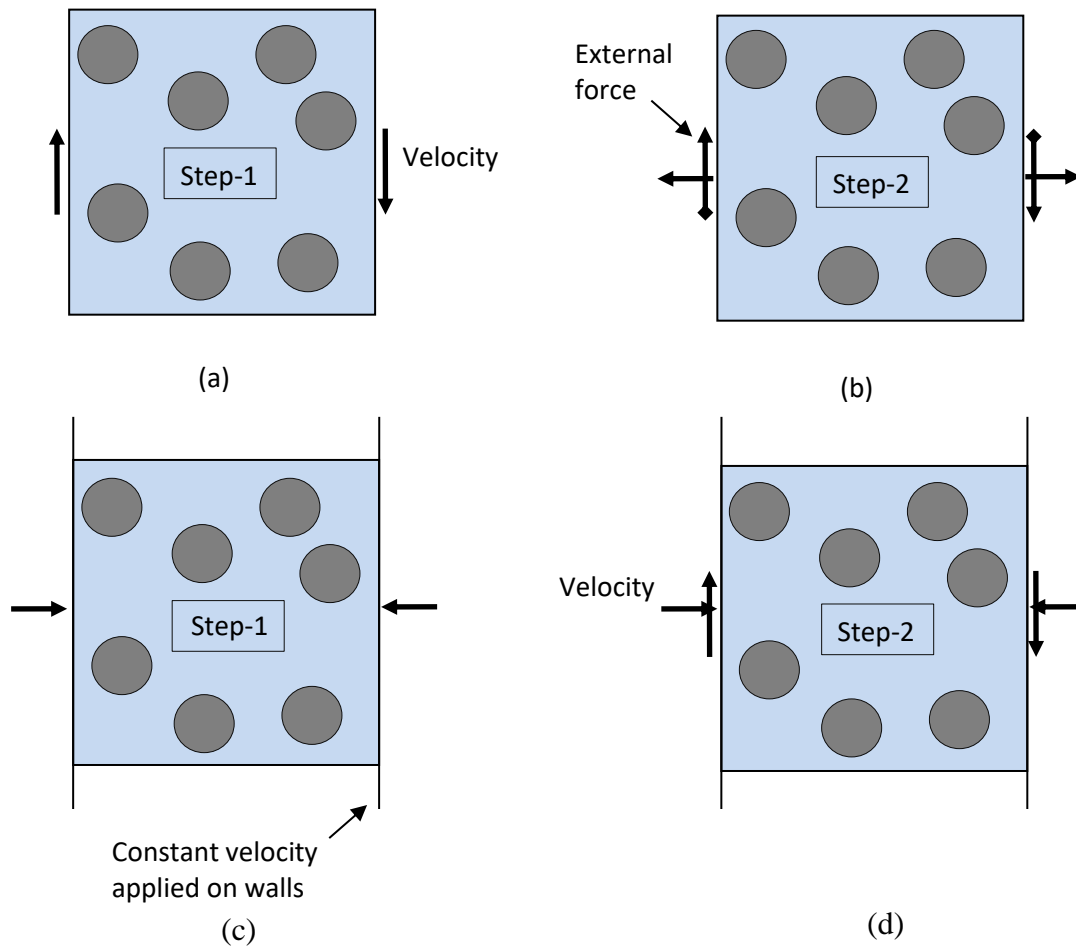


Figure 5.11: Loading schemes used to perform biaxial tests (arrows  $\leftrightarrow$  represent external force and arrows  $\rightarrow$  represent velocity applied): (a)-(b) shear and tension in Part-A, and (c)-(d) shear and compression in Part-B.

In the DEM simulations, the strength is the peak value on the stress-strain curve and the final failure takes place when the curve drops by 20% of the peak point, (e.g., point c in Figure 5.6a). The corresponding failure envelope is then generated and plotted in Figure 5.12 together with the predictions from Hashin ([Hashin, 1980](#)) and Puck and Schürmann ([Puck and Schürmann, 2002](#)) failure criteria.

It can be seen that the strength of the material predicted by DEM is generally lower than that predicted by the two failure criteria when the material is subjected to transverse tension and shear (in Part-A region), while it is higher when the material is subjected to transverse compression and shear (in Part-B region). This is expected since the current DEM modelling has considered residual strength attributed to any friction and contact between the fractured surfaces that occurs after a bond is broken.

The particle-particle interaction force depends on the friction coefficient as well as the stiffness of these two particles. Therefore, collectively the material can sustain more compression and shear and this leads to an increase of the ultimate failure strength of the RVE. The friction and sliding free contact behaviour clearly emerges only in presence of compression, which explains why a better comparison of the strength is observed in Part-A. In fact, the post-failure friction and contact behaviour in compression and/or shear is closer to physical tests whilst the analytical methods usually cannot take it into account. However, Puck's criterion was among the theories that performed well for predicting the strength of unidirectional lamina subjected to transverse normal stress and in-plane shear as compared with experimental results ([Soden et al., 2004](#)). In this study the criteria is further validated against our virtual modelling results for another type of biaxial loading scenario of transverse normal and transverse shear loading.

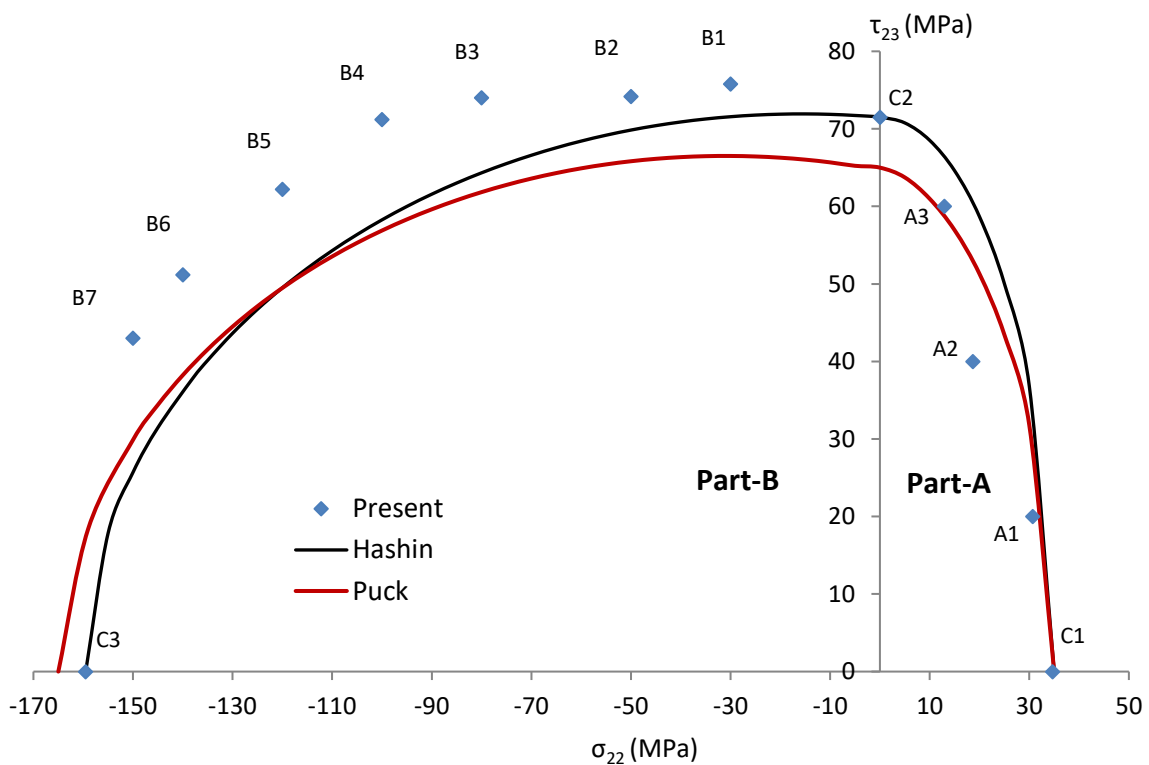


Figure 5.12: Failure envelope of a fibre-reinforced composite lamina in the  $\sigma_{22} - \tau_{23}$  stress space.

### 5.3.2 DEM visualisation of damage evolution

In Puck's model failure under transverse normal and transverse shear depends on the orientation of failure plane which in turn depends on the magnitude of the normal and shear stresses acting on the failure plane surface. Thus, it is important to investigate the final failure planes of a RVE. The crack paths discussed in this section is for RVE #1 under different loading combinations (or  $\tau_{23}/\sigma_{22}$  ratio) as shown in Figure 5.13. Each subfigure is associated with a loading combination along the failure envelope shown in Figure 5.12, such as C1, A1, A2, etc.

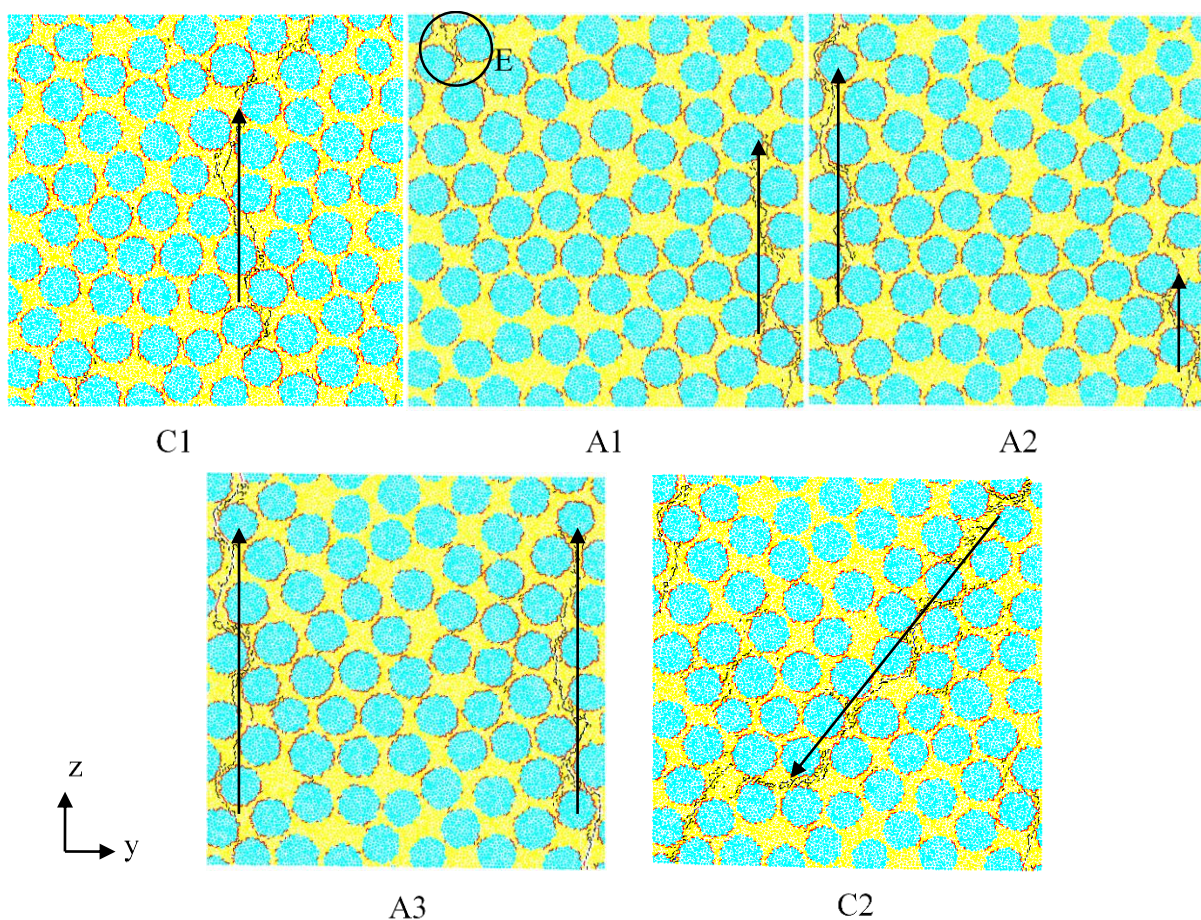


Figure 5.13: Accumulation of damages in the composite under different loading combinations in Part-A. (Each subfigure represents a data point on the failure envelope according to its label; Red dots represent fibre/matrix debonding and black dots represent matrix cracks.)

Figure 5.13C1, which is for the RVE under uniaxial transverse tension (point C1 in Figure 5.12), shows that the failure plane is found to be perpendicular to the loading axis and propagates between fibres in the middle of the RVE. After applying transverse shear (*i.e.*,  $\tau_{23}/\sigma_{22} = 2.1$  at A1), the failure plane is still about  $90^\circ$  but not literally in the middle, and another failure path also appears as shown by the circle 'E' in Figure 5.13A1. By increasing  $\tau_{23}/\sigma_{22}$  ratio to 2.13 and 4.63, it has been found that the second failure path propagates longer in the RVE and eventually two vertical crack paths present, as shown in Figure 5.13A2 and A3. Finally, the accumulated failure of the RVE subjected to pure transverse shear is plotted in Figure 5.13C2 where the plane angle is found to be around  $45^\circ$ , and the failure path is somehow diverted when fibres are present at the crack tip.

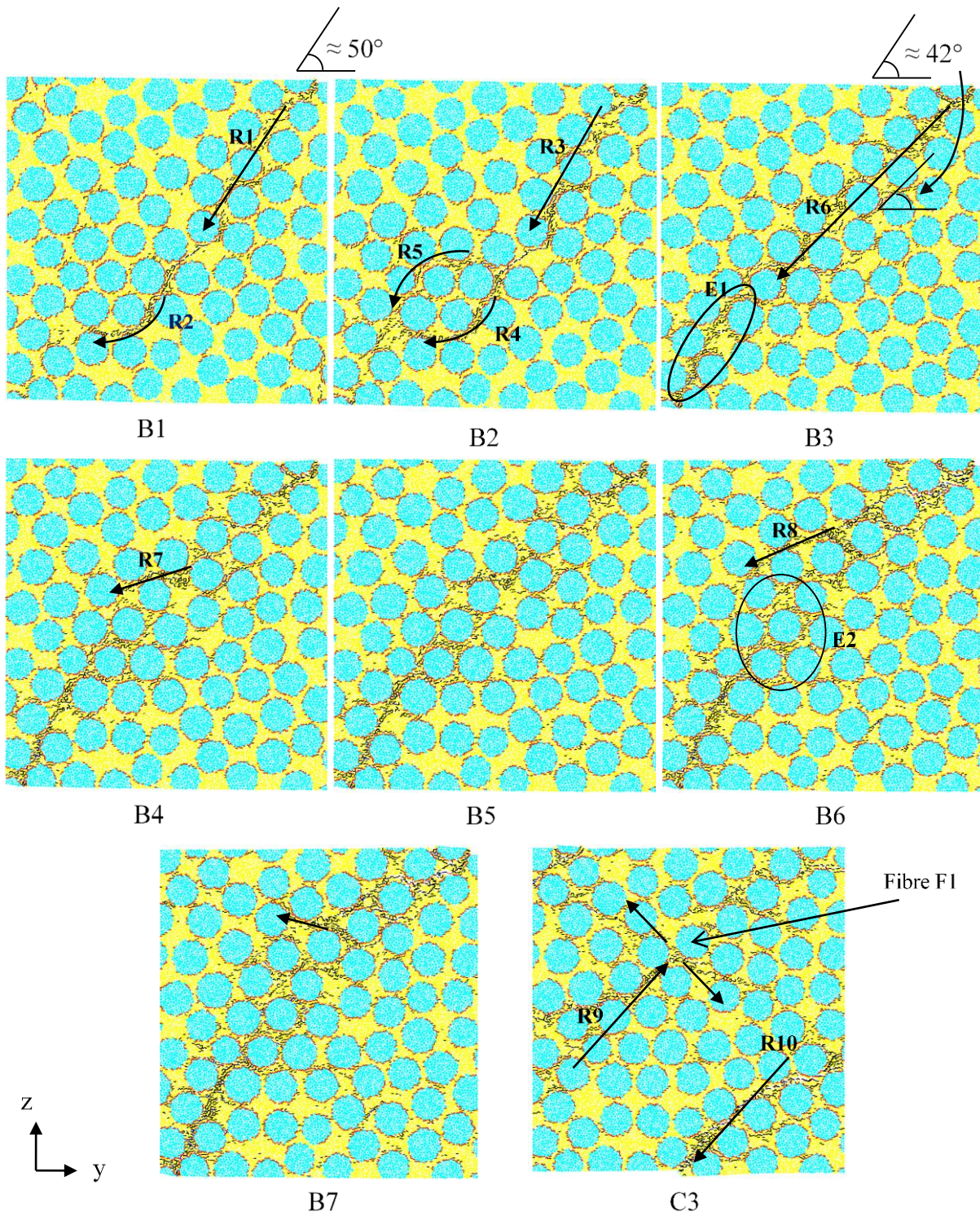


Figure 5.14: Accumulated cracks in the composite under different loading combinations. (Each subfigure represents a data point on the failure envelope according to its label; Red dots represent fibre/matrix debonding and black dots represent matrix cracks).

The accumulated cracks in the composite subjected to combined transverse shear and transverse compression as well as pure transverse compression (Part-B of Figure 5.12) are shown in Figure 5.14. Similar to what has been used above, each subfigure in Figure 5.14 is associated with one data point in Figure 5.12.

For low compression load (*i.e.*  $\tau_{23}/\sigma_{22} = 2.5$  or load case B1) in Figure 5.14B1, the critical failure plane is oriented at an angle of about  $50^\circ$  to the loading axis (*i.e.* y-axis), as indicated by the arrow R1. However, this fracture band cannot propagate through the fibres, the orientation alters slightly at the end and this variation is mainly caused by the fibre distribution, see arrow R2.

For smaller transverse shear and compression ratio, *i.e.*, point B2 in Figure 5.12, the initial fracture angle is almost the same as the previous case. However, another fracture band (which is indicated by the arrow R5) appears and follows the first one, see Figure 5.14B2.

In Figure 5.14B3, the orientation angle of fracture plane is reduced more to become about  $42^\circ$  and also more cracks take place just before the final failure as indicated by the elliptic E1. According to Eq. (1.19), the fracture angle decreases when  $\tau_{23}/\sigma_{22}$  is reduced, and this is confirmed by our DEM simulation results, *i.e.*, the fracture angle is reduced from  $50^\circ$  to  $42^\circ$  with increasing compression stress  $\sigma_{22}$ .

Failure patterns in Figure 5.14B4 and B5 are similar to that in Figure 5.14B3 except a new fracture path appears (indicated by the arrow R7) and has a small slope with y-axis.

Finally, it is found that with increasing transverse compression stress in Figure 5.14B6 and B7 more intensive cracks tend to occur between fibres which reduce the average fracture angle, In addition, more diverse crack paths appear (indicated by the arrow R8 in Figure 5.14B6) and the failure band becomes bigger than above cases.

The final failure of uniaxial compression stress is also included in and shown in the Figure 5.14C3. The damage evolution of this loading case is similar to the one that has already been discussed in Section 5.2.4. As can be seen from Figure 5.14C3, two main failure paths, R9 and R10, are present. The crack path R8 runs through the RVE

until it is constrained by fibre F1 and leads to new cracks occurring almost perpendicular to the initial path.

### **5.3.3 Quantitative analysis of damage events**

A quantitative analysis of fibre/matrix debondings and matrix cracks is also carried out for each loading case in Part-A and Part-B of Figure 5.12, and the results are plotted in Figure 5.15 and Figure 5.16, respectively. Each column of the figure shows the number of interfacial debonding and matrix cracks of the corresponding loading case in Figure 5.12. The matrix cracking includes both normal and shear breaking of bonds between the particles that represent the matrix. Columns labelled from A1 to A3 represent biaxial loads and are located in Part-A, whereas columns B1 to B7 are for those in Part-B and columns C1, C2 and C3 are for uniaxial transverse tension, shear and compression, respectively.

As shown in Figure 5.15 for the loading cases in Part-A, the number of fibre/matrix debondings is significantly high in the case of pure transverse tension (i.e., column C1) and more matrix cracks are found in transverse shear, (i.e., column C2). While for combined transverse tension and shear, fibre/matrix and matrix cracks number increase steadily with increasing ratio of  $\tau_{23}/\sigma_{22}$  from A1 to A3. It is important to mention that in all loading cases the fibre/matrix interfacial debonding is the main damage mechanism before the peak stress as the bond strength of the fibre/matrix interface is much smaller than that of the matrix. While the matrix cracks mostly happen after the ultimate stress and leads to the final failure.

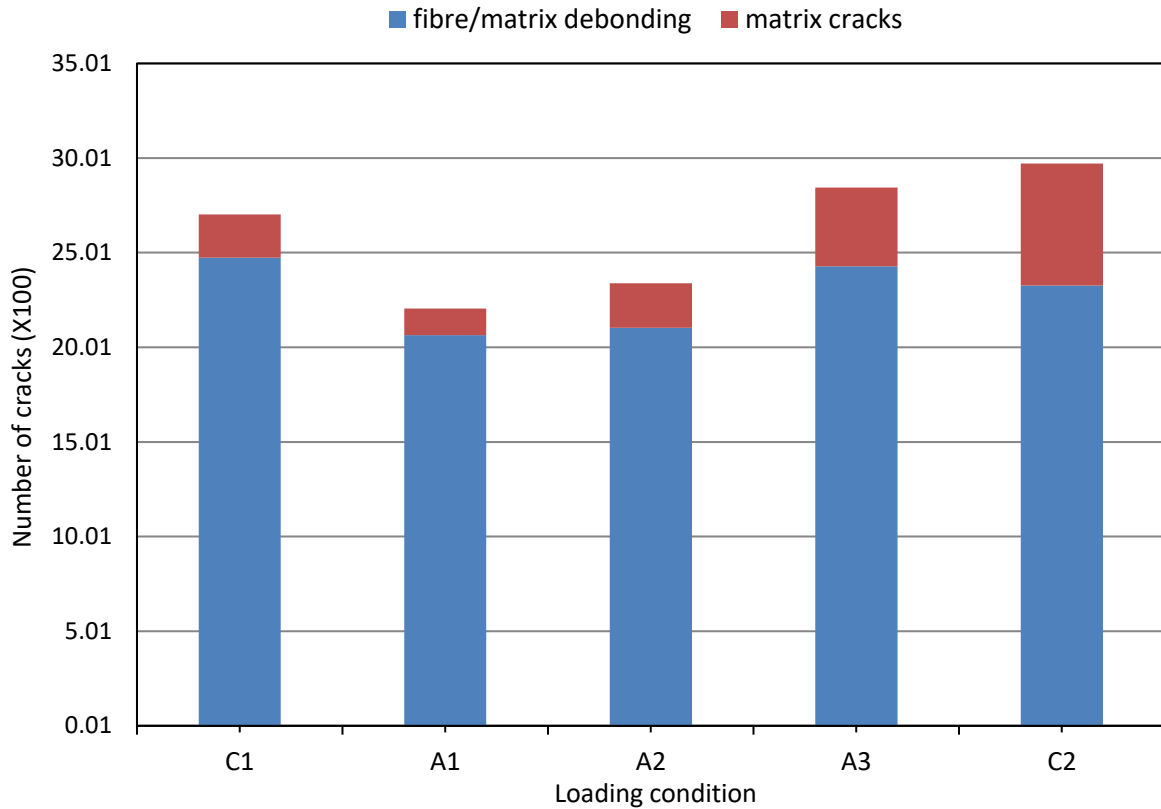


Figure 5.15: Number of fibre/matrix debonding and matrix cracks in loading cases in Part-A.

For Part-B of the failure envelope, it is found that the number of cracks in matrix has increased significantly with increasing compression loads from B1 to B6, as shown in Figure 5.16. Afterwards, the cracks number is almost the same as that in uniaxial compression loading case, C3. The number of fibre/matrix debonding also increases with load, but not as fast as matrix cracking. These results are reasonable as by increasing the confining compression load applied on the RVE in the first step (see Figure 5.11) would certainly leads to more cracks before the second step. In addition by increasing the initial stress in the bonds (that are not broken yet) before applying shear load on the RVE in the second step, would make them more susceptible to break in the subsequent shear load. High confining stress also increases strain softening which continues until the final failure, and thus more normal and shear cracks would occur. This explains the increase of the total number of damage events from B1 to B7 in Figure 5.16.

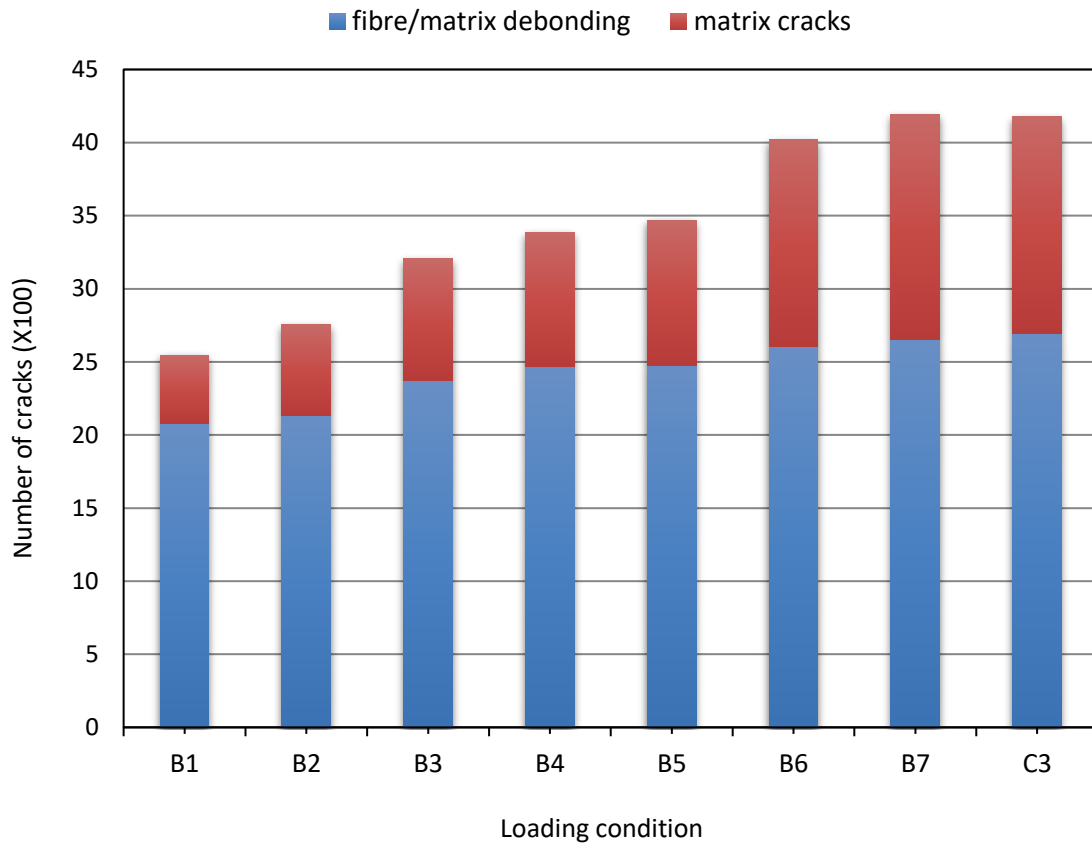


Figure 5.16: Number of fibre/matrix debonding and matrix cracks in loading cases in Part-B.

# Chapter 6

---

## 6 Conclusions and future work

This chapter provides a summary of achievements of the present thesis. The results of the current these laid the ground for future work in the field of using DEM to study the failure of composite materials. A list of activities that can be achieved based on current work is outlined, some of them easy to perform while others are difficult.

### **6.1 Conclusions**

This work devoted to study the damage initiation, evolution and visualising in fibre reinforced polymer composite using discrete element method. This method also used to develop a novel approach for generating random fibre distributions in chapter 2. The approach is capable of generating random distributions of fibres with high volume fractions and any specified inter-fibre distances. Varied fibre diameters were assigned by extracting the experimentally measured diameter distribution. The reason for not using identical diameter is to avoid regular distribution of fibres and to ensure they are distributed randomly. The generated fibre distributions have been statistically analysed, and it was found that the approach was adequately capable of generating fibre distributions which was statistically equivalent to the real microstructure. Finite element analysis was carried out to predict the effective elasticity of the generated microstructures, the results of which were compared with experimental and other methods. The predicted effective properties were found to be close to those measured from experiments and calculated using other algorithms. Especially, the predicted Poisson's ratios have shown excellent agreement with the experimental data. The developed algorithm will be particularly suitable for following chapters of DEM micromechanical modelling and will be used to generate RVEs to study the elasticity, strength and damage evolution of the composite materials using DEM. Also the

method can be easily combined with conventional FEM micromechanical modelling of damage progression in composite materials.

Chapter 3 presented a DEM model that has been developed and micromechanical analysis was carried out to examine the microscopic failure mechanisms of unidirectional fibre-reinforced polymer composites under transverse tension. The RVE of the lamina was discretised using the hexagonally packed particles that were bonded together using the parallel bond for the fibres and the matrix, and the displacement-softening model for the fibre/matrix interface. The simulation results clearly revealed a similar trend of initiation and propagation of the micro cracks to those observed in experiments. For example, the interfacial debonding occurred first at the regions where the inter-fibre distances were small. This was attributed to the stress concentration due to a high ratio of the fibres and matrix stiffness. Matrix cracks started to appear next mostly near the debonded areas. It was observed also that a few matrix cracks occurred in random places due to the introduction of random weakness of the material strength. Eventually the interfacial debonding joined the matrix cracks throughout the RVE and the final fracture occurred. Parametric studies were conducted to investigate the influence of microscopic properties, such as interfacial stiffness, strength and fracture energy on the ultimate failure of the composite RVE. It was concluded that the interface strength had a significant effect on the transverse strength of the composite, and the matrix cracking was the dominant damage when the interfaces were strong. Fibre– matrix interface fracture energy had no significant effect on the ultimate failure strength, but on the one-set of damage. Finally, interfacial stiffness affected only the stiffness but had less effect on the strength of the lamina.

In chapter 4 and 5, a 2D particle model based the discrete element method (DEM) has been developed to study the microscopic behaviour of unidirectional fibre reinforced composite lamina under different loading conditions. Calibration process is first carried out (in chapter 4) to relate micro parameters of the DEM models of fibre and matrix to macro properties of the materials. The critical size of RVE using DEM is investigated that a reasonable RVE size of  $63 \mu m \times 63 \mu m$  can be used provided that the material constituents are previously calibrated. This method shows good prediction of the elastic modulus of composite materials as compared with FEM models and other

analytical methods such as Voigt and Mori-Tanaka using the same approach for generating random fibre distributions.

Based on the micro parameters calibrated in chapter 4, a micromechanical analysis is then carried out to investigate the microscopic failure mechanisms of a composite lamina of MY750 matrix reinforced by E-glass fibres under transverse compression and shear loading in chapter 5. The stress-strain curves are also produced for five different RVEs with different fibre distributions, from which compressive and shear strength has been obtained in together with the failure strains. It is found that DEM can better predict the stress-strain response of the composite under transverse compression than FEM as it clearly shows the compressive strength and compressive failure strain on the stress-strain curve. The shear strength has also been predicted. Previous FEM work, such as ([Romanowicz, 2014](#)), shows more nonlinear behaviour of the stress-strain under transverse shear loads than DEM.

The DEM simulations have shown the microscopic failure mechanisms of the composite and the detailed damage evolution in the RVEs. For both transverse compression and shear loads, interfacial debonding occurs first and then matrix cracks become dominating in areas where inter-fibre distances are small. Eventually, interfacial debonding and matrix cracks are merged together to form the catastrophic failure of the RVEs.

The failure envelope of the composite is computed from DEM simulations under transverse compression and transverse shear. The results presented in this study show that DEM can be used as a useful tool to predict the failure envelope of a general composite lamina subjected to complex biaxial combination of transverse normal and transverse shear loads. Although the results tend to be underestimated for transverse tension and shear whilst overestimated for transverse compression and shear when compared with Hashin and Puck failure criteria, they are still reasonable as the post failure mechanism in the DEM modelling is closer to that in real experimental tests. The capability of DEM to accurately predict the macroscopic response as well as microscopic failure mechanisms makes it a very useful tool to explore the effect of constituent properties on the behaviour of composite lamina. This is important from a material viewpoint to choose critical parameters to improve and optimize lamina

stiffness as well as strength which are very difficult and expensive to obtain through experiments.

## **6.2 Future work**

The capability of DEM to accurately predict the macroscopic response as well as microscopic failure mechanisms makes it a very interesting tool to explore the effect of constituent properties on the behaviour of composite lamina. This is important from a material viewpoint to choose critical parameters to improve and optimise lamina stiffness as well as strength which are very difficult and expensive to obtain through experiments.

Extending the current 2D DEM model to 3D is essential in the future when modelling composite laminates under more complex triaxial loads. Composite laminates under different triaxial loads can be modelled by conducting the methodology developed in Chapter 4 and 5. For example, failure envelopes under hydrostatic pressure ( $\sigma_{11} = \sigma_{22} = \sigma_{33}$ ) versus in-plane shear ( $\tau_{12}$ ), case 2 in WWFE-II ([Kaddour and Hinton, 2013](#)) (Figure 6.1), and under axial loads ( $\sigma_{11}$ ,  $\sigma_{22}$  and  $\sigma_{33}$ ), case 5 in WWFE-II (Figure 6.2). Undoubtedly, it is essential to use 3D RVE with fibre failure strength must be introduced.

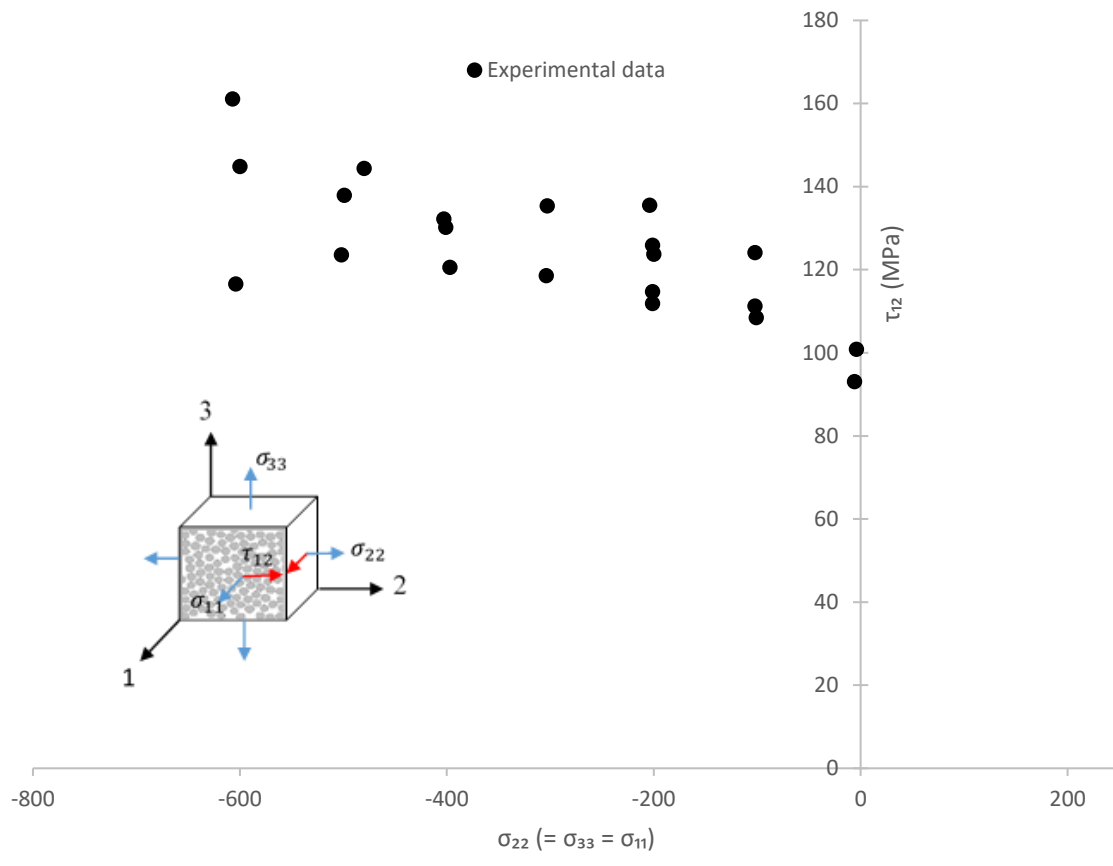


Figure 6.1: Experimental results of failure envelope of a fibre-reinforced composite lamina under  $\sigma_{11} = \sigma_{22} = \sigma_{33}$  versus  $\tau_{12}$  stresses ([Kaddour and Hinton, 2013](#)).

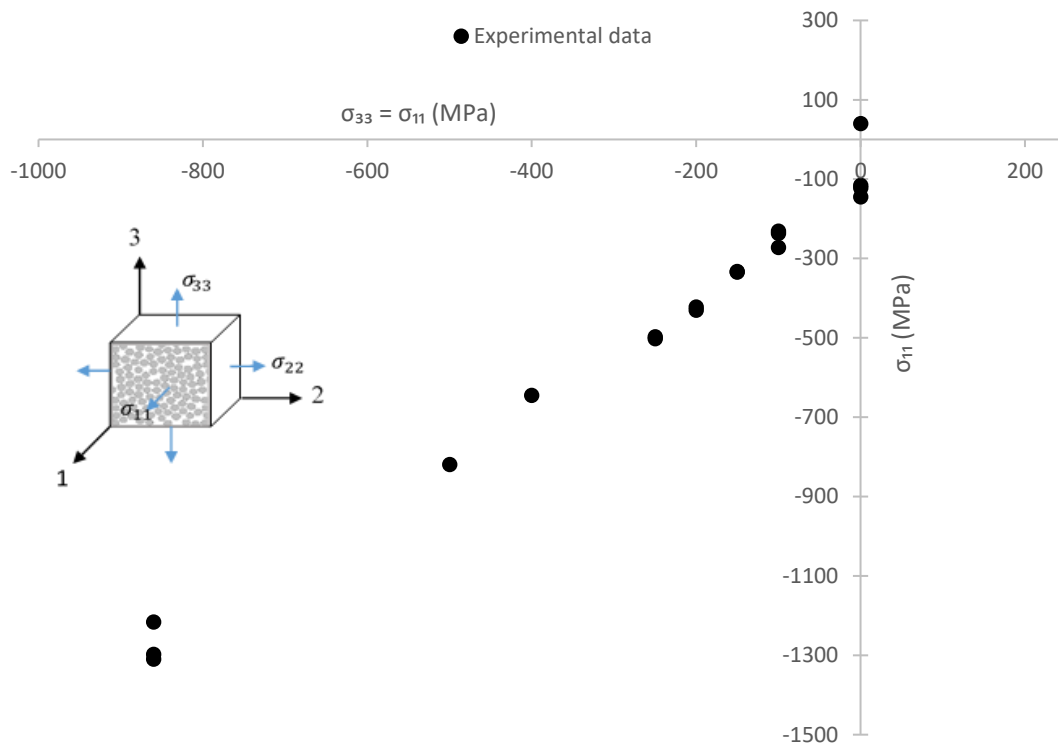


Figure 6.2: Experimental results of failure envelope of a fibre-reinforced composite lamina under  $\sigma_{11} = \sigma_{33}$  versus  $\sigma_{22}$  stresses ([Kaddour and Hinton, 2013](#)).

As this work used 2D DEM to study composite material at the micro-scale level, thus only two failure modes were studied, namely matrix cracking and fibre/matrix debonding. There are, however, a variety failure mechanisms that can be appeared in composite materials in the micro-scale level, such as fibre pull-out, fibre kinking, fibre fracture and fibre splitting. These failure modes can be taken into account only if the 3D model is used.

One of the most important aspects in the micromechanical analysis of composite material is to choose a right model to represent matrix and fibre/matrix interface. Previous researchers found that matrix material is pressure dependent and the stress-strain curve is extremely nonlinear under longitudinal shear. Therefore, it is important in the future to develop a new contact model that can capture this effect.

Delamination, as well as transverse cracking of a laminate consisting of several layers, can be visualised if a fully developed 3D DEM model is used to predict the damage evolution the failure envelope of for other cases in WWFE-II ([Kaddour and](#)

[Hinton, 2013](#)). Due to a large number of particles that require modelling the whole laminate, it is important to use regulate particle packing such as, cubic close packing (CCP), body-centred cubic (BCC), (face-centred cubic FCC) and hexagonal close packing (HCP), to reduce the computational time. Unlike 2D DEM in which relationship between contact parameters and material properties has been reported in the previous literature for cubic or hexagonal bonded particles of both isotropic and orthotropic materials, as discussed in Chapter 3. However, to the authors' best knowledge, there is no such a formulation for 3D DEM models of anisotropic or transversely isotropic materials reported in the literature. Therefore, as a first attempt to extend 2D DEM model to 3D is to derive relationships between contact parameters and material properties. By using 3D DEM to study failure envelopes, one can identify the reasons for which the existing failure criterions are not accurate in certain loading cases and subsequently modify them or develop a new universal failure criterion that takes into account the damage progression for higher accuracy.

## Bibliography

ABAQUS 2010. Theory manual HKS Inc.

ABBAS, A., MASAD, E., PAPAGIANNAKIS, T. & HARMAN, T. 2007. Micromechanical modeling of the viscoelastic behavior of asphalt mixtures using the discrete-element method. *International Journal of Geomechanics*, 7, 131-139.

ABOUDI, J. 1989. Micromechanical analysis of composites by the method of cells. *Applied Mechanics Reviews*, 42, 193-221.

ABOUDI, J. 1996. Micromechanical analysis of composites by the method of cells-update. *Applied Mechanics Reviews*, 49, S83-S91.

AGHDAM, M., PAVIER, M. & SMITH, D. 2001. Micro-mechanics of off-axis loading of metal matrix composites using finite element analysis. *International journal of solids and structures*, 38, 3905-3925.

ALLEN, D., HARRIS, C. & GROVES, S. 1987. A thermomechanical constitutive theory for elastic composites with distributed damage—I. Theoretical development. *International journal of solids and structures*, 23, 1301-1318.

AOKI, S., MORIYA, Y., KISHIMOTO, K. & SCHMAUDER, S. 1996. Finite element fracture analysis of WC-CO alloys. *Engineering Fracture Mechanics*, 55, 275-287.

ASP, L., BERGLUND, L. A. & TALREJA, R. 1996a. A criterion for crack initiation in glassy polymers subjected to a composite-like stress state. *Composites Science and Technology*, 56, 1291-1301.

ASP, L., BERGLUND, L. A. & TALREJA, R. 1996b. Prediction of matrix-initiated transverse failure in polymer composites. *Composites Science and Technology*, 56, 1089-1097.

ASP, L. E., BERGLUND, L. A. & GUDMUNDSON, P. 1995. Effects of a composite-like stress state on the fracture of epoxies. *Composites Science and Technology*, 53, 27-37.

AZZI, V. & TSAI, S. 1965. Anisotropic strength of composites. *Experimental mechanics*, 5, 283-288.

BATHE, K.-J. & WILSON, E. L. 1976. Numerical methods in finite element analysis. Englewood Cliffs: Prentice-Hall.

BELYTSCHKO, T., LOEHNERT, S. & SONG, J. H. 2008. Multiscale aggregating discontinuities: a method for circumventing loss of material stability. *International journal for numerical methods in engineering*, 73, 869-894.

- BENEDETTI, I. & ALIABADI, M. 2013. A three-dimensional cohesive-frictional grain-boundary micromechanical model for intergranular degradation and failure in polycrystalline materials. *Computer Methods in Applied Mechanics and Engineering*, 265, 36-62.
- BÖHM, H. J. 1998. A short introduction to basic aspects of continuum micromechanics. Vienna: CDLFMD Report, Technical Report 020624, 31998.
- BOUTT, D. & MCPHERSON, B. 2002. The role of particle packing in modeling rock mechanical behavior using discrete elements. *Geotechnical Special Publication*, 86-92.
- BOWDEN, P. & JUKES, J. 1972. The plastic flow of isotropic polymers. *Journal of Materials Science*, 7, 52-63.
- BULSARA, V., TALREJA, R. & QU, J. 1999. Damage initiation under transverse loading of unidirectional composites with arbitrarily distributed fibers. *Composites Science and Technology*, 59, 673-682.
- BURYACHENKO, V., PAGANO, N., KIM, R. & SPOWART, J. 2003. Quantitative description and numerical simulation of random microstructures of composites and their effective elastic moduli. *International journal of solids and structures*, 40, 47-72.
- CAI, W., MCDOWELL, G. R. & AIREY, G. 2013. Discrete element modelling of uniaxial constant strain rate tests on asphalt mixtures. *Granular Matter*, 15, 163-174.
- CAMBORDE, F., MARIOTTI, C. & DONZÉ, F. 2000. Numerical study of rock and concrete behaviour by discrete element modelling. *Computers and geotechnics*, 27, 225-247.
- CANAL, L. P., GONZÁLEZ, C., SEGURADO, J. & LLORCA, J. 2012. Intraply fracture of fiber-reinforced composites: Microscopic mechanisms and modeling. *Composites Science and Technology*, 72, 1223-1232.
- CANAL, L. P., SEGURADO, J. & LLORCA, J. 2009. Failure surface of epoxy-modified fiber-reinforced composites under transverse tension and out-of-plane shear. *International journal of solids and structures*, 46, 2265-2274.
- CASTANEDA, P. P. & SUQUET, P. 1998. Nonlinear composites. *Advances in applied mechanics*, 34, 171-302.
- CATER, C. & XIAO, X. 2013. Energy Based Multiscale Modeling with Non-Periodic Boundary Conditions. DTIC Document.
- CHAMIS, C. 1969. Failure criteria for filamentary composites. *Composite Materials: Testing and Design*. ASTM International.
- CHAWLA, N., SIDHU, R. & GANESH, V. 2006. Three-dimensional visualization and microstructure-based modeling of deformation in particle-reinforced composites. *Acta materialia*, 54, 1541-1548.

- CHEN, T. 1997. Exact moduli and bounds of two-phase composites with coupled multifield linear responses. *Journal of the Mechanics and Physics of Solids*, 45, 385-398.
- CHO, N. A., MARTIN, C. & SEGO, D. 2007. A clumped particle model for rock. *International journal of rock mechanics and mining sciences*, 44, 997-1010.
- COOPER, D. W. 1988. Random-sequential-packing simulations in three dimensions for spheres. *Physical Review A*, 38, 522.
- CORREA, E., MANTIĆ, V. & PARÍS, F. 2008. A micromechanical view of inter-fibre failure of composite materials under compression transverse to the fibres. *Composites Science and Technology*, 68, 2010-2021.
- CUNDALL, P. A. Year. A computer model for simulating progressive large-scale movements in blocky rock systems. *In: Proceedings of the Symposium of the International Society of Rock Mechanics, 1971 Nancy, France, Paper II-8.*
- CUNDALL, P. A. & STRACK, O. D. 1979. A discrete numerical model for granular assemblies. *Geotechnique*, 29, 47-65.
- DAVILA, C. G., CAMANHO, P. P. & ROSE, C. A. 2005. Failure criteria for FRP laminates. *Journal of Composite materials*, 39, 323-345.
- DE CARVALHO, N., PINHO, S. & ROBINSON, P. 2011. Reducing the domain in the mechanical analysis of periodic structures, with application to woven composites. *Composites Science and Technology*, 71, 969-979.
- DZENIS, Y. A. & QIAN, J. 2001. Analysis of microdamage evolution histories in composites. *International journal of solids and structures*, 38, 1831-1854.
- ECKSCHLAGER, A., HAN, W. & BÖHM, H. J. 2002. A unit cell model for brittle fracture of particles embedded in a ductile matrix. *Computational materials science*, 25, 85-91.
- ESHELBY, J. D. Year. The determination of the elastic field of an ellipsoidal inclusion, and related problems. *In: Proceedings of the Royal Society of London, 1957* 1957. 376-396.
- FENG, Y., HAN, K. & OWEN, D. 2003. Filling domains with disks: an advancing front approach. *International journal for numerical methods in engineering*, 56, 699-713.
- FERNANDES, G., PITUBA, J. & DE SOUZA NETO, E. 2015. FEM/BEM formulation for multi-scale analysis of stretched plates. *Engineering Analysis with Boundary Elements*, 54, 47-59.
- FEYEL, F. & CHABOCHE, J.-L. 2000. FE 2 multiscale approach for modelling the elastoviscoplastic behaviour of long fibre SiC/Ti composite materials. *Computer Methods in Applied Mechanics and Engineering*, 183, 309-330.

- FIEDLER, B., HOJO, M., OCHIAI, S., SCHULTE, K. & ANDO, M. 2001. Failure behavior of an epoxy matrix under different kinds of static loading. *Composites Science and Technology*, 61, 1615-1624.
- FISH, J. & YUAN, Z. 2005. Multiscale enrichment based on partition of unity. *International journal for numerical methods in engineering*, 62, 1341-1359.
- FLORES, E. S., DE SOUZA NETO, E. & PEARCE, C. 2011. A large strain computational multi-scale model for the dissipative behaviour of wood cell-wall. *Computational materials science*, 50, 1202-1211.
- GEERS, M., KOUZNETSOVA, V. & BREKELMANS, W. 2003. Multiscale first-order and second-order computational homogenization of microstructures towards continua. *International Journal for Multiscale Computational Engineering*, 1.
- GHIASI, H., FAYAZBAKHS, K., PASINI, D. & LESSARD, L. 2010. Optimum stacking sequence design of composite materials Part II: Variable stiffness design. *Composite structures*, 93, 1-13.
- GHOSH, S., LEE, K. & MOORTHY, S. 1995. Multiple scale analysis of heterogeneous elastic structures using homogenization theory and Voronoi cell finite element method. *International journal of solids and structures*, 32, 27-62.
- GHOSH, S., LEE, K. & MOORTHY, S. 1996. Two scale analysis of heterogeneous elastic-plastic materials with asymptotic homogenization and Voronoi cell finite element model. *Computer Methods in Applied Mechanics and Engineering*, 132, 63-116.
- GHOSH, S., LEE, K. & RAGHAVAN, P. 2001. A multi-level computational model for multi-scale damage analysis in composite and porous materials. *International journal of solids and structures*, 38, 2335-2385.
- GILAT, A., GOLDBERG, R. K. & ROBERTS, G. D. 2002. Experimental study of strain-rate-dependent behavior of carbon/epoxy composite. *Composites Science and Technology*, 62, 1469-1476.
- GONZÁLEZ, C. & LLORCA, J. 2006. Multiscale modeling of fracture in fiber-reinforced composites. *Acta materialia*, 54, 4171-4181.
- GONZÁLEZ, C. & LLORCA, J. 2007a. Mechanical behavior of unidirectional fiber-reinforced polymers under transverse compression: microscopic mechanisms and modeling. *Composites Science and Technology*, 67, 2795-2806.
- GONZÁLEZ, C. & LLORCA, J. 2007b. Virtual fracture testing of composites: A computational micromechanics approach. *Engineering Fracture Mechanics*, 74, 1126-1138.
- GOSSE, J. H. & CHRISTENSEN, S. 2001. Strain invariant failure criteria for polymers in composite materials. *AIAA paper*, 1184, 2001.

- HA, S. K., JIN, K. K. & HUANG, Y. 2008. Micro-mechanics of failure (MMF) for continuous fiber reinforced composites. *Journal of Composite materials*.
- HAHN, H. T. & TSAI, S. W. 1973. Nonlinear elastic behavior of unidirectional composite laminae. *Journal of Composite materials*, 7, 102-118.
- HARPER, L., QIAN, C., TURNER, T., LI, S. & WARRIOR, N. 2012. Representative volume elements for discontinuous carbon fibre composites–Part 1: Boundary conditions. *Composites Science and Technology*, 72, 225-234.
- HASHIN, Z. 1980. Failure criteria for unidirectional fiber composites. *Journal of applied mechanics*, 47, 329-334.
- HASHIN, Z. & ROTEM, A. 1973. A fatigue failure criterion for fiber reinforced materials. *Journal of Composite materials*, 7, 448-464.
- HENTZ, S., DAUDEVILLE, L. & DONZÉ, F. V. 2004a. Identification and validation of a discrete element model for concrete. *Journal of engineering mechanics*, 130, 709-719.
- HENTZ, S., DONZÉ, F. V. & DAUDEVILLE, L. 2004b. Discrete element modelling of concrete submitted to dynamic loading at high strain rates. *Computers & structures*, 82, 2509-2524.
- HERAKOVICH, C. T. 1998. Mechanics of fibrous composites.
- HILL, R. 1963. Elastic properties of reinforced solids: some theoretical principles. *Journal of the Mechanics and Physics of Solids*, 11, 357-372.
- HILL, R. 1998. *The mathematical theory of plasticity*, Oxford university press.
- HINRICHSSEN, E. L., FEDER, J. & JØSSANG, T. 1986. Geometry of random sequential adsorption. *Journal of statistical Physics*, 44, 793-827.
- HINTON, M. J., KADDOUR, A. S. & SODEN, P. D. 2004. *Failure criteria in fibre reinforced polymer composites: the world-wide failure exercise*, Elsevier.
- HOFFMAN, O. 1967. The brittle strength of orthotropic materials. *Journal of Composite materials*, 1, 200-206.
- HSU, S.-Y., VOGLER, T. & KYRIAKIDES, S. 1999. Inelastic behavior of an AS4/PEEK composite under combined transverse compression and shear. Part II: modeling. *International Journal of Plasticity*, 15, 807-836.
- HUND, A. & RAMM, E. 2007. Locality constraints within multiscale model for non-linear material behaviour. *International journal for numerical methods in engineering*, 70, 1613-1632.
- ILLIAN, J., PENTTINEN, A., STOYAN, H. & STOYAN, D. 2008. *Statistical analysis and modelling of spatial point patterns*, John Wiley & Sons.

- ITASCA 2003. PFC2D-particle Flow Code (Itasca Consulting Group Inc., Minnesta).
- JEONG, H.-Y. 2002. A new yield function and a hydrostatic stress-controlled void nucleation model for porous solids with pressure-sensitive matrices. *International journal of solids and structures*, 39, 1385-1403.
- KAČIANAUSKAS, R. & VADLUGA, V. 2009. Lattice-based six-spring discrete element model for discretisation problems of 2D isotropic and anisotropic solids. *Mechanika*, 76.
- KACZMARCZYK, Ł., PEARCE, C. J. & BIĆANIĆ, N. 2008. Scale transition and enforcement of RVE boundary conditions in second - order computational homogenization. *International journal for numerical methods in engineering*, 74, 506-522.
- KADDOUR, A. & HINTON, M. 2013. Maturity of 3D failure criteria for fibre-reinforced composites: Comparison between theories and experiments: Part B of WWFE-II. *Journal of Composite materials*, 47, 925-966.
- KANSAL, A. R., TORQUATO, S. & STILLINGER, F. H. 2002. Computer generation of dense polydisperse sphere packings. *The Journal of chemical physics*, 117, 8212-8218.
- KIM, H., WAGONER, M. P. & BUTTLAR, W. G. 2008. Simulation of fracture behavior in asphalt concrete using a heterogeneous cohesive zone discrete element model. *Journal of materials in civil engineering*, 20, 552-563.
- KOUZNETSOVA, V., GEERS, M. & BREKELMANS, W. 2004. Multi-scale second-order computational homogenization of multi-phase materials: a nested finite element solution strategy. *Computer Methods in Applied Mechanics and Engineering*, 193, 5525-5550.
- KOUZNETSOVA, V., GEERS, M. G. & BREKELMANS, W. M. 2002. Multi - scale constitutive modelling of heterogeneous materials with a gradient - enhanced computational homogenization scheme. *International journal for numerical methods in engineering*, 54, 1235-1260.
- LADVEZE, P. 2004. Multiscale modelling and computational strategies for composites. *International journal for numerical methods in engineering*, 60, 233-253.
- LI, S. 2001. General unit cells for micromechanical analyses of unidirectional composites. *Composites Part A: Applied Science and Manufacturing*, 32, 815-826.
- LI, S. 2008. Boundary conditions for unit cells from periodic microstructures and their implications. *Composites Science and Technology*, 68, 1962-1974.
- LIU, K. & LIU, W. 2006. Application of discrete element method for continuum dynamic problems. *Archive of Applied Mechanics*, 76, 229-243.

- LIU, Y. & YOU, Z. 2010. Accelerated discrete-element modeling of asphalt-based materials with the frequency-temperature superposition principle. *Journal of engineering mechanics*, 137, 355-365.
- LLORCA, J., GONZÁLEZ, C., MOLINA-ALDAREGUÍA, J. M. & LÓPES, C. 2013. Multiscale Modeling of Composites: Toward Virtual Testing... and Beyond. *JOM*, 65, 215-225.
- LOEHNERT, S. & BELYTSCHKO, T. 2007. A multiscale projection method for macro/microcrack simulations. *International journal for numerical methods in engineering*, 71, 1466-1482.
- LUBACHEVSKY, B. D. & STILLINGER, F. H. 1990. Geometric properties of random disk packings. *Journal of statistical Physics*, 60, 561-583.
- LUDING, S. 2008a. Cohesive, frictional powders: contact models for tension. *Granular Matter*, 10, 235-246.
- LUDING, S. 2008b. Introduction to discrete element methods: basic of contact force models and how to perform the micro-macro transition to continuum theory. *European Journal of Environmental and Civil Engineering*, 12, 785-826.
- MAHEO, L., DAU, F., ANDRE, D., CHARLES, J.-L. & IORDANOFF, I. 2015. A promising way to model cracks in composite using Discrete Element Method. *Composites Part B: Engineering*, 71, 193-202.
- MARKOVIC, D. & IBRAHIMBEGOVIC, A. 2004. On micro–macro interface conditions for micro scale based FEM for inelastic behavior of heterogeneous materials. *Computer Methods in Applied Mechanics and Engineering*, 193, 5503-5523.
- MARTIN, C., BOUVARD, D. & SHIMA, S. 2003. Study of particle rearrangement during powder compaction by the discrete element method. *Journal of the Mechanics and Physics of Solids*, 51, 667-693.
- MASSART, T., PEERLINGS, R. & GEERS, M. 2007a. An enhanced multi - scale approach for masonry wall computations with localization of damage. *International journal for numerical methods in engineering*, 69, 1022-1059.
- MASSART, T., PEERLINGS, R. & GEERS, M. 2007b. Structural damage analysis of masonry walls using computational homogenization. *International journal of damage mechanics*, 16, 199-226.
- MATLAB 2012. The MathWorks, Inc., 3 Apple Hill Dr., Natick, MA 01760.
- MATSUI, K., TERADA, K. & YUGE, K. 2004. Two-scale finite element analysis of heterogeneous solids with periodic microstructures. *Computers & structures*, 82, 593-606.
- MATZENMILLER, A., LUBLINER, J. & TAYLOR, R. 1995. A constitutive model for anisotropic damage in fiber-composites. *Mechanics of Materials*, 20, 125-152.

- MELRO, A., CAMANHO, P. & PINHO, S. 2008. Generation of random distribution of fibres in long-fibre reinforced composites. *Composites Science and Technology*, 68, 2092-2102.
- MIEHE, C. & KOCH, A. 2002. Computational micro-to-macro transitions of discretized microstructures undergoing small strains. *Archive of Applied Mechanics*, 72, 300-317.
- MIEHE, C., SCHOTTE, J. & SCHRÖDER, J. 1999a. Computational micro–macro transitions and overall moduli in the analysis of polycrystals at large strains. *Computational materials science*, 16, 372-382.
- MIEHE, C., SCHRÖDER, J. & SCHOTTE, J. 1999b. Computational homogenization analysis in finite plasticity simulation of texture development in polycrystalline materials. *Computer Methods in Applied Mechanics and Engineering*, 171, 387-418.
- MISHNAEVSKY JR, L. L. 2007. *Computational mesomechanics of composites: numerical analysis of the effect of microstructures of composites of strength and damage resistance*, John Wiley & Sons.
- MOFFAT, A., WRIGHT, P., BUFFIÈRE, J.-Y., SINCLAIR, I. & SPEARING, S. M. 2008. Micromechanisms of damage in 0 splits in a [90/0] s composite material using synchrotron radiation computed tomography. *Scripta Materialia*, 59, 1043-1046.
- MORALEDA, J., SEGURADO, J. & LLORCA, J. 2009. Effect of interface fracture on the tensile deformation of fiber-reinforced elastomers. *International journal of solids and structures*, 46, 4287-4297.
- MORI, T. & TANAKA, K. 1973. Average stress in matrix and average elastic energy of materials with misfitting inclusions. *Acta metallurgica*, 21, 571-574.
- MROZEK, A., KUS, W. & BURCZYŃSKI, T. 2007. Application of the coupled boundary element method with atomic model in the static analysis. *Computer Methods in Materials Science*, 7, 284-288.
- NGUYEN, N.-S., MAGOARIEC, H., CAMBOU, B. & DANESCU, A. 2009. Analysis of structure and strain at the meso-scale in 2D granular materials. *International journal of solids and structures*, 46, 3257-3271.
- O'SULLIVAN, C. & BRAY, J. D. 2004. Selecting a suitable time step for discrete element simulations that use the central difference time integration scheme. *Engineering computations*, 21, 278-303.
- OGIHARA, S. & KOYANAGI, J. 2010. Investigation of combined stress state failure criterion for glass fiber/epoxy interface by the cruciform specimen method. *Composites Science and Technology*, 70, 143-150.

- PAGANO, N. 1998. On the micromechanical failure modes in a class of ideal brittle matrix composites. Part 1. Coated-fiber composites. *Composites Part B: Engineering*, 29, 93-119.
- PARIS, F., CORREA, E. & CAÑAS, J. 2003. Micromechanical view of failure of the matrix in fibrous composite materials. *Composites Science and Technology*, 63, 1041-1052.
- PARÍS, F., CORREA, E. & MANTIČ, V. 2007. Kinking of transversal interface cracks between fiber and matrix. *Journal of applied mechanics*, 74, 703-716.
- PETIT, P. & WADDOUPS, M. E. 1969. A method of predicting the nonlinear behavior of laminated composites. *Journal of Composite materials*, 3, 2-19.
- PETTERMANN, H. E. & SURESH, S. 2000. A comprehensive unit cell model: a study of coupled effects in piezoelectric 1–3 composites. *International journal of solids and structures*, 37, 5447-5464.
- PIERRON, F., GREEN, B., WISNOM, M. R. & HALLETT, S. 2007. Full-field assessment of the damage process of laminated composite open-hole tensile specimens. Part II: Experimental results. *Composites Part A: Applied Science and Manufacturing*, 38, 2321-2332.
- PINHO, S., IANNUCCI, L. & ROBINSON, P. 2006. Physically-based failure models and criteria for laminated fibre-reinforced composites with emphasis on fibre kinking: Part I: Development. *Composites Part A: Applied Science and Manufacturing*, 37, 63-73.
- PLASSIARD, J.-P., BELHEINE, N. & DONZÉ, F.-V. 2009. A spherical discrete element model: calibration procedure and incremental response. *Granular Matter*, 11, 293-306.
- POTYONDY, D. & CUNDALL, P. 2004. A bonded-particle model for rock. *International journal of rock mechanics and mining sciences*, 41, 1329-1364.
- PUCK, A. & SCHÜRMAN, H. 2002. Failure analysis of FRP laminates by means of physically based phenomenological models. *Composites Science and Technology*, 62, 1633-1662.
- PYRZ, R. 1994. Quantitative description of the microstructure of composites. Part I: Morphology of unidirectional composite systems. *Composites Science and Technology*, 50, 197-208.
- QINGSHENG, Y., LIMIN, T. & HAORAN, C. 1994. Self-consistent finite element method: A new method of predicting effective properties of inclusion media. *Finite elements in analysis and design*, 17, 247-257.
- RAGHAVA, R., CADDELL, R. M. & YEH, G. S. 1973. The macroscopic yield behaviour of polymers. *Journal of Materials Science*, 8, 225-232.

- REUSS, A. 1929. Berechnung der fließgrenze von mischkristallen auf grund der plastizitätsbedingung für einkristalle. *ZAMM - Journal of Applied Mathematics and Mechanics/Zeitschrift für Angewandte Mathematik und Mechanik*, 9, 49-58.
- ROMANOWICZ, M. 2014. Determination of the first ply failure load for a cross ply laminate subjected to uniaxial tension through computational micromechanics. *International journal of solids and structures*, 51, 2549-2556.
- SAUTTER, M., DIETRICH, C., POECH, M., SCHMAUDER, S. & FISCHMEISTER, H. 1993. Finite element modelling of a transverse-loaded fibre composite effects of section size and net density. *Computational materials science*, 1, 225-233.
- SAWAMOTO, Y., TSUBOTA, H., KASAI, Y., KOSHIKA, N. & MORIKAWA, H. 1998. Analytical studies on local damage to reinforced concrete structures under impact loading by discrete element method. *Nuclear engineering and design*, 179, 157-177.
- SCHULTHEISZ, C. R. & WAAS, A. M. 1996. Compressive failure of composites, part I: testing and micromechanical theories. *Progress in Aerospace Sciences*, 32, 1-42.
- SCOTT, A., MAVROGORDATO, M., WRIGHT, P., SINCLAIR, I. & SPEARING, S. 2011. In situ fibre fracture measurement in carbon–epoxy laminates using high resolution computed tomography. *Composites Science and Technology*, 71, 1471-1477.
- SEGURADO, J., GONZÁLEZ, C. & LLORCA, J. 2003. A numerical investigation of the effect of particle clustering on the mechanical properties of composites. *Acta materialia*, 51, 2355-2369.
- SEGURADO, J. & LLORCA, J. 2002. A numerical approximation to the elastic properties of sphere-reinforced composites. *Journal of the Mechanics and Physics of Solids*, 50, 2107-2121.
- SEGURADO, J. & LLORCA, J. 2006. Computational micromechanics of composites: the effect of particle spatial distribution. *Mechanics of Materials*, 38, 873-883.
- SEGURADO, J., LLORCA, J. & GONZÁLEZ, C. 2002. On the accuracy of mean-field approaches to simulate the plastic deformation of composites. *Scripta Materialia*, 46, 525-529.
- SFANTOS, G. & ALIABADI, M. 2007. Multi-scale boundary element modelling of material degradation and fracture. *Computer Methods in Applied Mechanics and Engineering*, 196, 1310-1329.
- SHENG, Y., YANG, D., TAN, Y. & YE, J. 2010. Microstructure effects on transverse cracking in composite laminae by DEM. *Composites Science and Technology*, 70, 2093-2101.

- SHERWOOD, J. 1997. Packing of spheroids in three-dimensional space by random sequential addition. *Journal of Physics A: Mathematical and General*, 30, L839.
- SIHN, S., KIM, R. Y., KAWABE, K. & TSAI, S. W. 2007. Experimental studies of thinly laminated composites. *Composites Science and Technology*, 67, 996-1008.
- SODEN, P., HINTON, M. & KADDOUR, A. 1998a. A comparison of the predictive capabilities of current failure theories for composite laminates. *Composites Science and Technology*, 58, 1225-1254.
- SODEN, P., HINTON, M. & KADDOUR, A. 1998b. Lamina properties, lay-up configurations and loading conditions for a range of fibre-reinforced composite laminates. *Composites Science and Technology*, 58, 1011-1022.
- SODEN, P., KADDOUR, A. & HINTON, M. 2004. Recommendations for designers and researchers resulting from the world-wide failure exercise. *Composites Science and Technology*, 64, 589-604.
- SUN, C. & CHEN, J. 1989. A simple flow rule for characterizing nonlinear behavior of fiber composites. *Journal of Composite materials*, 23, 1009-1020.
- SUN, C. & VAIDYA, R. 1996. Prediction of composite properties from a representative volume element. *Composites Science and Technology*, 56, 171-179.
- SWAMINATHAN, S. & GHOSH, S. 2006. Statistically equivalent representative volume elements for unidirectional composite microstructures: part II-with interfacial debonding. *Journal of Composite materials*, 40, 605-621.
- SWAMINATHAN, S., GHOSH, S. & PAGANO, N. 2006. Statistically equivalent representative volume elements for unidirectional composite microstructures: Part I-Without damage. *Journal of Composite materials*, 40, 583-604.
- TAVAREZ, F. A. & PLESHA, M. E. 2007. Discrete element method for modelling solid and particulate materials. *International journal for numerical methods in engineering*, 70, 379-404.
- TAY, T.-E., TAN, S., TAN, V. & GOSSE, J. 2005. Damage progression by the element-failure method (EFM) and strain invariant failure theory (SIFT). *Composites Science and Technology*, 65, 935-944.
- TERADA, K. & KIKUCHI, N. 2001. A class of general algorithms for multi-scale analyses of heterogeneous media. *Computer Methods in Applied Mechanics and Engineering*, 190, 5427-5464.
- THORNTON, C. 2000. Numerical simulations of deviatoric shear deformation of granular media. *Geotechnique*, 50, 43-53.
- TOTRY, E., GONZÁLEZ, C. & LLORCA, J. 2008a. Failure locus of fiber-reinforced composites under transverse compression and out-of-plane shear. *Composites Science and Technology*, 68, 829-839.

- TOTRY, E., GONZÁLEZ, C. & LLORCA, J. 2008b. Influence of the loading path on the strength of fiber-reinforced composites subjected to transverse compression and shear. *International journal of solids and structures*, 45, 1663-1675.
- TOTRY, E., GONZÁLEZ, C. & LLORCA, J. 2008c. Prediction of the failure locus of C/PEEK composites under transverse compression and longitudinal shear through computational micromechanics. *Composites Science and Technology*, 68, 3128-3136.
- TOTRY, E., MOLINA-ALDAREGUÍA, J. M., GONZÁLEZ, C. & LLORCA, J. 2010. Effect of fiber, matrix and interface properties on the in-plane shear deformation of carbon-fiber reinforced composites. *Composites Science and Technology*, 70, 970-980.
- TRIAS, D., COSTA, J., TURON, A. & HURTADO, J. 2006. Determination of the critical size of a statistical representative volume element (SRVE) for carbon reinforced polymers. *Acta materialia*, 54, 3471-3484.
- TSAI, S. W. 1965. Strength characterisation of composite materials, Tech. Rep. NASA CR-224. *National Aeronautics and Space Agency*.
- TSAI, S. W. & WU, E. M. 1971. A general theory of strength for anisotropic materials. *Journal of Composite materials*, 5, 58-80.
- UGURAL, A. C. & FENSTER, S. K. 2003. *Advanced strength and applied elasticity*, Pearson education.
- VAN DER SLUIS, O., SCHREURS, P., BREKELMANS, W. & MEIJER, H. 2000. Overall behaviour of heterogeneous elastoviscoplastic materials: effect of microstructural modelling. *Mechanics of Materials*, 32, 449-462.
- VAUGHAN, T. & MCCARTHY, C. 2010. A combined experimental–numerical approach for generating statistically equivalent fibre distributions for high strength laminated composite materials. *Composites Science and Technology*, 70, 291-297.
- VAUGHAN, T. & MCCARTHY, C. 2011a. Micromechanical modelling of the transverse damage behaviour in fibre reinforced composites. *Composites Science and Technology*, 71, 388-396.
- VAUGHAN, T. & MCCARTHY, C. 2011b. A micromechanical study on the effect of intra-ply properties on transverse shear fracture in fibre reinforced composites. *Composites Part A: Applied Science and Manufacturing*, 42, 1217-1228.
- VAZIRI, R., OLSON, M. & ANDERSON, D. 1991. A plasticity-based constitutive model for fibre-reinforced composite laminates. *Journal of Composite materials*, 25, 512-535.
- VOGLER, T. & KYRIAKIDES, S. 1999. Inelastic behavior of an AS4/PEEK composite under combined transverse compression and shear. Part I: experiments. *International Journal of Plasticity*, 15, 783-806.

- VOIGT, W. 1889. Ueber die Beziehung zwischen den beiden Elasticitätsconstanten isotroper Körper. *Annalen der Physik*, 274, 573-587.
- WANG, Y. & TONON, F. 2010. Calibration of a discrete element model for intact rock up to its peak strength. *International journal for numerical and analytical methods in geomechanics*, 34, 447-469.
- WILLIAMS, S. & PHILIPSE, A. 2003. Random packings of spheres and spherocylinders simulated by mechanical contraction. *Physical Review E*, 67, 051301.
- WITTEL, F. K., KUN, F., KRÖPLIN, B.-H. & HERRMANN, H. J. 2003. A study of transverse ply cracking using a discrete element method. *Computational materials science*, 28, 608-619.
- WONGSTO, A. & LI, S. 2005. Micromechanical FE analysis of UD fibre-reinforced composites with fibres distributed at random over the transverse cross-section. *Composites Part A: Applied Science and Manufacturing*, 36, 1246-1266.
- WRIGHT, P., FU, X., SINCLAIR, I. & SPEARING, S. 2008. Ultra High Resolution Computed Tomography of Damage in Notched Carbon Fiber—Epoxy Composites. *Journal of Composite materials*, 42, 1993-2002.
- WU, J., COLLOP, A. C. & MCDOWELL, G. R. 2010. Discrete element modeling of constant strain rate compression tests on idealized asphalt mixture. *Journal of materials in civil engineering*, 23, 2-11.
- WULF, J., STEINKOPFF, T. & FISCHMEISTER, H. 1996. FE-simulation of crack paths in the real microstructure of an Al (6061)/SiC composite. *Acta materialia*, 44, 1765-1779.
- XIA, Z., CURTIN, W. & PETERS, P. 2001. Multiscale modeling of failure in metal matrix composites. *Acta materialia*, 49, 273-287.
- XIA, Z., ZHANG, Y. & ELLYIN, F. 2003. A unified periodical boundary conditions for representative volume elements of composites and applications. *International journal of solids and structures*, 40, 1907-1921.
- XIA, Z., ZHOU, C., YONG, Q. & WANG, X. 2006. On selection of repeated unit cell model and application of unified periodic boundary conditions in micro-mechanical analysis of composites. *International journal of solids and structures*, 43, 266-278.
- XIE, D. & WAAS, A. M. 2006. Discrete cohesive zone model for mixed-mode fracture using finite element analysis. *Engineering Fracture Mechanics*, 73, 1783-1796.
- YAN, G., YU, H.-S. & MCDOWELL, G. 2009. Simulation of granular material behaviour using DEM. *Procedia Earth and Planetary Science*, 1, 598-605.

- YANG, D., SHENG, Y., YE, J. & TAN, Y. 2011a. Dynamic simulation of crack initiation and propagation in cross-ply laminates by DEM. *Composites Science and Technology*.
- YANG, D., YE, J., TAN, Y. & SHENG, Y. 2011b. Modeling progressive delamination of laminated composites by discrete element method. *Computational materials science*, 50, 858-864.
- YANG, L., WU, Z., CAO, Y. & YAN, Y. 2015. Micromechanical modelling and simulation of unidirectional fibre-reinforced composite under shear loading. *Journal of Reinforced Plastics and Composites*, 34, 72-83.
- YANG, L., YAN, Y., LIU, Y. & RAN, Z. 2012. Microscopic failure mechanisms of fiber-reinforced polymer composites under transverse tension and compression. *Composites Science and Technology*, 72, 1818-1825.
- YANG, L., YAN, Y., MA, J. & LIU, B. 2013a. Effects of inter-fiber spacing and thermal residual stress on transverse failure of fiber-reinforced polymer–matrix composites. *Computational materials science*, 68, 255-262.
- YANG, L., YAN, Y., RAN, Z. & LIU, Y. 2013b. A new method for generating random fibre distributions for fibre reinforced composites. *Composites Science and Technology*, 76, 14-20.
- YE, J. & ZHANG, D. 2012. Prediction of failure envelopes and stress-strain curves of fiber composite laminates under triaxial loads. *Journal of Composite materials*, 46, 2417-2430.
- YOU, Z. & BUTTLAR, W. 2004. Discrete element modeling to predict the modulus of asphalt concrete mixtures. *Journal of materials in civil engineering*, 16, 140-146.
- ZHANG, D., XU, L. & YE, J. 2013. Prediction of failure envelopes and stress–strain curves of fiber composite laminates under triaxial loads: Comparison with experimental results. *Journal of Composite materials*, 47, 763-776.
- ZHANG, D., YE, J. & SHENG, H. Y. 2006. Free-edge and ply cracking effect in cross-ply laminated composites under uniform extension and thermal loading. *Composite structures*, 76, 314-325.
- ZHANG, Y., XIA, Z. & ELLYIN, F. 2004. Evolution and influence of residual stresses/strains of fiber reinforced laminates. *Composites Science and Technology*, 64, 1613-1621.
- ZHANG, Y., XIA, Z. & ELLYIN, F. 2005. Nonlinear viscoelastic micromechanical analysis of fibre-reinforced polymer laminates with damage evolution. *International journal of solids and structures*, 42, 591-604.
- ZHOU, X.-F., WAGNER, H. & NUTT, S. 2001. Interfacial properties of polymer composites measured by push-out and fragmentation tests. *Composites Part A: Applied Science and Manufacturing*, 32, 1543-1551.

## Appendix A: DEM script to generate random fibre distributions

```
NEW
set logfile output.log
set dt 1
set extra ball 1
set log on
set Echo off
;-----
def setdata
  array br_pnt1(dim)
  array br_pnt2(dim)
  L = 165.0      ;Lenght
  W = 165.0      ;Width
  R_fibre = 3.3  ;Radius
  Vol_fibre = 0.60 ;Volume fraction
  command
    set PERIODIC ON 0.0 @L 0.0 @W
  endcommand
end
;-----
def et2_setup
  _rc = R_fibre
  _r2 = 2.0 * _rc
  _b = sqrt(pi*_rc^2/(2*sqrt(3)*Vol_fibre))
  _b2 = 2.0*_b
  yinc = _b/sqrt(3.0) + _b2/sqrt(3.0)
  _xc = _rc
  _yc = _rc
  _idc = 1
  n_row = int(W/yinc) ;Number of balls in x-directions
  n_col = int(L/_b2)  ;Number of balls in y-directions
  loop row (1,n_row)
    loop col (1,n_col)
      _rnd = 0.5*(6.6+0.3106*grand)
      command
        ball id=@_idc x=@_xc y=@_yc rad=@_rnd
      endcommand
      _idc = _idc + 1
      _xc = _xc + _b2
    endloop
end
```

```

    _yc = _yc + yinc
    _xc = _rc
endloop
end
;-----
def plots_preprocessig
command
    plot create mg_Sample
        plot add fish Model_Boundary
    plot add fish percolor
    plot add ball yellow red green
    plot set background white
    plot show
end_command
end
;-----
def Model_Boundary
;Draw model boundary
plot_item
br_pnt1(1) = 0
br_pnt1(2) = 0
br_pnt2(1) = L
br_pnt2(2) = 0
_crk_draw2d_line = draw_line(br_pnt1, br_pnt2)
;
br_pnt1(1) = L
br_pnt1(2) = 0
br_pnt2(1) = L
br_pnt2(2) = W
_crk_draw2d_line = draw_line(br_pnt1, br_pnt2)
;
br_pnt1(1) = L
br_pnt1(2) = W
br_pnt2(1) = 0
br_pnt2(2) = W
_crk_draw2d_line = draw_line(br_pnt1, br_pnt2)
;
br_pnt1(1) = 0
br_pnt1(2) = W
br_pnt2(1) = 0
br_pnt2(2) = 0
_crk_draw2d_line = draw_line(br_pnt1, br_pnt2)
end
;-----
def percolor
plot_item
bp = ball_head
loop while bp # null
    b_color(bp) = 0

```

```

if and(b_perflag(bp),1) # 0
    b_color(bp) = 1 ;controller
    b_extra(bp, 1) = 1
else
    if and(b_perflag(bp),14) # 0
        b_color(bp) = 2 ;slave
        b_extra(bp, 1) = 2
    endif
endif
bp = b_next(bp)
endLoop
end
;-----
def N_ball1
idd=1000
n1 = 0
At_ = 0.0
bp = ball_head ;----
loop while bp # null ;|
    n1 = n1+1 ;|
        brdd = b_rad(bp) ;| Cacualte volume fraction
        At_ = At_ + pi*brdd^2 ;|
        bp = b_next(bp) ;|
endloop ;|
Vf1 = At_/(L*W) ;----
;
;Add balls until reaching target volume fraction
loop while 1#0
    if Vf1 > Vol_fibre then
        ii = out('Pause: please read the message bellow ...')
        ii = out('Volume fraction reached = '+string(Vf1))
        exit
    else
        idd=idd+1
        _rnd = 0.5*(6.6+0.3106*grand)
        command
            ball id=@idd x=30 y=30 rad=@_rnd
        endcommand
        At_ = At_ + pi*_rnd^2
        Vf1 = At_/(L*W)
        n1 = n1+1
    endif
endloop
end
;-----
def BVelocity
;Apply random velocity to each ball
bp = ball_head
loop while bp # null

```

```

    b_xvel(bp) = grand
      b_yvel(bp) = grand
    bp = b_next(bp)
  endLoop
  _cycle = abs(int(grand*1000))
  ii = out('Number of cycle = '+string(_cycle))
  command
    pause ;Pause to read the message
  endcommand
end
;-----
def N_ball
  ;Print out ball coordinations
  bp = ball_head
  loop while bp # null
    bx3 = b_x(bp)
    by3 = b_y(bp)
    brdd = b_rad(bp)
    oo = out(string(bx3)+' '+string(by3)+' '+string(brdd))
    bp = b_next(bp)
  endloop
end
;-----
setdata
et2_setup
plots_preprocessig
property density 1500 kn=1000000 ks=1000000 fric=0.2
pause
N_ball1
property density 1500 kn=1000000 ks=1000000 fric=0.2
BVelocity
ini rad mul 1.12121212
cycle _cycle
ini rad mul 0.891891
N_ball
set log off
return

```

## **Publications**

### **Journal articles**

ISMAIL, Y., SHENG, Y., YANG, D. & YE, J. 2015. Discrete element modelling of unidirectional fibre-reinforced polymers under transverse tension. *Composites Part B: Engineering*, 73, 118-125

ISMAIL, Y., D. YANG AND J. YE. 2016. Discrete element method for generating random fibre distributions in micromechanical models of fibre reinforced composite laminates. *Composites Part B: Engineering* 90: 485-492

ISMAIL, Y., D. YANG and J. YE (2016). A DEM model for visualising damage evolution and predicting failure envelope of composite lamina under biaxial loads. *Composites Part B: Engineering* **102**: 9-28

### **Presentations**

ISMAIL, Y. and YE, J. 2015. Microscopic modelling of fibre reinforced composite – a DEM approach. N8 HPC Network Event-Multiscale Computational Mechanics. Sheffield University.